Communauté
UNIVERSITÉ Grenoble Alpes

THÈSE

Pour obtenir le grade de

DOCTEUR DE L'UNIVERSITÉ DE GRENOBLE

Spécialité : **Modéles, mèthodes et algorithmes en biologie, santè et environnement**

Arrêté ministérial : du 7 août 2006

Présentée par

Ahmad BIJAR

Thèse dirigée par **Yohan PAYAN**
et codirigée par **Pascal PERRIER**

préparée au sein **laboratoire Techniques de l'Ingénierie Médicale et de la Complexité - Informatique, Mathématiques et Applications de Grenoble (TIMC-IMAG)**
et de **l'Ecole Doctorale Ingénierie pour la Santé, la Cognition et l'Environnement (EDISCE)**

Development of patient-specific biomechanical models using non-linear registration techniques

Thèse soutenue publiquement le **15 January 2017**,
devant le jury composé de :

M. Stéphane Cotin
DR INRIA, ICube Strasbourg, Rapporteur
M. Jean-Louis DILLENSEGER
MCF, Institut Universitaire de Technologie de Rennes, INSERM U1099, Rennes, Rapporteur
M. Laurent Lamalle
IR INSERM, UGA, Examinateur
M. Georges Bettega
PU-PH, CHU Annecy, Examinateur

Abstract

During the last years, there has been growing and considerable interest in using computer-aided medical design, diagnosis, and decision-making techniques that are rapidly entering the treatment mainstreams. These techniques play an important role in operating rooms where minimally invasive surgery is needed. Predicting surgical outcomes can be done using biomechanical simulations of the organs that are subjected to the manipulations. Finite Element Analysis (FEA) of 3D models is one of the most popular and efficient numerical methods that can be utilized for solving complex problems like deformation of soft tissues or orthopedic implant designs/configurations. However, the accuracy of solutions highly depends upon the quality and accuracy of designed Finite Element Meshes (FEMs). In clinical applications, the generation of such high-quality subject/patient-specific meshes can be extremely time consuming and labor intensive as the process includes geometry extraction of the target organ and meshing algorithms. Various studies have addressed these challenges by employing atlas-based frameworks (e.g., by deformation of an atlas FE mesh) that enable bypassing or collapsing this process. However, these methods still rely on the geometrical description of the target organ, such as contours, 3D surface models, or a set of land-marks. In this context, the aim of this thesis is to investigate how registration techniques can overcome these bottlenecks of atlas-based approaches.

We first propose an automatic atlas-based method that includes the volumetric anatomical/structural image registration and the morphing of an atlas FE mesh. The method extracts a 3D transformation by registering the atlas' volumetric image to the subject's one. The subject-specific mesh is then generated by deforming a high-quality atlas FE mesh using the derived transformation. The registration process is designed is such a way to preserve the regularity and the quality of meshes for subsequent FEAs. A first step towards the evaluation of our approach, namely the accuracy of the inter-subject registration process, is provided using a publicly available data set of CT ribcage. Then, with a particular focus on the mesh quality assessment, subject-specific tongue meshes are generated for two healthy subjects and two patients suffering from tongue cancer. Furthermore, in order to illustrate a tentative fully automatic process compatible with the clinical constraints, some functional consequences of a tongue surgery are simulated

for one of the patients, where the removal of the tumor and the replacement of the corresponding tissues with a passive flap are modeled. With a method that does not require any formal extraction of prior-knowledge on the shape of the target organ and any meshing algorithm, high-quality subject-specific FE meshes are generated while subject's geometrical properties are successfully captured.
Following this method, we accordingly develop an original atlas-based approach that employs the information provided by the anatomical images and diffusion tensor imaging (DTI) based muscle fibers for the recognition and registration of fiber-bundles that can be integrated in the subject-specific FE meshes. In contrast to the DT MR images registration techniques that include reorientation of tensors within or after the transformation estimation, our Image-and-Fiber based Identification-and-Registration technique (IFIR) avoids this issue and directly aligns fiber-bundles. This also enables one to handle limited or distorted DTIs by deformation of an atlas fibers' structure according to the most reliable and non-distorted subject's ones. Such a manner becomes very important, since the classification and the determination of muscular sub-structures need manual intervention of thousands or millions of fibers for each subject, which are highly influenced by the limitations associated with the DTI image acquisition process (e.g., geometrical distortions) and fiber tractography techniques. To evaluate the performance of IFIR in the recognition of subject's fiber-bundles and accordingly in the deformation of the atlas ones, a simulated data set is utilized. In addition, feasibility of IFIR is demonstrated on a clinically acquired human tongue data set. The obtained results show the efficiency of our method in recognition and registration of fiber-bundles.

Résume

Les techniques de chirurgie assistée par ordinateur suscitent depuis quelques années un vif intérêt, depuis l'aide au diagnostic jusqu'à l'intervention chirurgicale elle-même, en passant pas les prises de décision. On peut ainsi, en particulier, envisager de prédire et évaluer les conséquences fonctionnelles de l'acte chirurgical grâce à la simulation du comportement des organes impactés à l'aide de modèles biomécaniques. Dans ce but, l'Analyse par Éléments Finis (AEF) du comportement de modèles biomécaniques tridimensionnels est une des méthodes numériques les plus utilisées et les plus efficaces ; elle permet en particulier d'étudier des problèmes complexes comme la déformation des tissus mous ou la conception d'implants orthopédiques. Cependant, la fiabilité des solutions de l'AEF dépend fortement de la qualité et de la finesse de la représentation des organes sous la forme de maillages d'éléments finis (MEF). Or la génération de tels maillages peut être extrêmement longue et exigeante en ressources computationnelles, car dans le plus grand nombre des outils mis en œuvre pour cela, il est nécessaire de procéder à l'extraction précise de la géométrie de l'organe-cible à partir d'images médicales avant de recourir à des algorithmes sophistiqués de maillage. Ces problèmes deviennent de véritables verrous méthodologiques dans le cas d'applications cliniques, où il est essentiel que la spécificité de chaque patient soit prise en compte, ce qui implique pour chaque patient la génération de maillages spécifiques. Confrontés à ces enjeux, certains travaux se sont attachés à éviter la procédure de maillage en exploitant des méthodes fondées pour chaque patient sur la déformation géométrique d'un maillage défini sur un sujet de référence, dit « Atlas ». Mais ces méthodes nécessitent toujours une description géométrique précise de l'organe-cible du patient, sous la forme de contours, de modèles surfaciques tridimensionnels ou d'un ensemble de points de référence. Dans ce contexte, le but de la thèse est de développer une méthodologie de conception automatique de maillages « patient-spécifiques », basée sur un Atlas, mais évitant cette étape de segmentation de la géométrie de l'organe-cible du patient.

Dans une première partie de la thèse, nous proposons une méthode automatique qui, dans une première phase, procède au recalage volumétrique de l'image anatomique de l'Atlas sur celle du patient, afin d'extraire la transformation géométrique permettant de passer de l'Atlas au patient, puis, dans une seconde phase, déforme le maillage de l'Atlas et l'adapte au patient en lui

appliquant cette transformation. Le processus de recalage est conçu de telle manière que la transformation géométrique préserve la régularité et la haute qualité du maillage. L'évaluation de notre méthode, à savoir l'exactitude du processus de recalage inter-sujets, s'est faite en deux étapes. Nous avons d'abord utilisé un ensemble d'images CT de la cage thoracique, en accès libre. Puis nous avons exploité des données IRM de la langue que nous avons recueillies pour deux sujets sains et deux patients souffrant de cancer de la langue, en condition pré- et post-opératoire. Pour démontrer l'importance de notre méthode dans un contexte clinique, nous avons utilisé les maillages adaptés à l'un des patients pour simuler la réponse biomécanique de la langue à l'activation d'un muscle important de la langue, avant et après l'ablation de la tumeur.

Dans une seconde partie, nous développons une nouvelle méthode, toujours basée sur un Atlas, qui exploite à la fois l'information fournie par les images anatomiques et celle relative à la disposition des fibres musculaires telle qu'elle est décrite par imagerie par résonance magnétique du tenseur de diffusion (RM-DT). Cette nouvelle démarche s'appuie ainsi, d'abord sur le recalage anatomique proposé dans notre première méthode, puis sur l'identification d'un ensemble de faisceaux de fibres musculaires qui seront ensuite intégrés aux maillages « patient-spécifiques ». Contrairement aux techniques usuelles de recalage d'images RM-DT, qui impliquent pour chaque image la réorientation des tenseurs de diffusion soit au cours de l'estimation de la transformation géométrique, soit après celle-ci, notre technique ne nécessite pas cette réorientation et recale directement les faisceaux de fibres de l'Atlas sur ceux du patient. Cette méthode présente l'avantage de permettre le traitement d'images RM-DT de qualité limitée ou incluant des distorsions géométriques, en donnant la possibilité de sélectionner les faisceaux de fibres musculaires qui seront recalés, et de ne retenir que les plus fiables et les moins déformés dans les données du patient. Une telle démarche est très importante, car la détermination et l'identification précises de toutes les sous-structures musculaires nécessiteraient une intervention manuelle pour analyser des milliers, voire des millions, de fibres, qui sont grandement influencées par les limitations et aux distorsions inhérentes aux images RM-DT et aux techniques de tractographie des fibres. L'efficacité de notre méthodologie est démontrée par son évaluation sur un ensemble d'images IRM et RM-DT de la langue d'un sujet.

Contents

List of Figures

List of Tables

"Your task is not to seek for love, but merely to seek and find all the barriers within yourself that you have built against it."
- Jalaluddin Rumi

1

General Introduction

This chapter provides an overview of the thesis and its organization; beginning with an illustration of the motivation and objectives.

Orthognathic surgery involves a wide variety of surgical procedures performed to reposition maxilla, mandible and the dento-alveolar segments to achieve facial and occlusal balance. The consequences of these repositioning can be important as concerns facial soft tissues aesthetics and dynamics. In a similar way, tongue surgery can have severe consequences on tongue mobility and tongue deformation capabilities. It can generate strong impairments of three basic functions of human life, i.e. masticating, swallowing and speaking, which induce a noticeable decrease in the quality of life of the patients. Finite Element models of the patient face used to simulate the morphological modifications following bone repositioning could greatly improve the planning of orthognathic interventions, for both the surgeon and the patient. Similarly, a biomechanical patient-specific tongue model can be used to simulate the consequences of surgical gestures such as hemiglossectomies or resection of the mouth floor. However, if we want to apply such a model-driven approach in a routine clinical context, one of the bottlenecks will be

the automatic patient-specific generation of the Finite Element (FE) models. Indeed, such a process is still a long and tedious task, especially for the generation of the FE mesh for which a manual design is often needed with the inclusion of muscular sub-structures, skin layers as well as the constraint for an hexahedron-dominant meshing (to avoid any locking phenomena observed with tetrahedron-dominant meshes in the case of quasi-incompressible soft tissues). In this context, we think a very promising direction is the use of (1) an existing atlas FE mesh (manually designed from 3D CT and/or MRI exams) and (2) the registration of that atlas to make it fit to each patient data. This mesh-morphing process should be based on image voxels information with the determination of the optimal 3D transform that is going to match the CT (or MRI) exam of the atlas onto the CT (or MRI) exam of the patient. Such intensity-based 3D image registration should therefore avoid the complex segmentation process of patient data which is still difficult to be carried out automatically. In addition, we think other information provided by some imaging data (such as fiber directions measured on Diffusion Tensor Imaging) could be used by the registration process in order to estimate the patient-specific organization of tongue muscular structures, which is very important if we want to estimate post-operative tissues deformations due to muscles activations. In this context, the organization of this thesis manuscript is as follows

- In chapter 2, an introduction to finite element analysis (FEA) and its requirements is provided. Then, we review the standard/conventional methods that are being used to generate subject-specific finite element meshes (FEMs). This enables the reader to identify the bottlenecks of these techniques and more importantly to overview the investigations that are reported in the literature for various applications during the last years (to overcome the challenges associated to the standard strategies and facilitating the mesh generation process by employing an atlas FE mesh and subject-specific information).

- In chapter 3, considering the limitations of the standard and the current atlas-based/assisted mesh generation techniques, we propose an automatic atlas-based method for generating subject-specific meshes. Our main objective is to develop an approach that (1) does not require any prior-knowledge to be extracted from medical images for the

description of target organ's geometry and (2) does not include any meshing process. This is done through the deformation of an atlas FE mesh using a 3D transformation which is extracted by registering the atlas' 3D medical image to the subject's one. The main concern of this chapter is how to design a 3D image registration process that preserves the quality of FE meshes after deformation.

- In chapter 4, with the aim to include subject-specific information of muscle fiber-bundles within the generated FE meshes, an atlas-based approach is proposed. The fundamental scheme of the method is (1) to provide a correspondence between atlas' and subject's fiber-bundles and then (2) to deform atlas' fibers according to the subject's muscular fiber structure. The main concern of this chapter is how to design such a method that can overcome the limitations associated with DT-MR images registration and with DTI distortions.

- In chapter 5, we summarize our contributions in this dissertation and suggest some future research directions motivated by this work.

"You were born with wings, why prefer to crawl through life?"
- Jalaluddin Rumi

2

Introduction to the Subject-Specific FE Mesh Generation Techniques

Contents

During the last decades, Finite Element (FE) meshes are used for countless applications in biomedical engineering to model and simulate the behavior of biological structures. Traditionally, two critical points are encountered in the mesh generation process: (1) the extraction/segmentation of the region of interest (ROI), and (2) the meshing. For clinical applications, this process is time-consuming and many tasks need to be manually done. Therefore, many efforts are dedicated to the generation of subject-specific meshes on the basis of a previously designed atlas/template mesh. In this chapter, we are going to review these methods and introduce the limitations that face the designer of biomechanical models.

2.1 Mathematical Modeling and Numerical Analysis

Mathematical models play a prominent role in a wide range of fundamental and applied researches, including engineering design and decision making. The process of developing a mathematical model is called ***mathematical modeling***, and consists of extracting and formalizing an analytical description for a physical phenomenon. These descriptions of how a phenomenon or process in nature has emerged and developed, can be provided by applying fundamental laws of physics. Such models can give us unique qualitative and quantitative insights into the phenomena under investigation, which can be used to validate hypotheses made from experimental data and also provide predictions. With the aim to model a physical system or process, one may need to make assumptions about the nature of them (i.e., how they work) and also to use the laws and a set of premises or axioms governing the phenomena. On the whole, this modeling leads to a formalized representation that includes a functional relationship between dependent variables, independent variables, parameters, and forcing functions (Chapra and Canale [2011]). ***Forcing functions*** refer to those external influences that act upon the system. Although these models are developed using some simplifications, many control variables and adjustable parameters are often

included. In addition, the models may lead to very complex differential and/or integral equations posed on complex geometrical domains. Prior to the advancement of computer technology, the mathematical modeling needed to be simplified to a level that they could be solved analytically. Nowadays, however, ***Numerical methods*** are extensively used for simulating/solving/approximating sophisticated models of physical phenomena. The basic idea behind ***Numerical methods*** is to reformulate mathematical problems in order to simulate them using arithmetic operations (Chapra and Canale [2011]). In other words, numerical methods typically transform a continuum problem into a discrete one that can be approximated using computers. Fig. 2.1 shows an example of the use of ***Numerical methods*** in order to approximate the area under the graph of a function. In this example, Numerical integration is performed via the trapezoidal method in which the integration over an interval is approximated by breaking the area down into N trapezoids with more easily computable areas, in which the integral of f from $x = a$ to $x = b$ is approximated as

$$I = \int_a^b f(x)dx \quad \approx \quad \left(\frac{b-a}{2N}\right) \sum_{n=1}^{N} (f(x_n) + f(x_{n+1})) \quad = \tag{2.1}$$
$$\left(\frac{b-a}{2N}\right) [f(x_1) + 2f(x_2) + ... + 2f(x_N) + f(x_{N+1})] \,,$$

where the spacing between the points is equal to the scalar value $\left(\frac{b-a}{2N}\right)$. If the spacing between points is not constant, the fourmula generalizes to

$$I = \int_a^b f(x)dx \quad \approx \quad \left(\frac{1}{2}\right) \sum_{n=1}^{N} (x_{n+1} - x_n) [(f(x_n) + f(x_{n+1}))] \tag{2.2}$$

where $(x_{n+1} - x_n)$ is the spacing between each consecutive pair of points.

Generally, a wide range of numerical methods have been developed and applied during the last decades, each with its own inherent set of principles, aims, and of course, limitations. The ***Finite Element method (FEM)*** or ***Finite Element Analysis (FEA)*** is one of the most popular numerical methods in the literature. In FEA, the system or object is sub-divided into a finite number of smaller units, called finite elements. In other words, the analysis is performed by modeling an object into simplified representations of of discrete regions. Partial differential equations (PDE) that govern the

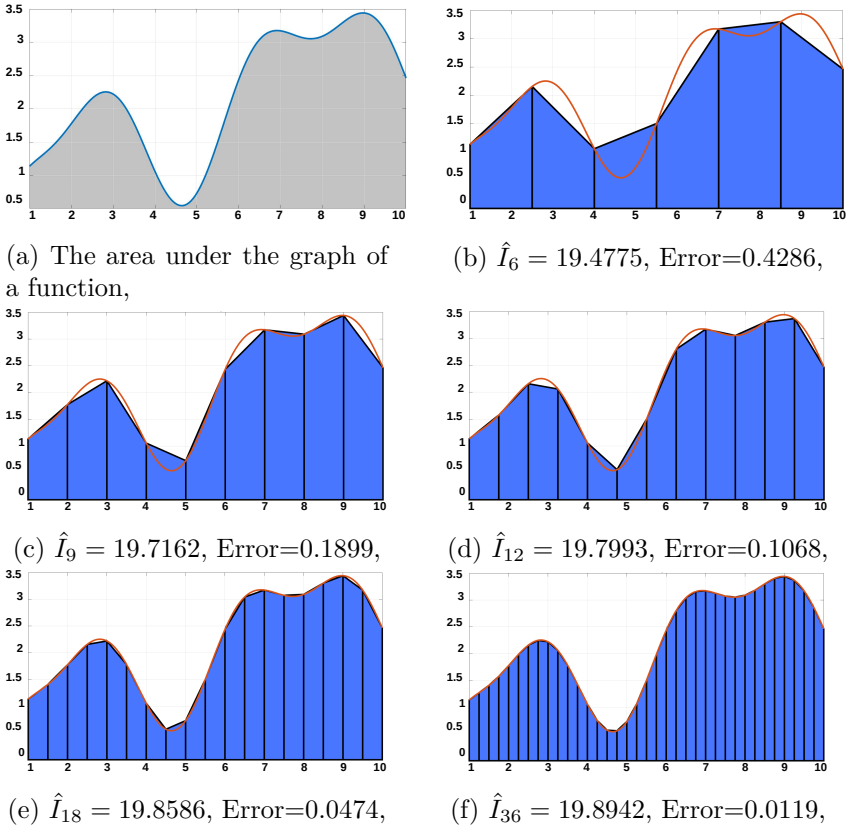

(a) The area under the graph of a function, (b) $\hat{I}_6 = 19.4775$, Error=0.4286, (c) $\hat{I}_9 = 19.7162$, Error=0.1899, (d) $\hat{I}_{12} = 19.7993$, Error=0.1068, (e) $\hat{I}_{18} = 19.8586$, Error=0.0474, (f) $\hat{I}_{36} = 19.8942$, Error=0.0119,

Figure 2.1: Approximation the area under the graph of a function by breaking the region into trapezoids; the Error is equal to the difference between the approximated and the real values.

model behavior are solved approximately. This is done by rendering the complex PDEs into equivalent ordinary differential equations and subsequently approximation of a solution using linear algebra techniques (Roduit et al. [2005]). Therefore, we can summarize the main steps in finite element analysis:

- Discretization of the main domain,

    1. The discretization of the physical object into a structure is *called* ***Mesh generation*** or ***Meshing***,
    2. Each sub-domain is called element,
    3. The points where elements connect are *called* ***nodes***,
    4. The collection of elements is *called* ***finite element mesh***,

- Considering the equations that are already defined within each subdomain or ***element***.
- Assembling the solutions or element equations.
- Error estimation and convergence.

2.1.1 Continuum Mechanics and FEA

Continuum Mechanics (CM) models materials as a continuum by ignoring the fact that they are made of micro structures or atoms. This allows to study the mechanical response of continuous media to applied forces or loadings. In biomedical sciences, CM covers essential principles and fundamental applications like computer-aided minimally invasive surgery in which deformation of soft tissues due to the surgical manipulations can be studied. On this matter, a deformable model that describes the target organ's geometry and its material properties is needed. For such contexts, according to the type of materials, CM provides mathematical models that are commonly based on partial differential equations (PDEs). The relationships between the strain and stress, which are measures of the deformation and the forces in the target organ, are formulated based on the PDEs. More information about such PDEs can be found in Timoshenko and Goodier [1971]; Ottosen and Petersson [1992]; Crouch [2003].
A wide range of models with different complexity are proposed for simulating the behavior of soft materials. To address the technical and practical aspects of finite element analysis in bio-mechanics, a finite element problem that assumes ***linear elasticity*** for modeling the *deformation process* is presented in the following (Crouch [2003]). Linear elasticity is the most idealized solid model that is defined under some assumptions: (1) deformations occur instantly, (2) the effects that temperature and strain rate may introduce to the deformation process are ignored, (3) a linear relationship between stress and strain is assumed, and (4) the solid object immediately returns to its primary form after removing a deforming stress. Before going into the detailed mathematical basis of a linear elastic model, it is important to describe *Strain* and *Stress* terms:

- **Strain** is a unitless measure of how an object deforms from an applied force or load. Considering a point $X = [X_x\ X_y\ X_z]$, its displacement

is represented by $u(X)$ and any change of distance between the points in the neighborhood of X is determined by normal strains $\epsilon_{xx} = \frac{\partial u_x}{\partial x}$, $\epsilon_{yy} = \frac{\partial u_y}{\partial y}$, and $\epsilon_{zz} = \frac{\partial u_z}{\partial z}$. Similarly, the deformation caused by any change in angle between two originally orthogonal material lines is defined as $\epsilon_{xy} = \frac{\partial u_x}{\partial y} + \frac{\partial u_y}{\partial x}$, $\epsilon_{xz} = \frac{\partial u_x}{\partial z} + \frac{\partial u_z}{\partial x}$, and $\epsilon_{yz} = \frac{\partial u_y}{\partial z} + \frac{\partial u_z}{\partial y}$. Therefore, a linear strain tensor that measures local deformation can be expressed as

$$\epsilon = \begin{bmatrix} \epsilon_{xx} & \epsilon_{xy} & \epsilon_{xz} \\ \epsilon_{xy} & \epsilon_{yy} & \epsilon_{yz} \\ \epsilon_{xz} & \epsilon_{yz} & \epsilon_{zz} \end{bmatrix} \tag{2.3}$$

- **Stress** is a measure of the forces in a deformable object. There are two types of forces: surface and body. Surface forces are applied locally to the object's surface while body forces like gravity are applied to the whole object's volume. Stress is the average force per unit area and a stress or traction vector is defined as the limiting value of the force to area ratio when the area shrinks to zero: $\overrightarrow{t} = \frac{\delta P}{\delta A} = [t_x\ t_y\ t_z]^T$, where P is the applied force to a patch of surface A. For patches perpendicular to the main coordinate axes, the traction vectors are defined as

$$\overrightarrow{t} = \begin{bmatrix} t_{xx} \\ t_{xy} \\ t_{xz} \end{bmatrix} \text{ when the patch surface normal is } \overrightarrow{n} = \begin{bmatrix} 1 \\ 0 \\ 0 \end{bmatrix},$$

$$\overrightarrow{t} = \begin{bmatrix} t_{xy} \\ t_{yy} \\ t_{yz} \end{bmatrix} \text{ when the patch surface normal is } \overrightarrow{n} = \begin{bmatrix} 0 \\ 1 \\ 0 \end{bmatrix},$$

$$\overrightarrow{t} = \begin{bmatrix} t_{xz} \\ t_{yz} \\ t_{zz} \end{bmatrix} \text{ when the patch surface normal is } \overrightarrow{n} = \begin{bmatrix} 0 \\ 0 \\ 1 \end{bmatrix},$$

subsequently, a stress tensor is defined as

$$\sigma = \begin{bmatrix} \sigma_{xx} & \sigma_{xy} & \sigma_{xz} \\ \sigma_{xy} & \sigma_{yy} & \sigma_{yz} \\ \sigma_{xz} & \sigma_{yz} & \sigma_{zz} \end{bmatrix} \tag{2.4}$$

and the traction vector $\overrightarrow{t}$ is computed for any surface patch normal using the obtained tensor, $\overrightarrow{t} = \sigma \overrightarrow{n}$.

For linearly elastic materials, according to the generalized Hooke's law, the relationship between the stress and strain is assumed linearly as

$$\sigma_{ij} \;=\; c_{ijkl}\, \epsilon_{kl} \tag{2.5}$$

where σ_{ij} and ϵ_{kl} are respectively the stress and strain tensors' components; and c_{ijkl} are constant coefficients based on the elastic properties of the material. In isotropic materials only two coefficients are considered and the constitutive equation can be rewritten as

$$\sigma_{ij} \;=\; 2\mu\epsilon_{ij} + \delta_{ij}\lambda(\epsilon_{xx} + \epsilon_{yy} + \epsilon_{zz}) \tag{2.6}$$

where δ_{ij} is Kronecker's delta function; and μ and λ are the Lamé coefficients that are related to two the parameters with a physical meaning, namely the Young's modulus (E) and Poisson's ratio (v). E is applied to the "*elasticity*" of the material and corresponds to the stress/strain ratio when a uniaxially force is applied. v is related to the "*compressibility*" of the material and is defined as a ratio of the lateral strain to the axial strain for a uniaxial stress state. In short, the governing equations can be summarized as

$$\underline{\sigma} \;=\; D\, \underline{\epsilon} \tag{2.7}$$

where

$$\underline{\sigma} = \begin{bmatrix} \sigma_{xx} \\ \sigma_{yy} \\ \sigma_{zz} \\ \sigma_{xy} \\ \sigma_{xz} \\ \sigma_{yz} \end{bmatrix} \qquad \underline{\epsilon} = \begin{bmatrix} \epsilon_{xx} \\ \epsilon_{yy} \\ \epsilon_{zz} \\ \epsilon_{xy} \\ \epsilon_{xz} \\ \epsilon_{yz} \end{bmatrix} \tag{2.8}$$

and

$$D = \begin{bmatrix} 2\mu+\lambda & \lambda & \lambda & 0 & 0 & 0 \\ \lambda & 2\mu+\lambda & \lambda & 0 & 0 & 0 \\ \lambda & \lambda & 2\mu+\lambda & 0 & 0 & 0 \\ 0 & 0 & 0 & 2\mu & 0 & 0 \\ 0 & 0 & 0 & 0 & 2\mu & 0 \\ 0 & 0 & 0 & 0 & 0 & 2\mu \end{bmatrix} \tag{2.9}$$

and accordingly, the Young's modulus (E), Poisson's ratio (v), λ, and μ coefficients are determined as

$$E = \frac{\mu(3\lambda+2\mu)}{\lambda+\mu} \tag{2.10}$$

$$v = \frac{\lambda}{2(\lambda+\mu)} \tag{2.11}$$

$$\lambda = \frac{Ev}{(1-2v)(1+v)} \tag{2.12}$$

$$\mu = \frac{E}{2v+2} \tag{2.13}$$

the coefficient matrix D can also be written in terms of Young's modulus and Poisson's ratio

$$D = \frac{E}{(1-2v)(1+v)} \begin{bmatrix} 1-v & v & v & 0 & 0 & 0 \\ v & 1-v & v & 0 & 0 & 0 \\ v & v & 1-v & 0 & 0 & 0 \\ 0 & 0 & 0 & \frac{1}{2}-v & 0 & 0 \\ 0 & 0 & 0 & 0 & \frac{1}{2}-v & 0 \\ 0 & 0 & 0 & 0 & 0 & \frac{1}{2}-v \end{bmatrix} \tag{2.14}$$

After establishing the relationships between the strain and stress coefficients, it is considered that all applied forces are balanced. In other words, for an object to be static/stationary, the net force is zero. In classical mechanics, such an object is *called* to be in *mechanical equilibrium*. The force equilibrium conditions are described by partial differential equations that accounts for the stress tensor and any applied body forces. Considering a body force

of $\overrightarrow{b} = [b_x\ b_y\ b_z]^T$, the force equilibrium equations are written as

$$\begin{aligned}
\frac{\partial \sigma_{xx}}{\partial x} + \frac{\partial \sigma_{xy}}{\partial y} + \frac{\partial \sigma_{xz}}{\partial z} + b_x = 0, \\
\frac{\partial \sigma_{xy}}{\partial x} + \frac{\partial \sigma_{yy}}{\partial y} + \frac{\partial \sigma_{yz}}{\partial z} + b_y = 0, \\
\frac{\partial \sigma_{xz}}{\partial x} + \frac{\partial \sigma_{yz}}{\partial y} + \frac{\partial \sigma_{zz}}{\partial z} + b_z = 0,
\end{aligned} \tag{2.15}$$

By substitution of Eq. 2.6 and normal strains into the above force equilibrium equations, the following formulations are derived

$$\begin{aligned}
&\mu\left(\frac{\partial^2 u_x}{\partial x^2} + \frac{\partial^2 u_y}{\partial x^2} + \frac{\partial^2 u_z}{\partial x^2}\right) + (\mu+\lambda)\frac{\partial}{\partial x}\left(\frac{\partial u_x}{\partial x} + \frac{\partial u_y}{\partial y} + \frac{\partial u_z}{\partial z}\right) + b_x = 0 \\
&\mu\left(\frac{\partial^2 u_x}{\partial y^2} + \frac{\partial^2 u_y}{\partial y^2} + \frac{\partial^2 u_z}{\partial y^2}\right) + (\mu+\lambda)\frac{\partial}{\partial y}\left(\frac{\partial u_x}{\partial x} + \frac{\partial u_y}{\partial y} + \frac{\partial u_z}{\partial z}\right) + b_y = 0 \\
&\mu\left(\frac{\partial^2 u_x}{\partial z^2} + \frac{\partial^2 u_y}{\partial z^2} + \frac{\partial^2 u_z}{\partial z^2}\right) + (\mu+\lambda)\frac{\partial}{\partial z}\left(\frac{\partial u_x}{\partial x} + \frac{\partial u_y}{\partial y} + \frac{\partial u_z}{\partial z}\right) + b_z = 0
\end{aligned} \tag{2.16}$$

that can be summarized in

$$\mu\nabla^2\overrightarrow{u} \ + \ (\mu+\lambda)\nabla(\nabla^T\overrightarrow{u}) + \overrightarrow{b} = 0 \tag{2.17}$$

As can be seen, this description of the model includes second order derivatives (*strong form*). Before applying finite element method, a *weak form* of PDEs that only includes first order derivatives is needed. Generally speaking *weak form* that governs integral equations is an alternative way and more convenient of stating the underlying mathematical basis of the problem. In this regard, a weighting function is multiplied to the equation and then integrated. Let $v(\overrightarrow{x}) = [v_x\ v_y\ v_z]$ be an arbitrary weighting function which is defined over the problem's spatial domain. This function is multiplied to the force equilibrium equations (2.15) and then the integration over the whole volume (V) leads to

$$\int_V (\widetilde{\nabla} v(\overrightarrow{x}))^T \underline{\sigma} \mathrm{d}V \ = \ \int_S v^T \overrightarrow{t}\, \mathrm{d}S \ + \ \int_V v^T \overrightarrow{b}\, \mathrm{d}V \tag{2.18}$$

where S is the surface of volume, and

$$\widetilde{\nabla} v(\overrightarrow{x}) = \begin{bmatrix} \frac{\partial v_x}{\partial x} \\ \frac{\partial v_y}{\partial y} \\ \frac{\partial v_z}{\partial z} \\ \frac{\partial v_x}{\partial y} + \frac{\partial v_y}{\partial x} \\ \frac{\partial v_x}{\partial z} + \frac{\partial v_z}{\partial x} \\ \frac{\partial v_y}{\partial z} + \frac{\partial v_z}{\partial y} \end{bmatrix} \tag{2.19}$$

For the detailed conversion mathematical process, the reader is directly refereed to Crouch [2003]. Now that a weak form is obtained, a discrete approximation of the solution can be achieved using the finite element method in three main steps: (1) generation of a mesh across the space for which a solution of problem is being seek, (2) estimation of a solution for the nodes of the mesh, (3) deriving a continuous solution for the whole space by interpolating the nodes' solutions.

In the case of linear finite element meshes, the displacement filed is interpolated between the nodes using linear functions. The interpolation of the solutions are controlled by the "*shape functions*" of the nodes that vary between one to zero across the elements that touch the nodes. This in turn means that the shape function is equal to one at node's location and is equal to zero at all points outside the corresponding elements. Therefore, for each point in an element, the displacement is computed as a weighted sum of the displacements of element's nodes. Considering a 3D mesh with n nodes, the shape function can be written as

$$N(\overrightarrow{x}) = \begin{bmatrix} N_1(\overrightarrow{x}) & 0 & 0 & N_2(\overrightarrow{x}) & 0 & 0 & \cdots & N_n(\overrightarrow{x}) & 0 & 0 \\ 0 & N_1(\overrightarrow{x}) & 0 & 0 & N_2(\overrightarrow{x}) & 0 & 0 & \cdots & N_n(\overrightarrow{x}) & 0 \\ 0 & 0 & N_1(\overrightarrow{x}) & 0 & 0 & N_2(\overrightarrow{x}) & 0 & 0 & \cdots & N_n(\overrightarrow{x}) \end{bmatrix} \tag{2.20}$$

where $\overrightarrow{x}$ is a position vector, and $N_1, \cdots, N_n$ are the shape functions. Then, the continuous displacement function can be written as

$$u(\overrightarrow{x}) = N(\overrightarrow{x})\underline{a} \tag{2.21}$$

where

$$\underline{a} = \begin{bmatrix} u_{1x} \\ u_{1y} \\ u_{1z} \\ \vdots \\ u_{nx} \\ u_{ny} \\ u_{nz} \end{bmatrix} \tag{2.22}$$

with $[u_{ix}\ u_{iy}\ u_{iz}]$ denoting the displacement of the i^{th} node. Now the components of strain tensor can be rewritten as

$$\underline{\epsilon} = \begin{bmatrix} \epsilon_{xx} \\ \epsilon_{yy} \\ \epsilon_{zz} \\ \epsilon_{xy} \\ \epsilon_{xz} \\ \epsilon_{yz} \end{bmatrix} = \begin{bmatrix} \frac{\partial u_x}{\partial x} \\ \frac{\partial u_y}{\partial y} \\ \frac{\partial u_z}{\partial z} \\ \frac{\partial u_x}{\partial y} + \frac{\partial u_y}{\partial x} \\ \frac{\partial u_x}{\partial z} + \frac{\partial u_z}{\partial x} \\ \frac{\partial u_y}{\partial z} + \frac{\partial u_z}{\partial y} \end{bmatrix} = \widetilde{\nabla} u = \widetilde{\nabla}(N(\overrightarrow{x})\underline{a}) = B\underline{a} \tag{2.23}$$

where

$$B = \widetilde{\nabla} N = \begin{bmatrix} \frac{\partial N_1}{x} & 0 & 0 & \frac{\partial N_2}{x} & 0 & 0 & \cdots & \frac{\partial N_n}{x} & 0 & 0 \\ 0 & \frac{\partial N_1}{y} & 0 & 0 & \frac{\partial N_2}{y} & 0 & \cdots & 0 & \frac{\partial N_n}{y} & 0 \\ 0 & 0 & \frac{\partial N_1}{z} & 0 & 0 & \frac{\partial N_2}{z} & \cdots & 0 & 0 & \frac{\partial N_n}{z} \\ \frac{\partial N_1}{y} & \frac{\partial N_1}{x} & 0 & \frac{\partial N_2}{y} & \frac{\partial N_2}{x} & 0 & \cdots & \frac{\partial N_n}{y} & \frac{\partial N_n}{x} & 0 \\ \frac{\partial N_1}{z} & 0 & \frac{\partial N_1}{x} & \frac{\partial N_2}{z} & 0 & \frac{\partial N_2}{x} & \cdots & \frac{\partial N_n}{z} & 0 & \frac{\partial N_n}{x} \\ 0 & \frac{\partial N_1}{z} & \frac{\partial N_1}{y} & 0 & \frac{\partial N_2}{z} & \frac{\partial N_2}{y} & \cdots & 0 & \frac{\partial N_n}{z} & \frac{\partial N_n}{y} \end{bmatrix} \tag{2.24}$$

Accordingly, the earlier weak form of the linear elastic PDE (Eq. 2.18) is rewritten as

$$K\underline{a} = \underline{f} \tag{2.25}$$

where $\underline{a}$ contains the displacements of nodes and

$$K = \int_V B^T D B \mathrm{d}V \tag{2.26}$$

$$\underline{f} = \int_S N^T \overrightarrow{t}\, \mathrm{d}S + \int_V N^T \overrightarrow{b}\, \mathrm{d}V \tag{2.27}$$

Assuming a mesh of n nodes, Eq. 2.25 holds a system of $3n \times 3n$. Some boundary conditions may also be specified to the problem; therefore, the size of the system is reduced and any conventional techniques can be employed for solving the linear system. In the solution, a displacement vector is estimated for each of nodes and a continuous deformation field can be approximated by interpolating the displacements between the nodes.

2.2 Subject-Specific FE mesh generation

According to the previous section, Finite element (FE) analysis of three-dimensional (3D) models provides an efficient computational framework to represent and investigate the actual behavior of complex systems (Salo et al. [2013a]). Conforming to the example provided in section 2.1.1, a volumetric FE mesh is a prerequisite to FE analysis, and computational meshes provide a domain for solving the mathematical description of physical, geometrical and mechanical properties (Naomis and Lau [1990]; Lamata et al. [2014]). Behavior simulations using these biomechanical models can be used to predict the consequences on health of changes in human tissues characteristics associated for example with tissue resections, radiotherapy or aging. FE models are extensively used in computer-aided surgery and diagnosis technologies. In clinical work flow, these models enable a better risk-assessment which is a critical component of treatment decision-making and allow the treatment procedures to be targeted to those most in need. They can be used to optimize the surgical outcome planning and to elaborate virtual tools for practical training of surgeons of physiotherapists, as well as for skills assessment (Dawson et al. [2000]; Cotin et al. [2005]; Wu et al. [2005]; McGregor et al. [2010]; Courtecuisse et al. [2010]; Doyle and McGloughlin [2011]; Miller et al. [2011]; Talbot et al. [2012]; Gomes et al. [2013]). Some studies have shown the effectiveness of virtual training systems in various clinical skills (Gallagher et al. [2005]; Aggarwal et al. [2006, 2007]; Scalese et al. [2008]). In cases where the main objective of such systems is training (e.g. teaching the surgeons new procedures using virtual simulators) or studying the behavior of a specific device (e.g, implant) under different conditions, a generic model can be sufficient. In this regard, the model can be developed from average geometries and material properties. However, when facing a treatment procedure which need great accuracy and specificity, subject/patient-

specific models have to be considered. In such contexts a volumetric mesh that conforms to the geometry of the subject/patient's organ is required. Generation of such meshes is the basic initial step in a successful numerical analysis with finite element method (FEM); as good numerical stability should be achieved when solving governing equations (Lamata et al. [2014]). The conventional process to generate subject/patient-specific meshes from 3D medical images generally involves the following steps (De Putter et al. [2006]; Sastry et al. [2013]):

1. segmentation of the medical images and modeling of invisible structures (if applicable);

2. surface mesh creation;

3. volume mesh generation;

4. optimization of the mesh.

Whereas the clinical decision-making is critically important and often happens on a time-scale of seconds to hours (Kerckhoffs [2010]), this process to generate subject/patient-specific meshes can be extremely time consuming and labor intensive, mainly because of the segmentation step. Indeed, segmentation is not a straightforward task in image processing or computer vision, and the accurate extraction of geometrical information about subject/patient-specific anatomy can require the processing of numerous medical images. Moreover, meshing is a kind of optimization problem taking into account the type and the number of elements and the preservation of accuracy requirements. The convergence rates and overall accuracy of the numerical analysis are highly dependent on the quality of generated meshes. Mesh quality in turn highly depends upon the type of finite elements and the application at hand (Firl et al. [2013]). For the past decades, researchers have been testing different methodologies to overcome these issues by improving segmentation, surface creation and/or meshing processes. However, these methods have shown limitations with efficiencies that are highly depending on the applications. In parallel, a wide range of scenarios employing a generic mesh is reported under different levels of automation, in order to refine the results. The primary purpose of all these studies is to make FE mesh generation compatible with the time constraints of the clinical practice

where the pre/intraoperative time-window is short and clinician availability is limited. In this section, a brief overview of the original framework is provided followed by a review of Generic-based mesh generation techniques (Ho-Le [1988]).

2.2.1 Conventional techniques

The conventional strategy for FE mesh generation is summarized in Fig. 2.2. These methods are also called traditional or standard mesh generation methods (McGregor et al. [2010]). As can be seen, the first step consists of gathering medical images which might be followed by noise reduction, smoothing, normalization and localization of scanned images. Then, ROIs' (Regions Of Interest) boundaries should be manually, semi-automatically, or automatically extracted from the images, depending upon the difficulty of the given task. This step plays a crucial role in mesh generation because it determines the geometry of the organs/structures that are being modeled. A wide range of methods and tools have been developed on medical image segmentation and they are mainly categorized into four groups (Lee et al. [2015]): 1) Thresholding-Based; 2) Region-Based ; 3) Edge-Based ; 4) Clustering-Based methods. Some other techniques exist though such as Level-set methods, Artificial Neural Networks, Registration-based methods, or any combination of them. Each type of method has its own limitation and their performance varies depending on the type of image modalities (CT, MRI, X-Ray, Ultrasound, etc.), on the type of organs or structures being processed (e.g., bones or soft tissues), and also on some other factors (e.g., noise level, motion artefacts, image resolution, partial volume effect, intra- and inter-operator variability, etc.). After the extraction of the ROIs corresponding to the structures being modeled, various meshing algorithms can be employed to generate 3D FE meshes. Two main approaches can be considered for such algorithms:

1. Geometry-based meshing,
2. Grid-based meshing,

Each technique has strengths and weaknesses relative to the others, and this will be explained in the next two sections. Moreover, other perspectives related to the meshing process, namely the element types and mesh quality, are discussed in section 2.2.1.3.

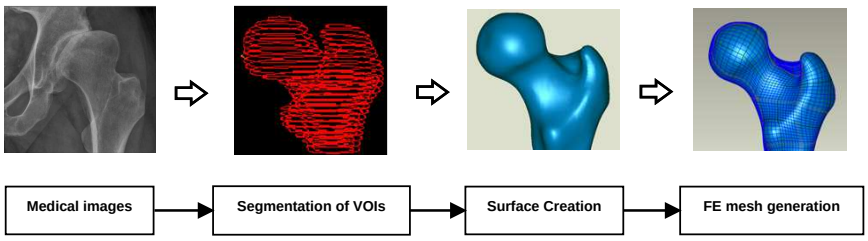

Figure 2.2: Conventional framework for the generation of FE meshes.

2.2.1.1 Geometry-based meshing

Geometry-based algorithms are the most commonly used frameworks (Taylor et al. [2013]). These methods create a 3D surface from segmentation-boundary and then convert it to a 3D FE mesh. Hence, surface creation is a prerequisite in the Geometry-based meshing algorithms. The input to the surface generator is a set of three-dimensional voxel coordinates located on the boundaries of ROIs (or their contours). Early methods assumed that the points lie on curves defined by slicing a surface in 3D space with a collection of parallel planes (Fuchs et al. [1977]; Meyers et al. [1992]; Edelsbrunner [2003]), and their main objective was finding a 3D surface that interpolates the points in the contour links (Park and Kim [1996]) thus approximating the 3D geometry of the ***sampled*** structure or organ (Dey [2006]). In other words, there are many possible surfaces, and one may seek the one that is somehow the most reasonable and best fits a finite set of points scattered in three-dimensional Euclidean space (Edelsbrunner [2003]). In their majority, reconstruction algorithms generate external surfaces using splines (Young et al. [2008]; Taylor et al. [2013]). They consists of three main steps in order to interpolate the surface from the contours (Woodward [1988]; Piegl and Tiller [1995]; Park [2003]): (1) B-spline curve interpolation of each 2D contour; (2) making the B-spline curves exactly compatible via degree elevation and knot insertion; and (3) computation of a B-spline 3D surface interpolating the curves via B-spline surface lofting. However, approximated surfaces suffer from drawbacks such as not capturing the sharp geometrical changes and a poor approximation of regions with bifurcations (Young et al. [2008]; Taylor et al. [2013]). Furthermore, fitting the splines to the segmented two-dimensional cross sections requires the manual selection of control points which may lead to geometric discrepancies between segmented-boundaries and estimated bounding curves (Young et al. [2008]).

Nowadays, thanks to the improvement of the 3D scanner resolution, the Marching Cube (MC) algorithm, that directly extracts a triangulated surface, has become a standard to generate isosurfaces (Lorensen and Cline [1987]; Rajon and Bolch [2003]). MC considers the centers of voxels as the vertices of a lattice or the grid of cubes, and uses voxels intensity values to interpolate the surface location along the segments that join the vertices (i.e., voxels centers). Through the scalar field, MC takes the eight neighbor locations at a time (four each from two adjacent slices) and forms an imaginary cube (see Fig. 2.3(a)), and then determines the polygons needed to represent the part of the isosurface that intersects this cube. In order to find the surface intersections within the cube, data values are evaluated for cube's vertices. If the value exceeds or equals the value of the surface, a *one* is assigned to the cube's vertex, which means this vertex of the cube is located inside the surface, otherwise a *zero* is assigned to the vertex, which means this vertex of the cube is located outside the surface. In this way, MC determines which vertices of the imaginary cube are located inside and outside of the surface, and then creates *surface intersections* within the cube. Since each cube contains eight vertices being inside or outside of the isosurface, there would be $2^8 = 256$ different combinations. However, most of these combinations are topologically equivalent and can be further reduced to 15 patterns (Lorensen and Cline [1987]), as illustrated in Fig. 2.3(b). In each pattern, different number of triangles are created to separate two groups of cube's vetices (i.e., the ones that are located inside the surface and those outside of the surface). Finally, the individual polygons are fused into the desired surface.

MC is very simple, robust, and produces C0 continuous triangulated surfaces that follow the segmentation-boundary. However, some post-processing techniques like smoothing are required to improve the shape of the generated surfaces (Young et al. [2008]; Preetha and Suresh [2012]). At the same time, it raises some challenges that might be addressed for further improvement of performance and capturing the possible geometric degeneracies and ambiguities. In this way, many researchers have focused on developing and improving the MC (Newman and Yi [2006]). After the creation of the surface using MC or its extensions, it can be used to generate higher order CAD representations, or employed by meshing algorithms (e.g., Advancing Front (GrnhH [1982]; Peraire et al. [1987]; Lohner [1988]; Löhner et al.

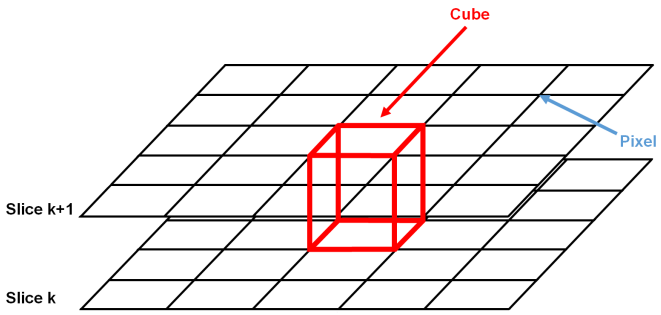

(a)

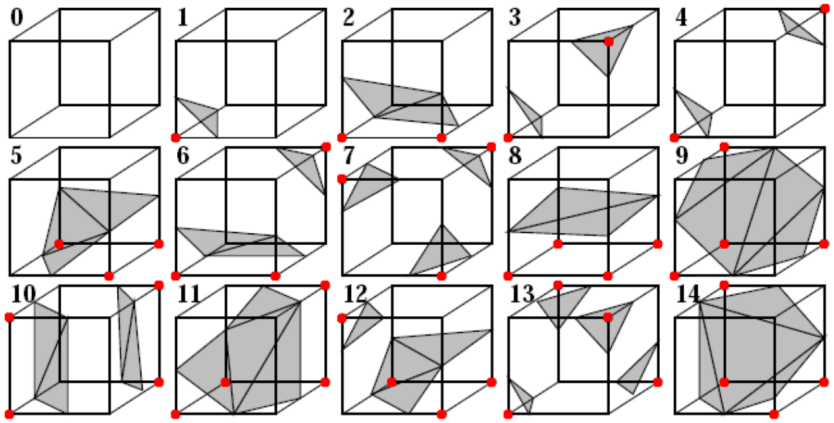

(b)

Figure 2.3: MC algorithm: (a) marching cube (inspired by Lorensen and Cline [1987]) and (b) triangulated cubes (Yanez [2009]).

[1992]; Jin and Tanner [1993]) or Delaunay (Caendish et al. [1985]; Shenton and Cendes [1985]) as a triangulated bounding surface (Young et al. [2008]). As a matter of fact, there are lots of commercial software tools to generate FE meshes automatically or semi-automatically from a segmented surface. They often need manual intervention in case of complex geometries.

2.2.1.2 Grid-based meshing

Previous section described the concept of meshing algorithms that employ a surface mesh. Although theses meshing approaches are designed to be accurate in preserving the geometry of the target organ/structure, a tolerance for geometric distortions may be considered for a better control over the meshing process (e.g., by smoothing the target surface). This in turn means that the conformity of the created surface, namely the one that is be-

ing used by meshing algorithm, to the *real* surface is decreased. Therefore, there would be still motivation to increase the correspondence between the generated surface and the real geometry. On this matter, after the creation of the surface meshes, some nodes may need to be repositioned before volume meshing. This can be done manually or using a geometry-preserving refinement post-processing step. In case of complex geometries, that may include some sub-sections or inner cavities, generating a 3D accurate surface with geometry-based algorithms like MC can become more complicated. Many efforts have been done to overcome these limitations by bypassing the surface creation step (e.g., voxel-based approach (Keyak et al. [1990])) or by collapsing both surface and volume mesh generation into a single process (e.g., VoMaC approach (Müller and Rüegsegger [1995])). These methods are generally referred as "***grid-based***" meshing techniques in the literature. In voxel-based approaches like Keyak et al. [1990], a structured FE mesh is generated directly from the 3D voxel grid after extraction of segmentation-boundary and voxel labeling, by converting each voxel within VOIs into a finite element (i.e., a hexahedral element). The term "***structured***" indicates that the generated mesh is a regular tessellation of a given space. These methods are straightforward because they use voxel grids. Also, when there is an isotropic sampling, it is assured that the generated mesh has an optimal quality. Another advantage is that they can easily handle meshing of multiple VOIs. Moreover, as there is a one-to-one correspondence between the voxels and finite elements, provided intensity information associated with each voxel can be used to assign more detailed and specific material properties to each element in order to study the mechanical behavior of the target organ/structure. However, it could be argued that the surface of generated mesh can be stepped in case of large voxels. On the contrary, if the size of the 3D image is large, such a method generates a huge number of elements leading to long computation times for the corresponding FE model.

Considering these limitations, some researchers have focused on improving the standard strategies (Young et al. [2008]). VoMaC-meshing (Müller and Rüegsegger [1995]) can be considered as one of these techniques which tailors the mesh generation to the original surface generation. VoMac is an extension of the Marching Cube algorithm in which tetrahedron templates are used instead of triangular surface facets. This is done by a complete tetrahedralization of the hexahedral volume and then the creation of a look-

up table for the marching cube algorithm. In comparison with voxel-based methods, the issue of stepped surface is solved by VoMaC thus producing smoother surfaces. However, VoMaC can only be employed to generate single part meshes; this issue can be solved within other improvements (e.g., EVoMAC (Young et al. [2008])).

2.2.1.3 Element types and mesh quality

According to the principles of 2D or 3D FE modeling, surface or volume elements are used to constitute the basic elements of the mesh. The three-dimensional elements are variations of the two-dimensional ones (Fig. 2.4). Generated FE meshes may be composed of different kinds of elements. The most common and basic 2D elements (Triangle and Quadrilateral) and 3D elements (Tetrahedron, Hexahedron, Prism/Wedge, Pyramid) are shown in Fig. 2.5 (see Chabanas et al. [2003]; Henak et al. [2013] for discussions as concerns these types of elements).
The elements can be delimited by straight sides or plans (they are then called ***linear*** elements) or by curved surfaces (for example ***quadratic*** elements). Examples of linear and quadratic elements are represented in Fig. 2.6. As can be seen, in the case of quadratic elements, the edges are quadratic functions and therefore an additional middle point is necessary to describe the function. Also, other higher-order triangular elements are shown in Fig. 2.7. In the literature, a wide range of 3D meshing algorithms are proposed to generate FE meshes containing various types of elements. Generally speaking, the majority of approaches use hexahedral and tetrahedral elements. There are some studies that discuss meshing techniques from the point of element types. For more information, the interested reader is referred to the papers Owen [1998]; Stegmann [2000]; Rousson et al. [2004].

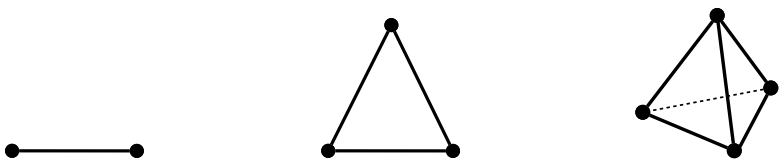

(a) 1D element: Line (b) 2D element: Triangle (c) 3D element: Tetrahedron

Figure 2.4: Finite elements.

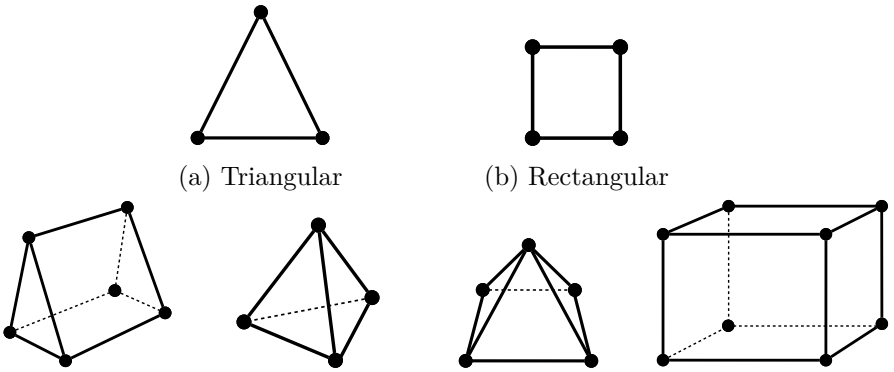

(a) Triangular (b) Rectangular

(c) Prismatic (d) Tetrahedral (e) Pyramidal (f) Hexahedral

Figure 2.5: Node placement and geometry for linear elements: 2D elements are represented in (a) and (b), and 3D elements are represented: (c), (d), (e), and (f).

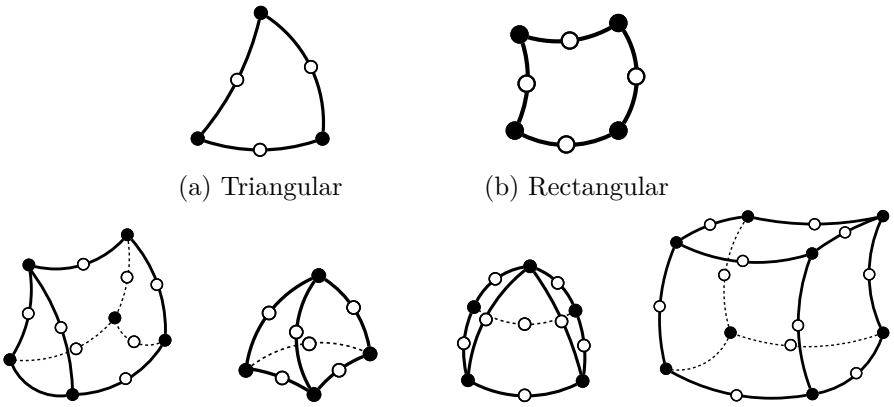

(a) Triangular (b) Rectangular

(c) Prismatic (d) Tetrahedral (e) Pyramidal (f) Hexahedral

Figure 2.6: Node placement and geometry for quadratic elements, 2D elements are represented in (a) and (b), and 3D elements are represented in (c), (d), (e), and (f).

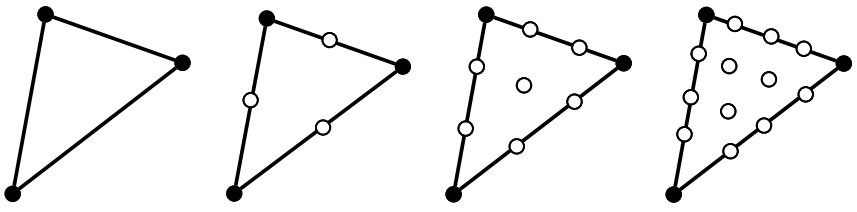

(a) Linear (b) Quadratic (c) Cubic (d) Quartic

Figure 2.7: Higher-order triangular elements.

As mentioned earlier, the meshing process is a kind of optimization problem on the type and number of elements while preserving the accuracy requirements. It is preferred to preserve the geometry of the target organ/structure; therefore, some nodal points of the finite element model might be moved, which is usually required near the boundaries. These displacements may cause large modifications in elements shape that will make FE analysis impossible. In other word, the accuracy of PDEs that are being solved using finite element method depends upon the mesh quality. Therefore, whatever the employed meshing algorithm, it is important to pose the question whether the produced meshes satisfy both ***regularity*** and ***quality*** criteria. For instance, meshes containing *tangled* elements (i.e., inverted elements) result in physically invalid solutions. These elements may appear in the mesh generation process or after large deformation of a valid/regular FE mesh. Therefore, it is essential to evaluate the ***regularity*** of the designed FE model by checking the validity of all elements. Fig. 2.8 shows a section of an irregular mesh. In this regard, the regularity of FE meshes must be recovered manually or by employing mesh repair procedures so that the quality of meshes is reached to an acceptable level. Once the regularity is presented, comes the question of "*mesh quality*". Knupp says (Knupp [2007]): "*Mesh Quality concerns the characteristics of a mesh that permit a particular numerical PDE simulation to be efficiently performed, with fidelity to the underlying physics, and with the accuracy required for the problem.*" There are a wide range of mesh quality metrics and their relevance is proportional to the corresponding element types and also to the computations being performed on the mesh. Such metrics can be found, for instance, in the commercial softwares' user guide (e.g. ANSYS, PATRAN, SDRC/IDEAS, and Fluent FIMESH), and also in the studies: Sheth [2010]; Aguado-Sierra et al. [2011]; Wittek and Miller [2011]; Miller et al. [2012]; Chen et al. [2013]; Baldock et al. [2013]; He et al. [2014]; Caiani et al. [2014]; Zhang [2015]. In the following, two *classical* quality criteria are described (Yanez [2009]; Shim et al. [2012a]; ANSYS [2013]).

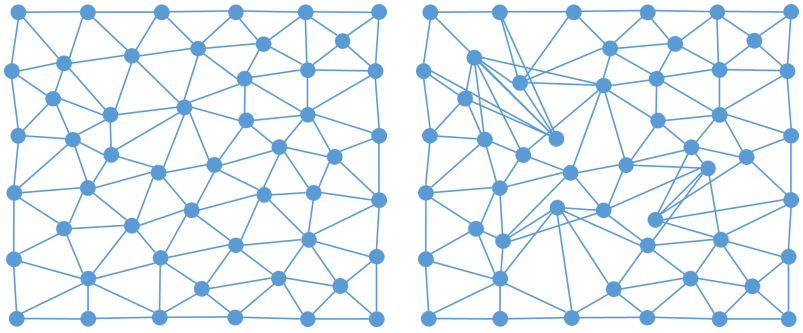

(a) (b)

Figure 2.8: FE mesh regularity: (a) a section of a ***regular*** FE mesh, (b) a section of an ***irregular*** FE mesh,

- **Aspect Ratio (AR)** is defined on the basis of the distances between element's faces, and is computed as the ratio of the maximal distance to the minimal distance (ANSYS [2013]). Therefore, for *well-designed* elements, **AR** should ideally approach to one, and on the contrary, it reaches high values for distorted elements (see Fig. 2.9(a)).

- **Warping Factor (WF)** is defined over the element's faces, and is evaluated by measuring the distances of the face's nodes to their average plane. For nodes that are ideally co-planar, the **WF** approaches to zero which means the face is said to be *well-designed* or *perfect*; and increases for low quality faces (see Fig. 2.9(b)). It should be noted that **WF** can not be considered for triangle faces as the three nodes are always co-planar.

2.2.2 A priori knowledge-based techniques

In the previous sections, the principles of standard subject-specific mesh generation techniques were explained. Although there have been significant improvements during the last years, subject-specific mesh generation is still a challenging task. Clearly, the main limitations come from: 1) image segmentation, which might need long and tedious manual interventions that could not be used routinely in a clinical protocol for a large number of patients, 2) the meshing processes, which can also need manual intervention when a specific mesh design is required. In the literature, a wide range of

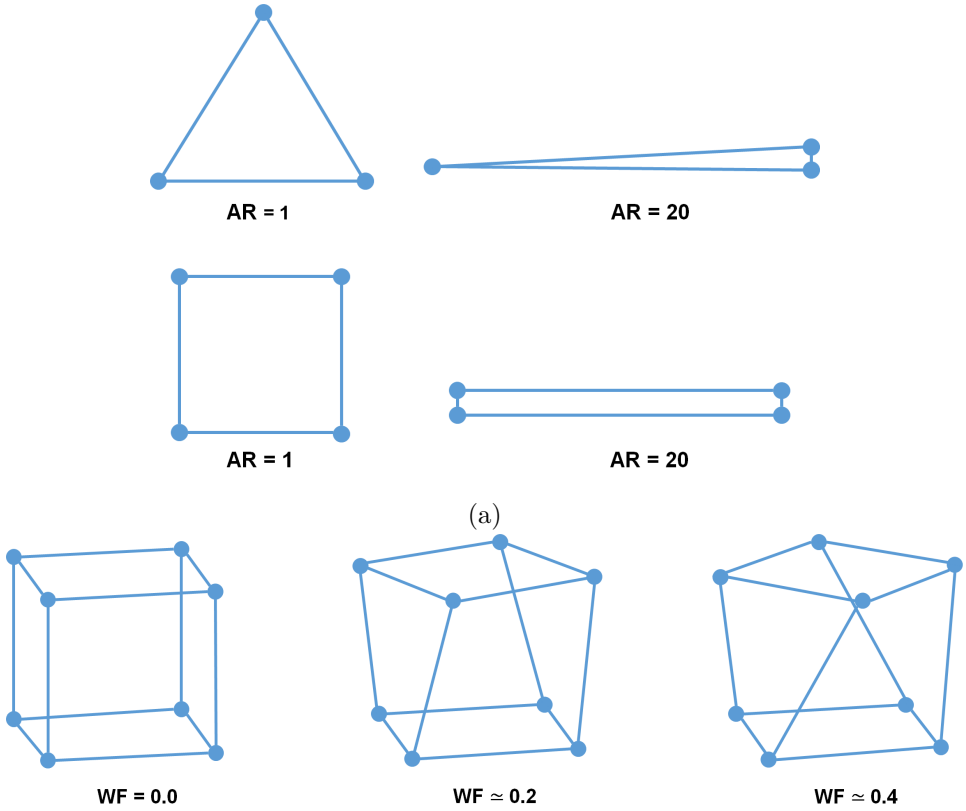

Figure 2.9: Aspect Ratio and Warping Factor: (a) ARs for triangles and quadrilaterals, and (b) WFs for a unit cube and the cases that the top face is twisted by 22.5° and 45° (ANSYS [2013]).

scenarios are reported under various levels of automation in order to refine segmentation, surface creation and/or meshing processes. The primary purpose of all these studies is to make FE mesh generation compatible with the time constraints of the clinical practice where the pre/intra-operative time window is short or clinician availability is limited.

In that perspective, a group of studies have employed ***mesh morphing*** techniques in order to deform a generic FE mesh or implementing a meshing process which is adapted to the geometry of the target subject/patient. The main advantage of these generic-based mesh morphing techniques is that all the subject meshes inherit the same structure from the atlas FE mesh (same nodes and same elements organization). However, it should be noted that after morphing, the quality of the meshes (or worse, the regular-

ity of these meshes) may decrease. That's why refinement post-processing procedures are often required for these frameworks. Fig. 2.10 shows a general block diagram of generic-based frameworks.

In the literature, apart from the point that the generic mesh is generated using the information provided by a training data set or a single data, both "*template*" and "*atlas*" terms are attributed to the mesh that is being deformed under subject-specific information. This means that both terms can be used to refer to the generic meshes. However, the critical point to be made here is "*if the training data set is being used to generate only an average geometry or, further, to facilitate some included steps like segmentation or landmark selection*". Therefore, ***here***, the methods of second group, in which the training data set is being used for landmark selection or segmentation of organs, are being called "***atlas-assisted***" subject-specific mesh generation techniques. Accordingly, all *a priori knowledge*-based techniques can be divided into two main categories: *atlas-based* methods and *atlas-assisted* methods. In short, atlas-based methods are those ones that use some subject-specific information in order to deform an atlas FE mesh or to have a subjective meshing process; and on the other side, atlas-assisted methods are referred generally to those using statistical models based on a priori knowledge, provided by a training set. These models describe the average feature-of-interest (FOI), for example, shape or appearance, and also the main modes of variation of FOI within the training set or population. Therefore, they can be used to compute estimates of FOIs for new data, which will be fully explained with application of FE mesh generation later.

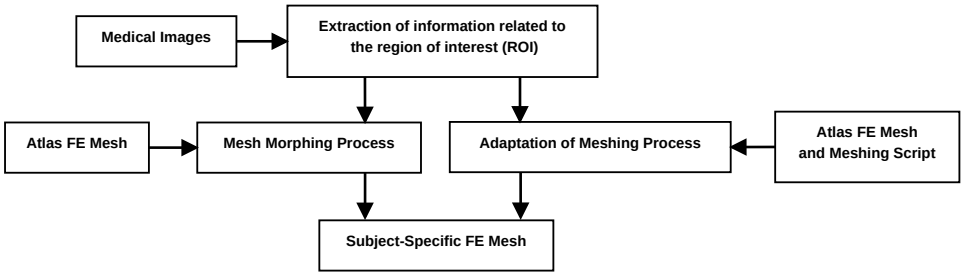

Figure 2.10: General block diagram of atlas-based subject-specific FE mesh generation.

2.2.2.1 Aatlas-based methods

As can be seen in Fig. 2.10, the preliminary step toward the generation of subject-specific meshes is to design a FE mesh from an appropriate subject, called ***atlas*** henceforth using conventional methods, which may involve manual operations for image segmentation or meshing process. The term ***appropriate*** refers to the atlas subject, within the population, which has a ***normal*** shape of VOI. In addition, the chosen atlas image volume must have good a quality and uniform intensity in order to facilitate, as much as possible, segmentation/boundary extraction. The next step is the extraction of subject-specific information from image data in order to deform the atlas FE mesh and to design a subject-specific meshing process. Hereafter, various strategies of the literature, aiming at generating a subject-specific FE mesh from an atlas one, are explained.

Basically, the core of these methods is the use of subject-specific prior knowledge in the form of a surface, a set of point cloud or landmarks. The first study that demonstrated the application of mesh morphing was proposed by Couteau et al. [2000]. A grid-based Mesh-Matching (M-M) algorithm was designed to generate subject-specific FE meshes. First, the point cloud of the VOIs' external surfaces was extracted. Then, in order to capture the geometry of the VOI, the external nodes of the Atlas FE mesh were morphed into the VOI's point cloud by a 3D elastic transformation which was a combination of a rigid transformation, a global warping and local deformation functions. The employed elastic registration was based on an adaptive three-dimensional displacement grid called an octree-spline. Finally, the obtained transformation was applied to all the nodes of the Atlas FE mesh, including the internal nodes (Fig. 2.11). This method was used to generate subject specific Femur meshes and the rate of distorted elements was around 15%. In another study Salo et al. [2013a], the same strategy was employed to morph structured FE meshes of the face. Although a post-treatment process was carried out on the generated meshes in order to recover the regularity and to improve the quality of finite elements, the generated meshes were prone to distortions. Hence, the Mesh-Matching method was improved by the authors into the Mesh-Match-and-Repair (MMRep) algorithm (Bucki et al. [2010b]) (Fig. 2.12). As in the method developed by Couteau et al. [2000], an ROI was segmented in the subject's images and its 3D surface

was used as the target to deform the atlas' FE mesh. It was shown that the level of distortion can be dramatically reduced, if the transformation satisfies three main constraints: being C1-differentiable, non-folding (a local property ensuring that space orientation is preserved) and invertible; these properties specify a C1-diffeomorphism (Bucki et al. [2010b]). In addition, regularity constraints were considered during the adaptation process, and mesh quality and validity were maintained using an a posteriori mesh repair step.

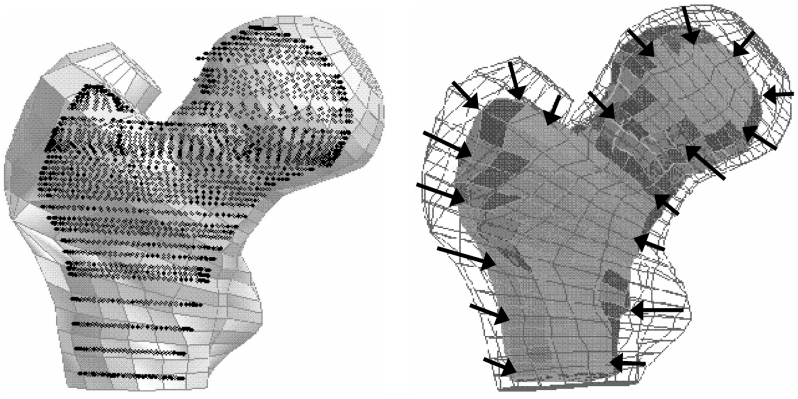

(a) (b)

Figure 2.11: Grid-based Mesh-Matching (M-M) algorithm: (a) Superimposition of the *Atlas* mesh (grey) with the 3D surface target points (black), (b) Generated subject-specific mesh (shaded grey) from the *Atlas* mesh (wireframe) (Couteau et al. [2000]).

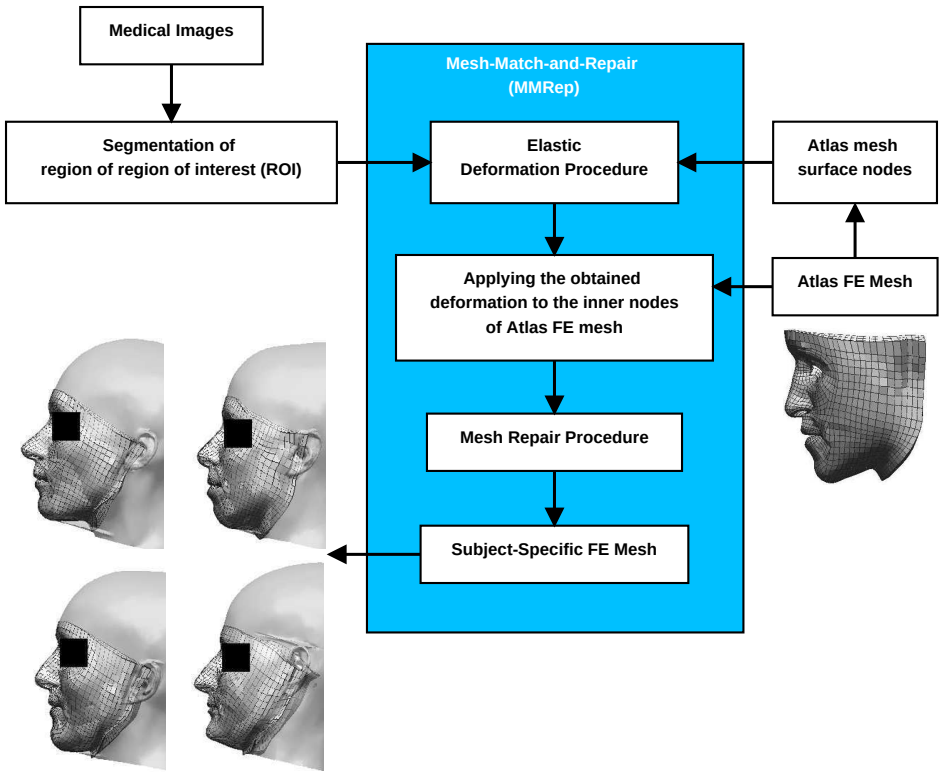

Figure 2.12: Block diagram of Mesh-Match-and-Repair (MMRep) algorithm.

In Magnotta et al. [2008], a similar mesh mapping strategy was employed to generate meshes for phalanx bones of the human hand. First, the surface nodes of the atlas mesh were mapped onto the input bony surface by computing the distance between the surfaces as the driving measure for the deformable registration. Then, the internal nodes of the atlas mesh were moved using thin-plate spline (TPS) transforms. The TPS transforms were obtained using the positions of the original and mapped nodes of the atlas surface mesh. Following this displacement-driven mesh mapping, a deformable registration technique based on the FE method was also introduced to deform an atlas FE mesh in Grosland et al. [2009]. In another study (McGregor et al. [2010]), the same methodology was employed to generate patient-specific meshes of the abdominal aortic bifurcation.

Although the previous studies have directly used the surface of VOIs as an input to the mesh morphing procedures, landmark-based morphing methods also have been developed to generate subject-specific meshes. In Fernandez

et al. [2004], a technique based on free form deformations (FFDs) was employed to generate tricubic Hermit volume meshes. It is worth pointing out that, in addition to the nodal coordinates, Hermit meshes nodes include information about the derivatives encoding the shapes. The idea behind this framework was to embed the baseline geometry in a control volume which is so-called ***host mesh***. In order to customize the generic geometry within a transformation, a set of landmarks were defined on both baseline and target geometries. These landmarks were used to guide the deformation of the host mesh; and finally, it was passed to the embedded baseline mesh and subject-specific mesh was achieved (Fig. 2.13). The proposed optimization-based geometric fitting procedure was also employed by other researchers to generate high order cubic Hermit meshes (Shim et al. [2007, 2012b, 2016]).

In Sigal et al. [2008], specimen-specific FE models of caudal rat vertebrae were generated using two morphing algorithms, automated wrapping (AW) and manual landmarks (ML). Similarly, the computed mappings from the source surface to the target surfaces were used to morph the source mesh and produce the target meshes. In AW, an auxiliary triangulated surface was used to warp the source and target surfaces and to obtain the mappings (Fig. 2.14(a)); while in ML, the mappings were computed by matching the landmarks which were manually located on both source and target surfaces (Fig. 2.14(b)).

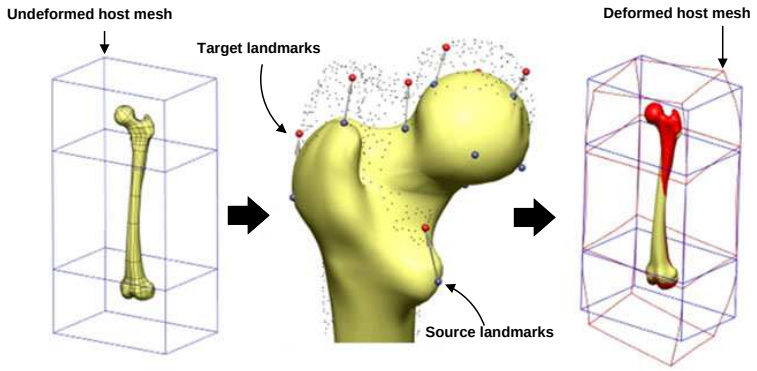

(a) Femur

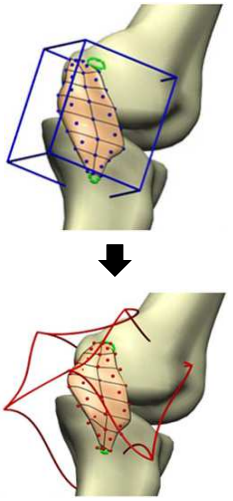

(b) Medial collateral ligament insertion

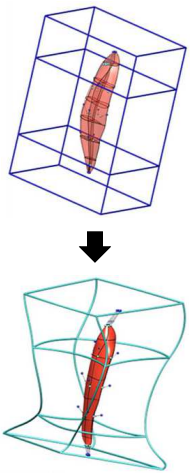

(c) Rectus femoris muscle

Figure 2.13: Subject-specific mesh generation based on Host-mesh customization (Fernandez et al. [2004]).

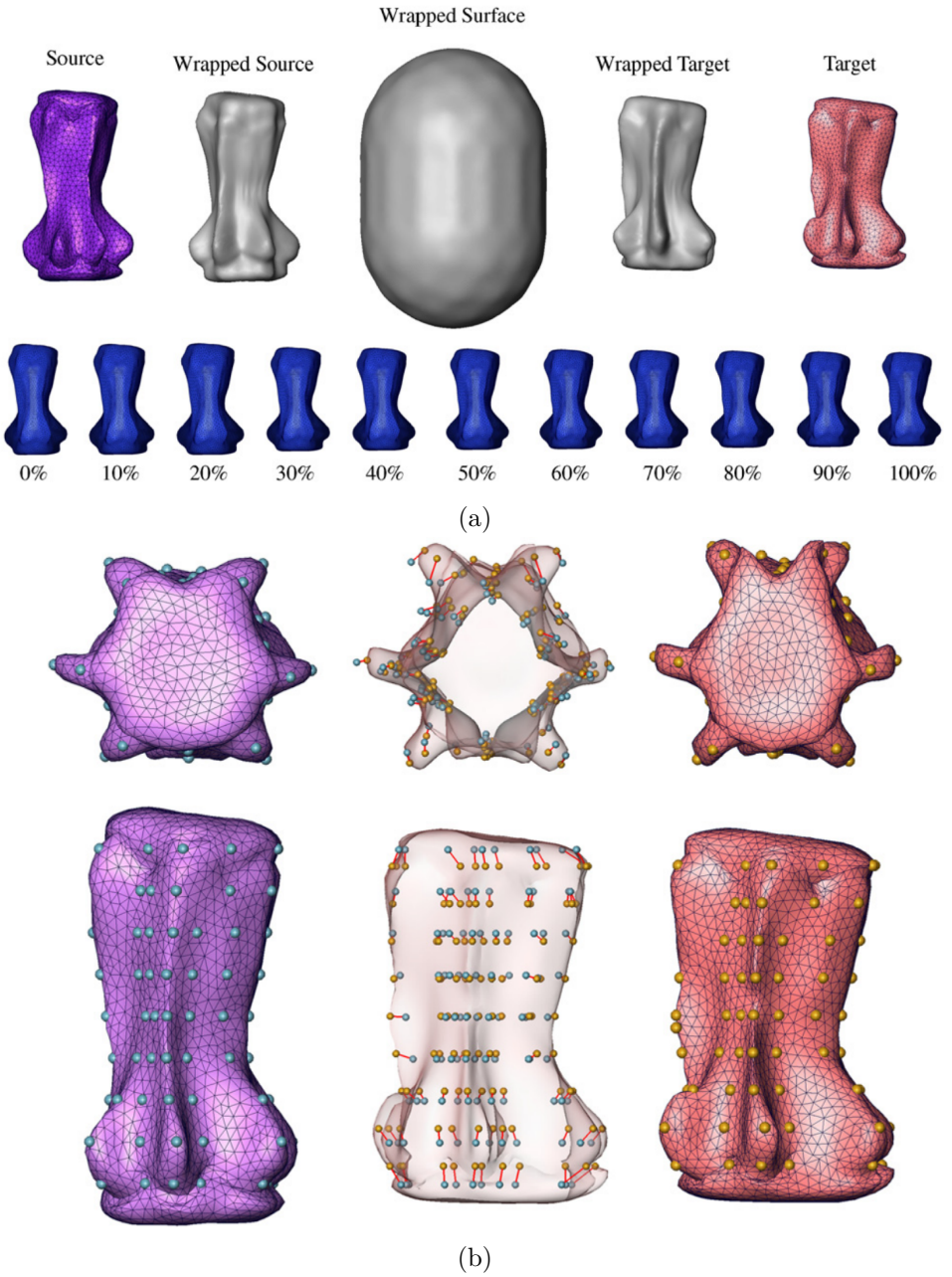

Figure 2.14: Automatic and landmark based mesh morphing: (a) ***Automatic Warping (AW)***: an auxiliary surface is wrapped to each of the source and the target surfaces. Then, in order to compute a transformation from the source's surface to the target's surface, the nodal difference between the two wrapped auxiliary surfaces is computed. The surface transform is interpolated to morph the source mesh onto the target surface. Various percentage points of the change in the source geometry are shown in the bottom row. (b) ***Manual landmarks***: landmarks are manually selected on the source (left) and the target (right); then the overall transformation is computed using thin-plate splines method. (Sigal et al. [2008]).

In Salo et al. [2015], a semi-automated landmark-based mesh morphing and mapping technique was proposed to generate patient-specific FE models of the human pelvis without segmentation. First, the template mesh was morphed onto a different pelvis using a set of landmarks manually defined on the volumetric imaging data (CT scan). And then, a multi-level mapping process was employed to refine the morphed pelvic surfaces (Peleg et al. [2014]). During the morphing step, nodes inside the template mesh were allowed to move along the six-degrees of freedom of the 3D space, in order to reduce the elements distortion.

Although morphing a template mesh based on some landmarks has been widely used to generate subject-specific meshes for various applications (e.g. facial soft tissue (Chen et al. [2012]; Lou et al. [2012]), Femur (Grassi et al. [2011]), Lumbar Vertebrae (Campbell et al. [2012]), human pelvis (Salo et al. [2013b]), even with incorporation of smoothing algorithms, such morphing techniques have difficulties to generate high quality meshes for geometrically complex models (Salo et al. [2013b]). Indeed, mesh repairment procedures that may include manually remeshing of not-repaired elements are sometimes required (Salo et al. [2013b]). In the front of such issues, landmark and surfaces based morphing techniques are combined in order to provide a balance between the fitting accuracy, anatomical correspondence and mesh quality (Campbell and Petrella [2015]; Zhang et al. [2016]). For instance, in Grassi et al. [2011], some landmarks were defined manually on both template and target as constraints within the surface morphing process, what was based on a radial basis function (RBF) regression. However, as a few number of landmarks were used for the morphing process, it resulted in an isotopological surface mesh with a poor recovery of the STL geometry. Therefore, each node of the morphed surface mesh was perpendicularly projected on the centroid of the closest triangle in the STL. This projection provides a good match between the two surfaces, but FE meshes quality was decreased because of intersecting triangles and high aspect ratios. So, a smoothing based on Laplacian operator was applied in order to improve the quality of the surface meshes. As concerns the shrinkage caused by the Laplacian smoothing, the resulting surface mesh was re-projected on the STL geometry; and finally, a Gaussian RBF was employed to replace the inner nodes of the template mesh (Fig. 2.15).

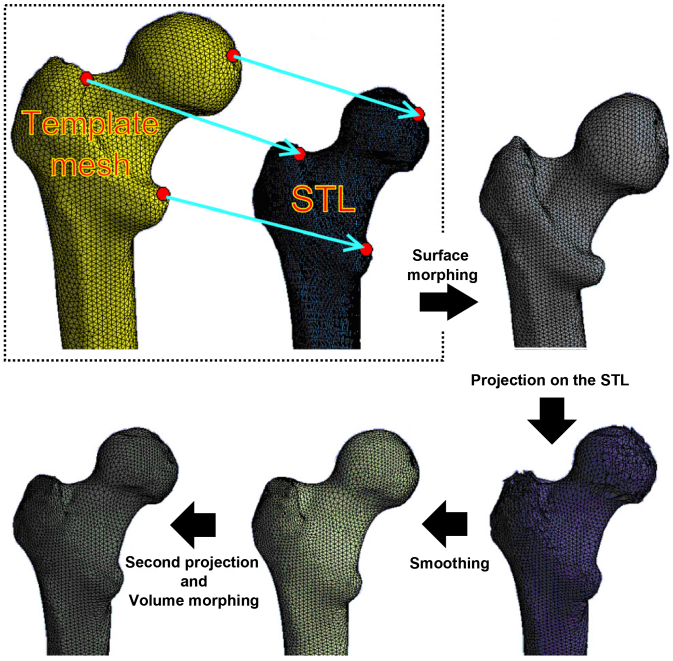

Figure 2.15: Steps of the morphing algorithm, shown on the proximal femur (Grassi et al. [2011]).

In Zhang et al. [2016], an efficient hybrid method was proposed to generate patient-specific anatomically-detailed facial soft tissue FE models. Like conventional surface-based mesh morphing techniques, this method also involves two main steps: surface registration and then volumetric mesh interpolation. The surface registration is done by employing a landmark-based thin-plate spline that needs the determination of a series of anatomical landmarks on both source and target surfaces.
In Klein et al. [2015], a two level mesh generation process (morphing and fitting) was proposed (Fig. 2.16). As a first step toward the adaptation of a template mesh (i.e. morphing), anatomic landmarks are identified on both source and target geometries (i.e., on the template mesh and extracted surfaces). Then, the template mesh is morphed using a thin-plate spline function for radial basis function guided by landmarks (Carr et al. [2001]; Bennink et al. [2007]). Finally, in order to fit the morphed meshes to the extracted surfaces, an implicit surface methodology is employed to move the nodes of the morphed meshes Reed et al. [2009]. In another study (Camp-

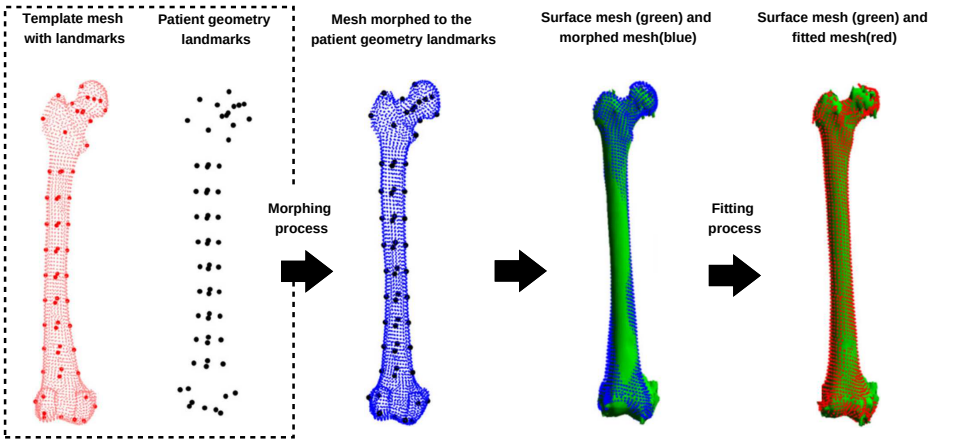

Figure 2.16: A two level mesh generation process (morphing and fitting): the morphing and fitting processes of a template femur FE mesh onto an example extracted bone surface geometry (Klein et al. [2015]).

bell and Petrella [2015]), in order to morph the template mesh based on the landmarks, the segmented surfaces were simply used to automatically identify in advance the landmarks of the Lumbar Spine.

Instead of using surface or landmarks to morph an atlas mesh, some studies have proposed to use binary image registration to generate customized FE meshes (Lamata et al. [2010a,b, 2011, 2014]; de Vecchi et al. [2013]). In Lamata et al. [2010a], a generic cubic Hermite heart ventricular model was personalized to the anatomy of a patient using this method. The mesh warping process included two main steps. The first step was the estimation of a 3D warping field that was obtained by registering the binary image representations of the atlas mesh to the target anatomy. Then the warping field was fitted into the cubic Hermite mesh by solving three linear systems of equations. Doing so, a smooth and accurate projection of the warping field into the basis functions of the mesh was estimated. The whole process is shown in Fig. 2.17. Again, it is noteworthy that in a Hermite mesh, both the 3D Cartesian coordinates of nodes and the derivatives of shape versus local finite element coordinates are used to encode the shape, which provides a smooth representation that is favorable for the simulation of large deformation mechanics. Although most studies have employed registration-based methods to deform an atlas mesh to match with a target anatomy, registration has also been used to automate the meshing process (Ji et al. [2011]; Kallemeyn et al. [2013]).

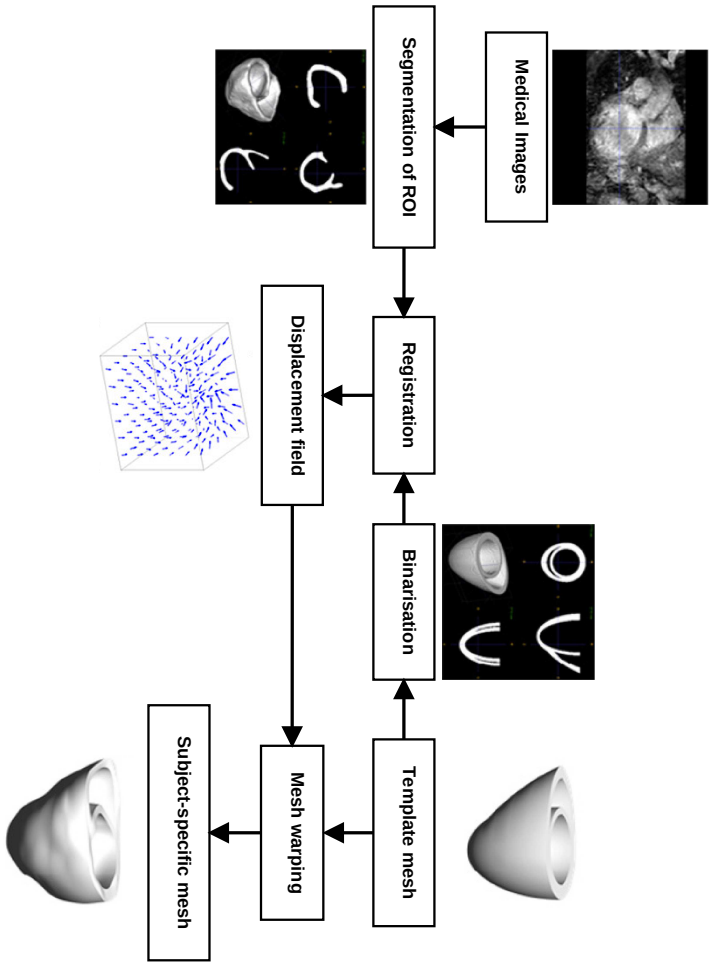

Figure 2.17: Dataflow designed to generate subject-specific cubic Hermite meshes (Lamata et al. [2010a]).

In Ji et al. [2011], for a given subject, image-based rigid registration was used to transfer the segmented surface of the ROI into the atlas space; then the subject-specific mesh was generated using the same meshing script that was previously used for the generation of the atlas mesh. Finally, the subject-specific mesh was transformed back into the subject space. Fig. 2.18 shows this framework, which has proven being useful for the generation of subject-specific hexahedral brain meshes.

In another study (Kallemeyn et al. [2013]), in order to automate multiblock meshing, the building block structure (BBS) was automatically defined for each subject. Exterior points of the BSS were locally mapped onto the target surfaces using nonlinear registration, and then final subject-specific meshes were generated.

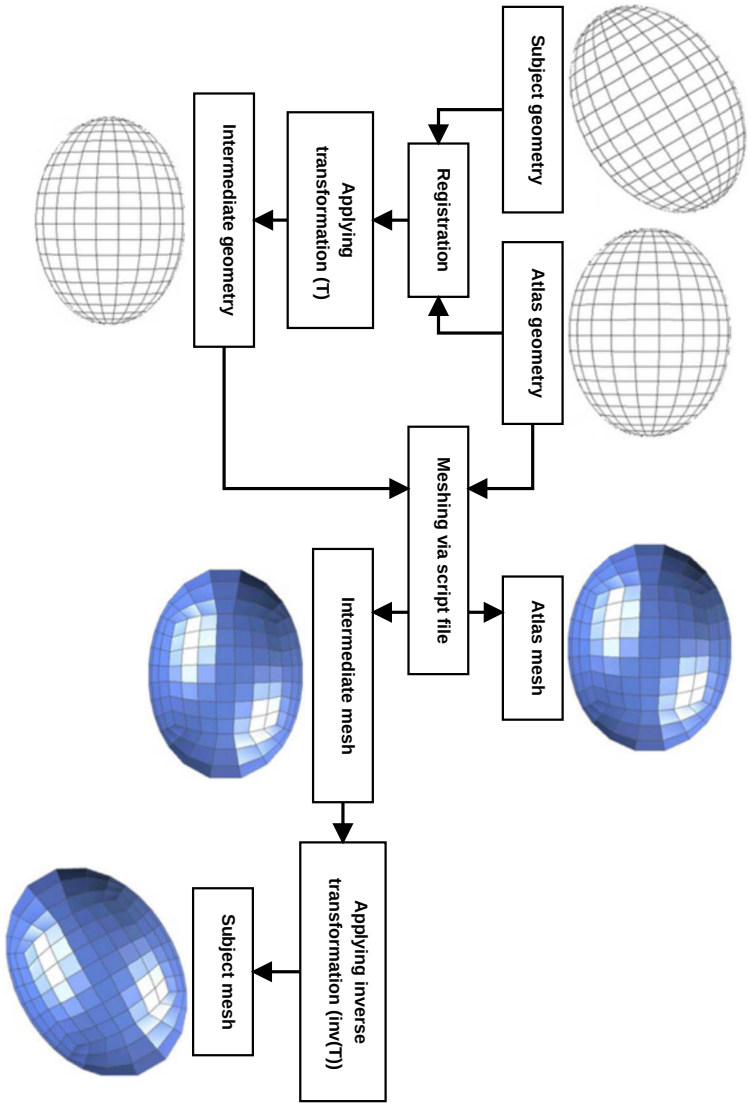

Figure 2.18: Subject-specific meshing process using a unique meshing script. The subject-specific geometry is transformed into the atlas space using rigid image registration. Then, an automated meshing script, which is used for atlas mesh generation, is applied for the subject. Finally, the the generated mesh is transformed back into the subject coordinate system (Ji et al. [2011]).

2.2.2.2 Atlas-assisted methods

As mentioned earlier, atlas-assisted methods are based on a training data set which permits to create statistical models, in order to describe average FOIs and also the main modes of variation of FOIs within the training set. In this regard, a brief overview on the basic principles of statistical modelling is provided and then relevant literature with focus on subject-specific FE mesh generation will be reviewed. The general framework of statistical modeling and also its attribute to the subject-specific FE mesh generation is shown in Fig. 2.19.

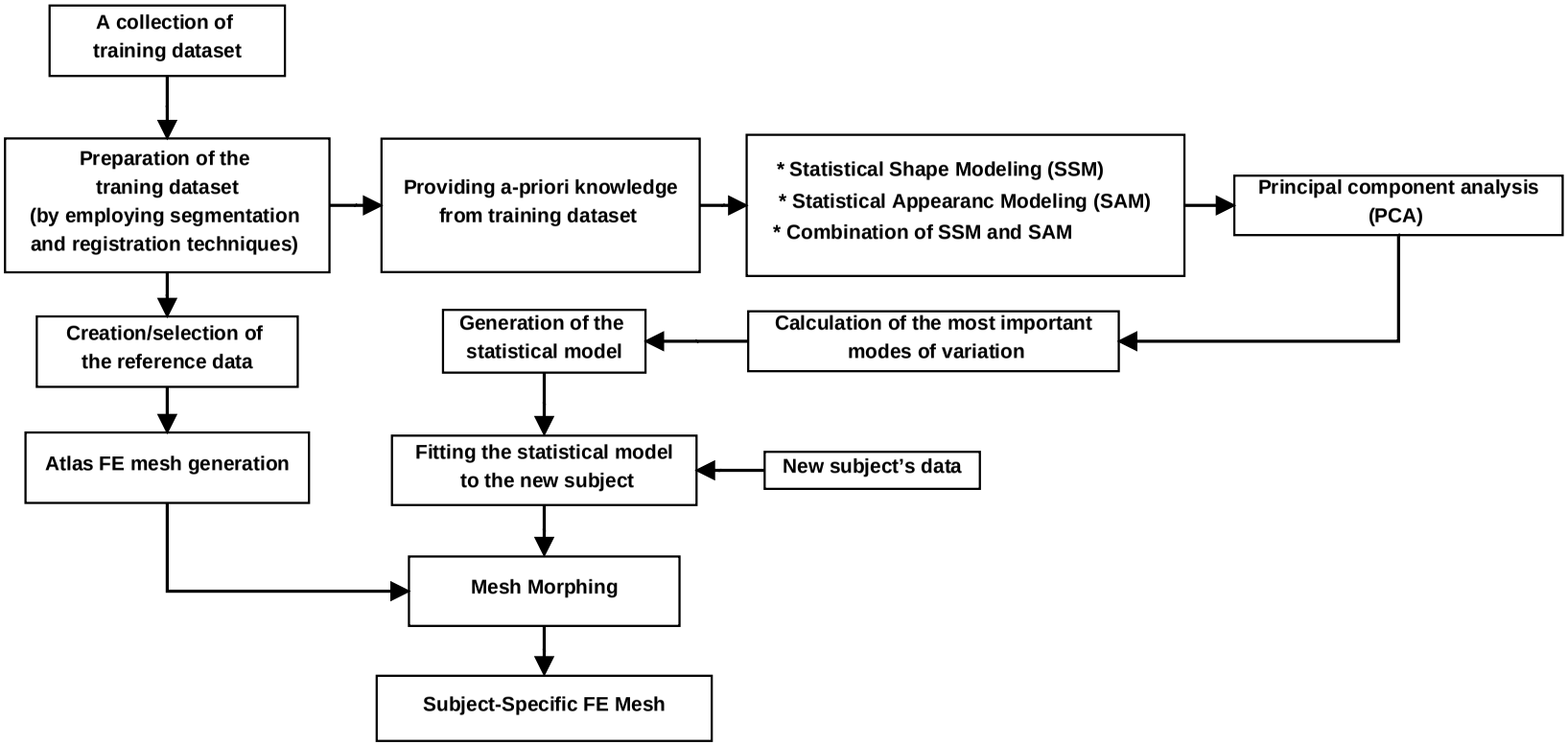

Figure 2.19: General framework of statistical modeling and its attribute to mesh generation.

The core of such a process consider in learning the prior knowledge by the statistical modeling of a population of training instances. Therefore, it's really important to compensate for variations across the training instances that are caused by factors other than variation in the shape or appearance. This compensation or pre-processing can be done by employing registration or alignment techniques. After alignment, a-priori knowledge about the FOI (e.g. shape or appearance) is provided for each subject within the training data. According to the application requirements, these information can be extracted manually or automatically, and also be in the form of a surface, a set of landmarks explaining anatomical structure, or intensity of gray values within the VOI, and etc. It should be reminded that in some studies, the alignment process is done after providing the a-priori knowledge; for example, the surface of all VOIs are extracted and then aligned in a common coordinate system. Once the training instances are provided and the correspondence between them is established, they can be employed to create the statistical model. To make it more understandable, let's assume that a set of shapes are being modeled using statistical models. In this way, at first, the average shape ($\overline{\mathbf{x}}$) is calculated among all training instances ($\mathbf{x}_i$):

$$\overline{\mathbf{x}} = \frac{1}{N}\sum_{i=1}^{N}\mathbf{x}_i \tag{2.28}$$

The average shape is also so-called ***Atlas***. Mention should also be made of the other methods that can be used to create the average shape. For example, it might be estimated by minimizing an average distance between $\overline{\mathbf{x}}$ and $\mathbf{x}_i$s (Rousson et al. [2004]). Or for simplicity, one of the instances can be chosen as the Atlas; but, in such a case the model might be biased toward the selected Atlas. Next, in order to capture the variations of the instances from the average shape, a covariance matrix is calculated as below:

$$\mathbf{S} = \frac{1}{N-1}\sum_{i=1}^{N}(\mathbf{x}_i - \overline{\mathbf{x}})(\mathbf{x}_i - \overline{\mathbf{x}})^T \tag{2.29}$$

Afterwards, Principle Component Analysis (PCA) is applied to the covariance matrix, which involves calculation of principal modes of variation (eigenvectors, Φ_s) and corresponding variances (eigenvalues, λ_s). Therefore,

it lets the statistical model to be described by the average shape ($\overline{\mathtt{x}}$) and the eigenvectors. It is important to note however, that the model can be described in a compact form using only the most significant modes of variation, which are defined by the eigenvectors corresponding to the largest eigenvalues (Barratt et al. [2008]). If the eigenvalues are ordered in the descending order of magnitude such that $\lambda_1 > ... > \lambda_{N-1}$, the first corresponding eigenvectors can therefore be used to describe the shape of other individuals, not presented in the training dataset. Finally, the new instance is approximated by a linear combination of the most important modes (Φ_s) as below:

$$\mathtt{x} = \overline{\mathtt{x}} + \sum_{s=1}^{C} b_s \Phi_s \tag{2.30}$$

Where b_s is the shape model parameter that describes the contribution of the s^{th} mode of variation. Of course, the best method to chose the number C of retained modes for the approximation can be questioned. Clearly, the accuracy of the approximate shape may depend critically on the number of retained modes; in addition the compactness of the created model is affected by it (Stegmann [2000]). In the literature, a wide range of techniques are reported to determine the number of retained modes (Stegmann [2000]; Heimann and Meinzer [2009]). The most common approach is to use the ratio of the accumulated variance to the total variance:

$$r = \frac{\sum_{s=1}^{c} \lambda_s}{\sum_{s=1}^{N-1} \lambda_s} \tag{2.31}$$

In this case, the number C of retained modes is chosen so that it leads to a desired ratio which is commonly from 0.9 to 0.98 (Heimann and Meinzer [2009]). Having considered statistical shape models (SSM), one might also need to capture texture variations within the training dataset. In other words, image intensity-based features can also be modeled around the VOIs (for boundary-based features) and/or inside the VOIs (for region-based features). These models are so-called statistical appearance models (SAM). In

summary, shape and texture instances can be generated respectively using the shape and texture model parameters. Also, both models can be unified to create a complete compact model. For more explanations, the reader is referred to Heimann and Meinzer [2009] and Sarkalkan et al. [2014]. In any case, it is clear that the only remained task is the determination of model parameters so that it fits to unseen data as well as possible. This is a kind of optimization problem which is also called a fitting, matching, or search process. Model parameters are tuned in such a way that the difference between the FOIs represented by the statistical model and FOIs of unseen data is minimized. In order to have a comprehensive overview of these algorithms, the reader is referred to latter studies. In the literature, statistical models are generally used to create FE mesh instances. For example, in Bryan et al. [2010], the statistical model was employed to generate human femur tetrahedral mesh instances with associated material properties (see Fig. 2.20). In this study, at first, the VOI, i.e., the femur, was segmented for all subjects in the CT images. Then, one subject was chosen as the atlas/reference/baseline, and subsequently, a high quality solid tetrahedral mesh was designed for the atlas VOI. In order to generate FE meshes for other subjects within the training dataset, the atlas FE mesh was morphed using a two-level registration strategy:

1. An elastic registration technique was applied to establish a correspondence between the atlas and the subjects' surfaces;

2. The atlas mesh was deformed based on the surface node displacement vectors and solving decoupled three dimensional Laplace equations.

Then, material properties, i.e., apparent bone density, were assigned to the meshes' nodes based on the CT images. This process leaded to the formation of subject-specific solid tetrahedral meshes with unique material properties for all members of the training dataset. Then, statistical models were constructed by subjecting the meshes to Principal Component Analysis (PCA).

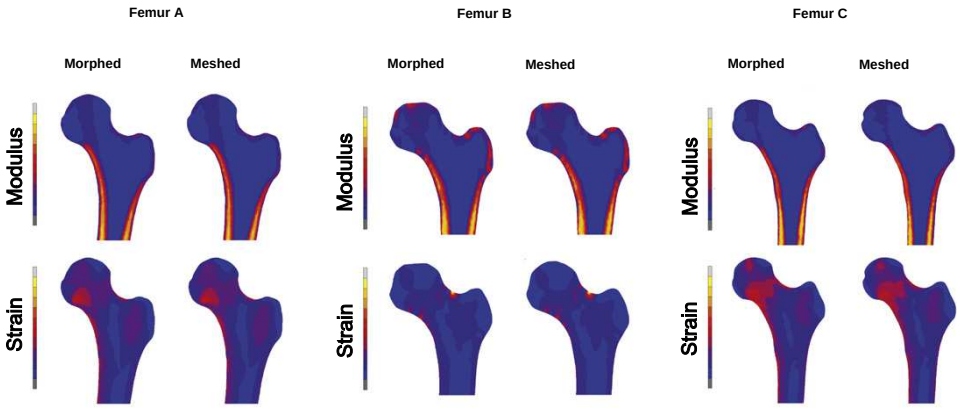

Figure 2.20: Plot of morphed and manually meshed instances of the same geometry, comparing material modulus representation and strain distribution resulting from a 1× body weight load applied vertically to femoral head, simulating one-legged stance (Bryan et al. [2010]).

As an improvement of previous works, a statistical atlas based approach was proposed to automatically generate subject-specific FE meshes in Wang and Qian [2016]. Block diagram of the current method is shown in Fig. 2.21. As can be seen, the input to this framework is the subject-specific shape, and the output is the FE mesh of the subject shape. The mesh generation process contains two main phases:

1. Establishing a boundary correspondence between the atlas shape and a new given shape via shape instantiation and projection;

2. Atlas FE mesh morphing based on the boundary correspondence.

The first phase, i.e. establishing a boundary correspondence, is based on the construction of a statistical shape model. The prior knowledge was learnt by statistical modelling of a training set of shapes using Principle Component Analysis (PCA). The most significant modes of variations were used to describe a linear shape space that was originated at the average shape. In order to correctly calculate the average shape, Free-From Deformation (FFD) was employed to establish a correspondence between the training shapes and a chosen template shape. To achieve an accurate correspondence, some landmarks were also defined as constraints within the registration process.

Then, all shapes were sampled by the same number of points and finally a statistical shape model was conducted. After creation of the statistical shape model, an atlas FE mesh was designed for the average shape. To instant a new given shape, optimal shape parameters (w) were measured (through an optimization or a search process) so that the shape instance fits to the given shape. Finally, in order to obtain the best synthesized shape, the instantiated shape was projected to the input shape along the normal. In the second phase, based on the established boundary correspondence between the Atlas and the final instantiated shape, the Atlas FE mesh was morphed onto the input shape. Numerical results on 2D hands are shown in Fig. 2.22.

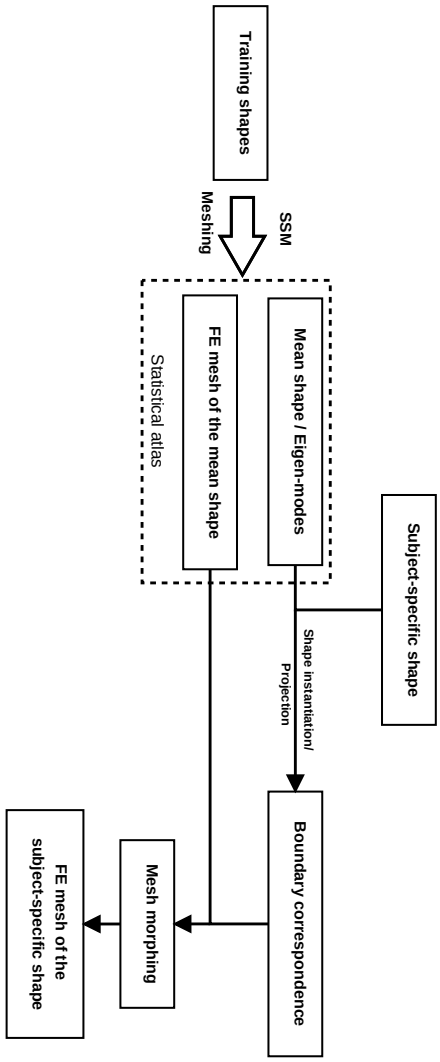

Figure 2.21: A schematic diagram of the statistical atlas based subject-specific FE modeling.

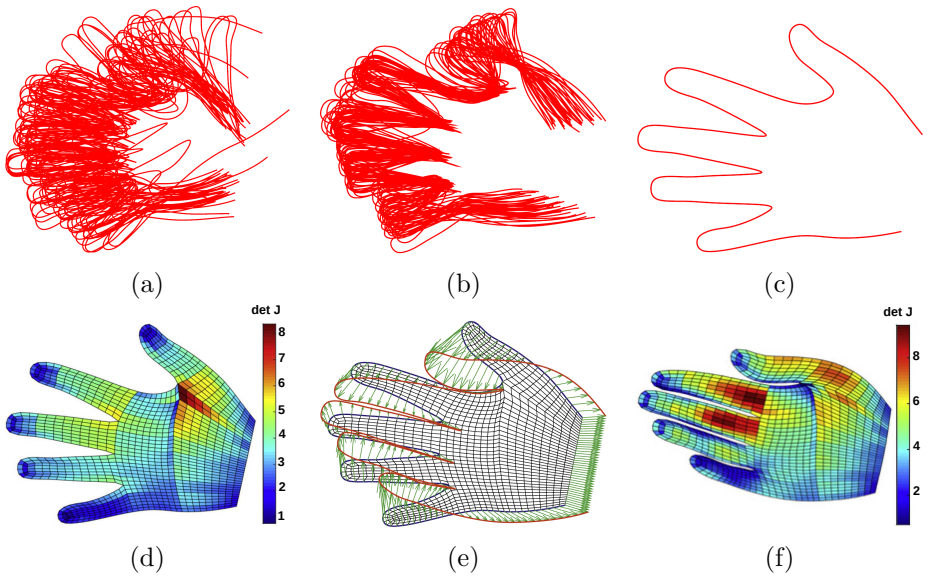

Figure 2.22: Statistical atlas based approach for automatic meshing of subject-specific hands shapes: (a) input shapes, (b) aligned shapes, (c) mean shape, (d) the quadrilateral mesh of the mean shape and the Jacobians, (e) the correspondence between the Mean and new shapes, and (f) a generated subject-specific FE mesh by morphing the atlas mesh (Wang and Qian [2016]).

In another study (Väänänen et al. [2015]), statistical appearance models (SAM) were employed to reconstruct the 3D shape and internal architecture of the VOIs (i.e., bones) using a single 2D image. This was done by aligning 2D images to the created statistical appearance models. The entire framework is shown in Fig. 2.23. VOIs were segmented manually and triangular surface meshes were generated for all subjects in the training dataset. In order to represent each shape by a set of point clouds, the mesh vertices and the centers of the surface triangles were used. A set of landmarks were defined on the segmented surfaces that were used to establish a global alignment (scaling and rigid transformation) between the samples using Generalized Procrustes Analysis (GPA). The obtained transformations were applied to the landmarks and finally the average of each anatomical landmark was calculated. Then, with the aim of creation of a template image, Thin-Plate Splines (TPS) was used to warp the medical images of the training VOIs to the shape described by the average landmarks. Also, a template mesh containing tetrahedral elements was generated for the tem-

plate image. Thereafter, based on the anatomical landmarks and previously extracted point clouds, the template mesh was warped to the training shapes using TPS in order to generate subject-specific meshes. Subsequently, density information were assigned to each element. Finally, all warped meshes containing shape and density information were used to construct the statistical appearance model. Fig. 2.24 shows a statistical model created for femur shapes. With the aim to generate subject-specific FE mesh using a 2D image, the subject-specific shape and the internal densities were reconstructed by minimizing a cost function including three terms: (1) the sum of absolute differences between the projection of the SAM (digitally reconstructed image) and the input image, (2) the quality of the mesh, and (3) the cost of anatomical positioning calculated using landmarks.

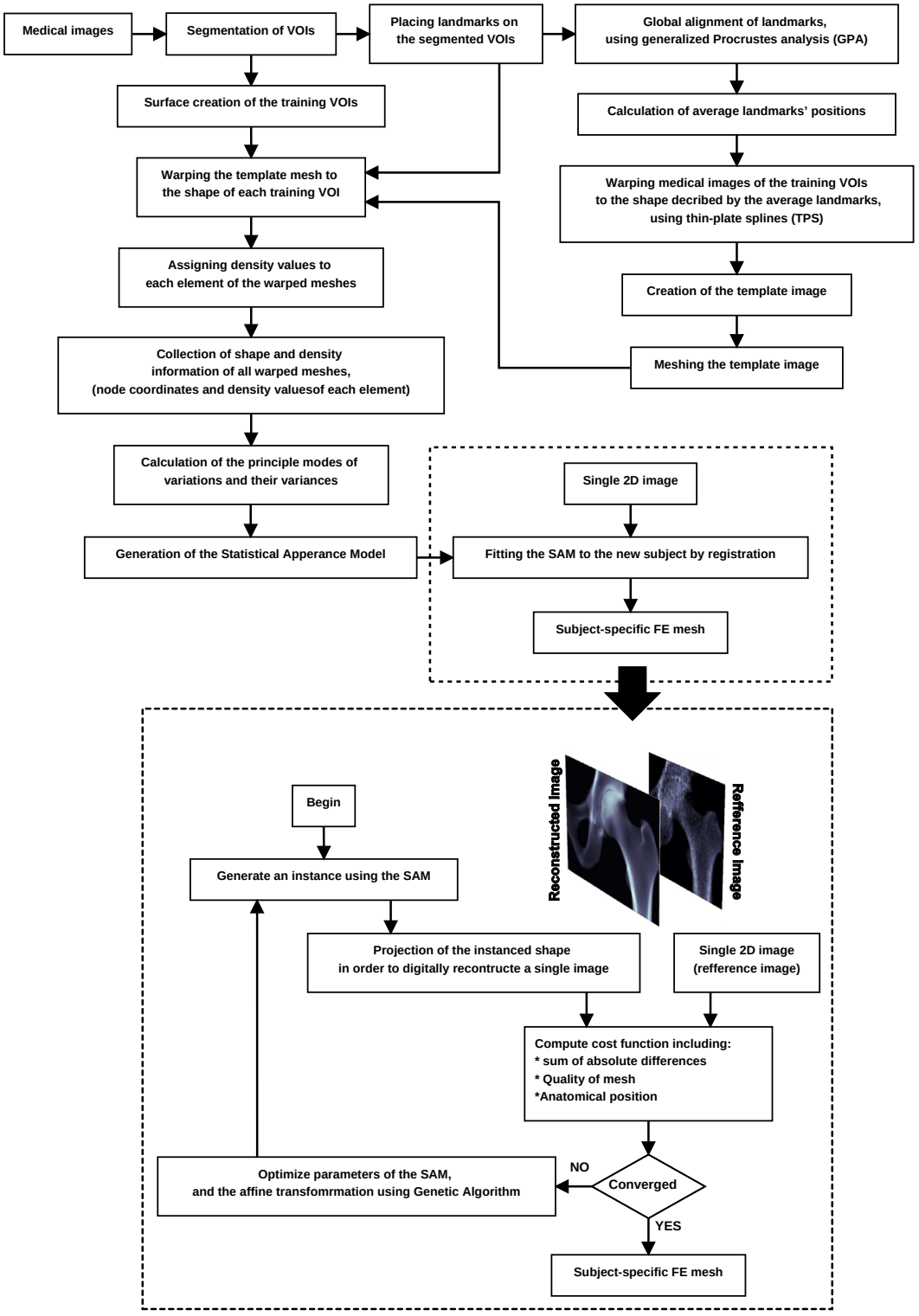

Figure 2.23: A schematic diagram of the statistical atlas based subject-specific FE modeling (inspired by Väänänen et al. [2015]).

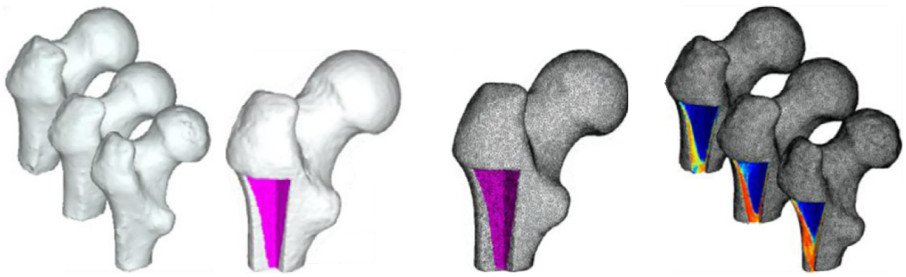

(a) (b) (c) (d)

Figure 2.24: Development of a SAM for femur application: (a) Extracted femur shapes from quantitative CT images, (b) Generated average shape using GPA and TPS, (c) Meshed average shape, (d) Generated FE meshes for each training subject, including density information (Väänänen et al. [2015]).

2.3 conclusion

Over the past years, there has been a rapidly increasing interest in making the mesh generation process compatible with the clinical constraints. This is done in two ways: (1) improving the standard mesh generation techniques, namely by making the segmentation, surface creation and meshing algorithms automatic as much as possible, and (2) employing atlas-based strategies. The second group of methods are being increasingly developed because they offer to bypass the need for any conventional meshing algorithm, namely by deforming an atlas FE mesh or by adapting a generic meshing process to the subject-specific information. Another advantage of these methods is that the subject-specific meshes inherit the same structure from the atlas FE mesh (i.e. same nodes and same elements organization). However, these methods have some limitations, which include: (1) the required subject-specific information that can be provided in different forms (e.g., a set of landmarks, contours, a created surface, and etc.), but is not extracted easily or automatically for all the applications, and (2) from the perspective of mesh morphing process, the deformation of an atlas mesh may result in an irregular or a low quality mesh that reduces the accuracy of subsequent FEAs. Therefore, developing subject-specific mesh generation techniques that avoid these limitations is of great importance and interest.

"There is a voice that doesn't use words, Listen."
- Jalaluddin Rumi

3

Atlas-Based Automatic Generation of Subject-Specific Finite Element Tongue Meshes

Contents

Generation of subject-specific 3D Finite Element (FE) models requires the processing of numerous medical images in order to precisely extract geometrical information about subject-specific anatomy. This processing remains extremely challenging. To overcome this difficulty, we present an automatic atlas-based method that generates subject-specific FE meshes via a 3D registration guided by Magnetic Resonance images. The method extracts a 3D transformation by registering the atlas' volume image to the subject's one, and establishes a one-to-one correspondence between the two volumes. The 3D transformation field deforms the atlas' mesh to generate the subject-specific FE mesh. To preserve the quality of the subject-specific mesh, a diffeomorphic non-rigid registration based on B-spline Free-Form Deformations (FFDs) is used, which guarantees a non-folding and one-to-one transformation. Two evaluations of the method are provided. First, a publicly available CT-database is used to assess the capability to accurately capture the complexity of each subject-specific Lung's geometry. Second, FE tongue meshes are generated for two healthy volunteers and two patients suffering from tongue cancer using MR images. It is shown that the method generates an appropriate representation of the subject-specific geometry while preserving the quality of the FE meshes for subsequent FE analysis. To demonstrate the importance of our method in a clinical context, a subject-specific mesh is used to simulate tongue's biomechanical response to the activation of an important tongue muscle, before and after cancer surgery.

3.1 Introduction

FE models are used extensively in computer-aided surgery. For such contexts subject-specific models need to be generated. As illustrated in the previous chapter, Atlas-based mesh morphing techniques show a great potential for subject-specific FE mesh generation. During the last years, a broad range of atlas-based mesh morphing strategies was proposed. Each method was developed to solve a specific problem within a set of constraints (e.g., being automatic, generating regular and high quality meshes, getting the target geometries accurately). These methods first need an atlas' FE mesh, which can be designed following usual procedures. The subsequent step is the extraction of information related to specific regions of interest (ROI) from subject's medical images. Such information is extracted in the form a geometrical description, such as contours, 3D surface models, or a set of land-marks. Finally, the atlas' FE mesh is "morphed" onto this geometrical description and subject-specific meshes are generated. The main advantage of all these techniques is that all the meshes inherit the same structure from the atlas' FE mesh (same nodes and same elements' organization). It should be noted that after morphing the quality of the meshes may decrease, and post-processing refinement procedures are often required. The level of distortion is also depending on the complexity of the atlas' and subject's geometries.

The extraction of the geometrical description of the ROIs is a challenging task, which can be time-consuming, especially for the applications requiring image segmentation. In some cases the segmentation procedure is sensitive to noise or image quality. To illustrate this, Fig. 3.1 shows CT and MRI 2D images of the oral cavity of three subjects. Assuming that such images are used to extract information as concerns the shape of the tongue, it seems quite clear that difficulties will be encountered do define the corresponding ROIs. Indeed, for the CT image plotted on Fig. 3.1(a) segmentation of tongue contours seems impossible. More information is provided on MR images such as the one displayed on Fig. 3.1(b) but the boundaries between tongue tissues and other edges of the oral cavity (lips, teeth, and cheeks) can still be difficult to detect. Moreover, in some cases such as in the MR image of a patient sufferings from tongue cancer displayed on Fig. 3.1(c). A bad quality volumetric image (low contrast and noise) is clearly observed,

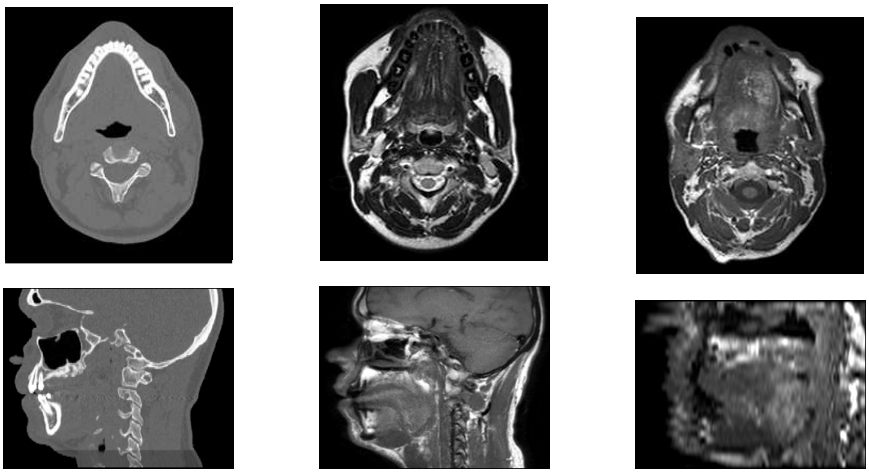

(a) Normal CT images (b) Normal MR images (c) MRIs of a patient

Figure 3.1: Tongue medical images.

abnormal tissue regions in the affected areas can cause high intensity variations inside the tongue. To overcome such limitations, there is a need for methods that avoid the segmentation steps. Considering all these aspects, although all the atlas-based mesh morphing techniques have unfolded an attractive prospect, there are still lots of difficulties that mostly go back to the prior knowledge needed to be brought into the mesh morphing process.

This chapter introduces and evaluates an original Atlas-based mesh morphing method that does not rely on any segmentation method. The idea consists in using the whole 3D image (CT and/or MRI) rather than a ROI extracted from this 3D image, to compute the 3D transformation that will automatically morph atlas FE mesh and to generate subject-specific meshes. The method extracts this 3D transformation by registering the atlas' volume image to the subject's one, and establishes a one-to-one correspondence between the two volumes. To preserve the quality of the subject-specific mesh, a diffeomorphic non-rigid registration based on B-spline Free-Form Deformations (FFDs) is used, which guarantees a non-folding and one-to-one transformation. It was shown that the level of distortion can be dramatically reduced, if the transformation satisfies three main constraints: being C^1-differentiable, non-folding (a local property ensuring that space orientation is preserved) and invertible; these properties specify a C^1-diffeomorphism (Bucki et al. [2010a]; Chenchen [2013]). In summary, the proposed method (Fig. 3.2) includes two major modules:

- Computing without any segmentation the displacement fields that can be used to register the volumetric atlas' images onto the subject's images;

- Morphing the atlas' FE mesh using the obtained displacement fields.

More specifically, at first, an initial Rigid/Affine transformation is performed to roughly approximate the global deformation between the atlas' and the subject's volume. Then, a non-rigid registration is done to locally refine the deformations from the atlas to the subject. The subject-specific FE mesh is then generated by deforming the atlas' FE mesh using the derived 3D transformation. Finally, the qualities of the morphed meshes is evaluated.
In the next sections, details of the method are provided and evaluated, and an illustration of its practical usability in a clinical context is proposed with an application in maxillo-facial computer-assisted intervention, which requires the generation of patient-specific tongue FE meshes. The method includes the volumetric image registration and the morphing of the atlas FE mesh. We propose as a first step an evaluation of our method based on a dataset of CT scans of the ribcage (including binary Lung masks) and consisting in evaluating the accuracy of the inter-subject registration process. In a second part tongue meshes are generated for two healthy subjects and two patients suffering from tongue cancer, with a particular focus on the assessment of the mesh's quality. Being able to generate accurate patient-specific tongue meshes is interesting because tongue segmentation from medical images is challenging (Iskarous [2005]) since the tongue is an extremely flexible organ that is in contact with many other structures in the oral cavity (cheeks, pharyngeal walls, palate, lips). Furthermore, regarding the patients with abnormal structures (in the case of tongue cancers for example), as there will be intensity variations in the affected regions, automatic segmentation could be even more complex (Lee et al. [2014]; M. Harandi et al. [2015]). Finally, the tongue model of one of the patients is used to qualitatively evaluate functional consequences of the surgery. The removal of the tumor and the replacement of the corresponding tissues with a passive flap are modeled. A tongue gesture is then simulated and analyzed, before and after surgery.

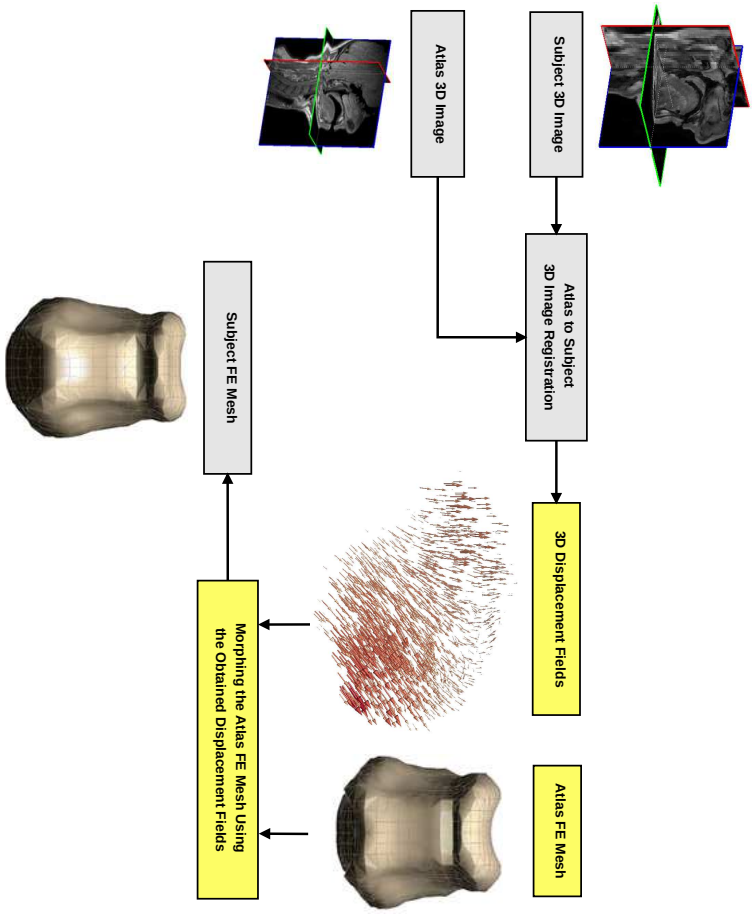

Figure 3.2: General dataflow proposed to generate 3D subject-specific FE meshes.

3.2 Volume Image Registration

3.2.1 Introduction

Image registration is a process by which the most accurate geometrical transformation that aligns features in two images or volumes is determined. The images/volumes may have been taken at various times and viewpoints, by the same or different sensors. These are fundamental problems in medical image processing as the volumes possibly come from different modalities (e.g., Magnetic Resonance (MR), Computed Tomography (CT), Positron Emission Tomography (PET), Single-Photon Emission Computed Tomography (SPECT), and etc.), different time points (e.g., in follow-up studies), and/or from different subjects (e.g., population based studies). Theoretically, such an optimal geometrical transformation ($\mathbf{T}$) that maps positions

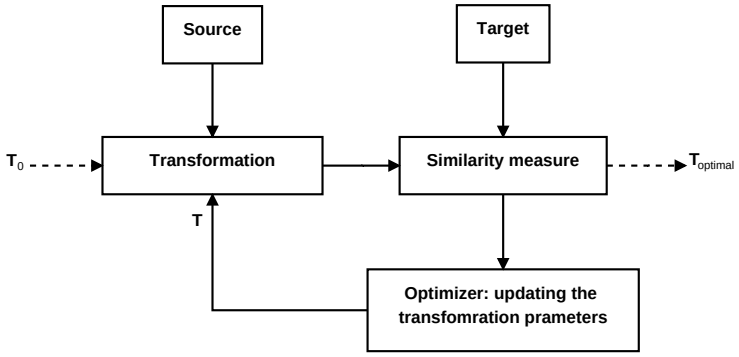

Figure 3.3: Iterative schematic overview of image registration process.

in one volume, *so-called* **source**, to positions in another, *so-called* **target**, is estimated under a certain criteria (**E**) that measures the goodness of matching between the two volumes. An iterative schematic overview of image registration process is shown in Figure 3.3. It should be reminded that there are two main steps in order to apply a geometric transformation to a volume data: 1) Determination of the transformed position for each voxel, and then 2) Computation of new voxel intensities for all grid positions in the resulting volume. The latter step employs interpolation techniques in order to approximate the voxel values.

3.2.2 Rigid/Affine and non-rigid transformations

Rigid body transformations are a subset of the more general affine transformations, and have six degrees of freedom in 3D space: there parameters for translations and three parameters for rotations about the orthogonal axes. Given a homogeneous voxel coordinate ($\mathbf{x}$), the new voxel position is computed by $\mathbf{T}_{Rigid}(\mathbf{x}) = \mathbf{R}\mathbf{x} + \mathbf{t}$, in which a translation matrix ($\mathbf{t}$) is defined as

$$\mathbf{t} = \begin{bmatrix} 1 & 0 & 0 & \mathrm{x}_{trans} \\ 0 & 1 & 0 & \mathrm{y}_{trans} \\ 0 & 0 & 1 & \mathrm{z}_{trans} \\ 0 & 0 & 0 & 1 \end{bmatrix} \tag{3.1}$$

and rotations about the orthogonal axes (X, Y and Z) are carried out by a rotation matrix (R) defined as

$$\mathrm{R_x}(\Theta) = \begin{bmatrix} 1 & 0 & 0 & 0 \\ 0 & \cos(\Theta) & \sin(\Theta) & 0 \\ 0 & -\sin(\Theta) & \cos(\Theta) & 0 \\ 0 & 0 & 0 & 1 \end{bmatrix},$$

$$\mathrm{R_y}(\Phi) = \begin{bmatrix} \cos(\Phi) & 0 & \sin(\Phi) & 0 \\ 0 & 1 & 0 & 0 \\ -\sin(\Phi) & 0 & \cos(\Phi) & 0 \\ 0 & 0 & 0 & 1 \end{bmatrix},$$

$$\mathrm{R_z}(\Omega) = \begin{bmatrix} \cos(\Omega) & \sin(\Omega) & 0 & 0 \\ -\sin(\Omega) & \cos(\Omega) & 0 & 0 \\ 0 & 0 & 1 & 0 \\ 0 & 0 & 0 & 1 \end{bmatrix},$$

$$\mathbf{R} = \mathrm{R_z}(\Omega)\mathrm{R_y}(\Phi)\mathrm{R_x}(\Theta) \tag{3.2}$$

It is clear that through the rigid transformations $\mathbf{T}_{Rigid}$, one can alter the roll, pitch and yaw of the object to move it in the space but the actual size and shape of the object will not change. Since, an affine transformation ($\mathbf{M}$) allows up to 12 degrees of freedom, the scale of the object can be altered or sheer can be introduced (Fig. 3.4).

$$\mathbf{T}_{Affine}(\mathbf{x}) = \mathbf{M}\mathbf{x} = \begin{bmatrix} \mathrm{m}_{11} & \mathrm{m}_{12} & \mathrm{m}_{13} & \mathrm{m}_{14} \\ \mathrm{m}_{21} & \mathrm{m}_{22} & \mathrm{m}_{23} & \mathrm{m}_{24} \\ \mathrm{m}_{31} & \mathrm{m}_{32} & \mathrm{m}_{33} & \mathrm{m}_{34} \\ 0 & 0 & 0 & 1 \end{bmatrix} \begin{bmatrix} x \\ y \\ z \\ 1 \end{bmatrix} \tag{3.3}$$

In practice, the input volumes to the registration process have different dimensions and voxels' sizes. These differences should be considered during the registration process. For simplicity, the Euclidian space can be used in

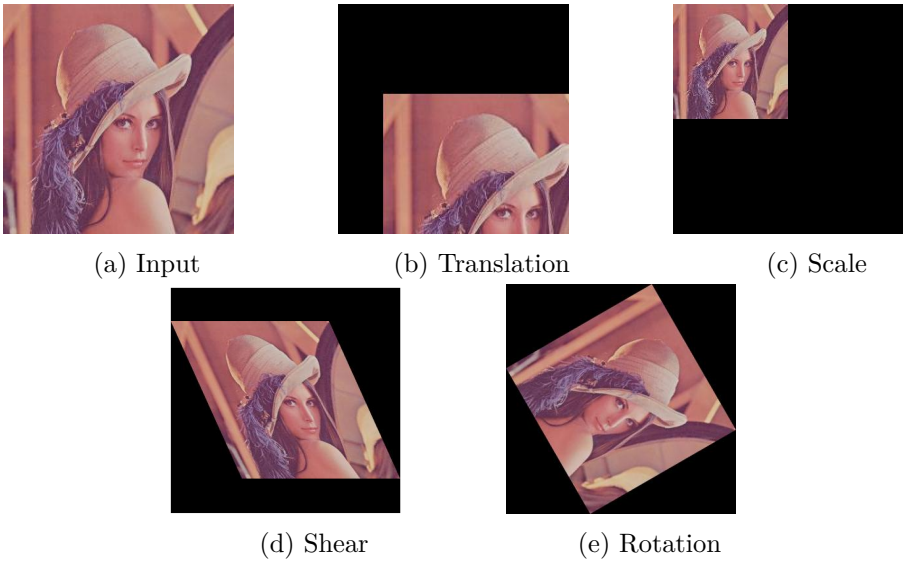

(a) Input (b) Translation (c) Scale

(d) Shear (e) Rotation

Figure 3.4: Affine transformations: translation, scale, shear, and rotation.

order to define distances in *millimeters*. Considering image's information (dimensions and voxels' sizes), one can apply a pre-affine transformation to map the voxels' coordinates into the Euclidian space whose axes are parallel to those of volume and distances are measured in *millimeters*, with an origin at the center of volume. For instance, given an image of size $256 \times 256 \times 54$ and voxels' sizes of $1.5mm \times 1.5mm \times 3mm$, the pre-affine transformation can be defined as

$$\mathbf{M} = \begin{bmatrix} 1.5 & 0 & 0 & -(\frac{256\times1.5}{2}) \\ 0 & 1.5 & 0 & -(\frac{256\times1.5}{2}) \\ 0 & 0 & 3 & -(\frac{54\times3}{2}) \\ 0 & 0 & 0 & 1 \end{bmatrix} = \begin{bmatrix} 1.5 & 0 & 0 & -192 \\ 0 & 1.5 & 0 & -192 \\ 0 & 0 & 3 & -81 \\ 0 & 0 & 0 & 1 \end{bmatrix} \tag{3.4}$$

It is obvious that Affine/Rigid transformations, as global transformation models, are often not sufficient to capture local deformations. For instance, linear transformations would not be able to model the local deformations between the two images shown in Fig.3.5(a) and Fig. 3.5(b). In this example, two different face mimics are presented and non-linear transformations (see section 3.3) has to be defined to register the source image to the target image (Fig.3.5(c)). In non-rigid registration, each point of image $\mathbf{x}$ is transformed

(a) Source image (b) Target image (c) Deformed source

Figure 3.5: Non-rigid registration.

by a specific displacement $D(\mathbf{x})$ as $T(\mathbf{x}) = \mathbf{x} + D(\mathbf{x})$. These displacements are estimated in such a way that the similarity between the deformed source and the target images is increased (see section 3.3.1 for more details).

3.3 Problem Formulation

To extract a transformation that provides an accurate match between atlas and subject volumetric images, a two-level 3D image registration is used. First, a global transformation is calculated to provide an initial Rigid/Affine alignment. Then, a nonrigid method is used to establish the voxel-wise correspondence between the two volumes. As mentioned in previous sections, based on preceding studies on Mesh-Match-and-Repair algorithm (Bucki et al. [2010a]), the morphing algorithm should be continuously differentiable, non-folding and invertible. In other words, the transformation model should be a smooth bijective (one-to-one) mapping with a smooth inverse. Fig. 3.6 simply shows the effect of those mapping functions which do not satisfy the above mentioned requirements. To give more understanding, only the 2D view of nodes is provided. Fig. 3.6(a) illustrates the result of a non-continuous mapping function. For the sake of example, such a mapping function is applied to a set of nodes (gray ones), and the transformed nodes are shown in yellow color. As can be seen, such transformation results in low quality mesh elements and sometimes causes mesh to tear. Fig. 3.6(b) represents the consequence of a non-bijective mapping function; it can be

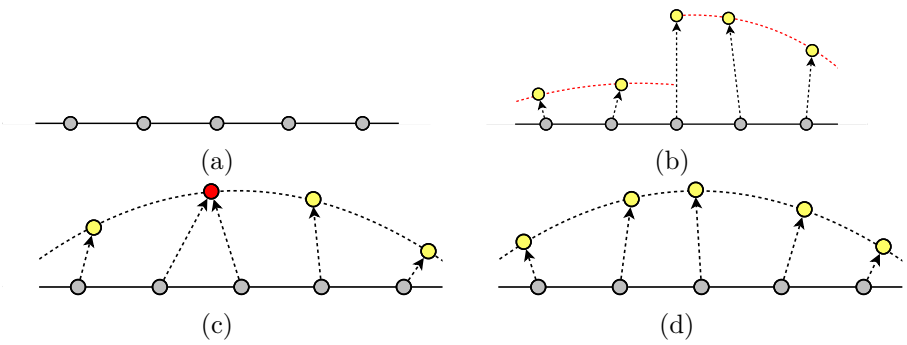

Figure 3.6: Effects of C^1-diffeomorphism transformations: (a) Nodes' original locations (in gray), (b) After applying a non-continuous mapping function, (c) After applying a non-bijective mapping function, (d) After applying an ideal mapping function.

seen that two nodes are mapped to the same coordinate (red node) that causes existence of irregular elements in the deformed mesh. And finally, the result of an ideal transformation (from the point of mesh distortions) is shown in Fig. 3.6(c).

There are two popular non-rigid diffeomorphic registration methods: (1) Free-Form Deformations (FFDs), which are modeled by B-splines (Rueckert et al. [2006]), and (2) the diffeomorphic Demons, which is a nonparametric diffeomorphic registration method based on Thirion's demons algorithm (Vercauteren et al. [2009]). Generally, the FFDs based registration algorithms are controlled by the underlying interpolation function, which provides more regular displacement fields than Demons-based approaches. Our group previously employed FFDs based algorithms. In this paper, the same FFD based method is chosen as the basis for the transformation model, which inherently generates smooth deformations. In addition, this model has been reformulated using discrete Markov Random Fields (MRF) (Glocker et al. [2008]). This amendment eliminates the procedure of customizing the optimization method for different similarity measures in multi-modal volumetric image registration, which is a challenging problem in medical imaging (Komodakis et al. [2007]). In the next sections, the explanations of the diffeomorphic FFDs, their implementation and the employed optimization method in the subject-specific FE mesh generation process, are provided.

3.3.1 Free Form Deformation (FFD)

Non-rigid registration algorithms based on FFDs map each voxel of the atlas image into the corresponding voxel in the subject image using a deformation field that is optimally computed. The basic idea of these methods is to characterize deformations based on a grid of control points that are uniformly distributed throughout the fixed image's voxel grid (herein the subject image). These control points partition the volume into equally sized regions (called *tiles*). The transformation model is a multilevel formulation of a FFDs based on tensor product of B-splines. B-splines enable interpolating the dense deformation field from a given set of control points. Let us denote the domain of the image volume as $\Omega = \{(x, y, z)|0 \leq x < X, 0 \leq y < Y, 0 \leq z < Z\}$. Let G denote a virtual deformable grid with spacings $\delta_x, \delta_y, \delta_z$, which is superimposed on the image volume. The nonlinear displacement field D is computed for each image point $\mathbf{x} = (x, y, z)$ by B-spline interpolation of the displacements of the grid control points:

$$D(\mathbf{x}) = \sum_{l=0}^{3} \sum_{m=0}^{3} \sum_{n=0}^{3} B_l(u) B_m(v) B_n(w) d_{i+l,j+m,k+n}, \tag{3.5}$$

where, i, j, and k denote the coordinates of the *tile* containing image point $\mathbf{x}$ and u, v, and w are the local coordinates of (x, y, z) within its housing *tile*: $i = \lfloor x/\delta_x \rfloor$, $j = \lfloor y/\delta_y \rfloor$, $k = \lfloor z/\delta_z \rfloor$, $u = x/\delta_x - \lfloor x/\delta_x \rfloor$, $v = y/\delta_y - \lfloor y/\delta_y \rfloor$, $w = z/\delta_z - \lfloor z/\delta_z \rfloor$ ($\lfloor\ \rfloor$ is rounding operation). B_l represents the lth basis function of the B-spline interpolation and the displacement of the grid control points are denoted by d. So, $d_{i+l,j+m,k+n}$ is the spline coefficient defining the displacement for one of the 64 control points that influence the image point $\mathbf{x}$ within *tile* (i, j, k). Indeed, the B-splines serve as a weighted averaging function for the set of control points. Finally, the transformation of image point $\mathbf{x}$ can be computed by

$$T(\mathbf{x}) = \mathbf{x} + D(\mathbf{x}) \tag{3.6}$$

Given the source (J) and target (I) volumes, one seeks the optimal transformation by posing an energy minimization problem where the objective function is defined by a matching criterion S:

$$\widehat{T} = arg \min_{T} S(I, J \circ T) \tag{3.7}$$

According to the application at hand, the matching criterion S may be Sum of Absolute/Squared Differences (SAD/SSD), Normalized Mutual Information (NMI) (Maes et al. [1997]), Normalized Correlation Coefficient (NCC), Correlation Ratio (CR) (Roche et al. [1998]), and etc.

The performance of registration methods based on FFDs is limited by the resolution of the control point grid, which generally determines the degrees of freedom and is linearly related to the computational complexity (Rueckert et al. [2006]):

- A coarse control point spacing enables modeling global and intrinsically smooth deformations.
- A finer control point spacing enables modeling more localized and intrinsically less smooth deformations.

Therefore, to refine the deformation field, a multi-level FFD is used to cover a wide range of transformations. The algorithm starts from a coarser control point spacing; when the algorithm reaches its optimal state, the control point spacing is reduced by a factor of two (in each dimension) to generate a finer grid. Also, for each level of control point spacing, several optimization cycles are performed to model a large deformation. Within each cycle of optimization process, an elementary transformation field is generated and the overall transformation can be computed as below:

$$T(\mathbf{x}) = \overbrace{T_J^{N_J} \circ \cdots \circ T_J^1}^{G_J} \circ \cdots \circ \overbrace{T_1^{N_1} \circ \cdots \circ T_1^1}^{G_1}, \tag{3.8}$$

where $G_j, j = 1, \cdots, J$ are successive grid refinements, and $T_j^i, i = 1, \cdots, N_j$ are elementary deformations which have been generated during each optimization cycle at grid level j.

As the FFDs are modeled by B-splines, the transformation model inherently satisfies the C^1-differentiability. In order to preserve the bijectivity of the transformation, each elementary transformation is estimated by restricting the displacement of control points to 0.4 times the current control point spacing (Rueckert et al. [2006]). Since the overall transformation is computed by the combination of the elementary ones, it will be likewise a diffeomorphism. Although the regularity properties of the elementary registrations, namely non-folding and bijection, are enforced by restricting the

amplitude of the displacement of the control points, it should be noted that the non-folding property is fulfilled locally at every point. Accordingly, the image-derived displacement fields may lead to unrealistic deformations and the deformed mesh may finally be prone to folding, as the consequence of crisscrossing of neighboring control points (Brock [2013]). Therefore, an additional regularization term, which reduces mesh distortion, is considered as below:

$$R(T) = \sum_{p \in G} \sum_{q \in N(p)} \mid d_p - d_q \mid^2, \tag{3.9}$$

where d_p is the displacement of the control point p in the virtual deformable grid G, and $N(p)$ is the set of control points which are located in the neighborhood of p, and defines the edges between p and others points in the control grid. This regularization term, which enforces a smooth transformation, leads neighboring control points to move in the same direction. Hence, the total cost function optimized in the registration problem is defined as the sum of two terms: a matching criterion (S) which quantifies the level of alignment between the two image volumes, and a regularization term (R) which imposes a smoothness constraint. The optimal transformation can be determined by posing an energy minimization problem where the objective function is a weighted sum of S and R:

$$\widehat{T} = arg \min_{T} \{S(I, J \circ T) + \lambda R(T)\}, \tag{3.10}$$

where λ parameter acts as a weighting factor, controlling the influence of the regularization term. To obtain deformation parameters, a wide range of optimization strategies can be employed, including gradient descent (Rueckert et al. [1999]), Newton's method (Nocedal and Wright [2006]; Mattes et al. [2003]) , Powell's method (Powell [1978]), and discrete optimization (Komodakis et al. [2008]). However, since the atlas and subject medical images can come from different modalities (e.g. CT or MRI), the possibility of using different similarity measures should be considered. In that case, the optimization process will be dependent on the type of cost function and should be customized based on the employed one. This is why a discrete optimization strategy which is computationally efficient and also robust with respect to local optima, has been selected, namely the Markov Random

Fields (MRF)-based optimization (Komodakis et al. [2007]).

3.4 Solution Estimation

To obtain the deformation parameters, a numerical method has to be used to optimize the objective function in Eq. 3.10. For all the reasons mentioned in the previous section, a discrete optimization is used (Komodakis et al. [2007]). Broadly speaking, this projects the objective function back to the level of the control points, in order to transform it into a function of control points displacements instead of voxels displacements. Then, the displacement space is sampled in a discrete manner and the quantized displacement vectors are associated with labels, so that the optimization problem is converted to what is called "a labeling problem". Finally, the appropriate optimization technique can be employed to extract a group of displacement vectors that collectively optimize the objective function. In this section, the employed discrete optimization strategy, from the conversion of the optimization problem to a labeling problem up to finding the best combination of labels or displacement fields, is briefly explained. For more details, the reader is referred to Komodakis et al. [2007]; Glocker et al. [2008].

3.4.1 MRF-based Optimization

The primary task is the reformulation of the optimization problem (Eq. 3.10) into a multi-labeling problem that can be expressed using first-order Markov Random Fields (MRFs) (Geman and Geman [1984]; Li [2009]). Generally, a "labeling problem" consists of a set of objects to be classified, and a set of classes or labels. The objective of such a problem is to assign a label to each object, in a way that is consistent with some observed data that may contain pairwise relationships among the objects to be classified (Breiman et al. [1984]; Ditterrich [1997]; Li [2009]). Markov random fields are used to model the statistical properties in the framework of probability theory. In the MRFs model, the probability of an object to belong to a specific class stands not only on its own feature but also on the labels of its neighboring objects. These objects can be considered as random variables whose values stand by the outcome of probabilistic experiments. Therefore, from the perceptive of MRFs, a labeling problem is defined in terms of a set of random

variables and a set of labels that can be interpreted as events that can be happen to the random variables (Li [2009]). Consequently, at first, the role of the random variables and the definition of a discrete label space should be characterized. Considering the registration problem, a random variable is associated with every control point, and "labels" are defined corresponding to the displacements of the control points. Therefore, the continuous displacement space of the control points is quantized to generate a discrete set of displacement vectors $\Theta = \{d^1, ..., d^i\}$, and each displacement vector is associated with a label ($L = \{l^1, ..., l^i\}$). Also, assigning a label (l_p) to a control point (p) is equivalent to applying the displacement vector d^{l_p} to the control point p. In this study, the displacements along the coordinate axes are sparsely sampled by a factor of n, from the minimum displacement to the maximum value (i.e., from zero to 0.4 times the current control point spacing (Rueckert et al. [2006]), which ends up having 6n+1 labels (displacements along the six main axes plus the zero-displacement vector are considered). The problem can then be reformulated using the energy of first-order MRFs, which consists of sums of *unary* and *pairwise* potential functions:

$$E_{MRF}(l) = \sum_{p \in G} V_p(l_p) + \lambda \sum_{p \in G} \sum_{q \in N(p)} V_{pq}(l_p, l_q), \tag{3.11}$$

where l is the labeling that we are looking for, $V_p(.)$ is a *unary* potential function that corresponds to the energy of assigning a label to the control point p, independently of all other control points (Li [2009]). As mentioned before, the labels are associated with the control points displacements. So, the *unary* potential term summed over all the control points encodes the matching criterion (S) in Eq. 3.10. $V_{pq}(.)$ is a *pairwise* potential function that evaluates the consistency between the labels of neighboring control points. In other words, it measures the cost of assigning displacements to the neighboring control points p and q. Therefore, the *pairwise* potential term summed over all the neighboring control points corresponds to the regularization term (R) in Eq. 3.10. The other two parameters $N(p)$ and λ respectively define the control points neighboring region and control the influence of the regularization term. To help understanding, Fig. 3.7 simply visualizes the conversion of a registration problem to a labeling problem. Fig. 3.7(a) depicts the voxel grid, which is partitioned into equally sized regions by the control points. Then, in Fig. 3.7(b), the continuous dis-

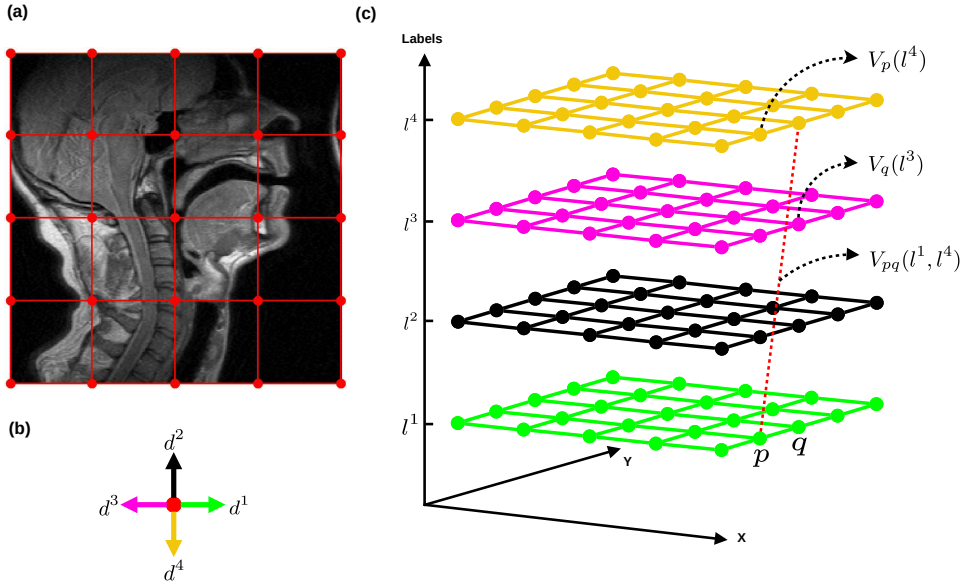

Figure 3.7: Conversion of registration problem to a labeling problem: (a) input image superimposed with the control points, (b) the continuous displacement space of control points is quantized: $\Theta = \{d^1, d^2, d^3, d^4\}$, (c) all possible labels that can be assigned to the control points.

placement space of control points is quantized to generate a discrete set of displacement vectors $\Theta = \{d^1, d^2, d^3, d^4\}$ and each displacement vector is associated with a label ($L = \{l^1, l^2, l^3, l^4\}$). Two neighboring control points p, q and all possible labels that can be assigned to the control points are shown in Fig. 3.7(c). For example, the *unary* potential terms $V_p(l^4)$ and $V_q(l^3)$ measure, respectively, the cost of assigning displacements d_4 and d_3 to the control points p and q, while *pairwise* potential function $V_{pq}(l^1, l^4)$ measures the cost of assigning displacements d_1 and d_4 to the *neighboring* control points p and q.

It is now important to note that, the matching criterion (S) in the energy optimization problem (Eq. 3.10) is defined on the image level. This criterion should therefore be projected back to the control points level using a weighting function so that the energy optimization problem could be

mathematically reformulated using MRFs:

$$\widehat{\eta}(|\mathbf{x}-p|) = \frac{\eta(|\mathbf{x}-p|)}{\sum\limits_{\mathbf{y}\in\Omega}\eta(|\mathbf{y}-p|)}, \tag{3.12}$$

where $\widehat{\eta}(.)$ quantifies the impact of an image pixel $\mathbf{x}$ to a control point p, while $\eta(.)$, quantifies the influence of a control point p to an image pixel $\mathbf{x}$. The amount of influence is related to the distance between the image pixel $\mathbf{x}$ and the control point p; the farther they are, the less is the influence, and vice versa. Herein, the $\eta(.)$ function is the B-spline function used in Eq. 3.5, that can be interpreted as a weighting function. Therefore, the *unary* potential function in the energy of MRF (in iteration t) can be rewritten as:

$$V_p(l_p) = \sum_{\mathbf{x}\in\Omega} \boldsymbol{\widehat{\eta}(|\mathbf{x}-p|)} \,.\, S(I(\mathbf{x}), J(T^{t-1}(\mathbf{x}) + \boldsymbol{d^{l_p}})), \tag{3.13}$$

where T^{t-1} is the overall transformation from the previous iteration and d^{l_p} is the next elementary displacement of control point p. Accordingly, the *unary* potential at control point p is defined as the weighted combination of the data cost of those pixels that have an impact on the control point p. However, as previously mentioned, the *unary* potential function is assumed to be independent of all other control points. So, the *unary* potential is computed approximately under two simplifications (Glocker et al. [2008]). First, the elementary displacement of each image point $\mathbf{x}$ (i.e., Eq. 3.5) is computed by direct translation of d^{l_p} (the displacement of control point p), instead of doing the interpolation between the displacement of the neighboring control points. Second, with the aim to decrease the approximation error, the overlapping area for each control point is reduced by replacing the B-spline weighting functions in $\widehat{\eta}(.)$ (Eq. 3.12) with the linear ones. It should be reminded that B-spline functions are still kept to generate smooth transformation.

By the same token, and to have a full regularization, the deformation fields generated from the previous iterations are considered in the *pairwise* potential function as below:

$$V_{pq}(l_p, l_q) = \mid (\mathcal{R}(p) + d^{l_p}) - (\mathcal{R}(q) + d^{l_q}) \mid, \tag{3.14}$$

where $\mathcal{R}(.)$ projects the current overall transformation or displacement fields

on the level of the control points as:

$$\mathcal{R}(p) = \sum_{\mathbf{x} \in \Omega} \widehat{\eta}(|\mathbf{x} - p|) D(\mathbf{x}) \tag{3.15}$$

Thus, the registration problem is converted to a discrete labeling problem in the form of MRFs, and various optimization strategies can be applied to find the registration parameters. An efficient algorithm called FastPD is used in this study (for a full explanation of this method the reader is referred to Komodakis et al. [2007]. To get accurate registration results, some parameters controlling the discretization of the solution space have to be set. The first parameter is the maximum value of displacement which has been set to 0.4 times the current control point spacing (Rueckert et al. [2006]). As mentioned before, to refine the deformation field, a multi-level FFD is employed to cover a wide range of transformations; also, for each level of control point spacing, several optimization cycles (the second parameter, O) are performed to model a large deformation. However, as FastPD generates quasi-optimal labelings on the discrete set of labels (Glocker et al. [2008]), it should be noticed that keeping the initial displacement set does not bring any further improvement. Therefore, each optimization cycle is done using a new set of displacement vectors. In this way, the initial maximum value of displacement is reduced by a scaling factor (the third parameter, α), and the new range has been re-sampled using the same method (with a specific number of steps, the fourth parameter, n). For the results provided later, the parameters are set to $O = 5$, $\alpha = 0.67$ and $n = 5$ (Glocker et al. [2008]).

3.5 Mesh Morphing

The atlas-to-subject volumetric image registration provides a pair of transformations that establishes a one-to-one correspondence between the two volumes (atlas J and subject I). The first one is a Rigid/Affine transformation ($T_{\textbf{Rigid/Affine}}$) that approximates the global transform between the two volumes, whereas the second one is a nonrigid transformation ($T_{\textbf{Nonrigid}}$) that locally refines the deformations from the Atlas to the subject. The next step towards atlas-mesh morphing consists in defining the total trans-

formation by combining the rigid and non-rigid transformations:

$$T_{\textbf{Total}} = T_{\textbf{Nonrigid}} \circ T_{\textbf{Rigid/Affine}} \tag{3.16}$$

Each node of the atlas mesh is transformed by $T_{\textbf{Total}}$ in order to generate the subject-specific mesh (with the same topology as for the atlas mesh since nodes connectivities are kept constant).

3.6 Evaluation

3.6.1 Image Registration Assessment

In order to quantitatively evaluate our method, manual segmentations of the atlas' and target's organs are used. After the registration between the atlas' and target's images, the obtained transformations are employed to deform the atlas' binary mask onto the target' images. Then, the Dice (Dice [1945]) and volumetric overlap metrics, Hausdorff distance, and mean absolute surface are computed (Gerig et al. [2001]). The Dice (**D**) and overlap fraction (**O**) are volumetric measures that compute the relative overlap of two volumes. For each subject, the Dice and volumetric overlap of the atlas-transformed mask ($V_{\textbf{Atlas-trans}}$) and the reference segmentation ($V_{\textbf{Manual}}$) are respectively defined as

$$\mathbf{D}(V_{\textbf{Atlas-trans}}, V_{\textbf{Manual}}) = \frac{2|V_{\textbf{Atlas-trans}} \cap V_{\textbf{Manual}}|}{|V_{\textbf{Atlas-trans}}| + |V_{\textbf{Manual}}|} \tag{3.17}$$

$$\mathbf{O}(V_{\textbf{Atlas-trans}}, V_{\textbf{Manual}}) = \frac{|V_{\textbf{Atlas-trans}} \cap V_{\textbf{Manual}}|}{|V_{\textbf{Atlas-trans}} \cup V_{\textbf{Manual}}|} \tag{3.18}$$

Both **D** and **O** values range from zero to one. A value close to one is desirable and means that there is a perfect match between the volumes. However, both volumetric measures depend on the size and shape complexity of the objects and on the volume sampling. Large objects such as the Lungs should be less sensitive to small local errors, which may exist at the boundaries. Therefore, the Hausdorff (**H**) distance is also considered as an evaluation of the similarity of the objects' surfaces. Given two surfaces $S_{\textbf{Atlas-trans}}$ and $S_{\textbf{Manual}}$, the Hausdorff distance is defined as

$$\mathbf{H}(S_{\textbf{Atlas-trans}}, S_{\textbf{Manual}}) = \max(h(S_{\textbf{Atlas-trans}}, S_{\textbf{Manual}}), h(S_{\textbf{Manual}}, S_{\textbf{Atlas-trans}})) \tag{3.19}$$

where

$$h(S_{\textbf{Atlas-trans}}, S_{\textbf{Manual}}) = \max_{p \in S_{\textbf{Atlas-trans}}} (d_{\boldsymbol{min}}(p, S_{\textbf{Manual}})), \tag{3.20}$$

$$h(S_{\textbf{Manual}}, S_{\textbf{Atlas-trans}}) = \max_{p \in S_{\textbf{Manual}}} (d_{\boldsymbol{min}}(p, S_{\textbf{Atlas-trans}})). \tag{3.21}$$

The Hausdorff distance is overly sensitive to outliers. A single outlier leads to misleading results. However, it can provide useful information in conjunction with other metrics such as the mean absolute surface distance (**M**), which is defined as

$$\mathbf{M}(S_{\textbf{Atlas-trans}}, S_{\textbf{Manual}}) = \frac{\overline{d}_{min}(S_{\textbf{Atlas-trans}}, S_{\textbf{Manual}}) + \overline{d}_{min}(S_{\textbf{Manual}}, S_{\textbf{Atlas-trans}})}{2} \tag{3.22}$$

where $\overline{d}_{min}(S_{\textbf{Atlas-trans}}, S_{\textbf{Manual}})$ is the average minimum distance from all points on the surface $S_{\textbf{Atlas-trans}}$ to the surface $S_{\textbf{Manual}}$, and vice-versa for $\overline{d}_{min}(S_{\textbf{Manual}}, S_{\textbf{Atlas-trans}})$. **M** indicates how much the two surfaces differ on average.

3.6.2 Mesh Quality Assessment

The regularity and quality of the deformed meshes are evaluated based on the Jacobian matrix (Knupp [2000]). The Jacobian matrix is the fundamental quantity describing all the *first-order* mesh properties (length, areas and angles) of interest (Knupp [2000]). The regularity assessment is function of the Jacobian matrix determinant (`detJ`, also called the *Jacobian*) and evaluates whether the employed FE mesh can be used for numerical analysis. The *Jacobian* must be checked for all the elements of the FE mesh as it is influenced by the configuration of the element nodes. Within each element, the *Jacobian* is computed for each node, and the element (and subsequently the FE mesh) is classified irregular if one of the nodes has a zero or negative

value. It is worth pointing out that the *Jacobian* measures the distortion of the actual mesh element with respect to its reference configuration, but not the overall distortion information. To deal with this problem, the quality of each element can be determined at the level of its nodes (e.g., node n) by a ratio of nodal *Jacobian* value to the maximal *Jacobian* value among those computed at all element nodes (thus interpreted as a global distortion information). Such a ratio measures the node quality within its element (e) and is called Jacobian Ratio (**JR**) (Knupp [2000]):

$$\mathbf{JR}_n^e = \frac{\mathtt{detJ}(n)}{\max\limits_{n \in e} \{\mathtt{detJ}(n)\}} \tag{3.23}$$

The **JR** values range from zero to one. Having a high (respectively low) value for $\mathbf{JR}_n^e$ means that the element (e) has a high (respectively poor) quality at node n. The **JR** is computed for all the element nodes and the minimum value is returned as an indicator of element quality ($\mathbf{JR}_{min}^e$). In the ideal state, all elements of a given mesh are expected to have high **JR** values; however in many cases this is impossible. That is why, for example, the commercial FE analysis software ANSYS sets a minimal value of $0.0\overline{3}$ for **JR** (Kelly [1998]). It should be noted that **JR** is not relevant for tetrahedral elements as the *Jacobian* value is the same for all nodes of a tetrahedron which means that the **JR** value is always one no matter how good or bad the element is. Therefore, we propose to measure the quality of tetrahedral elements by computing $\mathbf{Q} = 2\sqrt{6}R_{in}/L$ (R_{in} being the radius of the inscribed-sphere of the tetrahedron, and L the longest edge length (Field [2000]; Du and Wang [2005]). Similarly to **JR** computed on hexahedra, wedges and pyramids, the **Q** values computed on tetrahedra range from zero to one for low and high quality elements, respectively.

3.7 Results

Before showing the results of mesh generation, it is important to illustrate how effectively the regularization term prevents the introduction of folds in the deformed meshes. In this respect, Fig. 3.8 shows the results of applying two transformations that are obtained without and with the regularization term. The same evaluation is done at the level of mesh structure formation in

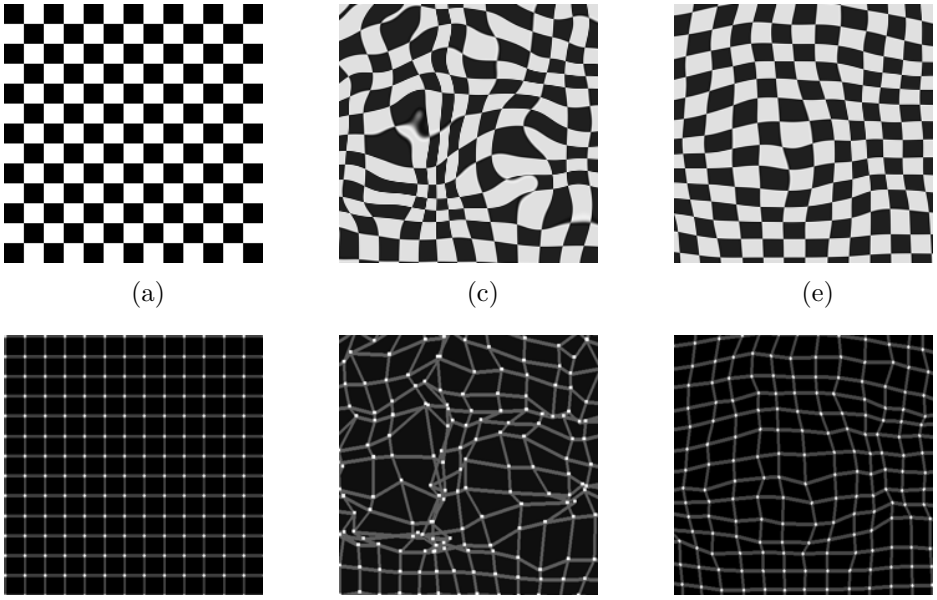

Figure 3.8: Effect of regularization term, at the level of image: (a) input image, (b) distribution of control points,(c) deformed input image without using the regularization term (***RT***), (d) distribution of control points after registration without using the regularization term, (e) deformed input image in the presence of the regularization term (***RT***), (f) distribution of control points after registration in the presence of the regularization term.

Fig. 3.9. To have a clear understanding, only a section of atlas tongue mesh (including 11 elements) is selected and depicted. As can be seen, the level of mesh distortions is dramatically reduced by virtue of the regularization term. These two examples illustrate how the regularity and quality of the meshes can be preserved thanks to the diffeomorphic constraints and the regularization term. The value of the weight λ of the regularization term (Eq. 3.10) has to be set according to the application and to the measure of similarity. Generally, a higher λ value provides a smoother deformation thus less quality degradation, but sharp morphological structures are modeled less accurately. This raises the issue of the level of accuracy provided by our method. To address this issue we have applied our method to a data set of ribcage CT scans and compared the results with the manual segmentation of the Lungs also available in the data set.

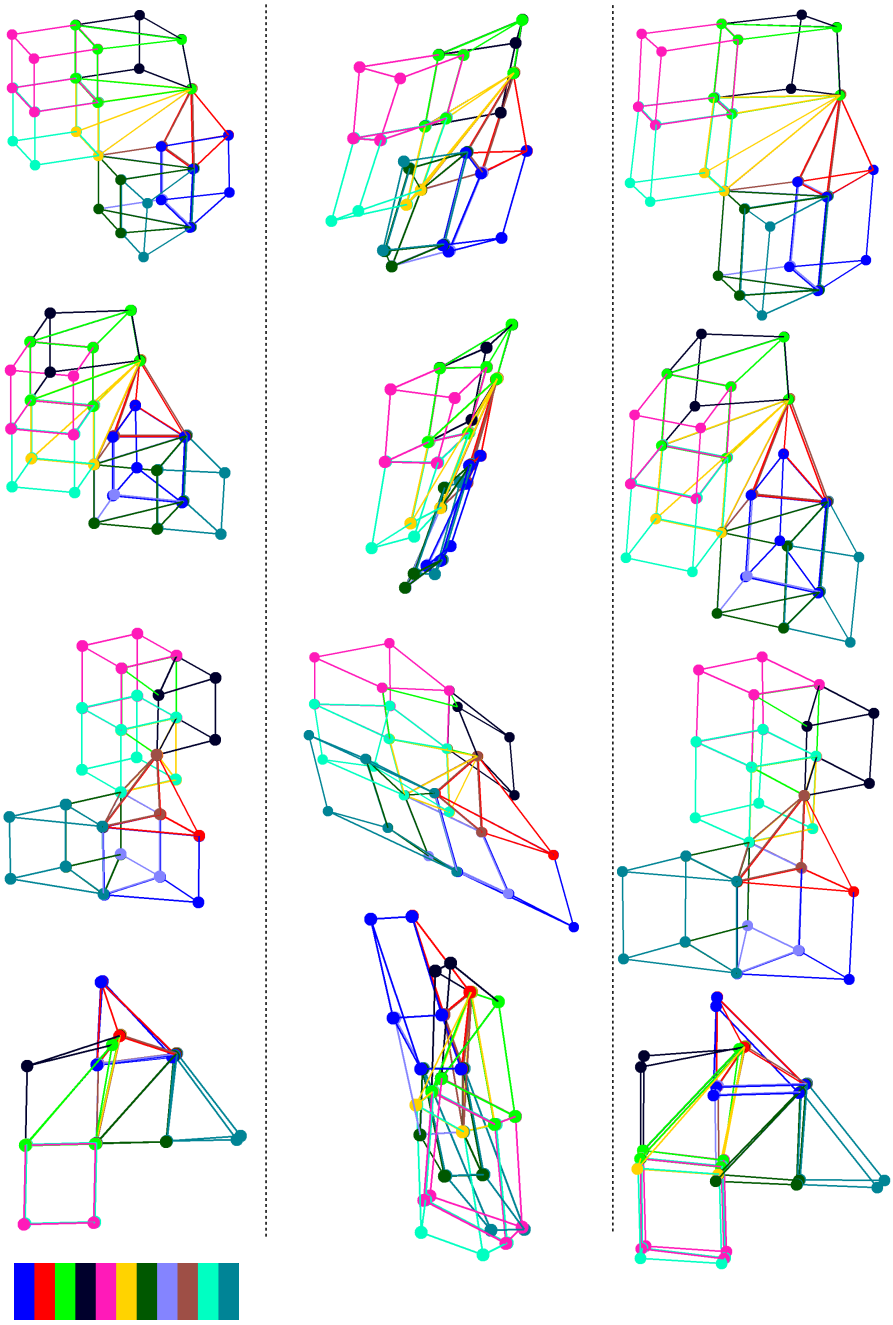

(a) (b) (c)

Figure 3.9: Effect of regularization term, at the level of mesh: (a) a section of atlas FE Mesh, (b) deformed section without using the regularization term (c) deformed mesh using the regularization term (different views are provided in each row: side, front, back, top, in order from top to bottom).

3.7.1 Ribcage CT Image Registration

3.7.1.1 CT Scans of the ribcage

EMPIRE10 competition, as part of MICCAI 2010 Grand Challenges, has provided 30 pairs of thoracic CT data (Murphy et al. [2011]). CT scans are obtained for both healthy and diseased subjects from various scanners with a variety of slice-spacings and image qualities. Most of the scans have a fine sub-millimeter image resolution (around 0.7mm isotropic). The data include binary Lung masks which were generated automatically (Van Rikxoort et al. [2009]) and corrected manually when necessary. We considered the first fifteen subjects to evaluate the performance of our method. Considering the quality and resolution of the scans, volume #2 of the EMPIRE10 database was chosen to be the atlas.

3.7.1.2 Simulation Results

Subject-specific Lung's masks were generated with our method for 12 subjects. Since Lungs are large objects, the non-rigid registration was applied in two steps. First, the SAD (Sum of Absolute Differences) similarity measure with a high value of λ (i.e., regularization weight) is employed in order to capture the main geometric properties of the target Lungs (with a very coarse initial control point spacing of 60 mm). Second, in order to get small details of the shape, the similarity measure is changed into SSD (Sum of Squared Differences), and λ is decreased and an initial control point spacing of $25mm$ is used. Fig. 3.10 shows the result of the Lung registration for a typical CT scan. Manual Lungs segmentation in the atlas' image and in the target image are shown respectively in Fig. 3.10(a) and (b). The Lung's mask provided by our method is superimposed on the manual segmentation in Fig. 3.10(c). We observe a good agreement between both masks. However, the sharp regions, especially at the bottom of the Lungs, are captured less accurately. The Dice (**D**), overlap fraction (**O**), Hausdorff distance (**H**), and mean absolute surface (**M**) are calculated for all subjects. Means and standard deviations of these variables across the subjects are as follows: $\mathbf{D} = 0.98 \pm 0.01$, $\mathbf{O} = 0.96 \pm 0.01$, $\mathbf{H} = 34.25 \pm 7.75$ (in mm), and $\mathbf{M} = 0.98 \pm 0.26$ (in mm). The values of the average quality measures (**D**, **O**, and **M**) show that our method captures efficiently the geometry of target organs; however, high values of **H** are observed, which show the existence of

some strong differences between both masks at some places and/or for some subjects. This will be discussed later in this paper.

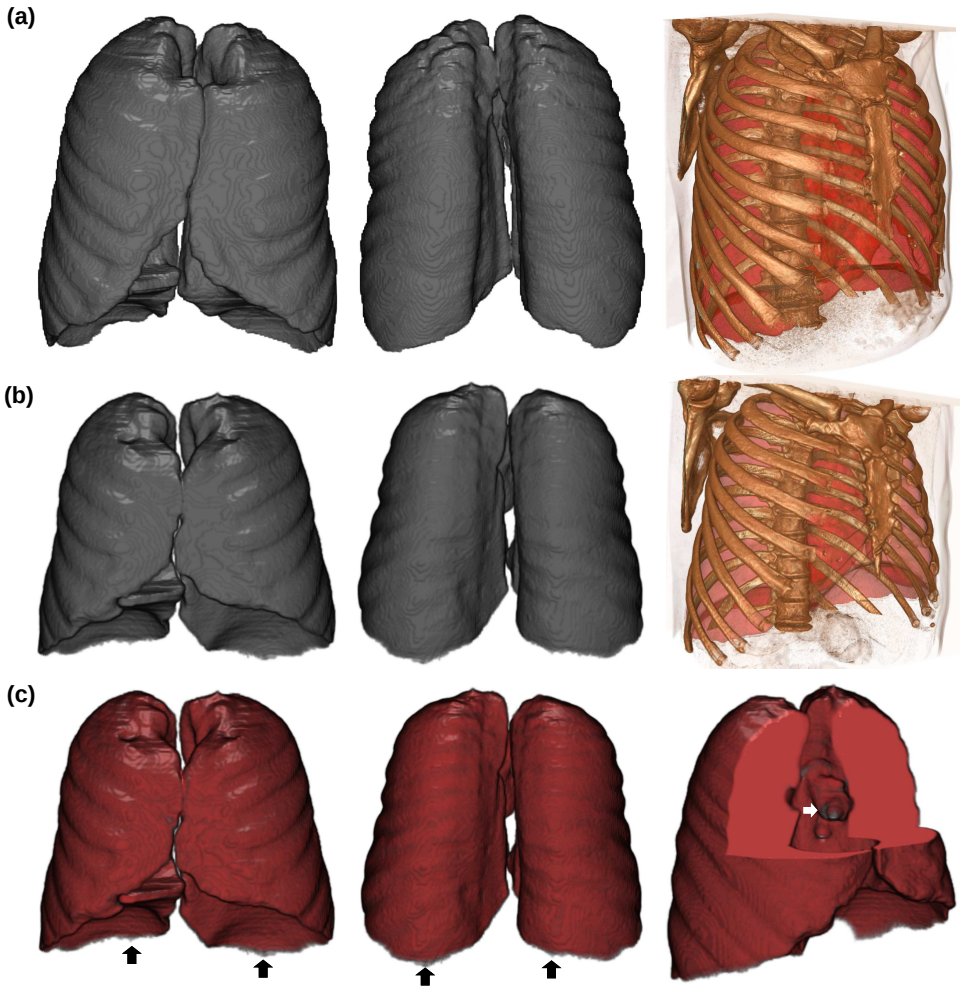

(a)

Figure 3.10: Result of the Lungs CT image registration: (a) Manual Lung segmentation in the atlas' CT-image (at each column, from left to right: front view, back view, and 3D ribcage CT reconstruction surrounding the Lung's manual segmentation), (b) Manual Lung's segmentation in a subject's CT-image (at each column, from left to right: front view, back view, and 3D ribcage CT reconstruction surrounding the Lung manual segmentation), (c) Atlas-driven subject-specific Lungs, in grey, superimposed on the manual segmentation, in red (at each column, from left to right: front view, back view, and a cut-out to the region having less accuracy).

3.7.2 FE tongue meshes generation

3.7.2.1 Tongue MR Images and Atlas' FE Mesh

Our method was also employed to generate subject-specific FE tongue meshes. Tongue T1-weighted MR images of two healthy volunteers (S1 and S2) and two patients suffering from tongue cancer (P1 and P2) were obtained with a Philips 3T scanner system (respective repetition time \ echo time: 426\10.74ms, 3.24\2.3ms, 2000\29.27ms (with injection), 400\10ms). The image volume consisted of 32 sagittal slices with a 256×256 scan matrix and voxel dimensions of 1×1×5mm for S1, 40 sagittal slices with a 160×160 scan matrix and voxel dimensions of 1×1×4mm for S2, 160 axial slices with a 224×224 scan matrix and voxel dimensions of 1×1×1mm for P1, and 29 sagittal slices with a 512×512 scan matrix and voxel dimensions of 0.5×0.5×3mm for P2. All subjects gave informed consent and the study had received approval from ethical committee of Grenoble University Hospital
An atlas FE tongue mesh, which was previously elaborated in our group (Buchaillard et al. [2009]), has been employed to generate subject-specific tongue FE meshes. The atlas' mesh was designed on the basis of 3D MR images of the vocal tract of a male subject, collected and segmented in the context of another study aiming at investigating the organization of articulatory configurations in the vocal tract during speech production (Badin et al. [2000]). After building a surface mesh from the segmented images, the hex-dominant FE tongue mesh was automatically generated using a method that optimizes the process in terms of elements quantity and quality (Gérard et al. [2003]; Lobos et al. [2013, 2010]; Rohan et al. [2014]). To assess the coarseness of the mesh, a mesh sensitivity analysis was performed based on the influence of the mesh density on the biomechanical response of the tongue to the posterior genioglossus muscle activation (computed as the global displacement). The atlas' mesh is made of 2180 nodes forming 3172 elements: 796 tetrahedrals, 766 pyramids, 432 wedges, and 1178 hexahedra. Fig. 3.11 shows the atlas' MR images (25 sagittal slices with a 256×256 scan matrix and voxel dimensions of 1×1×4mm) superimposed to the tongue FE mesh.

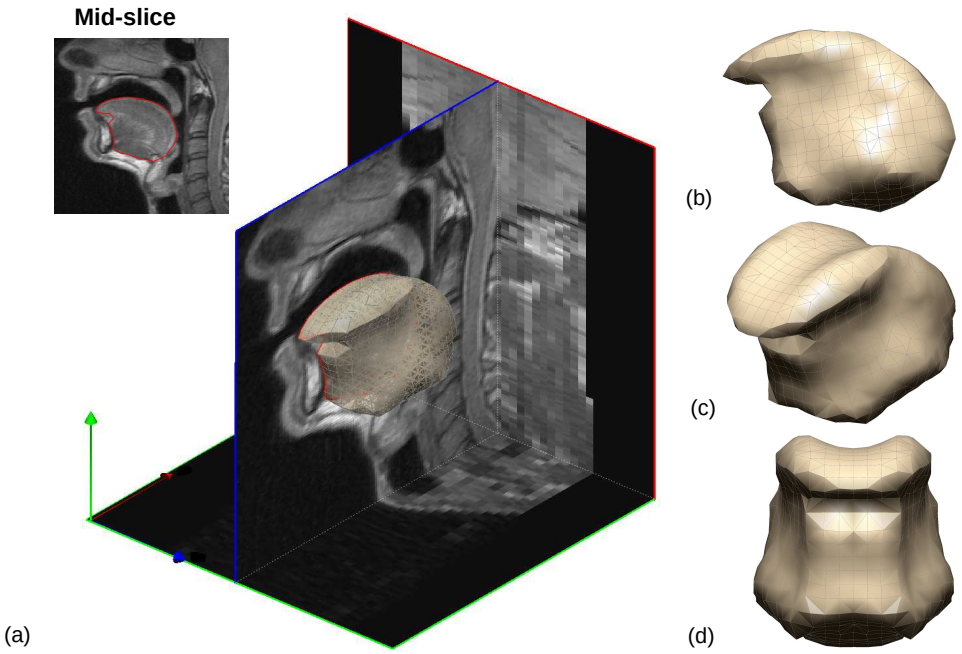

Figure 3.11: 3D tongue atlas' FE mesh: (a) Atlas' MR data superimposed with the 3D atlas' FE tongue mesh, (b) Side view, (c) isometric view and (d) front view respectively of the 3D FE tongue mesh.

3.7.2.2 Simulation Results

The subject-specific tongue FE meshes are shown in Fig. 3.12. The data set includes two healthy subjects and two patients suffering from tongue cancer. The regularity and quality of generated meshes are assessed using the **JR** and **Q** (for tetrahedrals). The results are presented in Table 3.1. None of the meshes contains any irregular element ($\mathbf{JR} < 0$ or $\mathbf{Q} = 0$). To have a more detailed assessment of mesh quality, the elements are classified into six categories. None of the meshes includes any element with a **JR** or **Q** smaller than the threshold 0.03 considered to characterize unacceptable poor quality. Our method is efficient to generate subject-specific FE meshes while preserving the regularity and quality of the elements.

Fig. 3.13 focuses on the results obtained for subject S1. The external contours of the FE mesh are superimposed with sagittal, axial and coronal slices extracted from the MR exam. The enlarged tongue regions for some slices are provided in Fig. 3.13 (d-g). In addition, elements-size-distribution for

the atlas FE tongue mesh and their nodal displacements, when our method is applied to S2 depending on whether the constraints are used or not, are shown in Fig. 3.14. The generated mesh using the pure non-rigid transformations contains 58 irregular elements. Volumes of all elements are computed and plotted in Fig. 3.14(a), according to their element-order within the original mesh file. Fig. 3.14(b) displays the difference (in mm) between the maximal and the minimal nodal displacements for all element. This gives an interesting information since large differences are likely to be associated with strong geometrical distortions of the elements. Fig. 3.13 focuses on the results obtained for subject S1. The external contours of the FE mesh are superimposed with sagittal, axial and coronal slices extracted from the MR exam. The enlarged tongue regions for some slices are provided in Fig. 3.13 (d-g). In addition, elements-size-distribution for the atlas FE tongue mesh and their nodal displacements, when our method is applied to S2 depending on whether the constraints (i.e., the regularization term) are used or not, are shown in Fig. 3.14. The generated mesh using the pure (i.e. without the regularization term) non-rigid transformations contains 58 irregular elements. Volumes of all elements are computed and plotted in Fig. 3.14(a), according to their element-order within the original mesh file. Fig. 3.14(b) displays the difference (in mm) between the maximal and the minimal nodal displacements for all elements. This gives an interesting information since large differences are likely to be associated with strong geometrical distortions of the element.

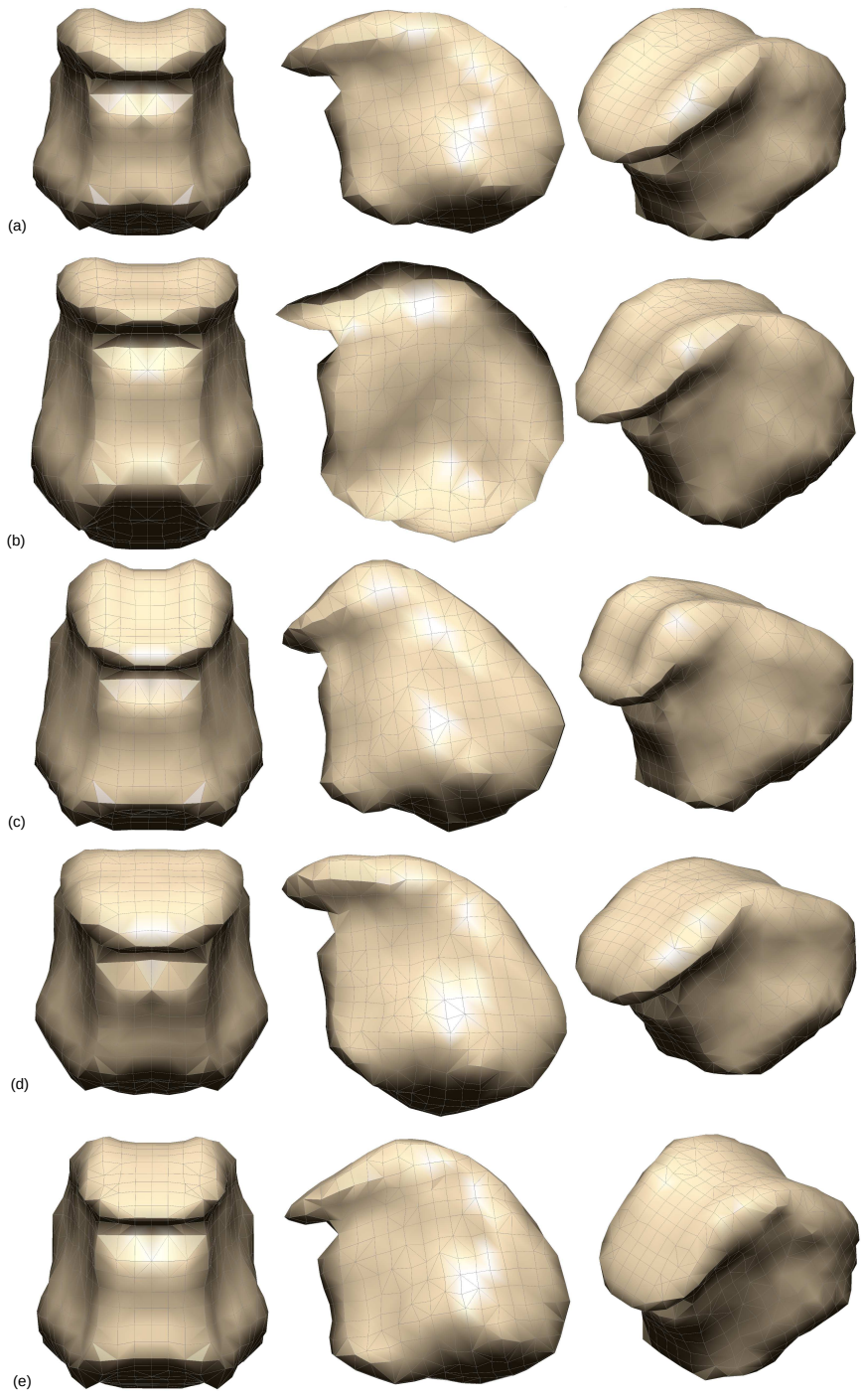

Figure 3.12: Result of atlas' FE mesh morphing using our method: (a) Atlas' FE tongue mesh (b) Subject-specific FE tongue mesh (subject S1), (c) subject-specific FE tongue mesh (subject S2), (d) Patient-specific FE tongue mesh (patient P1), (e) Patient-specific FE tongue mesh (patient P2).

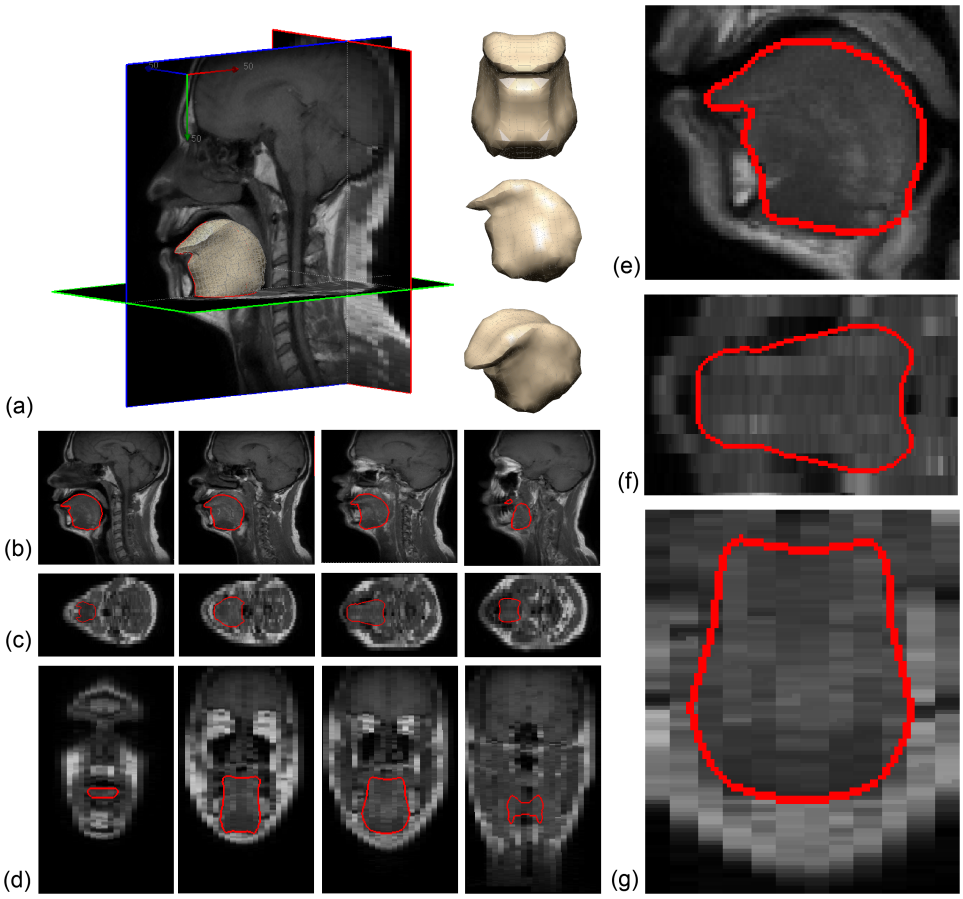

Figure 3.13: Mesh derived tongue contours superimposed on the MR image: (a) 3D subject-specific FE tongue mesh (Normal #1), (b) Sagittal views (mid-sagittal to the lateral side), (c) Axial views (inferior to superior), (d) Coronal views (anterior to posterior), (e) enlargement of the tongue region in a sagittal slice, (f) enlargement of the tongue region in the coronal slice, (g) enlargement of the tongue region in an axial slice.

Meshes	# of irregular elements	Mesh quality (%)					
		< 0.03	0.03-0.2	0.2-0.4	0.4-0.6	0.6-0.8	0.8-1
Atlas	0	0	24.28	2.08	13.30	15.32	45.32
S1	0	0	24.28	3.40	14.50	17.97	39.85
S2	0	0	24.28	3.15	14.00	15.26	43.31
P1	0	0	24.28	2.40	16.20	13.30	43.82
P2	0	0	24.28	5.80	12.86	18.63	38.43

Table 3.1: Mesh quality distribution for the atlas' and subject's FE tongue meshes generated by our method.

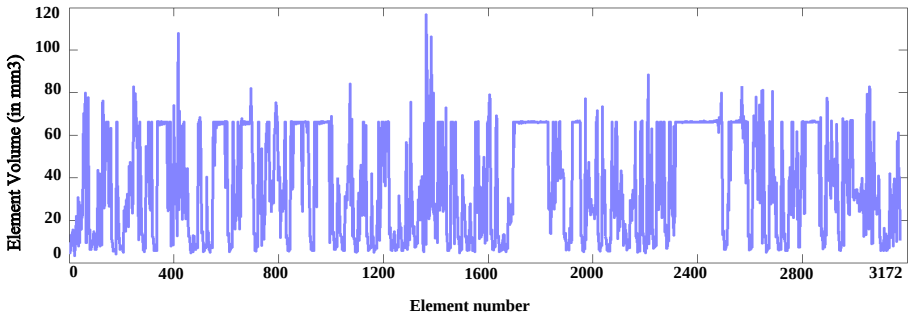

(a) Elements-volumes-distribution for the atlas FE tongue mesh (in mm).

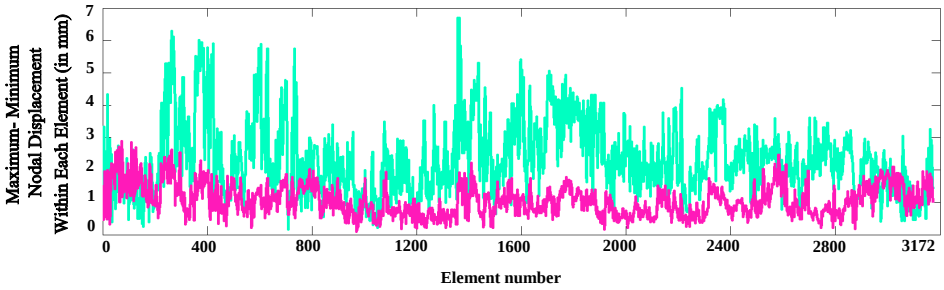

(b) Maximum-Minimum nodal displacement (in mm) within each element.

Figure 3.14: Representation of elements size in the atlas FE tongue mesh, and their displacements with and without constraints: (a) Elements-volumes-distribution for the atlas FE tongue mesh (in mm^3), (b) Maximum-Minimum nodal displacement (in mm) within each element for subject S2 in the mesh generated with the constraints (purple) and in the mesh generated without constraints (green), which contains 58 irregular elements ($\mathbf{JR} < 0$ or $\mathbf{Q} = 0$).

3.7.3 Qualitative evaluation with a patient-specific tongue model

For patient P2, the activation of the posterior genio-glossus (GGp) muscle (one of the most important muscles of the tongue) is simulated before and after surgery. This muscle compresses the tongue in its lower part and its activation propels the tongue frontwards and upwards in its front part, as a consequence of the quasi-incompressibility of the tissues. Its role in speech production is crucial since it is strongly involved in the production of the phonemes /i/ and /s/, which exist in all the world languages. Muscle activation is modeled using the FE formulation of the Hill muscle model proposed by Blemker et al. [2005]; Nazari et al. [2013]. This model was implemented

using the USERMAT functionality of ANSYS. For the passive response, we used a simplified 5-parameter Mooney-Rivlin hyperelastic model with constitutive parameters (C10 = 1037 Pa, C20 = 486 Pa and bulk modulus K = 2.107 Pa) derived from previous work (Buchaillard et al. [2009]). As concerns boundary, the nodes located in the front (which should be in contact with the mandible) and at the bottom of the tongue are fixed (i.e. all 6 degrees of freedom are fixed u1=u2=u3=r1=r2=r3=0). The assignment of the muscle fiber direction in each element in the tongue mesh is performed automatically based on the fibers direction extracted for the atlas' mesh in a previous work (Gérard et al. [2003]). Tongue surgery consisted of a hemi-glossectomy during which half the upper tongue, mainly made of muscle tissues, has been removed and reconstructed with a flap having passive mechanical properties. It is accounted for in the tongue model by modifying the biomechanical properties of the excised tongue tissues: the active material properties of the GGp elements that are removed and reconstructed are replaced with passive material properties.

Fig. 3.15 plots the response of the tongue model to the activation of the GGp before and after the hemi-glossectomy. Both the distribution of the Von mises equivalent strain in the GGp muscle and the displacement of the tongue are provided.

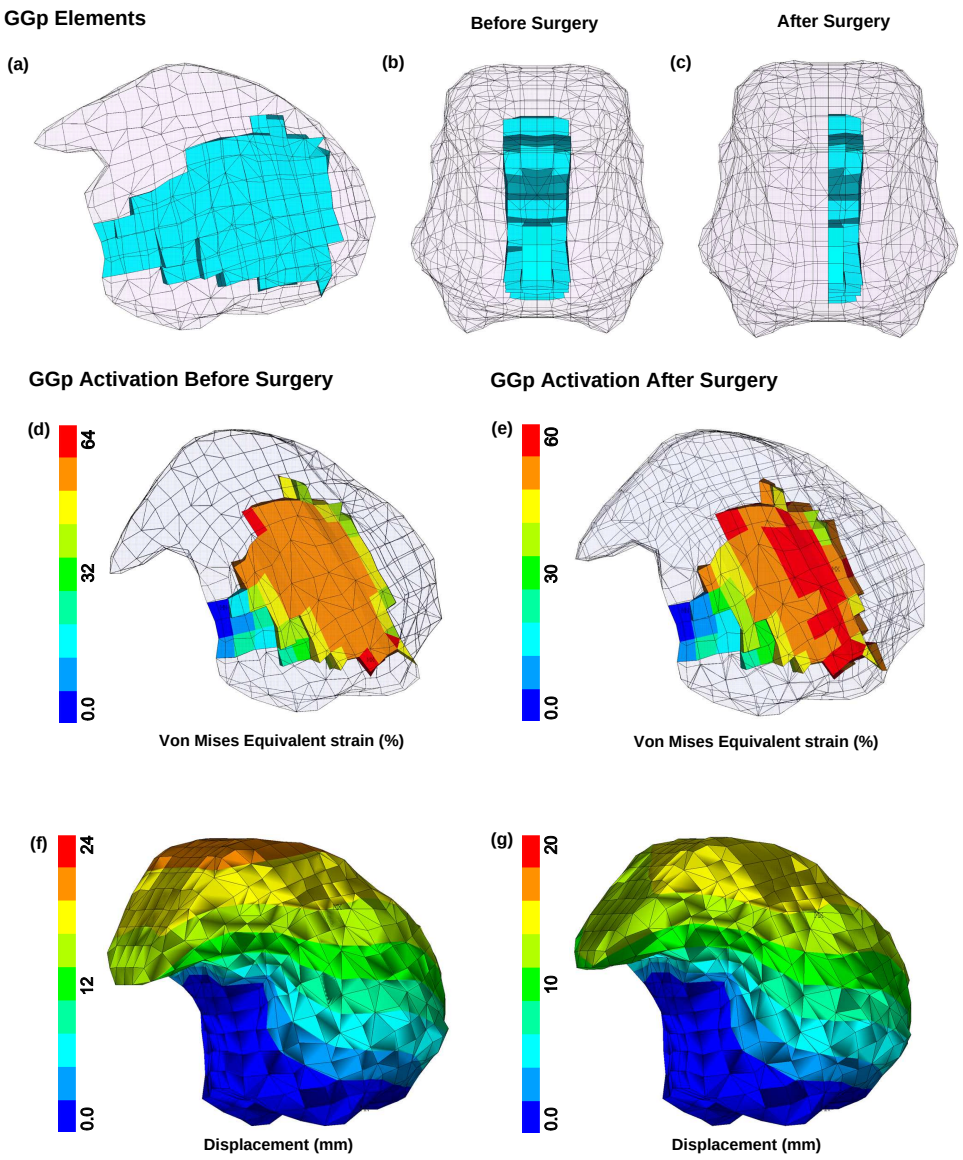

(a)

Figure 3.15: Biomechanical response of the tongue model to the activation of the GGp before and after surgery: (a) Sagittal view of the tongue showing the implementation of the GGp, (b) Front view of the tongue before surgery , (c) Front view of the tongue after surgery; the right part of the muscle has been removed and replaced by passive tissues, (d) Distribution of the Von Mises equivalent strain in the GGp after its activation in pre-surgery condition, (e) Distribution of the Von Mises equivalent strain in the GGP after its activation in post-surgery condition, (f) Displacement map in the tongue after GGP activation in pre-surgery condition, (g) Displacement map in the tongue after GGP activation in post-surgery condition.

3.8 Discussion

In this paper an original method for automatic subject-specific FE mesh generation is proposed and evaluated. Contrary to the previous efforts in the literature, our method does not require any formal extraction of prior-knowledge on the shape of the target organ, no meshing algorithm. We propose to use an image-based registration method to deform an atlas FE mesh and to automatically generate subject-specific meshes.

Our method was first evaluated on a publicly available set of images of the ribcage by comparing manual segmentations of the lungs for various subjects with the subject-specific Lungs masks obtained with our method. Two steps were used, the first one with a parameterization adapted to the capture of global geometrical properties and the second one with a parametrization adapted to the capture of finer details. The match between results provided by both methods is very good in average as shown by the Dice, the overlap fraction and the mean average distance. However, the Hausdorff distance shows that strong differences might exist at some places. A careful analysis of our results shows that these strong differences occur in sharp regions that exist only in the atlas' or in the subject's images. This is a well-known problem in registration methods, as shown for example in Zhang and Reinhardt [2000]; Li et al. [2002]; Garcia et al. [2010]; Mansoor et al. [2015]. Applying a third registration step with less strong constraints might be useful. Another idea would be to use a third registration step that does not include any mesh quality preservation constraints. These possible solutions will be investigated in a future work, in particular to check whether the quality of the elements in the deformed meshed is still preserved. Also, multi-atlas approaches can partly overcome some of these errors by selection of the most similar atlas among a large database (Acosta et al. [2011]).

Fig. 3.12 illustrates well the capacity of the method to generate various kinds of speaker-specific tongue anatomy at rest. From a more quantitative point of view, the quality assessments reveal that the regularity and quality of the meshes are preserved. Contrary to Mesh-Morphing methods that sometimes need to post-process the mesh because of irregular elements (Bucki et al. [2011]), all generated meshes are regular and can be used for FE analysis. Moreover, the quality of the mesh is almost maintained. Indeed, the percentage of elements within the quality range of $0.8 - 1$ is slightly de-

creased by less than 7% (table 3.1). This small reduction in the number of high quality elements results in small increment in the lower quality ranges (maximally 3.31%, 2.9%, and 3.72% for the ranges of $0.6 - 8$, $0.4 - 0.6$, and $0.2 - 0.4$ respectively).
Fig. 3.13 plots the contours of one generated mesh superimposed with the corresponding MR slices. The various slices displayed in the figure illustrate the efficiency of the method since the contours fit well with the observed boundaries of tongue tissues. Moreover, for some slices for which it is quite difficult to see tongue contours (the lateral sagittal views close to cheeks tissues or tongue basement), registration method is able to suggest tongue contours thus maintaining a coherent structure for the whole 3D mesh.
In Fig. 3.14 results of our method and the pure non-rigid registration are shown for S2. The maximal difference between the maximum and the minimum displacements within each element is decreased from 6.69 mm to 2.87 mm. This means that the probability of strong element distortion is significantly reduced and that the employed constraints have managed to control the movement of nodes within the elements.

Focusing on patient P2, we have proposed to simulate some functional consequences of a tongue surgery. Whereas the relevance of such use of a biomechanical model for computer assisted surgery has already been provided (Buchaillard et al. [2007a]), the objective here was to propose an illustration of a tentative fully automatic procedure compatible with the clinical constraints. Therefore, starting from an MRI exam of a patient, we were able to automatically generate an FE model of that patient. All the information included in the tongue atlas model was automatically transferred in the model of the patient. It was thus straightforward to simulate the activation of the posterior genioglossus muscle. The corresponding results provided by Fig. 3.15 confirm a clinical observation, namely the fact that, after a hemi-glossectomy, the tongue response is no more symmetric. The results also predict that the patient might have difficulties to move its tongue in the front and upper part of the oral cavity since the simulated displacements after surgery are significantly lower than the ones simulated before hemiglossectomy.
The atlas-based subject-specific FE model generation method proposed in this paper seems to provide efficient results that were qualitatively and quan-

titatively evaluated on four subjects. Tongue models were used here since it is a clinical case for which the manual delineation of tongue contours is a particularly complex and sometimes impossible task (M. Harandi et al. [2015]). The counterpart of this choice is that it is impossible to design a gold standard case to which we could compare the results proposed by our method. Indeed, since boundaries are difficult to identify for some regions of the tongue (e.g. at the bottom and laterally), we were not able to ask an expert to segment a whole tongue and to guaranty that this segmentation would be considered as the gold standard. In any case it seems clear that when the disease is advanced and the size of tumors are high, the general shape of the target organ is divided into sub-shapes. In other words, the tumors can be considered as new organs inside the target organ that disturb the registration process. To sum up, when the original shape is still remained or there is no significant tumor size progression, the proposed method, that employs a multi-level FFDs, is able to capture the geometry of the organs well.

Our method still needs to define the weighting factor lambda that controls the influence of the regularization term. This highly depends on the image modality as well as the type of organ. Our method needs therefore definitively to be more extensively evaluated on a larger set of tongue MR images.

"You are not a drop in the ocean. You are the entire ocean in a drop."
- Jalaluddin Rumi

4

DTI and Atlas-Based Automatic Integration of Muscle Fibers in Subject-Specific FE Meshes

Contents

Following the previous chapter on generation of subject-specific FE meshes via 3D registration of MR images, this chapter describes a novel approach for the integration of DTI-based muscle fibers information in subject-specific FE meshes. Performing diffusion-based fiber tractography enables to visualize structural connections in muscles. In addition, such fibers can be used to correlate mechanical functions of muscular structures with the underlying myoarchitecture. However, associating and linking the subject-specific organization of muscular structures with the elements of FE meshes is extremely challenging due to a variety of reasons. Most importantly, classification and determination of muscular sub-structures need manual detection of thousands or millions of fibers for each subject, which is highly influenced by the limitations associated with the DTI image acqemployuisition process (e.g., time, number of diffusion gradient directions, geometrical distortions, etc.) and fiber tractography techniques. This may lead to poor estimations of the true fibers' orientations. In order to overcome theses challenges in an atlas-based registration framework, we propose a method that combines information provided by scalar images and DTI-based muscle fibers. The method (1) extracts a 3D displacement field that can be used to deform an atlas mesh which is then aligned with the vector coordinates of the obtained fiber tracks[a] or (2) provides a mapping from the elements of the atlas mesh to the subject's ones. In order to demonstrate the efficiency of our approach, an atlas tongue mesh and its fibers are deformed in order to generate subject-specific mesh and to capture the underlying myoarchitecture.

[a] fiber tracks or fiber tracts

4.1 Introduction

Various atlas-based Finite Element (FE) model generation strategies were reviewed in chapter 2. Accordingly, each possesses certain inherent advantages and disadvantages. However, an important drawback of such methods is that they either require user intervention (e.g. selection of landmarks) or another not automated process (e.g. segmentation) to provide a priori knowledge about the target organ. To overcome these difficulties, an atlas-based method was developed in chapter 3 in order to automate the generation of subject-specific FE meshes. The method is based (1) on an existing atlas FE mesh (manually designed from medical images) and (2) on the registration of that atlas to make it fit each patient data. This mesh-morphing process is based on image voxels information with the determination of an optimal 3D transform that matches the volume image of the atlas onto the volume image of the patient. Such intensity-based 3D image registration therefore avoids the complex segmentation process of patient data which was still difficult to be carried out automatically. Although the proposed method seems successful in generating FE meshes of muscular and non-muscular structures, no subject-specific information about fiber bundles was included in the generated meshes. Biomechanical patient-specific tongue models were produced using anatomical images and it was shown that such models can be used to simulate the consequences of surgical gestures such as hemiglossectomies or resections of the mouth floor. However, if one wants to estimate the patient-specific organization of tongue muscular structures, which is very important for predicting the post-operative tissues deformations due to muscles activations, additional information (such as fiber directions) has to be included in the models. This chapter aims at contributing to this issue, by applying Diffusion Tensor Imaging (DTI) techniques and developing registration methods to estimate subject-specific bundles of muscles fibers, and finally integrating them in the generated subject-specific FE meshes.

Diffusion-weighted magnetic resonance imaging (DT-MRI) (Basser et al. [1994a]) is a dominant non-invasive imaging technique that provides the integrity and connectivity of the fibers by measuring water diffusion, its directionality and the diffusion anisotropy (Basser [1995a]). In DTI, a specific number of non-collinear gradient directions (diffusion weighting) are

applied in order to produce images of the MR signal attenuation (due to anisotropic diffusion). The reconstructed images are used to calculate a three-dimensional diffusion tensor for each voxel and to describe the directional dependence of water diffusion. In conventional DTI, this diffusion process is assumed to be Gaussian, and is estimated by a rank-2 tensor for each voxel (Basser et al. [1994a]). Fig. 4.1 provides a schematic example for different diffusivity of the water molecules that may happen within each voxel.

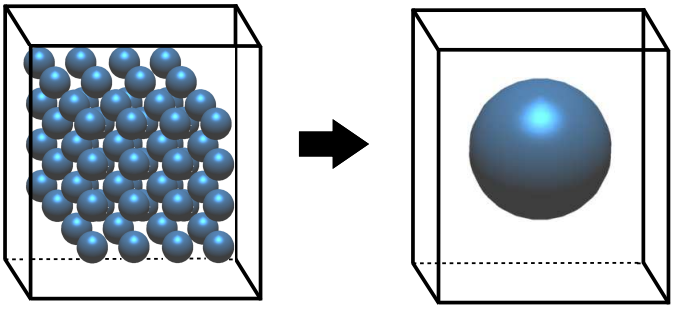

(a) Isotropic diffusion

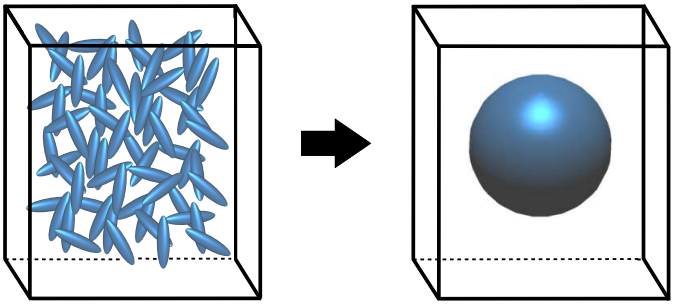

(b) Random diffusion

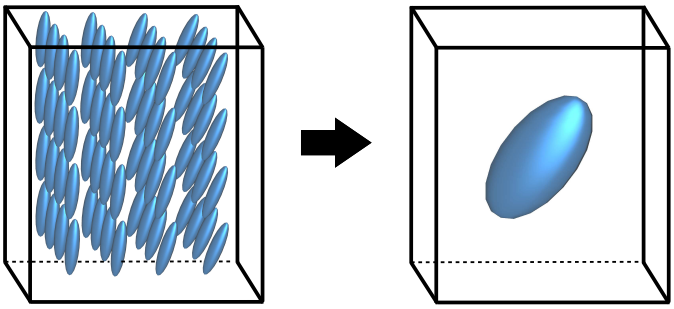

(c) Bending fiber structure

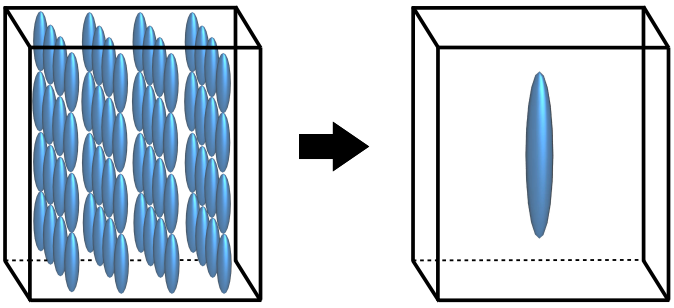

(d) Coherent fiber structure

Figure 4.1: Schematic overviews of tensors are shown for voxels with different diffusivity in left column, and also their average-tensors in right column: (a) water molecules are moving in an isotropic way, (b) water molecules are moving randomly in different directions, (c) water molecules diffuse in the direction of bending fiber structure (d) all molecules are moving in a specific directions.

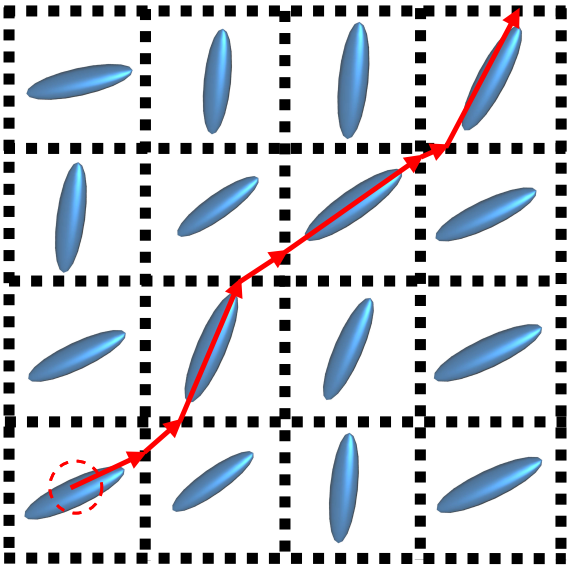

Figure 4.2: Fiber tractography: a seed point is selected in the voxel right down in order to track fiber according to the extension of diffusion tensors.

Fiber tracks are then reconstructed by combining the diffusion tensors of multiple voxels which correlate with the principle direction of water molecules in tissue structures at a microscopic scale. This process is called ***fiber tractography*** or ***fiber tracking*** and can be done by tracing the paths through the tensor fields (Fig. 4.2). Also, fiber tracks can be analyzed by utilizing diffusion indicies (e.g., fractional anisotropy and mean diffusion, see section 4.2.2.1) derived from the obtained tensors.

Although DTI has opened entirely new horizons to analyze and visualize the detailed anatomical structure of muscular tissues, it has inherent limitations such as inability to represent voxels containing multiple fibers with different orientations, splitting and crossing fiber bundles. Of course, these issues can be solved by reducing the voxel size (in which the chance of containing a single fiber per voxel is increased) and subsequently the calculated tensors are more reliable. However, it should be kept in mind that there is a converse relationship between the spatial resolution and the acquisition time. Reducing the voxel size results in decrease of signal-to-noise ratio (SNR) and makes the sequence largely sensitive to bulk motion artifacts. As an alternative, it was further found that increasing the number of gradient

directions improves the tensor fit quality and brings the possibility of using high order tensors (high angular resolution diffusion imaging (HARDI) (Tuch et al. [2002]) and diffusion spectrum imaging (DSI) (Wedeen et al. [2005])). Anyhow, this strategy also increases the acquisition time. On the other side, there are some muscular structures that need the acquisition time to be shortened as much as possible. For instance, in the case of tongue-DTI, involuntary swallowings change the shape and position of the tongue. In such a case, geometrical distortions will negatively and considerably affect the performance of the ***fiber tractography*** process. In other words, tracking algorithms can in that case lead to poor estimation of the true fibers' orientation and their uncertainty. In this regard, many studies have been dedicated to the acceleration of the imaging process (Bilgic et al. [2012]; Gramfort et al. [2012]; Merlet et al. [2012]), and to the fitting of multi-tensor models and the improvement of the ***fiber tractography*** techniques (Peled et al. [2006]; Behrens et al. [2007]; Ramirez-Manzanares et al. [2007]; Landman et al. [2012]; Zhou et al. [2014]; Ye et al. [2014, 2015]). However, even considering all these improvements and efforts, a trade-off between spatial resolution, acquisition time, the level of noise caused by motions, and SNR is required by clinical applications in DTI imaging.

In this chapter, an ***atlas-based registration*** method is proposed with the aim to overcome the mentioned shortcomings of ***limited or distorted***-DTI imaging and to generate subject-specific meshes. The main idea behind the proposed approach is to employ registration techniques, both at the levels of anatomical images and fibers, in order to deform an atlas FE mesh. During the last years, DT-MR images registration has received great interest from both the academic researchers and clinicians because of its unique role in studying metabolism of different neural and muscular tissues (such as brain, tongue, heart and etc.) and assessing properties (e.g., age-related loss of fiber integrity) . By spatially normalizing the DT-MR images of different subjects, diffusion-derived-parameters (e.g., fractional anisotropy) are mapped accurately and subsequently clinicians are able to assess them and study their variations among normal and pathological populations. However, registration of DT-MR images is more complicated than for scalar images, not only because of their multi-dimensionality, but also because the tensor orientations must remain consistent with the anatomy after image

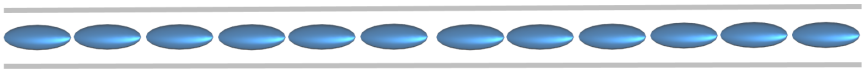

(a) Original fiber

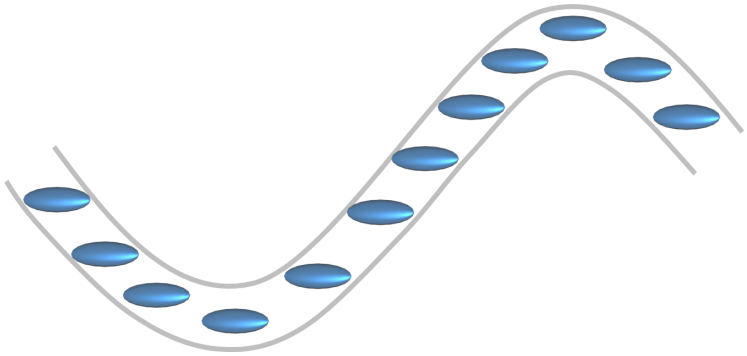

(b) Wrong-deformed fiber

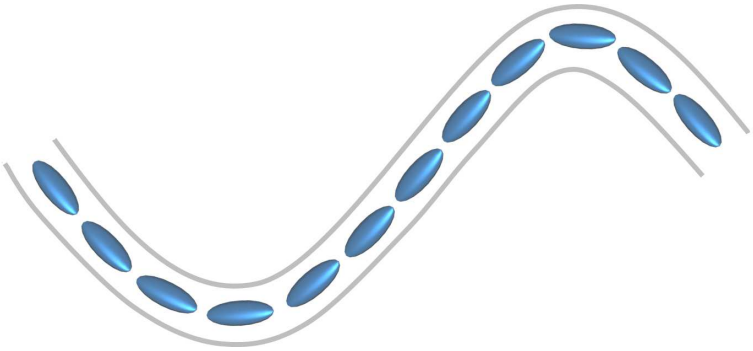

(c) Correct-deformed fiber

Figure 4.3: Reorientation of fiber tensors after applying a typical deformation.

transformations (Alexander et al. [2001]) (Fig. 4.3).

During the last years, a variety of methods have been proposed to address the problem of DT-MR images registration. These methods can generally be divided into two main categories. The first category relies on scalar-mapped based techniques that do not consider the specificity of DT images and process scalar images derived from DT images like non-diffusion image registration strategies (Jones et al. [2002]; Guimond et al. [2002]; Xu et al. [2003]; Gee and Alexander [2006]; Muñoz-Moreno et al. [2009]; Wang et al. [2011]; Irfanoglu et al. [2016]). It should be mentioned that some studies belonging to this category have combined information from various

non-diffusion images, diffusion indices and tensor components[1] to produce a multi-channel registration framework (Guimond et al. [2002]; Park et al. [2003]; Rohde et al. [2003, 2004b]; Goh and Vidal [2006]; Yang et al. [2008]; Yap et al. [2009a,b, 2010]; Wang et al. [2013b, 2014]). The other category includes methods based on full information provided by the tensors. This means that some additional constraints based on tensors' characteristics (i.e., eigenvalues and eigenvectors) are considered to guide the registration process. It is important however to note that these techniques are classified into three major subgroups depending upon the ***tensor reorientation*** (Irfanoglu et al. [2016]): methods that do not reorient the tensors (Alexander et al. [1999]; Alexander and Gee [2000]; Ruiz-Alzola et al. [2002]; Rohde et al. [2004a]), methods that ignore tensors information but then reorient them after the estimation of the final transformation (Hecke et al. [2007]; Irfanoglu et al. [2008, 2009]), and methods that consider tensors reorientation information during the optimization of the registration problem (Zhang et al. [2006]; Cao et al. [2006]).

Although the above-mentioned studies perform well for their specific purposes, there are some points that should be noted:

- The performance of image registration techniques is limited by the quality of the input images. In other words, these techniques need non-distorted diffusion images as a prerequisite. For instance, we know that echo planar imaging (EPI)-based DTI acquisitions are being used widely; however they suffer from geometric distortions that are caused by local magnetic field inhomogeneities and eddy current effects (Ardekani and Sinha [2005]). Many investigations have been dedicated to the correction of distortions, but they fail in the presence of high geometric distortions that may appear in some regions of the images (Fig. 4.4).

- It is shown that methods considering tensors reorientation, whether during the optimization process or after the estimation of the final transformation, outperform the methods that do not reorient the tensors (Park et al. [2003]), and can preserve anatomically consistent

[1]The full explanation of the terms *diffusion indices* (e.g., fractional anisotropy and mean diffusion), *tensor components* and *tensor eigenvalues* are provided in section 4.2.2.

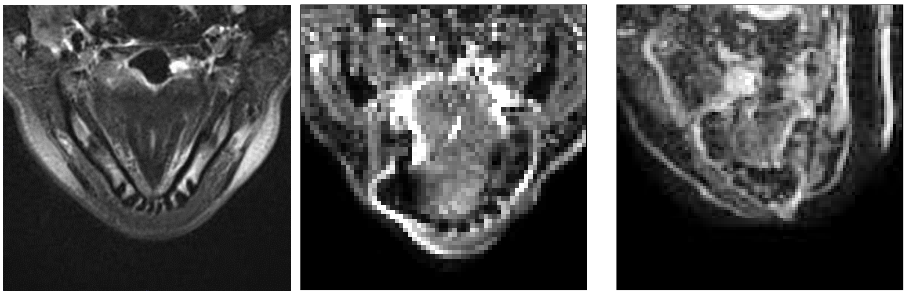

(a) (b) (c)

Figure 4.4: Normal and distorded geometric images of the tongue: (a) axial slice of a tongue volume, (b) and (c) axial slices of geometric distorted tongue volumes.

structures (Adluru et al. [2013]).

- Tensor image based registration techniques rely on estimations of DTI directions, which are intrinsically ***error-prone***. This influences the robustness and the accuracy of the registration.

Considering these limitations, there has been growing interest in the registration of fiber bundles (Leemans et al. [2006]; Ziyan et al. [2007]; Mayer and Greenspan [2007]; Shadmi et al. [2010]; Zvitia et al. [2010]). Leemans et al. [2006] proposed a method for intrasubject rigid registration of white matter fiber tracts, in which each fiber is described by curvature and torsion features. Similarity measures between fibers are then evaluated at different scale levels based on the mean squared difference. Finally, the global rigid transformation is obtained using the most similar matched fibers. In another study, Mayer and Greenspan [2007], proposed to represent fibers using 3D points to be registered. A 12-parameters affine transformation (i.e. 3 parameters for the 3D translation and 9 parameters for the Matrix that combines rotation, scaling and shearing) is estimated using an efficient iterative "*closest feature point*" algorithm (called ICF) that overcomes the congestion of high dimensional search using a fast approximate nearest-neighbor (NN) computation. Shadmi et al. [2010] proposed a fiber-based piecewise-smooth affine registration, in which the fibers are first projected into a D-dimensional feature space based on the sequence of their 3D coordinates. In this space, each fiber is represented by a D-dimensional point and fibers alignment is considered as a problem of probability density estimation

in the D-dimensional space. The optimized transformation parameters are obtained by maximizing the likelihood of correspondence between the two fiber sets to be registered. Zvitia et al. [2010] also projected fibers into a high dimensional feature space. Each fiber set is then represented by a compact set of representative fiber-modes (FM) which are extracted by applying adaptive mean-shift clustering (ACM). A Gaussian mixture model (GMM) is later fitted to each FM and the registration problem between two fiber sets is considered as an optimal alignment problem of two GMMs. Affine transformation parameters are then obtained by maximizing the correlation ratio between the GMMs. Similarly, Wassermann et al. [2011] used Gaussian Processes (GPs) for representation of tract density maps. This representation associates each tract and each bundle of tracts with a GP. Accordingly, each point in space is mapped to the density of tracts crossing that point, then generating a tract density map (TDM). Then, a diffeomorphic registration is performed based on the Log-Euclidean poly-affine framework (Arsigny et al. [2009]), by evaluating the similarity between two bundles in terms of the mass of common density areas. Ziyan et al. [2007] explored the use of fiber bundles for inter-subject nonlinear registration of brain diffusion MR images. Subsequent to a global alignment of the subject's fractional anisotropy (FA) image and atlas' one, subject's major bundles are detected and the correspondence between the fiber-bundles is obtained across the brains. Then, the set of bundle-based correspondences is used to calculate a smooth and invertible poly-affine nonlinear deformation between atlas and subject. It can be seen from the above analysis that the fiber-based registration methods gain their strength from the fact that they avoid error-prone estimation of DTI direction; however, they are mostly limited to linear registration models and can be time-consuming (e.g., Mayer and Greenspan [2007]).

Here, in this chapter, a novel approach for the integration of DTI-based muscle fibers in subject-specific FE meshes is proposed. In order to benefit from the advantages of both ***image-based*** and ***fiber-based*** registration techniques, the method combines information provided by scalar images and by the extracted fiber bundles. This help us to avoid reorientation of tensors. It increases the robustness to interrupted and deviating fiber artifacts as well as outliers, that may appear because of the limitations associated

with the DTI image acquisition (e.g., time, number of diffusion gradient directions, geometrical distortions, and etc.) that leads to poor estimation of the true fibers' orientation and their uncertainty. We specifically address the challenge of identifying tongue muscles and embedding them within a subject-specific tongue mesh. At the beginning of the whole process we have scalar images and DT images of the atlas and of the subject, and we have fiber-bundles labeled according to muscle anatomy for the atlas, resulting from fiber tractography on the Atlas' DT images. Then, our methodology consists of three phases, as follows:

- **Phase I**: Registration of atlas and target's images (anatomical or non-diffusion (B0) images) using the method proposed in chapter 3. Within this phase, the general shape of the target's organ is captured by deforming the atlas's anatomical shape. In order to generate the mask of target's organ, the obtained deformation fields ($\mathbf{T}_{Anatomical}$) are used to deform the atlas' mask.

- **Phase II**: The goal of Phase II is to refine the anatomical transformation ($\mathbf{T}_{Anatomical}$) resulting from phase I, by using fiber-based information, and then identification of subject's fiber-bundles according to the atlas' fiber-bundles. Subject's fiber tracks are extracted by utilizing fiber tractography algorithms on estimated diffusion tensors. Atlas' fibers are then deformed according to $\mathbf{T}_{anatomical}$. Then, track-density information is incorporated into the anatomical subject and the deformed-atlas images. The generated images are locally registered together. So, the refined-anatomical transformation ($\mathbf{T}_{Re-anatomical}$) is produced by the combination of the obtained transformation and $\mathbf{T}_{Anatomical}$. Afterward, with the aim to overcome the complexity of large fiber tracks and more specifically to select non-distorted fiber bundles and decrease the effect of incorrect fibers, subject's fibers are automatically classified into a set of fiber bundles and labeled by evaluating a similarity measure between them and the atomically-deformed-atlas' fiber-bundles. Although the result of this labeling process help us to assign each element of the anatomically generated subject-specific mesh to a specific fiber bundle, a more accurate transformation can be achieved according to the fibers structures (see phase III).

- **Phase III**: The main objective of this phase is to estimate a transformation that can be used for deformation of meshes, in which the elements are organized according to the target's governing fiber structures and not only based on the target's geometry. On this matter, each pair of corresponding fiber-bundles, namely an atlas-deformed-fiber-bundle and its corresponding subject's one, are non-rigidly registered together ($\mathbf{T}_{Bundle}$), via the Coherent Point Drift (CPD) algorithm. To do this, each fiber-bundle is considered as a set of 3D points and the alignment of two point sets is considered as a probability density estimation problem. Finally, the overall transformation is generated based on the two anatomical and bundle-based transformations.

The remainder of this chapter is organized as follows. In the next section, a brief background on diffusion tensor imaging is provided. In section 3, we describe in details the proposed method, including the above-mentioned three phases. Section 4 provides experimental results on a diffusion tensor imaging data set of the tongue in order to demonstrate the effectiveness and the performance of our proposed method for the integration of tongue fibers within subject-specif FE meshes. Finally, the advantages and disadvantages of the proposed method are discussed in section 5.

4.2 Diffusion Tensor Imaging (DTI)

Diffusion Tensor Imaging (DTI) or Diffusion Tensor Magnetic Resonance Imaging (DT-MRI) reconstructs structural connections by relating diffusion-weighted measures across voxels. Therefore, we first go through the basic concepts of diffusion weighted magnetic resonance imaging (DW-MRI) and then describe the DTI process.

4.2.1 Principle of DW-MRI

Diffusion weighted magnetic resonance imaging (DW-MRI) is a non-invasive imaging modality that enables to visualize and quantify the random Brownian motion of water molecules in tissues. Water molecules can not diffuse freely in tissues; however, their movement reveals information about their interactions with lots of obstacles such as fibers, membranes, and macromolecules. This information provides microscopic details about tissue struc-

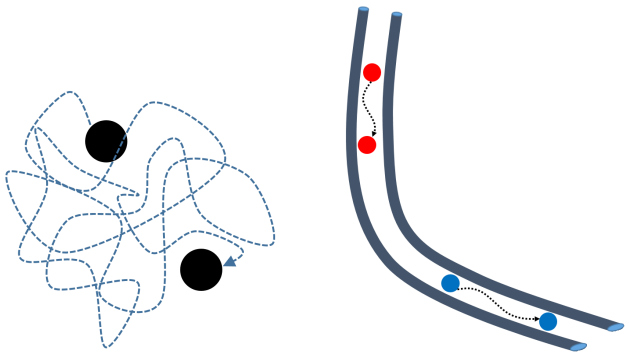

(a) (b)

Figure 4.5: The Brownian motion of water molecules: (a) when there is no fiber structure, (b) when there is fiber structures.

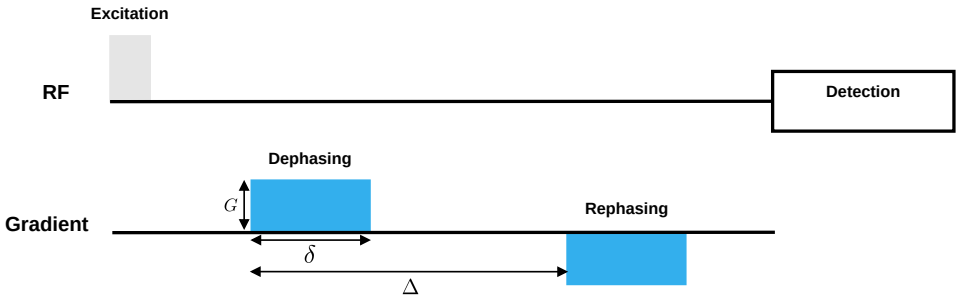

Figure 4.6: Bipolar gradients.

tures. In other words, DW-MRI probes the microscopic structure and organization of biological tissues by measuring the Brownian motion of water molecules (Fig. 4.5). In DW-MRI, an MR pulse is designed in such a way that it is sensitive to the diffusion of water molecules. In this regard, a pair of gradients that are equal in magnitude but opposite in direction are employed. These bipolar gradients, shown in Fig. 4.6, introduce diffusion weighing into the MR signal intensity by dephasing (the fist gradient) and rephasing (the second gradient) water molecules. Therefore, the movement of water molecules between the dephasing and rephasing gradient pulses leads to a loss in the MR signal (Fig. 4.7).

Now, let's turn to the question of how to measure the diffusion constants of water molecules from MR signals. To answer this question, we first need to know what factors influence the signal loss:

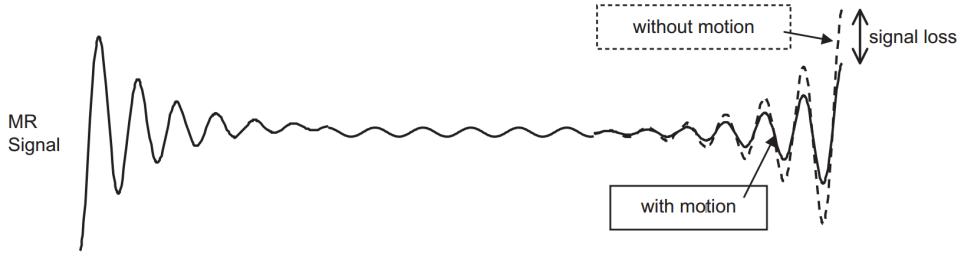

Figure 4.7: Signal loss in DW-MRI which is proportional to the motion of water molecules (Mori and Tournier [2013]).

- Δ: The time interval between the bipolar gradients; the high Δ values give more time to the water molecules to move around, leading to a larger signal loss.

- D: The diffusion constant of the particles that is proportional to the variance of the particle movement. A high diffusion constant leads to a low signal as it allows water molecules to diffuse more over a larger distance within a fixed time Δ. Fig. 4.8 shows an application of bipolar gradients in which the measured MR signal is maximized when there is no diffusion among the water molecules.

- G **and** δ: Magnitude and duration of the gradient pulse determine the amount of initial dephasing (the area of the gradient: $G \times \delta$). More signal loss will occur when a larger initial dephasing is applied.

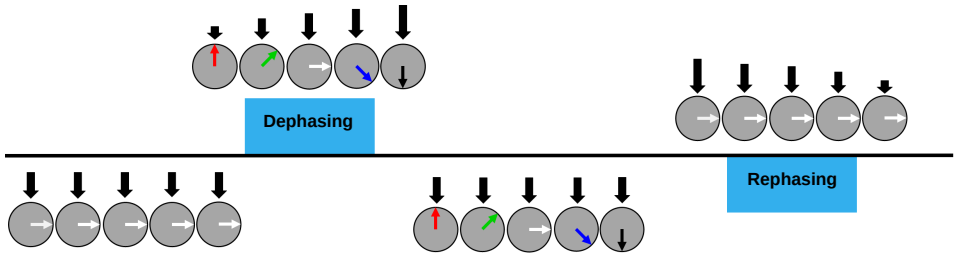

(a) Diffusion weighting while there is no water motion.

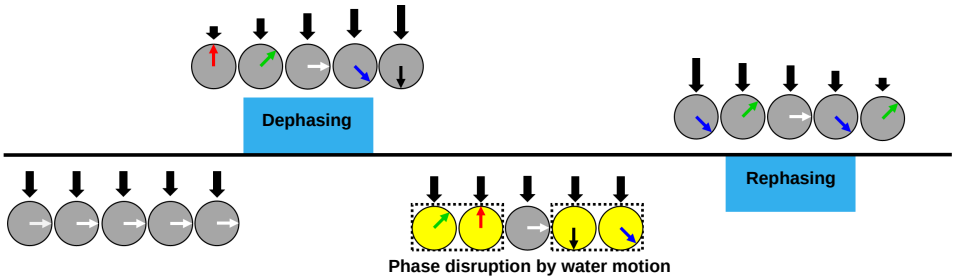

(b) Diffusion weighting when there is water motion.

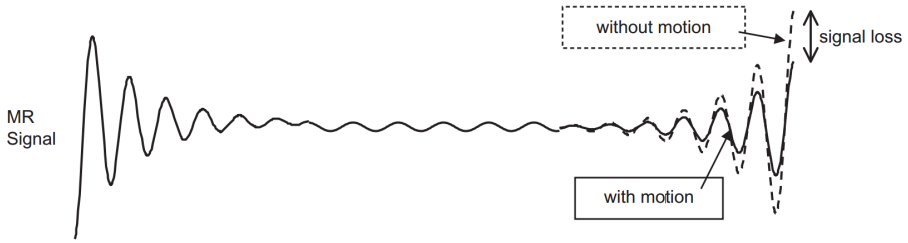

(c) MR signal illustrating signal loss after rephasing.

Figure 4.8: An application of bipolar gradients without and with the existence of diffusion among water molecules. The magnitude of magnetic field is shown by black arrows. Also, the phase of water molecules is shown by colors' gradation. (a) The gradients cause desynchronizing (the fist gradient) and resynchronizing (the second gradient) of water molecules; however, as there is no diffusion among water molecules the measured MR signal is maximized; but in (b), water molecules are randomly moved between the two gradients and it leads to the imperfect rephasing and loss of signal intensity (molecules changing their location are indicated by boxes and yellow color); (c) signal intensity for both cases (a) and (b).

Let S and S_0 denote the signal intensities with and without the existence of the diffusion gradients, respectively. So, the amount of signal loss is related

to the above mentioned parameters as

$$\frac{S}{S_0} = f(\Delta, D, G, \delta), \tag{4.1}$$

Δ, G, and δ are experimental parameters that can be controlled. S and S_0 are experimentally measured MR signals. Thus, the diffusion constant (D) can be calculated from the equation above. As mentioned earlier, the amount of phase difference is introduced by gradient pulses. After setting the parameters G, and δ, the phase difference ($\phi(x)$) can be calculated in the space with respect to an arbitrary reference point ($x = 0$):

$$\phi(x) = e^{i\gamma G\delta x}, \tag{4.2}$$

where x is the distance from the reference point and γ is the gyromagnetic ratio. Also, under the assumption of free diffusion, the population of water molecules that move by x during the diffusion time (t) can be estimated using a Gaussian distribution:

$$P(x,t) = \frac{1}{\sigma\sqrt{2\pi}} e^{-\frac{x^2}{2\sigma^2}}, \tag{4.3}$$

mathematically, σ controls the width of the Gaussian function; and here, it determines how far the water molecules can move on average. The average distance can be replaced by the estimation of Einstein's equation: $\sigma = \sqrt{2Dt}$. Thus, Eq. 4.3 can be rewritten as below

$$P(x,t) = \frac{1}{\sqrt{4\pi Dt}} e^{-\frac{x^2}{4Dt}}, \tag{4.4}$$

Now, the total signal can be computed by summing up the product of population of water molecules and signal phase over x:

$$\text{Signal} = \int_x P(x,t)\phi(x)\mathrm{d}x = \frac{1}{\sqrt{4\pi D\Delta}} \int_x e^{-\frac{x^2}{\sqrt{4D\Delta}}} \quad e^{i\gamma G\delta x} \quad \mathrm{d}x, \tag{4.5}$$

By solving this integration, the signal becomes

$$\text{Signal} = e^{-\gamma^2 G^2 \delta^2 D\Delta}, \tag{4.6}$$

It's clear that when there is no diffusion weighting (G=0), the signal value

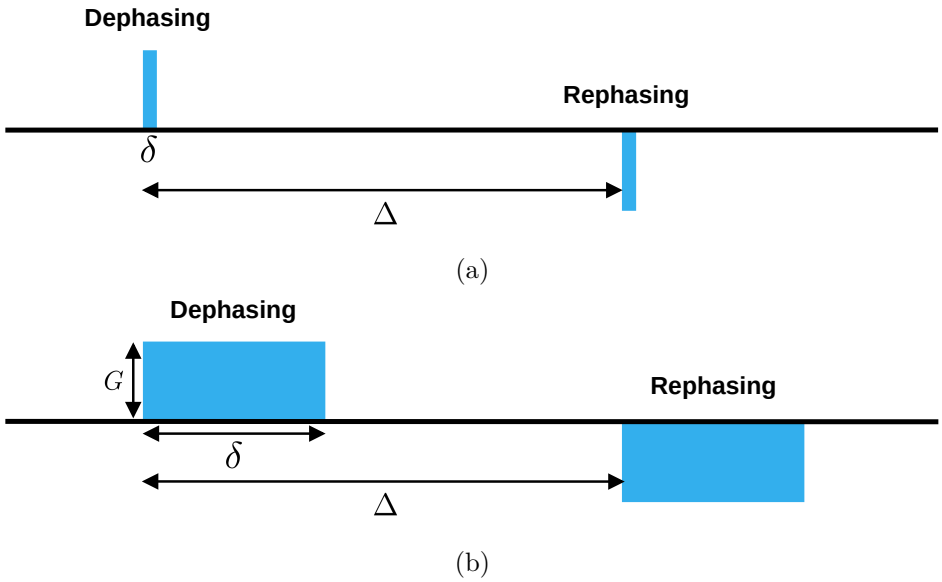

Figure 4.9: Diffusion-weighting sequences: (a) a simplified version ($\delta << \Delta$), in which the gradients are applied instantaneously and diffusion of water molecules can be negligible, and (b) a more realistic case.

is equal to one, which is the maximum value. This in turn means that the signal intensity is normalized. Accordingly, in practical applications that there exist diffusion gradients, Eq. 4.6 can be rewritten as

$$S = S_0 e^{-\gamma^2 G^2 \delta^2 D \Delta}, \tag{4.7}$$

It should be reminded that the above result is achieved under the assumption that the gradient duration is much smaller than the time interval between the bipolar gradients, Δ (Fig. 4.9a). This assumption means that during the application of gradients there is no diffusion among water molecules that can be considered. In fact, in Eq. 4.5, the variable t was substituted by Δ. However, in practical applications, the gradient duration (δ) is long and it is incorrect to neglect the movement of water molecules during the gradient pulses (Fig. 4.9b). Therefore, in such cases, the gradient magnitude (G) and its areas ($G\delta$) are time-dependent variables. Consequently, the introduced phase gradation, defined in Eq. 4.2, will be a function of both time and location:

$$\phi(x,t) = e^{\int i\gamma G(t)tx}, \tag{4.8}$$

Subsequently, the signal equation (Eq. 4.5) is rewritten as

$$\text{Signal} = \int_x P(x,t)\phi(x,t)\mathrm{d}x = \frac{1}{\sqrt{4\pi Dt}} \int_x e^{-\frac{x^2}{\sqrt{4Dt}}} \quad e^{\int i\gamma G(t)tx} \quad \mathrm{d}x, \tag{4.9}$$

and after solving the integral with respect to x and t, it concludes to

$$S = S_0 e^{-\gamma^2 G^2 \delta^2 (\Delta - \frac{\delta}{3})D}, \tag{4.10}$$

For more details about the mathematical procedure leading to these equations, the interested reader is highly suggested to read Mori and Tournier [2013]. As reminded earlier, G, δ, and Δ are the parameters that are already set by us; and S and S_0 are experimentally measured. So, the term $\gamma^2 G^2 \delta^2 (\Delta - \frac{\delta}{3})$ can be abbreviated by a single parameter b (b-factor or b-value), which corresponds to so-called ***Stejskal–Tanner*** equation

$$b = \gamma^2 G^2 \delta^2 (\Delta - \frac{\delta}{3}), \tag{4.11}$$

and Eq. 4.10 can be simplified to

$$S = S_0 e^{-bD}, \tag{4.12}$$

The computed diffusion constant from Eq. 4.10 is called ***apparent*** diffusion constant (ADC), as it varies depending on the direction of applied diffusion gradient or the sample's orientation.

There is no optimal b-value that can be generalized for various applications; and its value should be specified according to the anatomical features, predicted pathology, field strength, and number of signals averaged. There are lots of studies dedicated to the investigation of the optimal b-value for different applications; for example Burdette et al. [2001]; Tang et al. [2007]; Goshima et al. [2008]; Metens et al. [2012]. Fig. 4.10 shows brain images that are acquired at different b-values. As can be seen, white matter regions are generally significantly hypointense compared with gray matter regions when no diffusion gradient is applied (b-value=0). By raising the b-value to 1000,

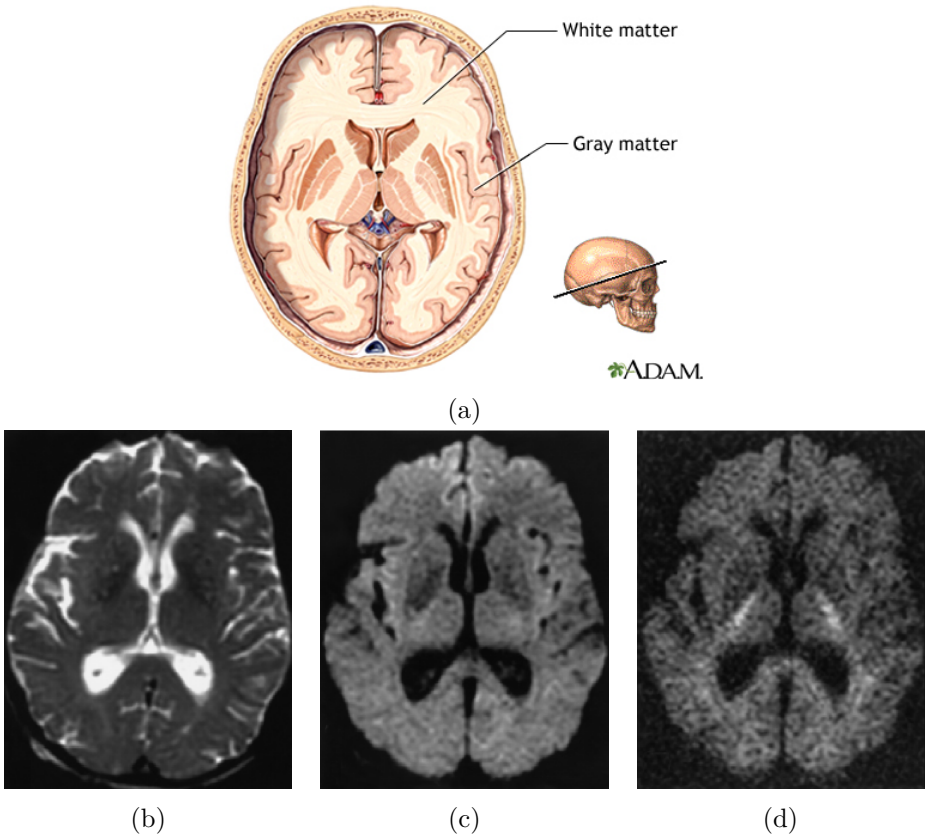

Figure 4.10: Brain DWI images using 3 different b-values (s/mm^2): (a) Gray and white matter of the brain(A.D.A.M. [2017]), and T2-weightedecho planar images with (b) b-value = 0, (c) b-value = 1000, and (d) b-value = 3000 (Burdette et al. [2001]).

white matter regions' signal is increased relative to gray matter regions, even though they are still remained slightly hypointense. On b-value=3000, majority of white matter tracts are hyperintense compared with deep gray matter and cortex structures. In addition, by comparing the images, it is obvious that image noise is increased by increasing the b-value.

4.2.2 Principle of DTI and Fiber Tracking

Previous section introduced the concepts of diffusion weighted imaging in which applying gradient pulses in a specific direction enables us to determine the diffusion constant for that specific direction. For example, a gradient which is applied in x direction makes the MR signal to be sensitized to the

diffusion process along the x-direction. The measurement in one direction can be generalized to other directions only when water molecules diffuse in all directions with the same amount. In other words, if the diffusion constant (D) for all directions is the same, we need only one measurement to determine it, which is so-called ***isotropic*** diffusion. But within the living systems, the diffusion process has sometimes directionality, so-called ***anisotropic*** diffusion, and there is a specific direction or some directions where water molecules tend to diffuse along it or them (Fig. 4.11). In this case, more measurements are necessary to describe the diffusion process that has directionality. Diffusion tensor imaging (DTI) extends the concepts of DWI by modeling the diffusion process through a mathematical tensor Basser et al. [1994b]. Although an anisotropic diffusion can be characterized by measuring the diffusion constants along a sufficiently large amount of directions, DTI represents the tensor as an ellipsoid whose main axis present the principle direction of diffusion. We know that each ellipsoid is characterized by six parameters: the length of main axes (the longest, the middle, and the shortest) and the orientation of them. The lengths are called ***principal diffusivities*** or ***eigenvalues*** (λ_1,λ_2, and λ_3), and the unit vectors defining their orientations are called ***eigenvectors*** (v_1,v_2, and v_3). Therefore, in order to estimate an ellipsoid diffusion tensor, it technically requires imaging with at least six diffusion gradient directions (Fig. 4.12).

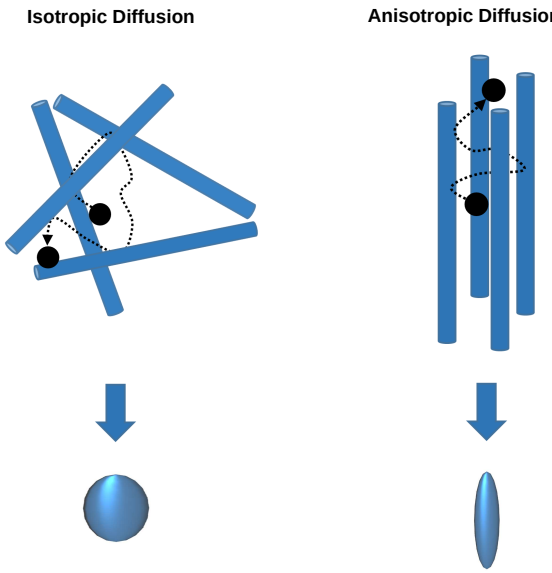

Figure 4.11: Diffusion of water molecules.

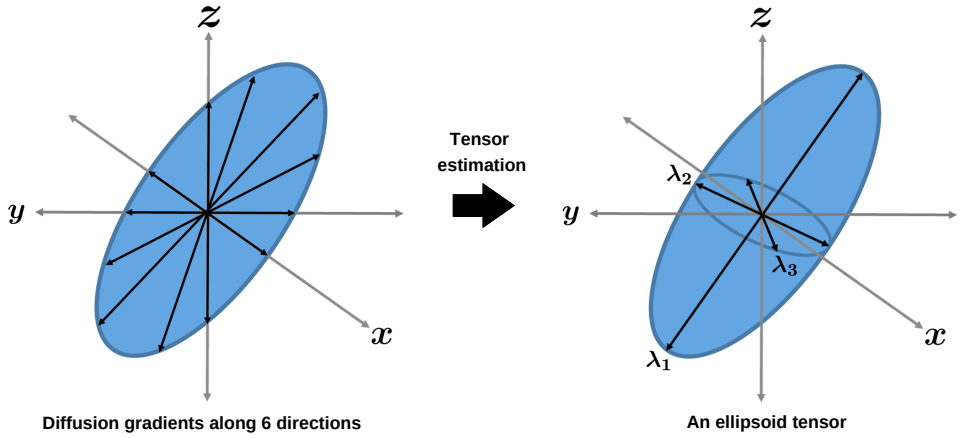

Figure 4.12: Geometric representation of the ellipsoid diffusion tensor: its corresponding parameters (eigenvalues and eigenvectors), and the minimum number of diffusion gradients that are necessary to estimate the tensor are shown.

Mathematically in DTI model, second-order tensors[2] are employed in order to describe the anisotropic diffusion within each voxel; a symmetric 3×3 tensor (having six independent parameters) that encodes elliptic shape geometry and its diagonalization leads to the ellipsoid parameters.

$$\boldsymbol{D} = \begin{bmatrix} D_{xx} & D_{xy} & D_{xz} \\ D_{yx} & D_{yy} & D_{yz} \\ D_{zx} & D_{zy} & D_{zz} \end{bmatrix} \xrightarrow{\text{Diagonalization}} \{\lambda_1, \lambda_2, \lambda_3, v_1, v_2, v_3\} \quad (4.13)$$

So, the eigendecomposition of $\boldsymbol{D}$ results in

$$\boldsymbol{D} = E \Lambda E^{-1}, \quad (4.14)$$

where

$$\Lambda = [v_1 \quad v_2 \quad v_3] \quad \text{and} \quad \boldsymbol{E} = \begin{bmatrix} \lambda_1 & 0 & 0 \\ 0 & \lambda_2 & 0 \\ 0 & 0 & \lambda_3 \end{bmatrix}$$

Subsequently, the spectral decomposition of $\boldsymbol{D}$ can be written as

$$\boldsymbol{D} = \lambda_1 v_1 v_1^T + \lambda_2 v_2 v_2^T + \lambda_3 v_3 v_3^T$$

where the superscript T denotes matrix transposition. The diagonal elements of $\boldsymbol{D}$ represent the diffusion constant along x, y, and z directions ($ADC_x = D_{xx}, ADC_y = D_{yy}$, and $ADC_z = D_{zz}$). In other words, they represent the diffusion perpendicular and parallel to the fiber. Imagine there is a fiber structure oriented along x direction, then ADC_x is larger than ADC_y and ADC_z. In contrast to diagonal elements, off-diagonal elements carry information about the rotations or the correlation of random motions between each pair of principal directions. In case of a pure liquid for which a perfect isotropic diffusion is expected, the diagonal elements are equal to

[2] A mathematical framework which is called "*tensor calculus*" allow to interpret mathematically and physically the geometric quantities using tensors.

a single diffusion constant, D, and off-diagonal elements are all zero.

$$\boldsymbol{D}_{\text{isotropic}} = \begin{bmatrix} D & 0 & 0 \\ 0 & D & 0 \\ 0 & 0 & D \end{bmatrix} \tag{4.15}$$

Similar to the function of signal attenuation for DWI (Eq. 4.10), a same mathematical process can be performed in order to achieve a tensor based function for DTI:

$$S = S_0 e^{-b\bar{g}^T \boldsymbol{D}\bar{g}}, \tag{4.16}$$

where $\boldsymbol{D}$ is the diffusion tensor represented by a symmetric positive definite 3×3 matrix and $\bar{g}$ is a unit vector determining gradient direction. In this equation, S is measured in the presence of diffusion weighted gradients, S_0 is taken in the absence of a diffusion weighted gradient, and b is also known. Thus, for estimating the diffusion tensor $\boldsymbol{D}$, which holds six distinct elements, at least six measurements must be done using different noncollinear gradient directions. Generally, a wide range of range of parametric methods can be employed to estimate tensors; for example, the least squares (Basser et al. [1994b]; Jones and Basser [2004]; Salvador et al. [2005]; Koay et al. [2006a,b]; Collier et al. [2015]) or the maximum likelihood (Andersson [2007, 2008]; Fillard et al. [2007]). Within the optimization process some a priori information such as positive definiteness constraint (Wang et al. [2004]; Koay et al. [2006a,b]; Andersson [2007, 2008]) or spatial regularization (Wang et al. [2004]; Koay et al. [2006b]; Andersson [2007]; Fillard et al. [2007]) can be incorporated in order to improve the precision and accuracy (Jones [2010]; Koay [2010]).

After estimating the diffusion tensors for each voxel, we need to analyze them within the same or different regions. Fig. 4.13 shows the computed tensor elements for a slice of human brain, which interpretation is difficult. This is why other methods of visualization should be considered. The simplest way can be the visualization of the 3D ellipsoids. They also can be colored following the RGB one dimensional map, where RGB values are set to the major eigenvector. Fig. 4.14 shows three tensors whose major eigenvectors are directed toward x, y, and z axes.

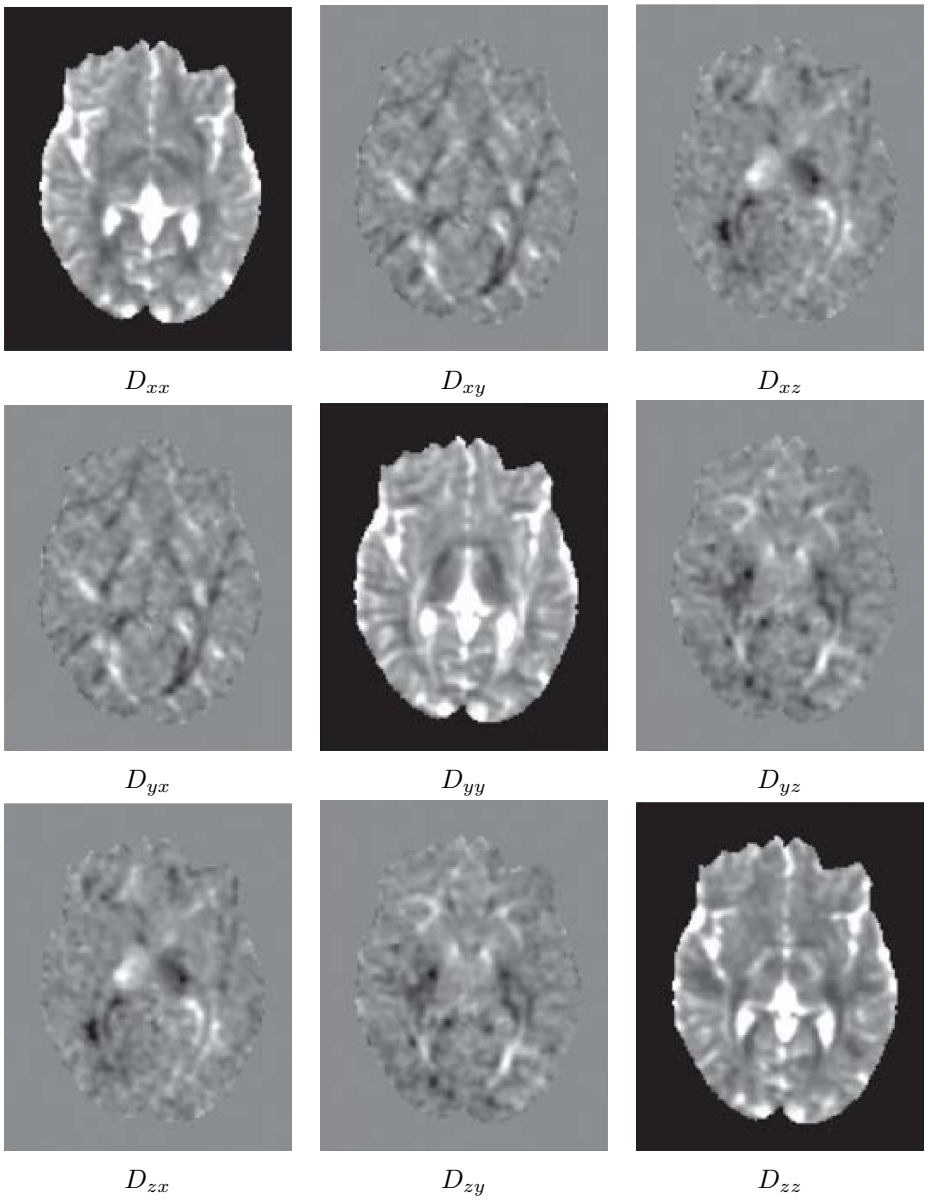

Figure 4.13: A diffusion tensor image of a human brain. Each element of tensor is shown in an indivigual image. As can be seen $D_{xy} = D_{yx}$, $D_{xz} = D_{zx}$, and $D_{yz} = D_{zy}$ (Jones [2010]).

Although, direct visualization of tensors are interesting, some scalar maps or indices may be extracted from tensors within the voxels. These scalar indices are visualized using a grayscale or a color-coded. In addition, tracking techniques are employed to generate paths representing the fiber tracks. In the following sections, we briefly explain both scalar maps and

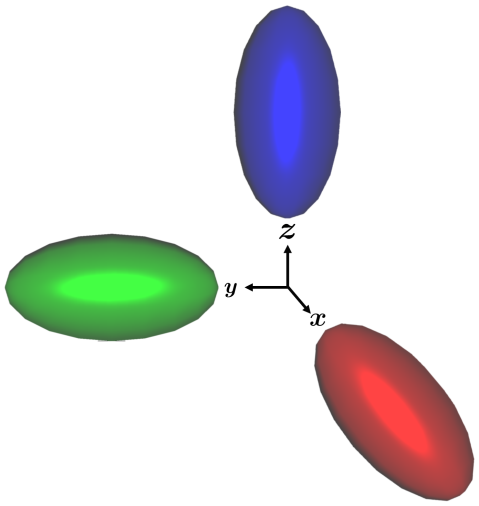

Figure 4.14: Color coding of tensors: the main axis of each tensor (i.e., the major eigenvector) is directed to one of the main axes. Here, red indicates directions in the x axis, green indicates directions in the y axis, and blue indicates directions in the z axis.

fiber tracking methods.

4.2.2.1 Diffusion scalar maps

This section briefly reviews the most popular diffusion derived scalar maps that are obtained from diffusion tensors eigenvalues or eigenvectors.

- **Trace**, that summarizes the total diffusivity (Basser et al. [1994a]),

$$\text{Trace} = \lambda_1 + \lambda_2 + \lambda_3, \tag{4.17}$$

- Mean Diffusivity (**MD**), that indicates the overall magnitude of water molecules diffusion independent of anisotropy and also overall obstacles to diffusion (Mori and Van Zijl [1995]; Basser and Pierpaoli [1996]).

$$\text{MD} \quad \text{or} \quad \bar{\lambda} = \frac{\text{Trace}}{3}, \tag{4.18}$$

- Fractional Anisotropy (FA), that reveals the degree of water diffusion anisotropy by evaluating how much the eigenvalues differ (Basser and Pierpaoli [1996]). Simply, this tells us how far the obtained tensor is

from a sphere (indicating an isotropic diffusion). In other words, FA is a normalized factor that basically describes the normalized variability across the levels of diffusion measured in the different directions. Therefore, the higher values of FA specify how strongly the diffusion is directed along the principal eigenvector orientation.

$$\begin{aligned} \mathrm{FA} &= \sqrt{\frac{3}{2}}\sqrt{\frac{(\lambda_1-\bar{\lambda})^2+(\lambda_2-\bar{\lambda})^2+(\lambda_3-\bar{\lambda})^2}{\lambda_1^2+\lambda_2^2+\lambda_3^2}} \\ &= \sqrt{\frac{1}{2}}\sqrt{\frac{(\lambda_1-\lambda_2)^2+(\lambda_2-\lambda_3)^2+(\lambda_3-\lambda_1)^2}{\lambda_1^2+\lambda_2^2+\lambda_3^2}} \end{aligned} \tag{4.19}$$

- Relative Anisotrophy (RA), that quantitatively assesses the level of out-of-roundness of the diffusion ellipsoid (Basser and Pierpaoli [1996]). Similar to FA, it is considered as an indice of diffusion anisotropy.

$$\mathrm{RA} = \frac{\sqrt{6}}{6}\frac{\sqrt{(\lambda_1-\bar{\lambda})^2+(\lambda_2-\bar{\lambda})^2+(\lambda_3-\bar{\lambda})^2}}{\bar{\lambda}} \tag{4.20}$$

- Volume Ratio (VR), that evaluates the ratio between the sphere volume and the ellipsoid volume (Basser [1995b]).

$$\mathrm{VR} = \frac{\lambda_1\lambda_2\lambda_3}{\bar{\lambda}^3} \tag{4.21}$$

Although the above mentioned diffusion indices are generally visualized as custom grayscale images, orientation information may be added in order to generate color-coded (cc) maps. In this regard, each component of the major eigenvector (v_1) of diffusion tensors can be multiplied by an anisotropy map such as FA as below

$$\mathrm{FA}_{cc} = \begin{bmatrix} \mathrm{FA}_{cc}^{\boldsymbol{R}} \\ \mathrm{FA}_{cc}^{\boldsymbol{G}} \\ \mathrm{FA}_{cc}^{\boldsymbol{B}} \end{bmatrix} = \begin{bmatrix} v_{1_x} * FA \\ v_{1_y} * FA \\ v_{1_z} * FA \end{bmatrix} \tag{4.22}$$

Fig. 4.15 shows some of the obtained maps and their color-coded ones for the human brain.

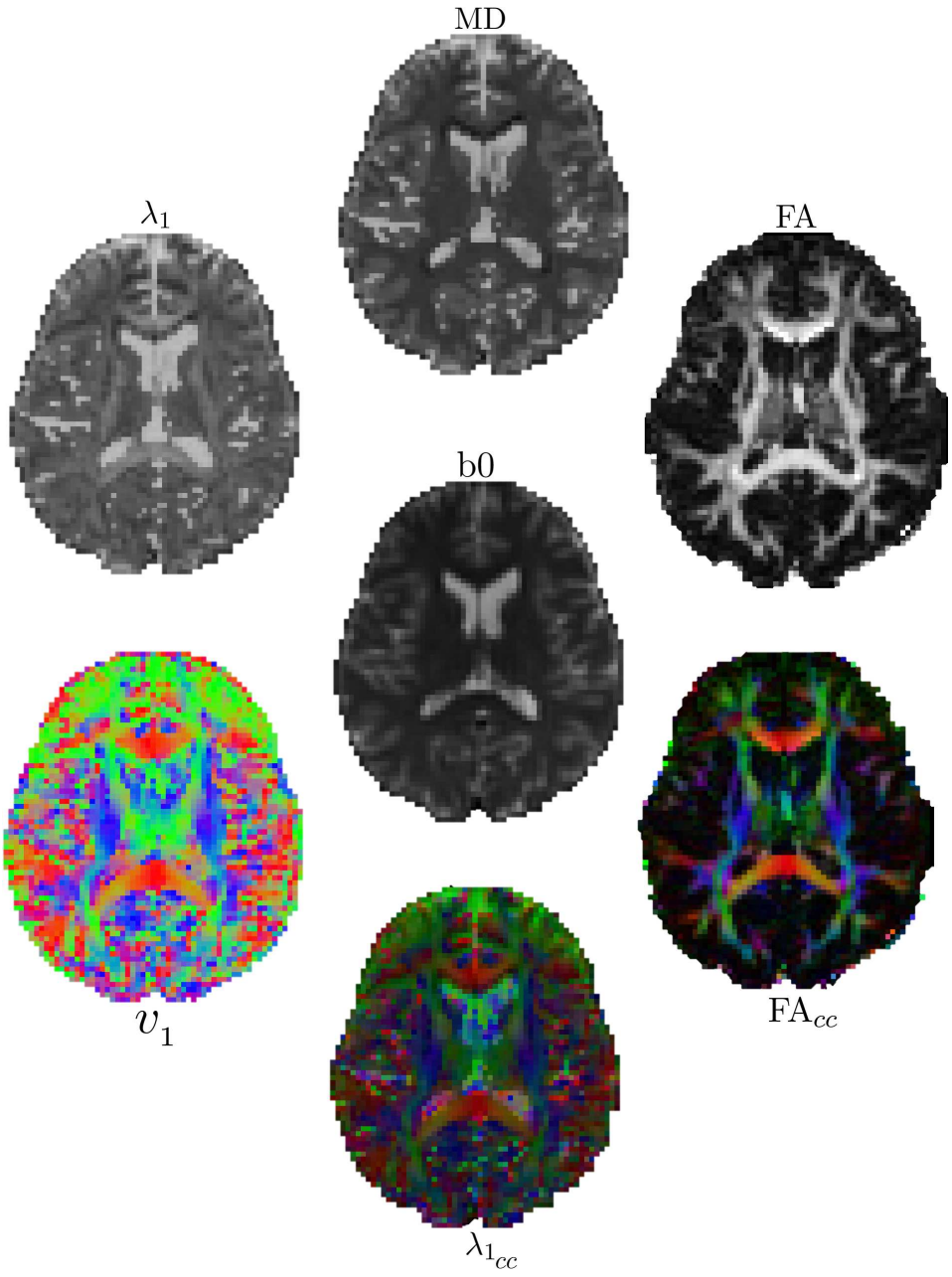

Figure 4.15: Example of diffusion derived parameters: maps of λ_1, MD, FA, directionally encoded color map of v_1 (red,green,blue), and color-coded maps of λ_1 and FA using v_1 through the Eq. 4.22.

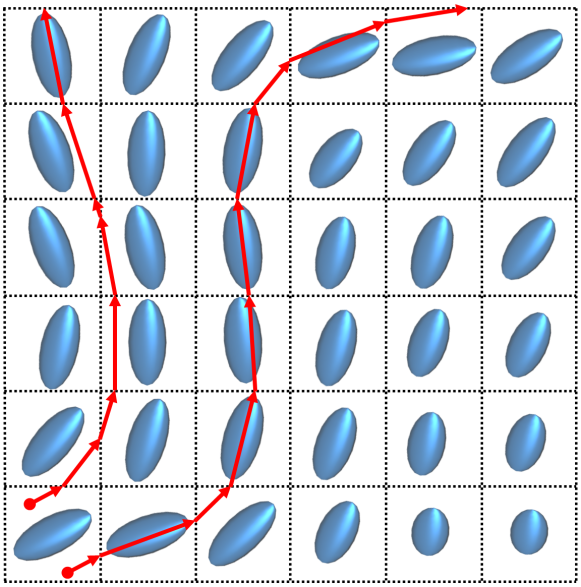

Figure 4.16: Fiber tractography: two seed points are selected in the voxel right down in order to track fibers according to the extension of diffusion tensors.

4.2.2.2 Fiber tractography

Fiber tractography (Jones et al. [1999]; Mori et al. [1999]; Basser et al. [2000]) is a kind of modeling that virtually provides a 3D visualization of fiber bundles. This technique assumes that the major eigenvector of the estimated diffusion tensors are locally parallel to the fiber tracks. Simply put, ellipsoids are elongated in such a way that they locally reflect the main fiber direction. Therefore, it can be considered that the direction of fibers is changing slowly and we can reconstruct fibers by moving from one voxel to another one according to the shape and direction of the ellipsoids (Fig 4.16). Also, color-coded fibers are generated using the direction of major eigenvector such as the scalar maps. Deterministic approaches can be used based on the estimated diffusion tensors. However, these methods can be quite inaccurate because: (1) the obtained results are prone to noise and to error-estimation of tensors; (2) the accuracy is not high due to the fact that crossing "×" and kissing ")(" fibers can not be detected within the voxels. Hence probabilistic methods could be more efficient (Tuch et al. [2000]; Koch et al. [2001]; Batchelor et al. [2001]; Beaulieu [2002]; Behrens et al. [2002];

Parker et al. [2002]). These methods are similarly based on seed points; however, they assume that each seed point could be connected to all other points within the volume. The algorithm evaluates the probability of all the possible connections and chooses the most probable one that optimizes a specific cost function. That is to say, probabilistic tractography methods estimate most likely fiber orientations and a probability distribution of orientations that represents how likely is each other orientation to lie along a fiber.

4.3 Integration of Muscle Fibers in the Subject-Specific FE Meshes

In chapter 3, subject-specific FE meshes were generated by deforming an atlas mesh according to a transformation that establishes a correspondence between the subject's and atlas' anatomical volumetric images (e.g., MRI or/and CT exams). Such transformations were extracted inherently based on the 3D registration of anatomical images. This section explains a novel approach that enables us to integrate additional subject-specific information related to fiber-bundles to the generated meshes. As the elements of atlas meshes can be organized according to the organ's geometry or its governing fiber structures, different methodologies are taken into account for integrating such information into the meshes. For more clarification, before going into the details of the proposed method, let us represent different atlas meshes that can be considered for a muscular structure containing fibers. Fig. 4.17a shows an atlas mesh designed only based on the anatomical shape of a region of interest, called here ***anatomical-mesh***. For generating such types of meshes, like the atlas tongue mesh used in chapter 3, only the information about the shape is required; and the information about fiber bundles can be added subsequently by defining in each element the main direction of each specific fiber bundles. In contrast, we can generate meshes by considering fiber structures such as the one represented in Fig. 4.17b, called here ***muscular-mesh***. As can be seen, the elements are designed and placed along the curved boundary of the fibers. This means that muscular-meshes inherently hold information about fiber bundles, and deformation of such an atlas mesh needs a mapping from the atlas' fibers to the subject's one.

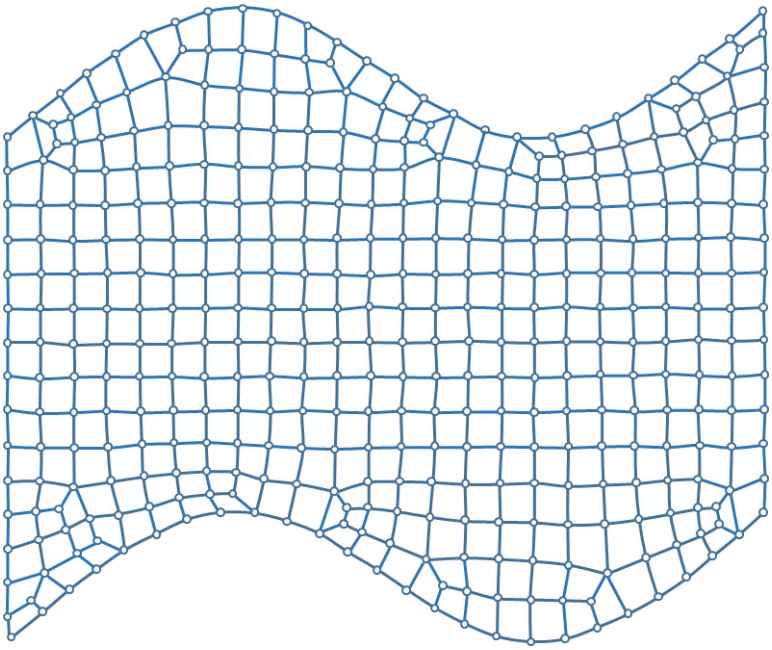

(a) Generated mesh based on the anatomical shape.

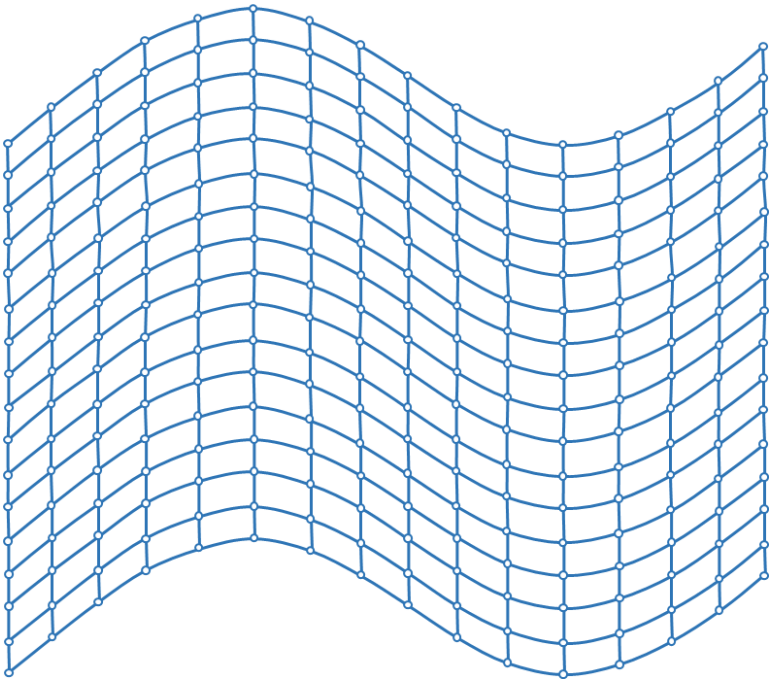

(b) Generated mesh based on the fibers structure.

Figure 4.17: Anatomical- and Fiber-based generated meshes.

Consequently, we propose an approach that considers both types of atlas meshes as follow

- In a methodology based on anatomical-meshes, subject-specific meshes that include fibers distribution information are generated in two steps: deforming an atlas mesh by registration of anatomical images (**Phase I**), and then determining which elements of the generated mesh are associated with specific fiber bundles in the atlas mesh (**Phase II**). In other words, subject's fibers can be labeled/grouped according to the atlas fiber-bundles and this information can be added to the anatomical mesh in order to be used during the mechanical simulations.

- In a methodology based on muscular-meshes, both anatomical information and information related to the muscles are incorporated for estimation of an overall transformation that can be used to directly deform a muscular-atlas mesh. This deformation is modeled by combination of an anatomical and a fiber-based transformations. On this matter, like the process used for the anatomical-meshes, an anatomical transformation is first estimated and then subject-specific fiber-bundles are identified (**Phase I** and **Phase II**). Afterwards, a fiber-based transformation is extracted by registration of fiber-bundles through **Phase III**. Combination of such transformations can be further used to directly deform the muscular-atlas mesh.

General dataflow proposed to embed fibers information within the generated meshes is shown in Fig. 4.18; and the three main phases are being explained in the following sections.

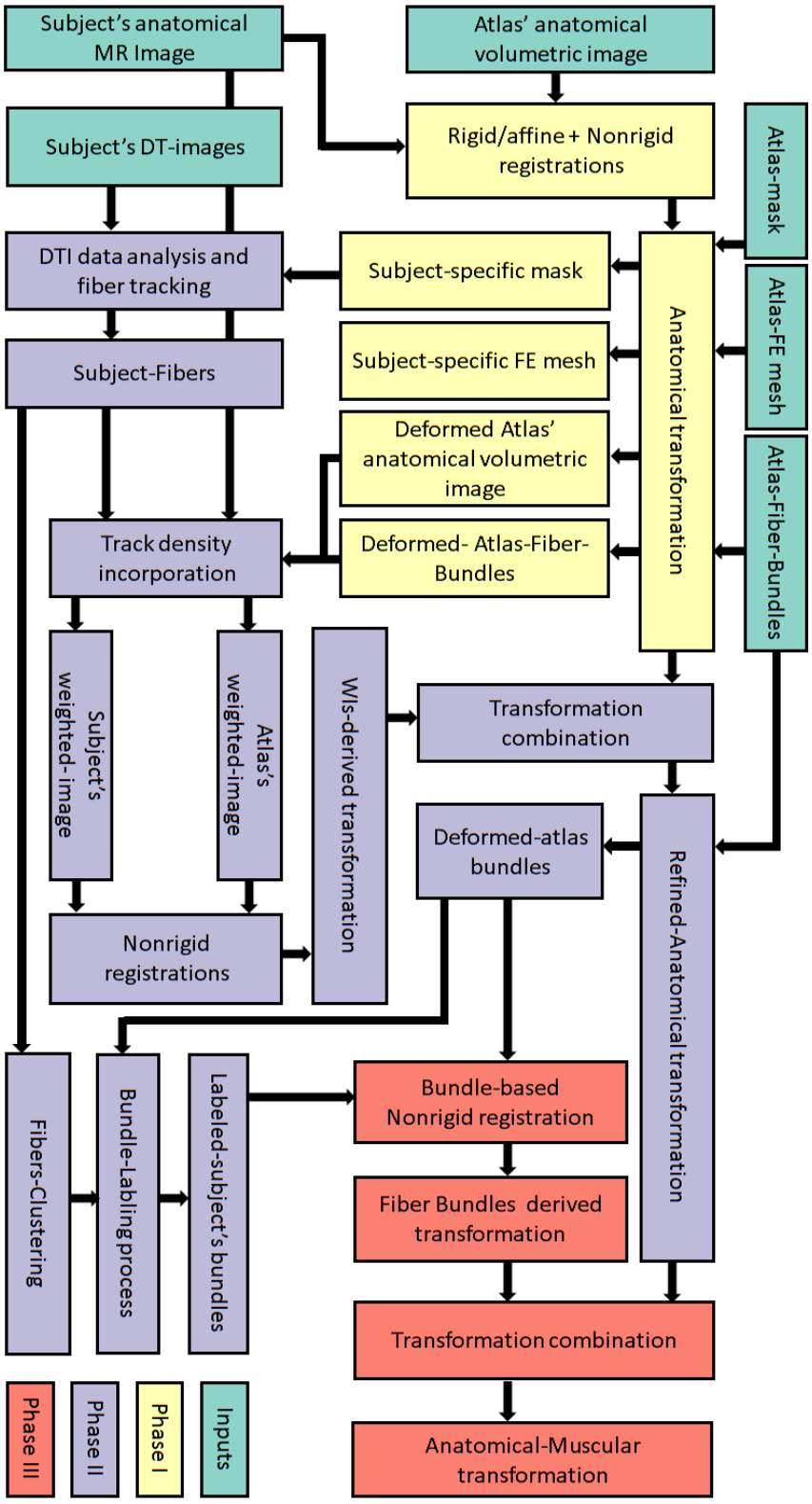

Figure 4.18: General dataflow proposed to generate 3D subject-specific FE meshes.

4.3.1 Phase I: Anatomical Registration (yellow boxes of the Fig. 4.18)

In order to establish a one-to-one correspondence between the atlas' and subject's MR images, and to extract a 3D displacement field that deforms the atlas mesh while preserving mesh quality, the method proposed in chapter 3 is employed. Briefly, a diffeomorphic non-rigid registration based on B-spline Free-Form Deformations (FFDs), which guarantees a non-folding and one-to-one transformation, is employed to produce an ***anatomical*** transformation ($T_{anatomical}$). For more details on the process, the reader is referred to chapter 3.
As explained before, depending on the type of atlas mesh that might be an anatomical-mesh or a muscular-mesh, different strategies are considered. For anatomical meshes such as our atlas tongue mesh, the obtained transformation is used to deform the atlas mesh and to generate subject-specific ones. However, mesh elements still need to be assigned to specific fiber-bundles according to the information provided in the atlas data (Phase II). On the contrary, in the case of muscular-meshes, the anatomical transformation is considered as an elementary transformation; and another transformation is extracted based on the fiber-bundles (Phase III). The combination of these two transformations results in an ***anatomical-muscular*** transformation, that subsequently can be used to deform muscular-meshes. It is important to note that Phase II is a prerequisite for Phase III.

4.3.2 Phase II: Detection of subject's fiber-bundles (purple boxes of the Fig. 4.18)

In order to add information about the fiber-bundles to the meshes, it is assumed that DTIs are acquired for both atlas and subject. Also, atlas' fibers are extracted in advance, manually or automatically, and grouped into a specific number of fiber-bundles. Then, subject's fiber-bundles are automatically estimated based on the atlas fiber-bundles. The primary step to this phase is fiber tracking for the subject using fiber tractography algorithms and the deformed-atlas mask. This step is explained below.

4.3.2.1 Refinement of anatomical transformation

In the previous phase, an anatomical transformation providing a geometrical correspondence between the atlas' and subject's organs was achieved. Although this transformation is not estimated based on the muscular structures, it can be used to deform atlas fibers and bring them into the subject's space. The transformation of fiber point x can be computed by

$$T(\mathrm{x}) = \mathrm{x} + D(\mathrm{x}), \tag{4.23}$$

where D is the 3D displacement field obtained from phase I. Therefore, both atlas' fibers and anatomical image are deformed using $T_{anatomical}$. At this stage, in the aim to refine $T_{anatomical}$, deformed-atlas and subject's anatomical images are weighted using the fibers information (see below for details about how "weighted-images" are generated). The produced weighted-images are registered together using the same method as in Phase I.
In this regard, track density images (TDIs) (Calamante et al. [2010]) are first created by sampling the deformed-atlas' and subject's fiber tracks in isotropic intervals (e.g, $0.5mm$) and counting the fibers that pass through each voxel. Then, weighted-images (WIs) are created by linear combination of anatomical images and TDIs as

$$\mathrm{WI} = (1-\omega) \times \mathrm{MRI} + \omega \times \mathrm{TDI}, \tag{4.24}$$

where ω is a weighting factor between zero and one. Fig. 4.19 shows a weighted-image which is created for a human brain (the phantom DTI data set is obtained from ISMRM−challenge [2015 (accessed November 28, 2016]). More weighted-images for different slices of the same DTI are provided in Fig 4.20. By looking at the weighted-images, it can be noted that the increment of anatomical contrast is achieved in the regions having high density of passing-fibers. This means that we can map fibers information into the anatomical images and use them to refine $T_{anatomical}$. In light of this, weighted-images are subsequently registered using the same process as defined in phase I; and the anatomical transformation is refined as below

$$T_{Ref-Anat} = T_{\mathrm{WI}} \circ T_{anatomical}, \tag{4.25}$$

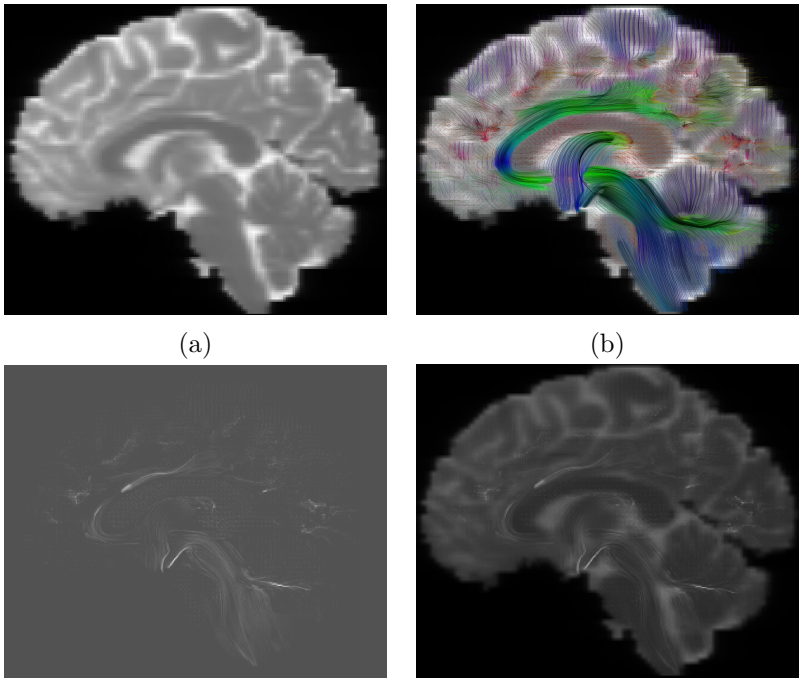

(a) (b)

(c) (d)

Figure 4.19: Linear combination of anatomical MR and track density images: (a) Anatomical MR image, (b) MR image superimposed with the 3D fiber tracks, (c) Track density image, (d) Linear combination of (a) and (c).

where $T_{Ref-Anat}$ and T_{WI} are respectively the refined-anatomical transformation and the transformation derived from registration of weighted-images.

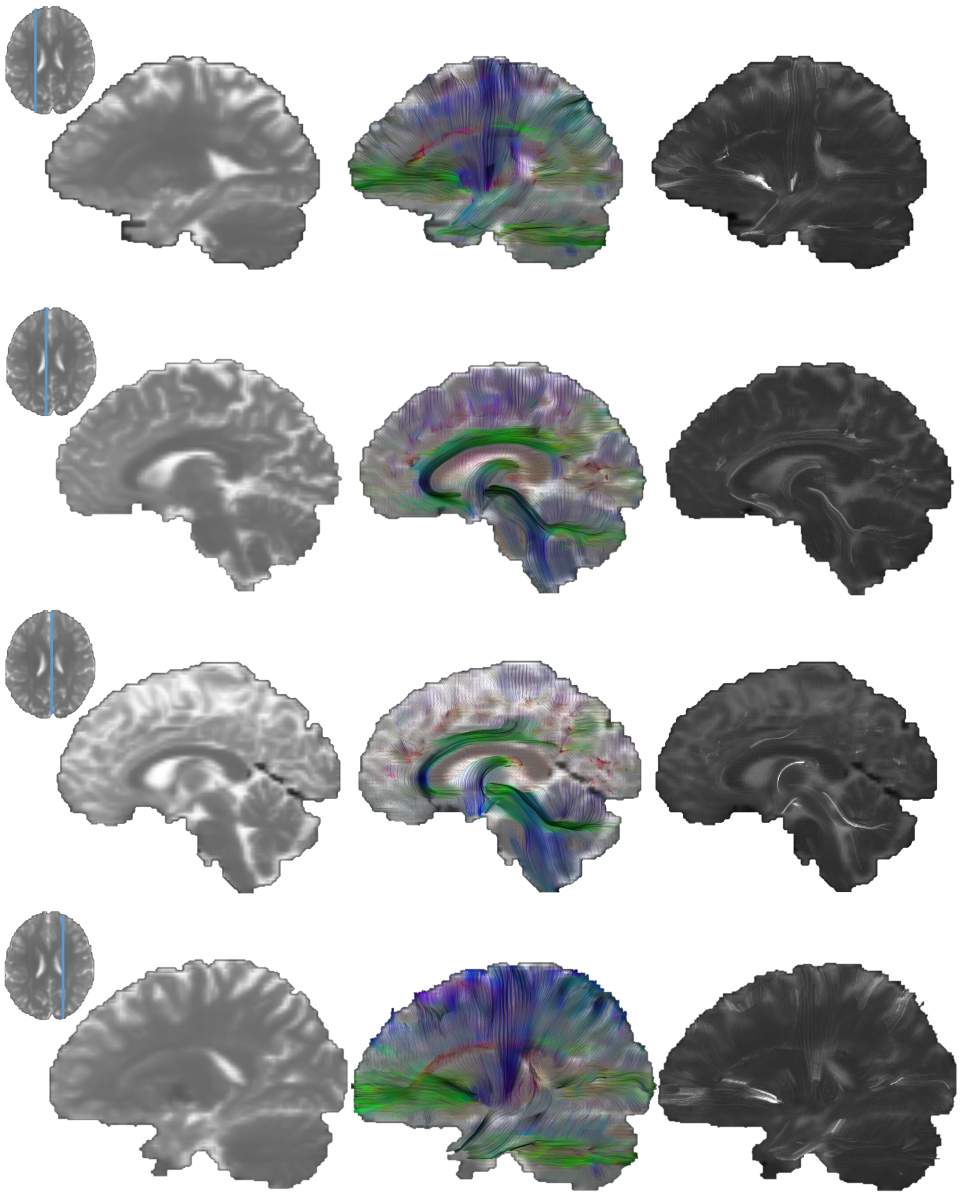

Figure 4.20: Examples for linear combination of anatomical MRIs and TDIs: the left, middle, and right columns respectively represent the anatomical images, MRIs superimposed with the 3D fiber tracks, and generated weighted-images.

4.3.2.2 Determination of subject's fiber-bundles

Within the refinement process, the anatomical transformation was guided by regions having high-density of fibers, as natural landmarks within the muscular regions. However, it should be noted that we can not expect such a transformation could provide an accurate mapping for low density regions. In other words, as $T_{Ref-Anat}$ is not achieved *solely* by the registration of atlas' and subject's fibers, and should be rather seen as a transformation that captures anatomical geometries including the overall distribution of fibers. At this stage, we can deform the atlas fiber using $T_{Ref-Anat}$ through an equation similar to Eq. 4.23, and obtain refined atlas-deformed-fiber-bundles (ADFB) that will serve at reference to automatically group subject's fiber tracks into subject-specific fiber-bundles. In this aim, a similarity measure ($\boldsymbol{S}$) is evaluated for each fiber of the subject by computing its distance to the centroids of the atlas-deformed-fiber-bundles, according to the method that is explained in details below.
Each fiber is represented by a variable number of points that may differ from one fiber to another. Since some similarity measures require fibers to be represented with the same number of points, each fiber of subject f is re-sampled along its trajectory using B-spline interpolation at a fix number N of points (p), and represented by a $N \times 3$ matrix.

$$f = \begin{bmatrix} p_1 \\ \vdots \\ p_N \end{bmatrix} = \begin{bmatrix} x_1 & y_1 & z_1 \\ \vdots & \vdots & \vdots \\ x_N & y_N & z_N \end{bmatrix} \tag{4.26}$$

Also, each Atlas-Deformed-Fiber-Bundle (ADFB) is represented by a triple $b = (b^{Ind}, b^{Cnt}, b^n)$, in which b^{Ind} is a list containing indices of the fibers that are included in the bundle, b^n is the number of fibers in the ADFB, and b^{Cnt} is the centroid of the bundle that is computed as

$$b^{Cnt} = \frac{\sum_{i=1}^{b^n} f_{b_i^{Ind}}}{b^n} \tag{4.27}$$

where $\sum$ is matrix-addition. Now, let's define the index subject's **fibers** and ADFBs respectively with $i = 1, \cdots, N_S$ and $j = 1, \cdots, N_{atlas}$, and summarize the whole process that enables grouping subject's fibers into the N_{atlas}

Data: Subject's fibers (f) and ADFBs (b)
Result: Subject's fiber-bundles
Initialization:

Re-sampling all fibers using N number of points;
Computation of ADFBs' centroids (b^{Cnt});
Defining a fiber-similarity measure ($\boldsymbol{S}$);

for $i \leftarrow 1$ **to** N_S **do**

$f_i^{label} \leftarrow \arg\max_j(\boldsymbol{S}(f_i, b_j^{Cnt}))$;

end

Algorithm 1: Determining subject's fiber-bundles based on atlas-deformed-fiber-bundles.

number of bundles, as shown in Algorithm 1.

As described in this Algorithm, the automatic determination of subject-specific fiber-bundles is based on a pairwise similarity or distance between each pair of subject's fibers and ADFBs' centroids. In the literature, a wide range of similarity measures are proposed that could be used to group/cluster fibers for *inter*- and *intra*-subject applications: Hausdorff distance (Gerig et al. [2004]; Xia et al. [2005]; Corouge et al. [2004]), Closest point distance and Mean distance of closest distances (Corouge et al. [2004]), Symmetrized mean closest point distance, which is the average of the two directed mean closest points distances between the two fibers (Guevara et al. [2011]), pairwise Euclidean distance of the fiber descriptors, including mean and square root of the covariance matrix of fiber points (Brun et al. [2004]), Mahalanobis distance (Maddah et al. [2008]), the average mean distance (Gerig et al. [2004]; Xia et al. [2005]; O'Donnell et al. [2006]; Corouge et al. [2004]), associativity vector which describes the relationship between the fiber and a certain anatomical ROI in a fuzzy manner (Wang et al. [2013a]), minimum average direct-flip distance (Garyfallidis et al. [2010]; Visser et al. [2011]), etc. Some methods like the Hausdorff distance ignore the sequential nature of fibers' points and treat them as a cloud of points. Given two fibers f_1 and f_2, the Hausdorff distance is computed as

$$d_H(f_1, f_2) = \max(d_h(f_1, f_2), d_h(f_2, f_1)) \tag{4.28}$$
$$\text{with} \quad d_h(f_1, f_2) = \max_{p_k \in f_1} \left(\min_{p_l \in f_2} \|p_k - p_l\| \right)$$

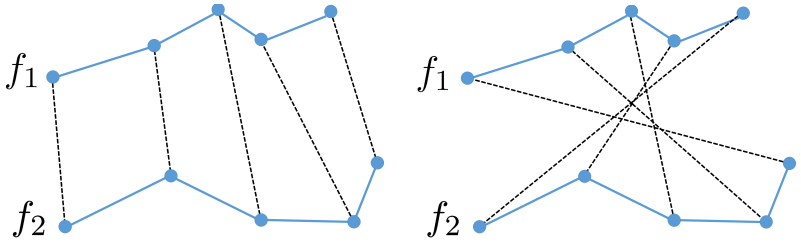

(a) d_{direct} (b) $d_{flipped}$

Figure 4.21: The components of MDF distance: (a) direct distance and (b) flipped distance; fibers are drawn in solid lines, and the pairs of points which distances contribute to the MDF are connected with dashed lines.

where $\| \, . \, \|$ is the Euclidean norm. Evidently, d_H does not require the fibers to be sampled with the same number of points. In contrast, often methods like the minimum average direct-flip distance (MDF) consider the sequential order of points and need the fibers to be sampled with the same number of points. Given two fibers $f_1 = [\, p_1^{f_1}, \cdots, p_N^{f_1} \,]$ and $f_2 = [\, p_1^{f_2}, \cdots, p_N^{f_2} \,]$, and their flipped version $f_1^{flipped} = [\, p_N^{f_1}, \cdots, p_1^{f_1} \,]$ and $f_2^{flipped} = [\, p_N^{f_2}, \cdots, p_1^{f_2} \,]$, MDF is computed as

$$\text{MDF}(f_1, f_2) = \min(d_{direct}(f_1, f_2), d_{flipped}(f_1, f_2)), \tag{4.29}$$

with

$$d_{direct}(f_1, f_2) = d(f_1, f_2) = \frac{1}{N} \sum_{i=1}^{N} \left\| p_i^{f_1} - p_i^{f_2} \right\|,$$

$$d_{flipped}(f_1, f_2) = d(f_1, f_2^{flipped}) = d(f_1^{flipped}, f_2),$$

The components of MDF, namely *direct* and *flipped* distances, are shown in Fig.4.21. To sum up, each distance or similarity measure has specific advantages and shortcomings. For instance, closest point distance encodes coarse information about fibers' similarity and closeness, and therefore can not be expected to achieve a good discrimination (Corouge et al. [2004]). However, since the atlas fibers are mapped into the space of subject's fibers using $T_{Ref-Anat}$ before measuring similarity, it is reasonnable to think that the performance of all these different similarities measures should be good. Coming back to Algorithm 1, it should be mentioned that, due to robustness limitations of fiber tractography methods in noisy low-contrast regions or at junctions, there might be some outliers in the subject's fibers. With the

Data: Subject's fibers (f) and ADFBs (b)
Result: Subject's fiber-bundles
Initialization:

Re-sampling all fibers using N number of points;
Computation of ADFBs' centroids (b^{Cnt});
Defining a fiber-similarity measure ($\boldsymbol{S}$);
Selecting $\boldsymbol{S}_{min}$, according to the type of $\boldsymbol{S}$;

for $i \leftarrow 1$ **to** N_S **do**
  $label \leftarrow \arg\max_j(\boldsymbol{S}(f_i, b_j^{Cnt}))$;
  if $\boldsymbol{S}(f_i, b_{label}^{Cnt}) < \boldsymbol{S}_{min}$ **then**
    This is an outlier;
  else
    $f_i^{label} \leftarrow label$;
  end
end

Algorithm 2: Determining subject-specific fiber-bundles based on ADFBs, with similarity constraint.

term "outliers" we understand subject-specific fibers that cannot reliably related to a ADFB. Indeed the ADFB is considered as a reliable information about muscle organization in the subject-specific anatomy. Hence, to be treated as a reliable fiber, a subject-specific fiber should be close enough to one of the ADFBs. This is why, to evaluate whether a subject-specific fiber is an outlier or not, we have introduced a constraint at the level of similarities or distances. In other words, the highest similarity measure between a subject's fiber and ADFBs should be more than a minimum value ($\boldsymbol{S}_{min}$). Adding this constraint in Algorithm 1, we obtain Algorithm 2.
If we now come back to the problem of subject-specific meshes, our main objective is to determine the muscular affiliation of each element in the generated subject-specific anatomical-meshes using the knowledge provided by the atlas. As a result of phase II, we can identify which element of the subject-specific mesh belongs to which muscle-fiber-bundle and, on this basis, attribute to each element specific mechanical properties and functionality. Fig. 4.22 shows an example of such an anatomical transformation and of the derived-correspondence between the elements. Thanks to the detec-

tion of fiber-bundles in the geometrical space of the subject, we are now in a position where we can consider computing a fiber-bundle-based transformation mapping the atlas-fiber-bundles into the subject-specific-fiber bundles. Focusing on fiber-bundles instead of fibers, we overcome the problems linked to the inaccuracy of fiber-tracks detection that we mentioned above. The next phase will address this problem by non-rigid registration of ADFBs to the subject's identified fiber-bundles (SIFBs).

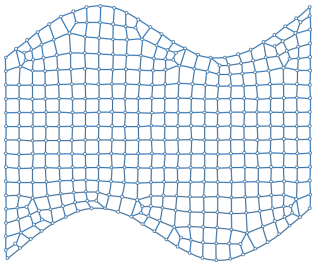

(a) Atlas anatomical-mesh,

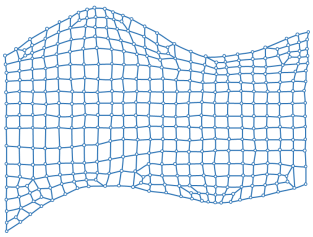

(b) Subject-specific mesh,

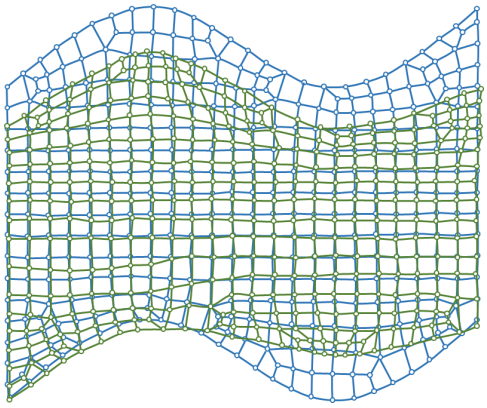

(c) Atlas mesh superimposed with the subject-specific mesh

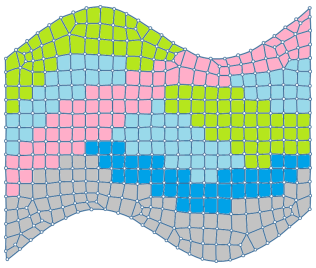

(d) Elements in the atlas' mesh,

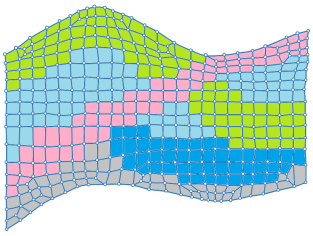

(e) Elements in the subject' mesh

Figure 4.22: An example of an anatomical-mesh deformation and achieved elements correspondence: (a) Atlas anatomical-mesh, (b) Deformed-atlas mesh or subject-specific mesh, (c) Atlas mesh superimposed with the subject-specific mesh, (d) Elements belonging to different fiber-bundles in the atlas mesh, (e) Elements belonging to different bundles in the subject-specific mesh (the correspondence is achieved by Phase II).

4.3.3 Phase III: Fiber-bundles non-rigid registration (pink boxes of the Fig. 4.18)

In Phase II, subject-specific fiber-bundles (SIFBs) were identified and associated with atlas's fiber-bundles. This correspondence could be used to identify elements belonging to different bundles in the generated anatomical subject-specific meshes. However, we need to compare each pair of fiber-bundles locally for inter-subject studies of functional data or intra-subject longitudinal studies of fiber tracts (e.g, to study normal aging (Sullivan et al. [2010]) or age-related decline in fiber tracts (Voineskos et al. [2012])). In addition, a fiber-derived transformation could be used to deform muscular-meshes. In this respect, we are going to non-rigidly register each pair of fiber-bundles.
Before going into the details of the registration process, let us remind a few facts:

- Each fiber-bundle contains a variable number of fibers. Hence, even if all the fibers were re-sampled to the same number of points, each bundle is represented by a different number of 3D points;
- Although we are going to locally register two sets of 3D points, we should keep in mind that the **topological structure** of the fiber-bundles ***must*** be preserved. In other words, we are interested in exploiting global relationships in the point sets;
- It is very important to keep **local structures**[3] among neighboring points.

In light of these considerations, it is quite important that the registration method should use the global and local structures, and also preserves the topological structure of the point sets. Accordingly, a probabilistic method called Coherent Point Drift (CPD) (Myronenko and Song [2010]) is employed to provide a correspondence between the two fiber-bundles, using motion coherence theory (MCT) (Yuille and Grzywacz [1988, 1989]) and regardless of the transformation model. According to this theory, points that are close to each other tend to move coherently. Considering this theory and the need for a smooth transformation, CPD deals with the movements as a

[3]The terms ***topological*** and ***local*** structures refer to the ***connectivity*** and ***adjacency*** of the ***points*** that form a ***fiber*** and the ***fibers*** that form a ***fiber-bundle***.

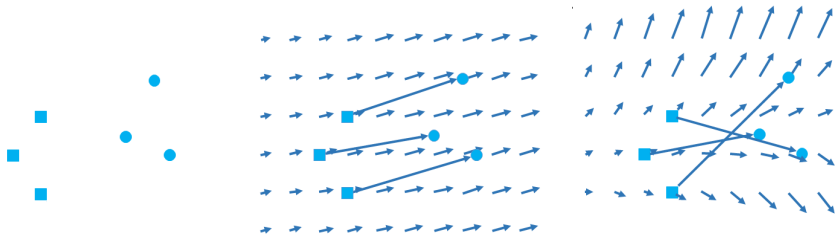

(a) (b) (c)

Figure 4.23: Velocity fields having different level of coherency with the given point correspondences: (a) two point sets, Coherent velocity field, (b) high coherent velocity field, (c) less coherent velocity field (Myronenko et al. [2006]).

temporal motion process, and then enforces a motion coherence constraint over the velocity field or displacement. Velocity fields having different level of coherency with the given point correspondences are illustrated in Fig. 4.23.

4.3.3.1 Coherent Point Drift (CPD)

Basically, CPD considers the alignment of two point sets as a problem of probability density estimation. In order to preserve the topological structures, the first data set, which is represented by Gaussian Mixture Model (GMM) centroids, is fitted to the second data set by maximizing the likelihood (Dempster et al. [1977]). As a consequence of the motion coherence constraint over the velocity field, the centroids move coherently as a whole so that the topological structure of the second data set is preserved. In the optimal state estimation, the two point sets are aligned and the correspondence is achieved by the posterior probabilities of the GMM components. In addition, regularization of displacement field is considered to have a smooth non-rigid registration. In the following the problem formulation and CPD algorithms are briefly described.

Given a pair of corresponding fiber-bundles being aligned, $f_{ADFB} \mathrel{\widehat{=}} f_{SIFB}$, two sets of different point count are considered:

- $\mathbf{Y} = [f_{ADFB} \quad \text{points}]_{M\times 3}$
- $\mathbf{X} = [f_{SIFB} \quad \text{points}]_{N\times 3}$

where M and N represent the number of points in each fiber-bundle. The points in $\mathbf{Y}$ are considered as the centroids of a GMM to be fitted to the points in $\mathbf{X}$, by maximizing the likelihood function. The current positions of centroids are defined as

$$\mathbf{Y} = v(\mathbf{Y}_0) + \mathbf{Y}_0 \tag{4.30}$$

where $\mathbf{Y}_0$ is the initial centroid position and v is a continuous velocity or displacement function. In order to model the problem, the points in $\mathbf{X}$ are looked as the data points generated by the GMM.
Therefore, a Gaussian mixture density $p(\mathrm{x}) = \sum_{m=1}^{M} \frac{1}{M} p(\mathrm{x}|m)$ with $p(\mathrm{x}|m) \sim \mathcal{N}(\mathrm{y}_m, \sigma^2 I_3)$ is considered, where $\mathbf{Y}$ includes 3D centroids of equally-weighted Gaussians with equal isotropic covariance matrices. Also, in order to apply a smooth motion constraint over the movement of the centroids, the prior $p(\mathbf{Y}|\lambda) \propto exp(-\frac{\lambda}{2}\phi(\mathbf{Y}))$ is defined, where λ is a weighting factor and $\phi(\mathbf{Y})$ is a regularization function that smooths the motion. In other words, ϕ brings our prior knowledge about the motion to the problem. In this manner, the optimal values of $\mathbf{Y}$ are estimated by maximizing the a posteriori probability:

$$E(\mathbf{Y}) = -\sum_{n=1}^{N} log \sum_{m=1}^{M} e^{-\frac{1}{2}\left\|\frac{\mathrm{x}_n - \mathrm{y}_m}{\sigma}\right\|^2} + \frac{\lambda}{2}\phi(\mathbf{Y}) \tag{4.31}$$

Knowing the fact that the smoothness of a function can be considered as a measure of its *oscillatory* behavior (Girosi et al. [1995]), the regularization term (ϕ) is replaced by a function measuring the high frequency content, and the energy function in Eq. 4.31 is then rewritten as

$$E(\tilde{v}) = -\sum_{n=1}^{N} log \sum_{m=1}^{M} e^{-\frac{1}{2}\left\|\frac{\mathrm{x}_n - \mathrm{y}_m}{\sigma}\right\|^2} + \frac{\lambda}{2}\int \frac{|\tilde{v}(\mathrm{s})|^2}{\tilde{G}(\mathrm{s})} d\mathrm{s} \tag{4.32}$$

where $\tilde{v}(\mathrm{s})$ and $\tilde{G}(\mathrm{s})$ represent the Fourier transform of the velocity, and a symmetric positive definite low-pass filter that approaches zero when $\|\mathrm{s}\| \to \infty$, respectively. Using a variational approach (Myronenko et al. [2006]), it is shown that the energy function in Eq. 4.32 is minimized for all vectors z

by a radial basis function as below

$$v(\mathrm{z}) = \sum_{m=1}^{M} \mathrm{w}_m G(\mathrm{z} - \mathrm{y}_{0m}), \tag{4.33}$$

with

$$\mathrm{w}_m = \frac{1}{\lambda} \sum_{n=1}^{N} \frac{e^{-\frac{1}{2}\left\| \frac{\mathrm{x}_n - \mathrm{y}_m}{\sigma} \right\|^2} \frac{1}{\sigma^2}(\mathrm{x}_n - \mathrm{y}_m)}{\sum_{m=1}^{M} e^{-\frac{1}{2}\left\| \frac{\mathrm{x}_n - \mathrm{y}_m}{\sigma} \right\|^2}}$$

where $G_{M\times M}$ is chosen to be a Gaussian affinity matrix. Such a Gaussian kernel form for G brings some advantages:

- the required properties are satisfied: being a symmetric positive definite matrix and when $\|\mathrm{s}\| \to \infty$, $\tilde{G}$ approaches zero;
- no fluctuation is included in both time and frequency domains for a low-pass filter having a Gaussian form;
- the size of Gaussian filter enables us to control the range of filtered frequencies or the level of spatial smoothness;
- the regularization term imposes the points to move coherently according to the Motion Coherence Theory (MCT) (Yuille and Grzywacz [1988, 1989]), as it becomes equivalent to the sum of weighted squares of all order derivatives of the velocity field (Yuille and Grzywacz [1988])

$$\phi_{MCT}(v) \;=\; \int \sum_{m=1}^{\infty} \frac{\beta^{2m}}{m!2^m} (D^m v(\mathrm{x}))^2 d\mathrm{x} \tag{4.34}$$

where D is a derivative operator in that $D^{2m}v = \nabla^{2m}v$ and $D^{2m+1}v = \nabla(\nabla^{2m}v)$.

The obtained solution for v, Eq.4.33, is subsequently substituted into Eq.4.32

$$E(\mathbf{W}) = \tag{4.35}$$
$$-\sum_{n=1}^{N} log \sum_{m=1}^{M} e^{-\frac{1}{2}\left\| \frac{\mathrm{x}_n - \mathrm{y}_{0m} - \sum_{k=1}^{M} w_k G(\mathrm{y}_{0k} - \mathrm{y}_{0m})}{\sigma} \right\|^2} + \frac{\lambda}{2} tr(\mathbf{W}^T \mathbf{G} \mathbf{W}),$$

where the kernel matrix is represented by $\mathbf{G}_{M\times M}$ whose elements are $g_{ij} = e^{-\frac{1}{2}\left\|\frac{y_i - y_j}{\beta}\right\|^2}$, and $\mathbf{W}_{M\times 3} = (w_1, \cdots, w_M)^T$ includes the Gaussian kernel weights in Eq. 4.33.

In order to derive an optimal transformation, as the problem is equivalent to the Expectation Maximization (EM) algorithm for GMM, the upper bound of the energy function in Eq. 4.35 can be find as (E-step)

$$Q(\mathbf{W}) = \sum_{n=1}^{N}\sum_{m=1}^{M} P^{old}(m|x_m)\frac{\|x_n - y_{0m} - \mathbf{G}(m,.)\mathbf{W}\|^2}{2\sigma^2} + \frac{\lambda}{2}tr(\mathbf{W}^T\mathbf{G}\mathbf{W}), \tag{4.36}$$

where P^{old} is a posteriori probability distributions of mixture components which is calculated using previous parameter values, $\mathbf{G}(m,.)$ is the m^{th} row of $\mathbf{G}$. Minimizing the upper bound, Eq. 4.36, will decrease the value of energy function in Eq. 4.35. On this matter, the optimal parameters can be achieved by taking the derivative of Eq. 4.36 with respect to $\mathbf{W}$ (M-step)

$$\frac{\partial Q}{\partial \mathbf{W}} = \frac{1}{\sigma^2}\mathbf{G}(diag(\mathbf{P1})(\mathbf{Y}_0 + \mathbf{G}\mathbf{W}) - \mathbf{P}\mathbf{X}) + \lambda\mathbf{G}\mathbf{W} = 0 \tag{4.37}$$

where $diag(.)$ specifies a diagonal matrix, 1 is a column vector of all ones, and P is the matrix of posterior probabilities with elements

$$p_{mn} = \frac{e^{-\frac{1}{2}\left\|\frac{y_m^{old} - x_n}{\sigma}\right\|^2}}{\sum_{m=1}^{M} e^{-\frac{1}{2}\left\|\frac{y_m^{old} - x_n}{\sigma}\right\|^2}} \tag{4.38}$$

For consideration of outliers, a uniform probability density function is also added to the mixture model and the whole process of CPD is summarized as (Myronenko et al. [2006]; Myronenko and Song [2010])

- Initialize parameters λ, β, and σ,
- Construct $\mathbf{G}$ matrix, and intitialize $\mathbf{Y} = \mathbf{Y}_0$
- Deterministic annealing:

  EM algorithm, repeat until optimization:

  – E-step: Compute $\mathbf{P}$

  - M-step: Solve for $\mathbf{W}$ from Eq. 4.37
  - Update $\mathbf{Y} : \mathbf{Y} = \mathbf{Y}_0 + \mathbf{GW}$

  Anneal $\sigma = \alpha \times \sigma$

- Compute the velocity field: $v(\mathrm{z}) = \mathbf{G}(z, .)\mathbf{W}$
- Establish the correspondence from posterior probabilities $\mathbf{P}$

For more details about the mathematical procedure leading to the equations and EM algorithm, the interested reader is highly suggested to read (Myronenko et al. [2006]; Myronenko and Song [2010]). Fig.4.24 shows a 2D example of CPD registration. It is evident that the points in the template set (blue) are moved coherently so that the inherent topological structure is preserved while they are aligned to the reference point set (red). Also, a 3D example of nonrigid CPD registration for a pair of corresponding fiber-bundles is shown in Fig. 4.25.

4.3.3.2 Mesh Morphing

Nonrigid CPD registration was introduced as a technique that can be used to align each pair of fiber-bundles while preserving **topological structures**. On this matter, a nonrigid transformation is estimated for mapping each ADFB to its corresponding SIFB.

$$f_{ADFB} \mathrel{\widehat{=}} f_{SIFB} \quad \xrightarrow[registration]{CPD} \quad f_{CPD-ADFB} \mid\mid\mid f_{SIFB}$$

here, $\mathrel{\widehat{=}}$ and $\mid\mid\mid$ mean *corresponding* and *aligned*, respectively. This in turn means that the number of CPD-derived transformations would be equal to the fiber-bundles count. However, from a mesh morphing perspective, a smooth overall transformation is required that can be applied to the whole mesh. This point of view is particularly important in the case of neighboring or crossing fiber bundles "×", where neighboring elements belong to different fiber-bundles. Fig. 4.26 shows a tongue mesh which was generated according to muscles' distribution (Buchaillard et al. [2007b]). It can be seen that elements are designed and placed along the curved boundary of the muscles, and the mesh inherently holds information about fiber bundles. It is for this reason that an overall transformation should be computed for the whole mesh space using interpolation techniques such as thin-plate spline

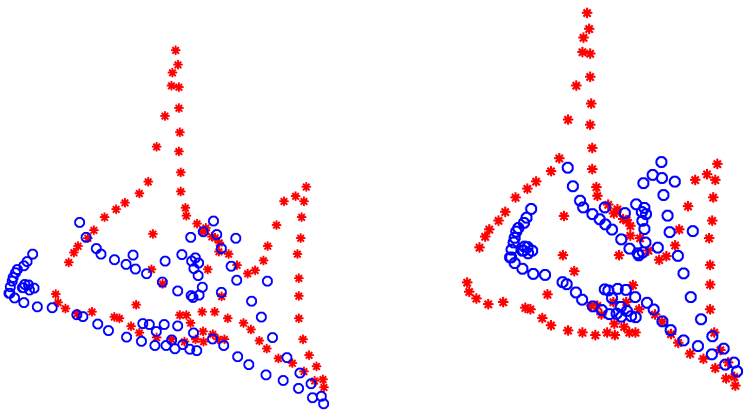

(a) Initialization

(b) Iteration 5

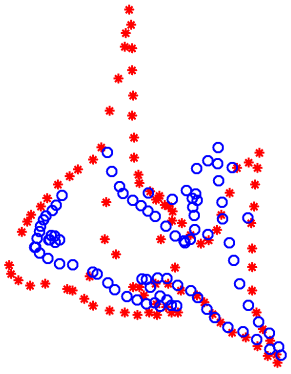

(c) Iteration 10

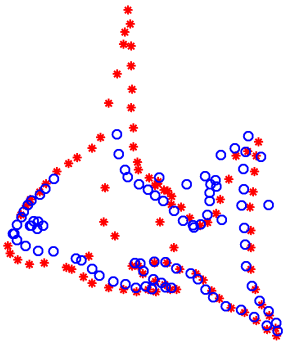

(d) Iteration 20

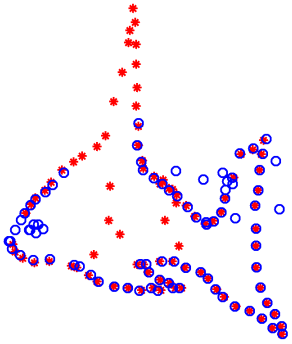

(e) Iteration 30

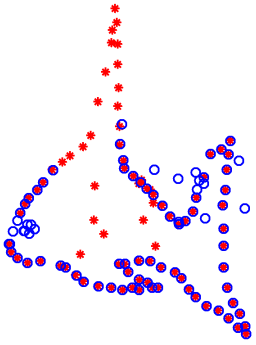

(f) Iteration 40

Figure 4.24: A 2D example of nonrigid CPD registration: (a) the two point sets before registration, the template and reference point sets are shown in blue and red colors receptively, (b)-(f) achieved correspondences using CPD registration after different number of iterations.

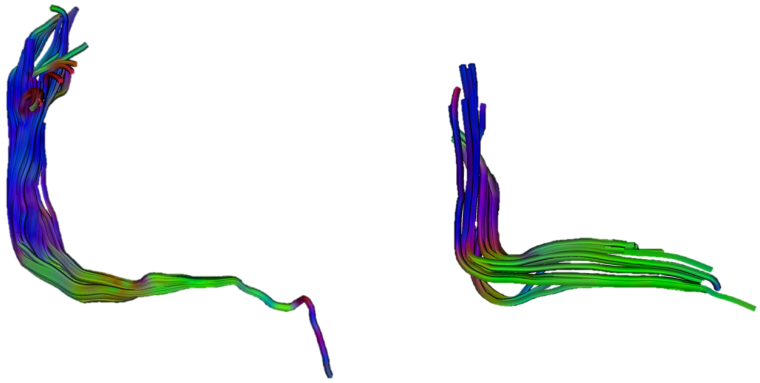

(a) Template

(b) Reference

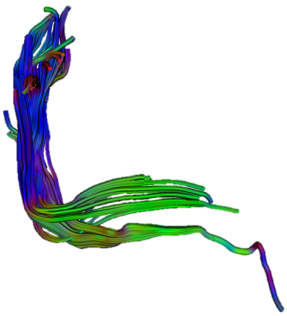

(c) Before-Reg

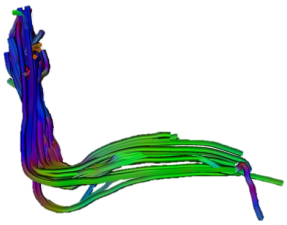

(d) After-Reg

Figure 4.25: A 3D example of nonrigid CPD registration for a pair of corresponding fiber-bundles: (a) template fiber-bundle, (b) reference fiber-bundle, (c) both fiber-bundles before registration, (d) both fiber-bundles after registration.

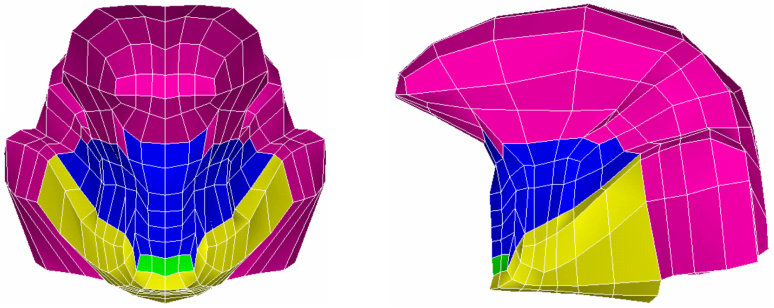

(a) Frontal view (b) Sagittal view

Figure 4.26: A muscular tongue mesh; muscles are displayed in different colors (Buchaillard et al. [2007b]).

(TPS) (Bookstein [1988]). In this context, the TPS transform is created by consideration of two point sets, ADFBs and *CPD*-ADFBs, as the source landmark positions and their target positions. The obtained TPS transform subsequently could be considered as an overall muscular transformation that introduces a smooth mapping for deformation of muscular-meshes.

4.4 Results

In chapter 3, an automatic method was proposed to generate subject-specific tongue FE meshes using anatomical images, while no subject-specific information about fiber bundles were included. With the aim to continue our previous study, we are going to investigate the performance of our Image-and-Fiber based Identification-and-Registration (IFIR) technique using tongue diffusion tensor images. However, prior to the tongue application, it is necessary to have a comprehensive understanding on the performance of IFIR approach using a physical phantom which contains several crossing fiber configurations. Therefore, the evaluation in this section consisted of two parts: a phantom test and a human tongue test.

4.4.1 FiberCup Phantom

FiberCup competition, as part of MICCAI 2009, has provided an MR phantom for the evaluation of fiber tractography methods (Fillard et al. [2011]). Different realistic fibers configuration such as bending, crossing and kissing are included in this phantom. Also, other replications of the FiberCup phan-

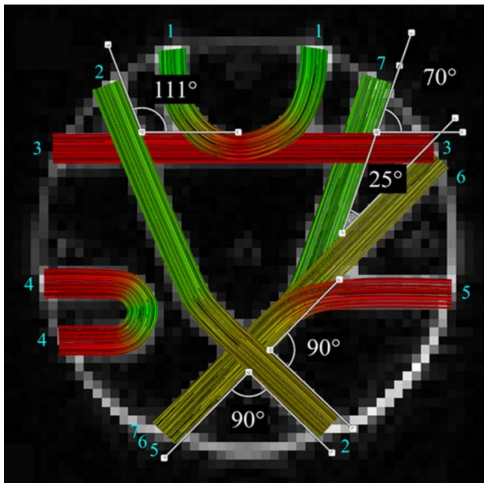

Figure 4.27: Replication of the FiberCup phantom (Neher et al. [2014b]): the seven fiber-bundles of the recreated FiberCup phantom are superimposed on the original acquisition.

tom are generated using an extensible system for the generation of phantoms (so called Fiberfox) (Neher et al. [2014a,b]). Although this phantom has been employed as a ground truth for fiber tracking methods, we are going to use a recreated FiberCup phantom (Neher et al. [2014b]), which is shown in Fig. 4.27, as our reference fiber-bundles. For the template/atlas phantom, we followed the same method and generated a new one with the same structure but having different geometries and shapes for fiber-bundles. Fig. 4.28 shows both the template (our generated) and the reference FiberCup data. As can be seen, additional bending, crossing and kissing structures are embedded in our template that do not exist in the reference one; this should help us to evaluate the performance of IFIR method in recognition and registration of various fiber-bundles. Some information about fiber-bundles for both reference and template is given in Table 4.1. The template phantom is then deformed using IFIR approach so that it captures muscular structure of the reference phantom.

In the explanation of IFIR technique, it was mentioned that we *primarily* are seeking an optimal *anatomical* transformation that captures the geometrical shape of the target organ. However, by having a look at the Fig. 4.27 and Fig. 4.28, it can be noted that there is no remarkable geometrical difference between the phantoms. In fact, the phantoms are being

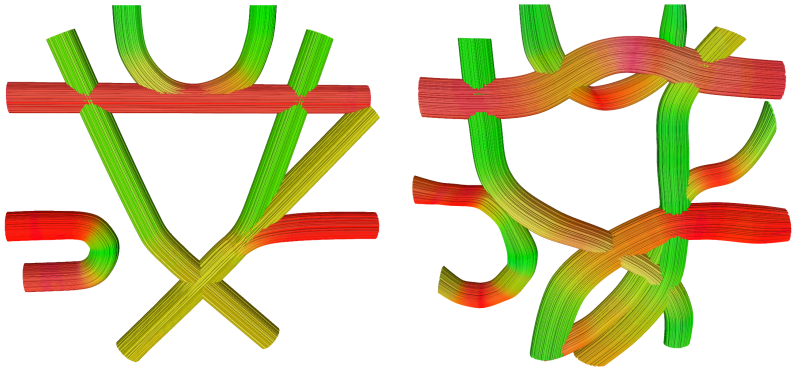

(a) Reference FiberCup (b) Template FiberCup

Figure 4.28: Recreated FiberCup phantoms: (a) reference FiberCup data (Neher et al. [2014b]) and (b) our generated template FiberCup data.

Fiber-bundles		Information			
		# of fibers	Min Length	Max Length	Mean Length
F1	Reference	1500	80.106	106.372	93.331
	Template	900	79.001	106.592	92.189
F2	Reference	1500	139.442	143.755	141.613
	Template	900	151.461	151.799	151.607
F3	Reference	1500	129	129	129
	Template	900	132.283	133.43	132.854
F4	Reference	1500	57.156	87.932	72.432
	Template	900	74.769	104.21	89.84
F5	Reference	750	111.438	119.215	115.474
	Template	900	109.67	129.945	120.081
F6	Reference	656	132.016	132.018	132.017
	Template	900	128.603	130.946	129.729
F7	Reference	750	142.109	146.565	144.251
	Template	900	143.603	143.659	143.621

Table 4.1: Information of the recreated FiberCup phantoms fiber-bundles : the number of fibers and the minimum, maximum, and mean lengths (mm).

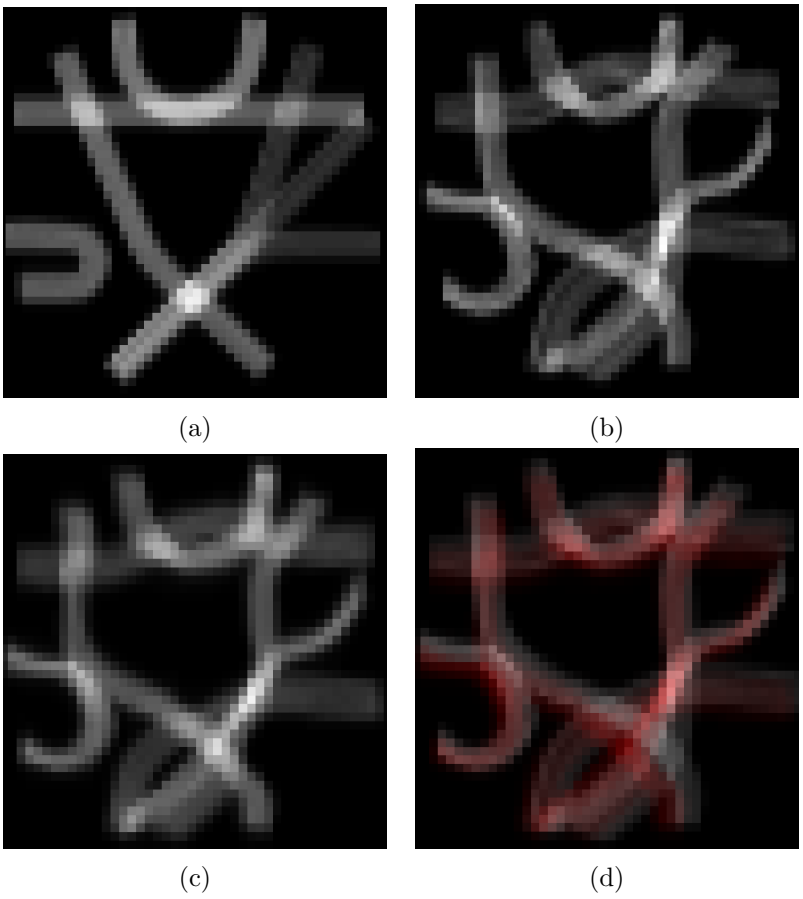

Figure 4.29: Anatomical image registration of FiberCup phantoms: (a) reference (b) template, (c) deformed-template, and (d) superimposition of template (gray) onto its deformed one (red).

used to specifically evaluate the performance of fiber-bundles recognition and registration processes (phases II and III). Therefore, we decided to perform a coarse registration of template and reference phantoms to estimate $T_{Anatomical}$. The obtained results are shown in Fig. 4.29. Template fibers are deformed using $T_{Anatomical}$ in order to bring them into the space of reference's fibers. With the aim to refine anatomical transformation, the weighted-images for both deformed-template and reference are produced (see section 4.3.2.1), as illustrated in Fig. 4.30(a-b), and then registered together using the same strategy (Fig. 4.30(c-d)). Accordingly, the obtained refined-anatomical transformation ($T_{Ref-Anat}$) is applied to the template fibers, Fig. 4.30(e-f).

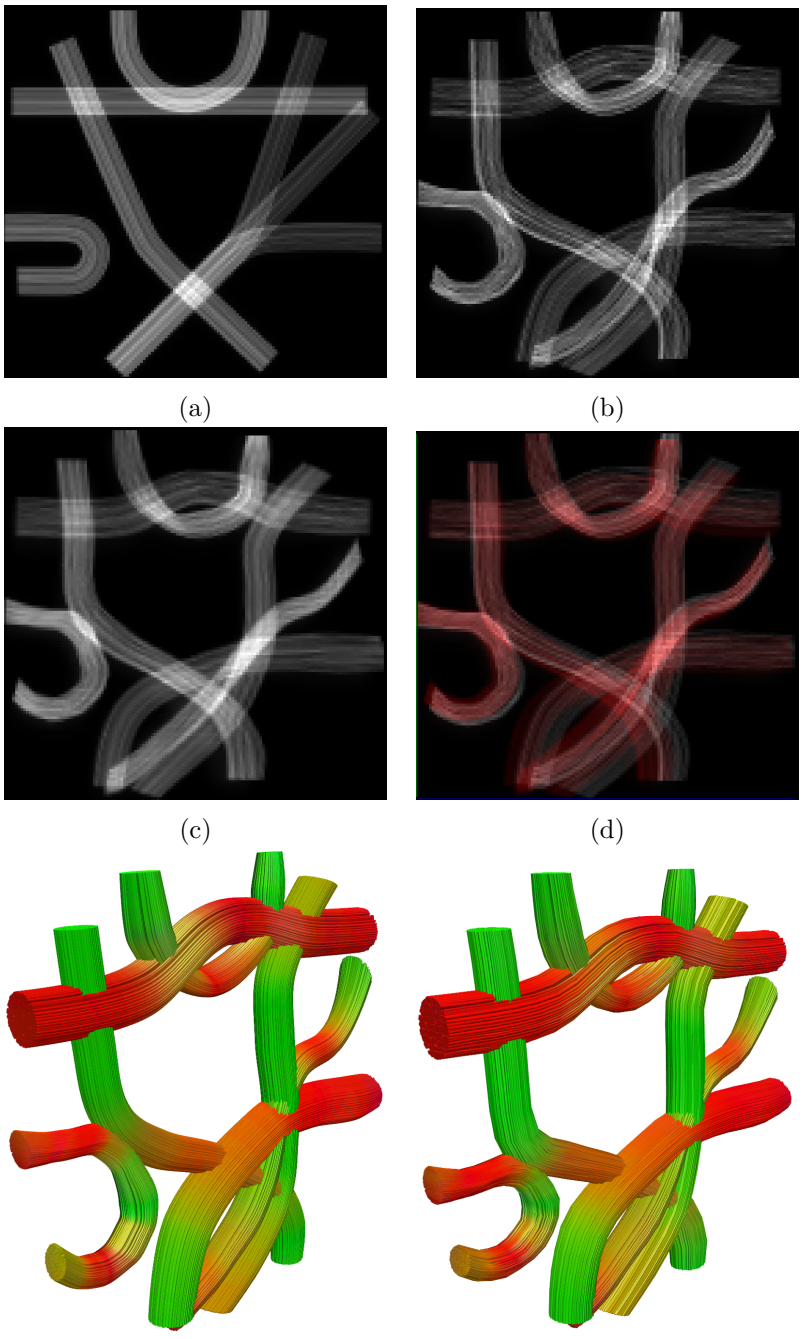

(a) (b)

(c) (d)

(e) Template FiberCup (f) Deformed-template FiberCup

Figure 4.30: Registration of FiberCup's weighted-images and fibers deformations: (a) reference's weighted-image, (b) weighted-image of deformed-template ($T_{Anatomical}$), (c) registered (b) to (a), (d) superimposition of (a) and (b), respectively in gray and red, (e) template fibers, and (f) deformed fibers using the obtained $T_{Ref-Anat}$.

After deformation of template fibers using $T_{Ref-Anat}$, we can expect that the template-deformed-fiber-bundles are the most similar to the reference's ones and they can be used to group template's fibers (see section 4.3.2.2). On this matter, all template-deformed and reference fibers are re-sampled along their trajectories using B-spline interpolation at a fix number of points ($N = 20$). Then, the minimum average direct-flip distance (MDF), equation 4.29, is chosen as the similarity measure. MDF is evaluated for each fiber of deformed template by computing its distance to the centroids of reference-fiber-bundles (Fig. 4.31). All deformed-template fibers are successfully grouped and the average MDF of them is computed with respect to all the reference-fiber-bundles, namely their centroids, and the obtained values are reported in Table 4.2. It is clear that each identified fiber-bundle has the least distance from its corresponding fiber-bundle.

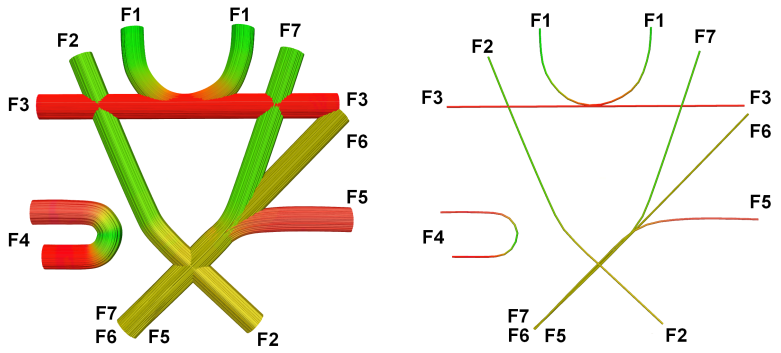

(a) (b)

Figure 4.31: Centroids of reference-fiber-bundles: (a) Reference fiber-bundles and (b) their centroids.

Finally, each pair of corresponding fiber-bundles are registered together using CPD algorithm (phase III). During the registration process, the width of the Gaussian kernel (β), the regularization weight (λ), and the max number of iterations are set to 20, 50, and 50, respectively. After registration of fiber-bundles, the average MDF is again computed for the registered-template and reference fiber-bundles, and reported in Table 4.3. Comparing to Table 4.2, the distance between each pair of corresponding fiber-bundles is evidently decreased, which means that the similarity between them is increased. Also, the template, the reference, and the registered-template are illustrated in Fig. 4.32.

I-Fiber-bundles	Reference fiber-bundles						
	F1	F2	F3	F4	F5	F6	F7
IF1	0.4971	4.9262	1.9292	7.3034	6.9753	6.0331	5.0991
IF2	5.6352	0.8118	4.6793	3.8203	5.4306	5.2369	4.7599
IF3	2.1346	4.7045	0.5927	7.0051	6.1511	5.0940	4.7410
IF4	7.7691	4.2733	7.0179	0.3656	6.2112	6.4813	6.3768
IF5	6.9924	4.9140	5.6236	5.5369	0.7927	1.7952	2.6297
IF6	6.5201	4.6509	5.1977	6.0792	1.0810	0.6658	1.4304
IF7	5.4705	3.9287	4.9468	6.5156	2.6920	1.6351	0.8487

Table 4.2: The average MDF of each identified fiber-bundle in the template data (IF1 to IF7) is computed with respect to all the reference-fiber-bundles (F1 to F7), namely their centroids. The least-distances of identified fiber-bundles are colored in blue.

R-Fiber-bundles	Reference fiber-bundles						
	F1	F2	F3	F4	F5	F6	F7
RF1	0.2857	5.3108	2.0506	7.6660	7.3215	6.3359	5.3688
RF2	5.3276	0.3146	4.4964	4.2274	5.1472	4.8300	4.3130
RF3	2.0607	4.4486	0.3169	6.9268	5.9637	4.8927	4.5877
RF4	7.6301	4.2308	6.9084	0.2612	6.0975	6.3793	6.2866
RF5	7.3171	5.1377	5.9792	6.1588	0.3500	1.4060	2.3384
RF6	6.2031	4.8140	4.8075	6.5758	1.5879	0.4556	1.1140
RF7	5.1085	4.3469	4.3691	6.5886	2.7072	1.5264	0.6107

Table 4.3: The average MDF of each registered fiber-bundle in the template data (RF1 to RF7) is computed with respect to all the reference-fiber-bundles (F1 to F7), namely their centroids. The least-distances of identified fiber-bundles are colored in blue.

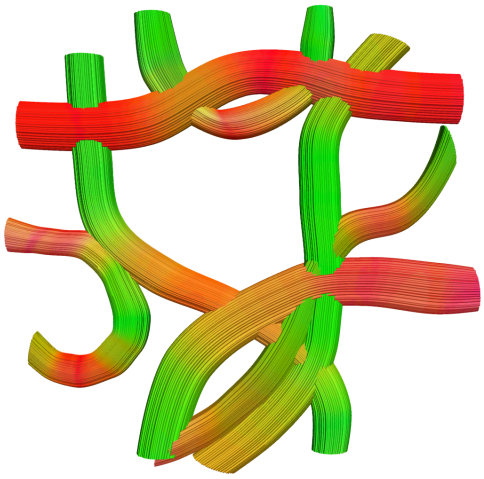

(a) Template

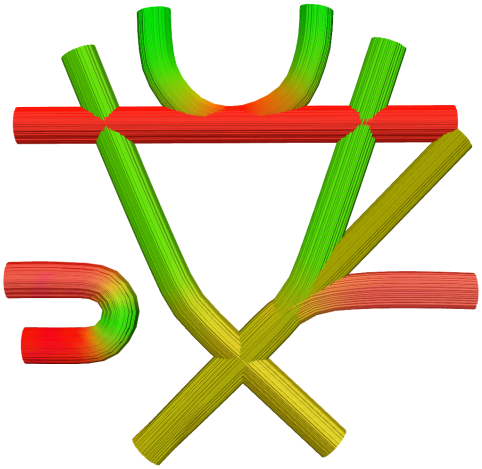

(b) Reference

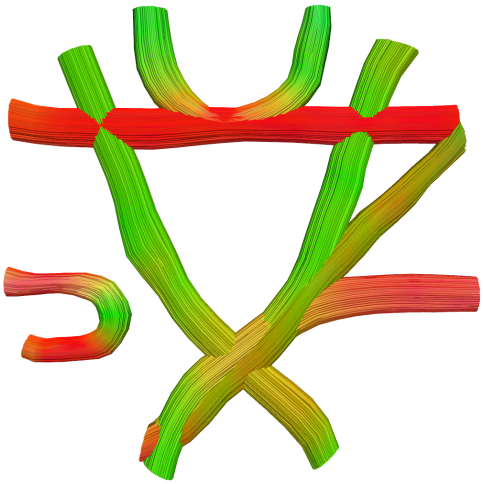

(c) Registered-Template

Figure 4.32: Result of IFIR method for FiberCup data.

4.4.2 Tongue DTI imaging

To simulate lingual deformations during swallowing, masticating and speaking, it is necessary to design a tongue FE model considering muscle fibers that can be extracted by DTI tractography. Fig.4.33 shows a schematic representation of principle fiber-bundles and also two fibers paths that are extracted by tracking algorithms. However, it is worth noting that the DTI-derived fibers might be noisy on account of tractography and DTI imaging limitations, e.g., low resolution and crossing fibers issues. Therefore, the analysis of the complete tracks (that may contain spurious bundles) can be extremely complicated and it needs manual intervention. Herein, we are going to investigate how IFIR method can be used for the tongue-DTI application, under the assumption that the fiber-bundles associated with the main tongue muscles are previously detected and identified for an atlas data on the basis of classical anatomical knowledge.

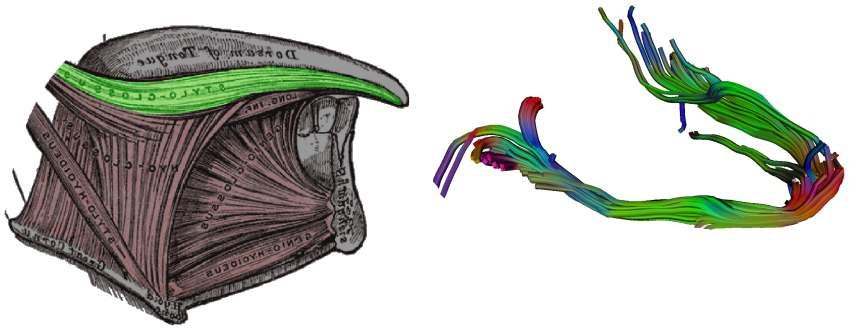

(a) Styloglossus fibers

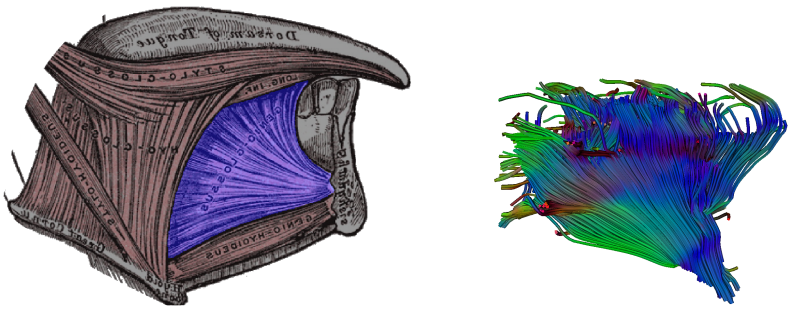

(b) Genioglossus fibers

Figure 4.33: DTI tractography of the human tongue: (a) Styglossus fibers and (b) Genioglossus fibers.

4.4.2.1 Image acquisition and preprocessing

MRI DTI data was acquired at 3T for two subjects in a rest position: (1) the atlas/template with an in-plan resolution of 1.52 mm, a slice thickness of 2 mm, and a b-value of 750 $seconds/mm^2$, and (2) the reference/subject with an in-plan resolution of 1.74 mm, a slice thickness of 2 mm, and a b-value of 1000 $seconds/mm^2$. DTI weighting gradients were applied in 32 directions for both acquisitions.

Preprocessing of DTI data consists of atlas' tongue mask generation and correction for eddy current distortion that is caused by diffusion-sensitizing and spatial encoding gradients. The level of distortions (i.e., the strength and appearance) depends on the diffusion-sensitizing gradients directions. Practically, these distortions result in misalignment errors between the images (shear, scale, and shift). Therefore, affine transformations are used to correct them and to compensate for small subject movements. Also, the region of interest (ROI) was previously generated by doing the segmentation in a non-diffusion MR image for the atlas' data. In this scheme, to warp the binary mask to the diffusion space, the participant's MR image is linearly co-registered to the image with a b-value of 0 seconds/mm^2. The obtained binary image is used later to mask tensor images.

To extract the main tongue muscle fibers, a single tensor model is first fitted for each voxel of the preprocessed corrected diffusion-weighted MR data in order to calculate diffusion maps. Then, to reconstruct tongue fiber tracks, a deterministic tractography is performed[4] using the interpolated streamline algorithm with fixed step-length of 0.5 mm which follows the direction of the interpolated principle eigenvector (Conturo et al. [1999]; Basser et al. [2000]). Fiber tracts are launched from every voxel in the tongue and end up entering a voxel if one of the following circumstances is present: (1) voxel-to-voxel deflection angle would be larger than 35°, or (2) streamline exceeds the participant's tongue mask.

[4]Probabilistic methods were also implemented; however, because of the existence of noises and distortions, better results were obtained via the deterministic methods.

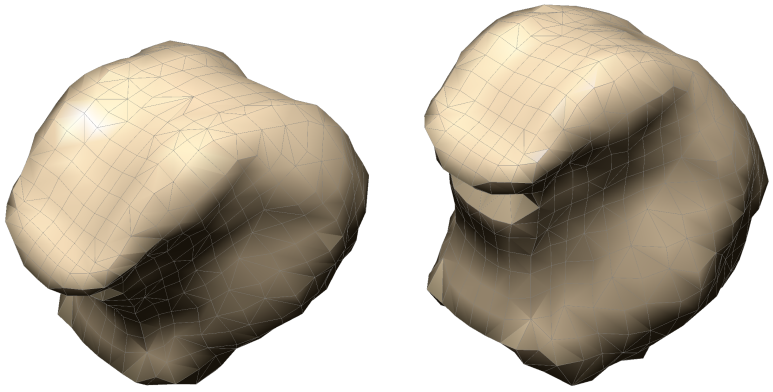

(a) (b)

Figure 4.34: Tongue FE meshes: (a) Atlas mesh and (b) subject-specific mesh.

4.4.2.2 Phase I: generation of subject-specific tongue FE mesh

Anatomical guidance images, that were acquired for DTI imaging, are used to generate subject-specific tongue mesh. As the atlas tongue FE mesh was designed based on the geometrical shape of the tongue, subject's anatomical mesh is designed using the process explained in chapter 3. Atlas and subject-specific meshes are illustrated in Fig. 4.34. Also, the atlas tongue mask is deformed by employing the obtained anatomical transformation so that the subject's ROI is defined and its tensor images are masked for fiber tractography process.

4.4.2.3 Phase II: Detection of subject's fiber-bundles

Under the assumption that atlas' fibers are extracted and grouped into a specific number of fiber-bundles in advance, this section shows how subject's fiber-bundles could be determined automatically based on the atlas ones. As explained in section 4.3.2, the refinement of the anatomical transformation is the primary step to the identification of subject's fiber-bundles. This is done by registering the atlas' and subject's weighted images (see section 4.3.2.1), namely the images that are created by combining the anatomical and track density images. Whereas it is very difficult to map atlas' fibers to the subject's ones using only fibers' density information, it is important to note that the high dense muscular structures within the soft tissues can be considered as natural landmarks for the image registration process. Some

weighted-images are therefore created for tongue images of different modalities and shown in Fig. 4.35, the subject, and Fig. 4.36, our atlas.

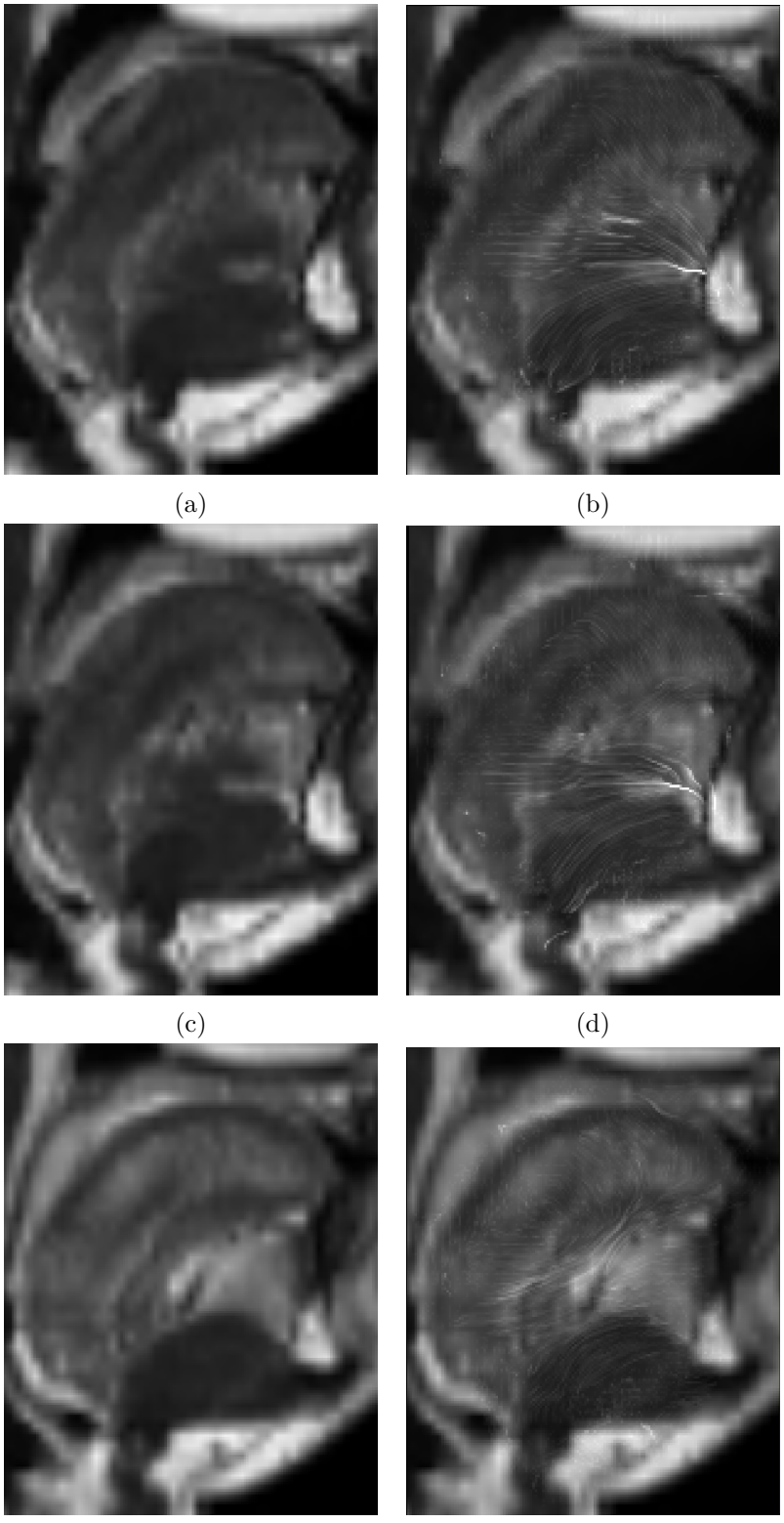

(a) (b) (c) (d) (e) (f)

Figure 4.35: An example of tongue weighted-images (subject): (a), (c), and (e) are anatomical images, from medial to lateral slices, and (b), (d), and (f) are the corresponding weighted images.

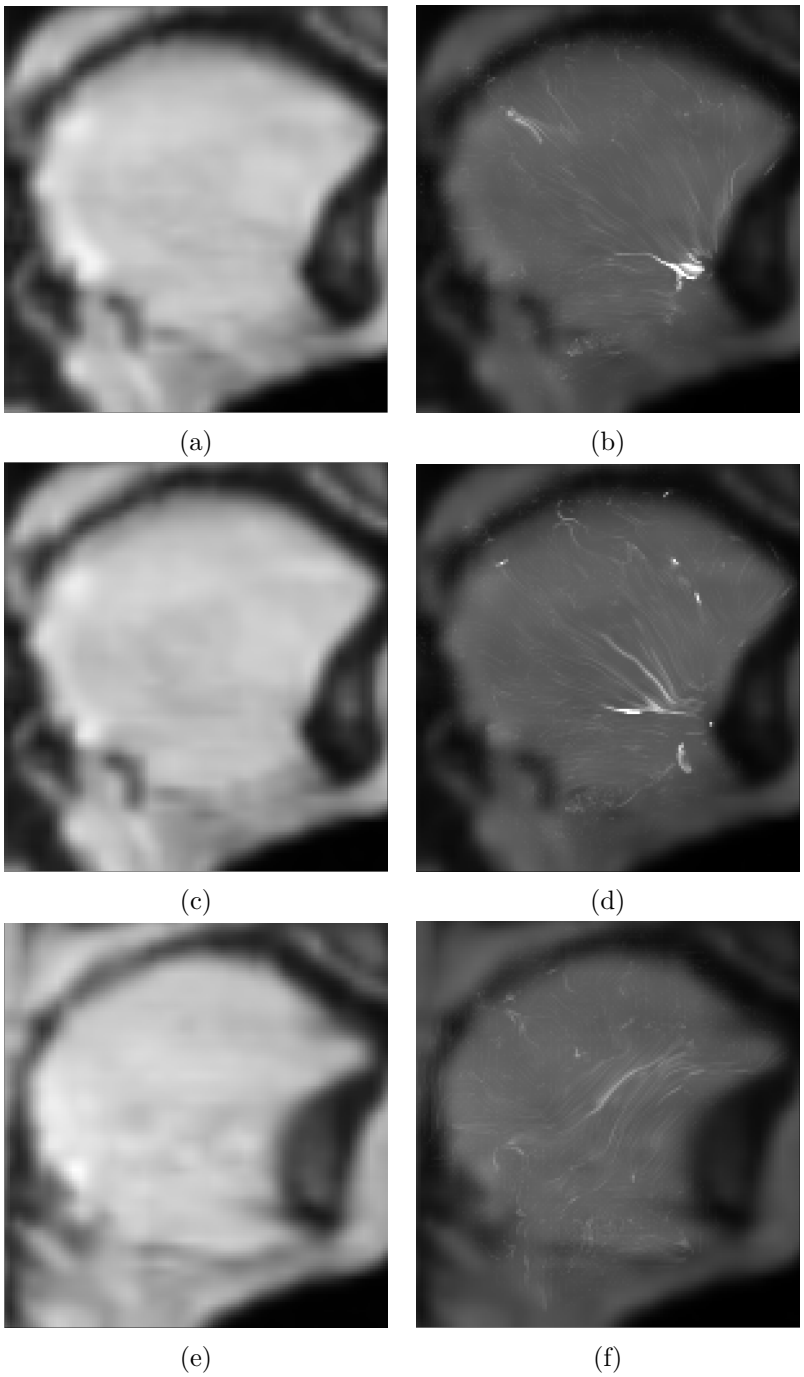

(a) (b)

(c) (d)

(e) (f)

Figure 4.36: An example of tongue weighted-images (atlas): (a), (c), and (e) are anatomical images, from medial to lateral slices, and (b), (d), and (f) are the corresponding created weighted images.

Looking at the images shown in Fig. 4.35 and Fig. 4.36 it seems that even though a good visualization is provided for embedded fibers, only the regions having high density of passing-fibers could improve anatomical registration. Therefore, the registration of tongue-weighted images is employed as a procedure to refine the anatomical transformation ($T_{Anatomical}$). To do this, the atlas' anatomical image and its fibers are first deformed using $T_{Anatomical}$; weighted-images are then created and registered using the same process as in phase I. Finally, the anatomical transformation is refined according to Eq. 4.25. In Fig. 4.37, atlas' fibers and their deformations, by $T_{Anatomical}$ and $T_{Ref-Anat}$, are respectively superimposed on the atlas' and subject's anatomical images. A section of deformed fibers is zoomed in and illustrated in Fig. 4.38. As expected, fibers' deformation is refined by regions having high density of fibers, such as the region identified by a circle. More sections from different slices are shown in Fig. 4.39.

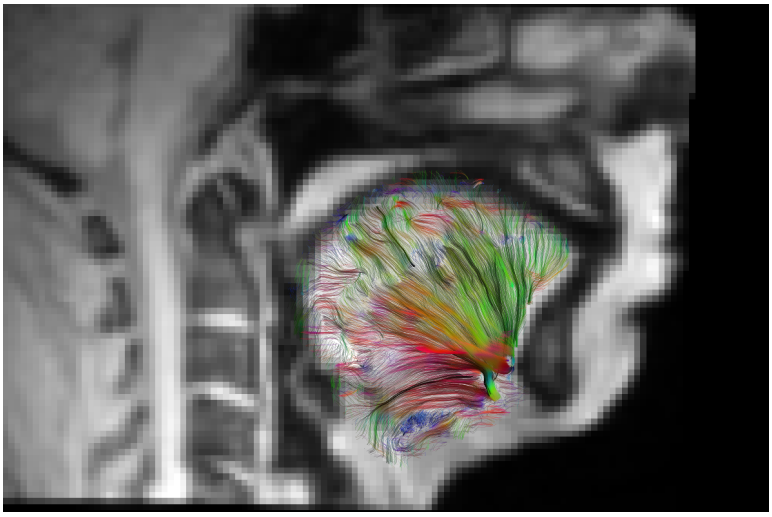

(a)

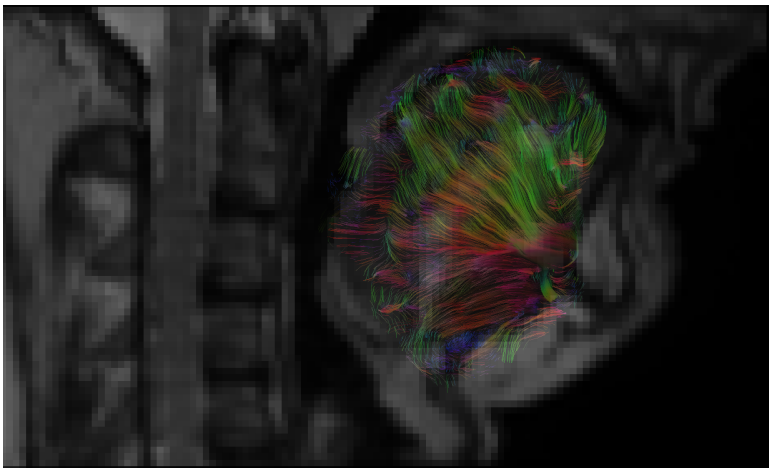

(b)

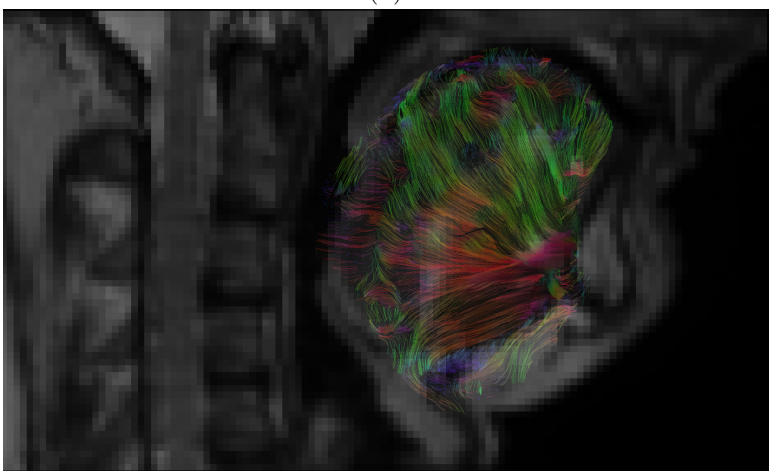

(c)

Figure 4.37: Deformed atlas tongue fibers: (a) atlas' fibers superimposed on its anatomical image, (b) deformed atlas fibers, by $T_{Anatomical}$, superimposed on subject's anatomical image, (c) deformed atlas fibers, by $T_{Ref-Anat}$, superimposed on subject's anatomical image.

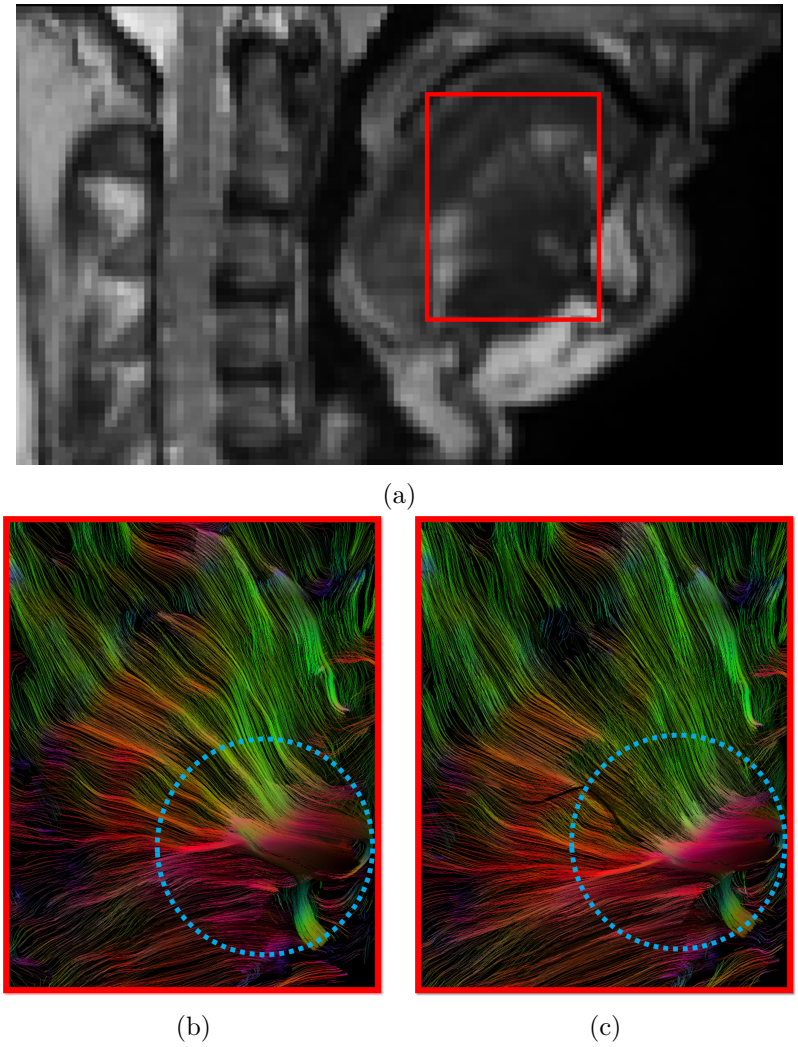

(a)

(b) (c)

Figure 4.38: Enlargement of deformed atlas tongue fibers: (a) subject's anatomical image and a selected bounding box, (b) deformed atlas fibers by $T_{Anatomical}$ within the box, (c) deformed atlas fibers by $T_{Ref-Anat}$ within the box, which has more similarity to the subject's ones.

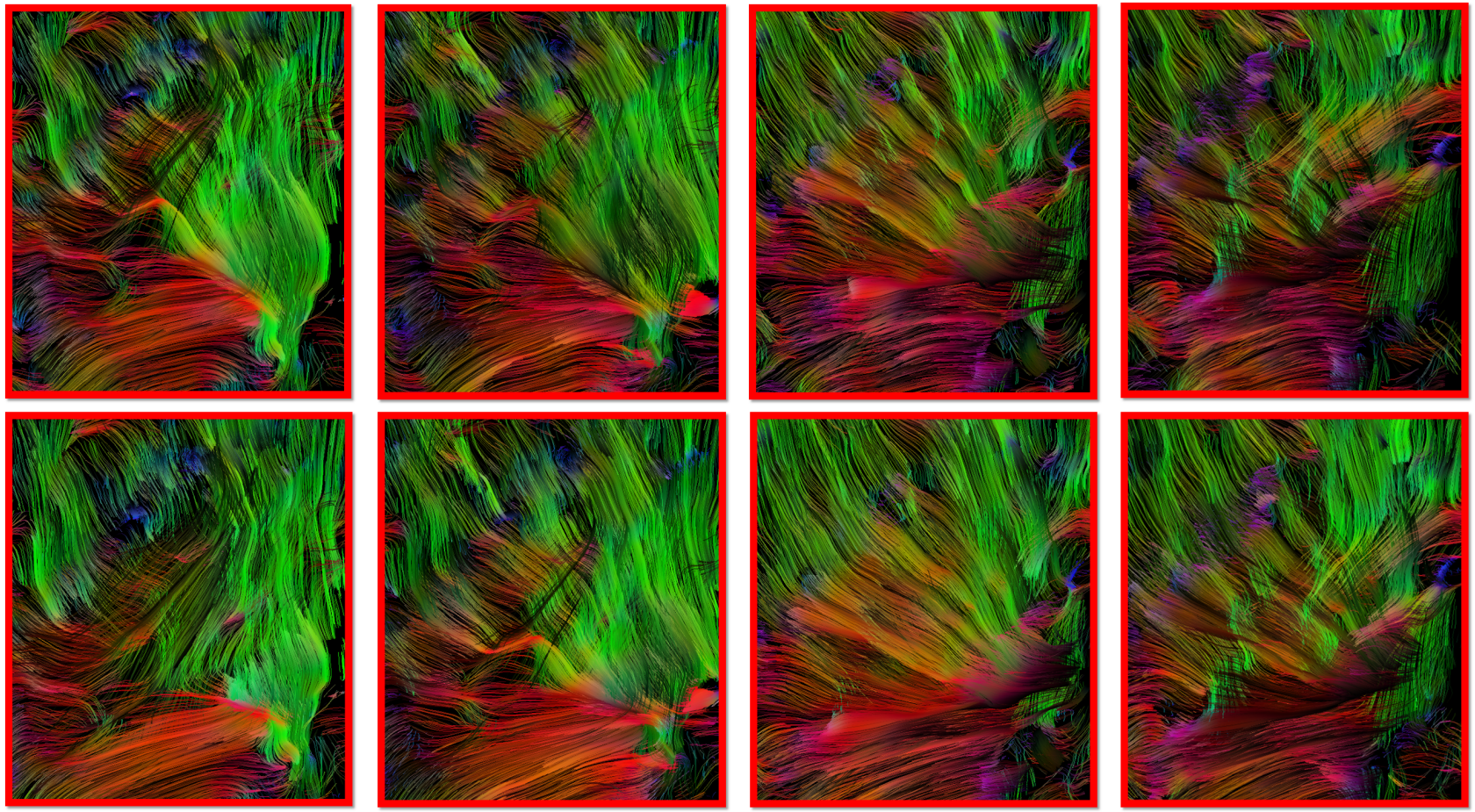

Figure 4.39: Anatomically deformed atlas tongue fibers; the upper row represents the fibers deformed by $T_{Anatomical}$, while the other contains fibers deformed by $T_{Ref-Anat}$, and mid to lateral slices are shown in each column (from left to right).

After deforming the atlas fibers using $T_{Ref-Anat}$, it is the time to determine corresponding fiber-bundles in atlas and subject data through the method explained in section 4.3.2.2. In order to show the generality of our technique, five fiber-bundles are selected within/surrounding the atlas tongue. These fiber-bundles are illustrated in Figs. 4.40, 4.41, and 4.42. The corresponding subject's fiber-bundles are determined as shown in Figs. 4.43, 4.44, and 4.45.

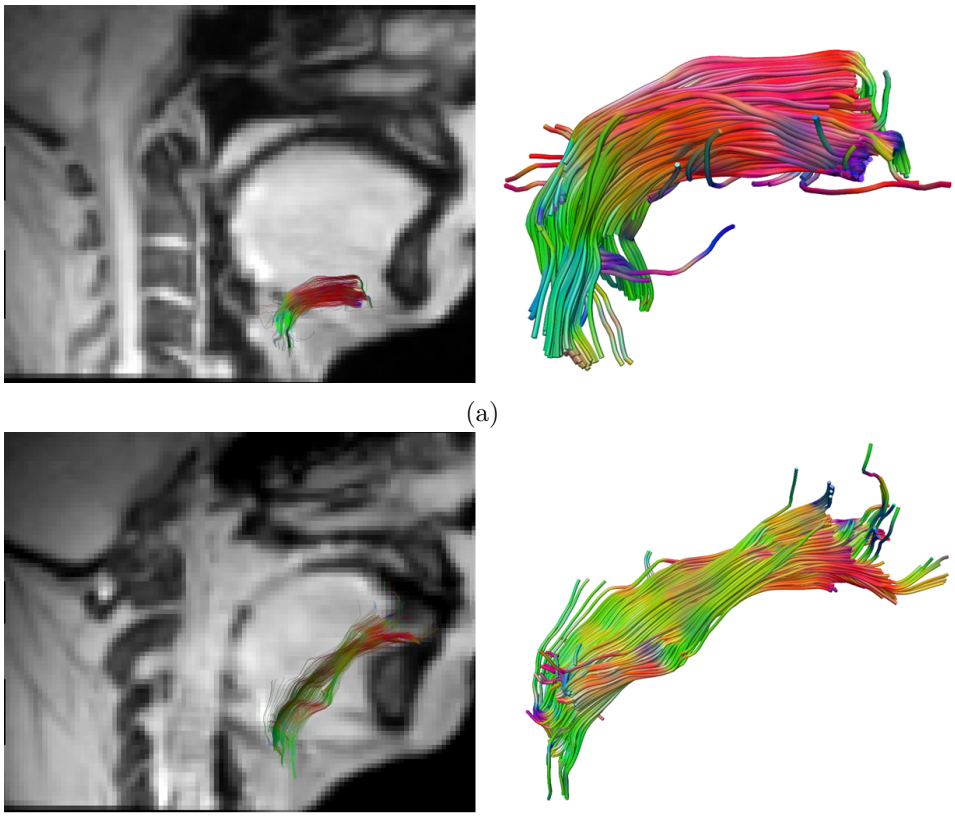

(a)

(b)

Figure 4.40: Atlas tongue fiber-bundles (1-2).

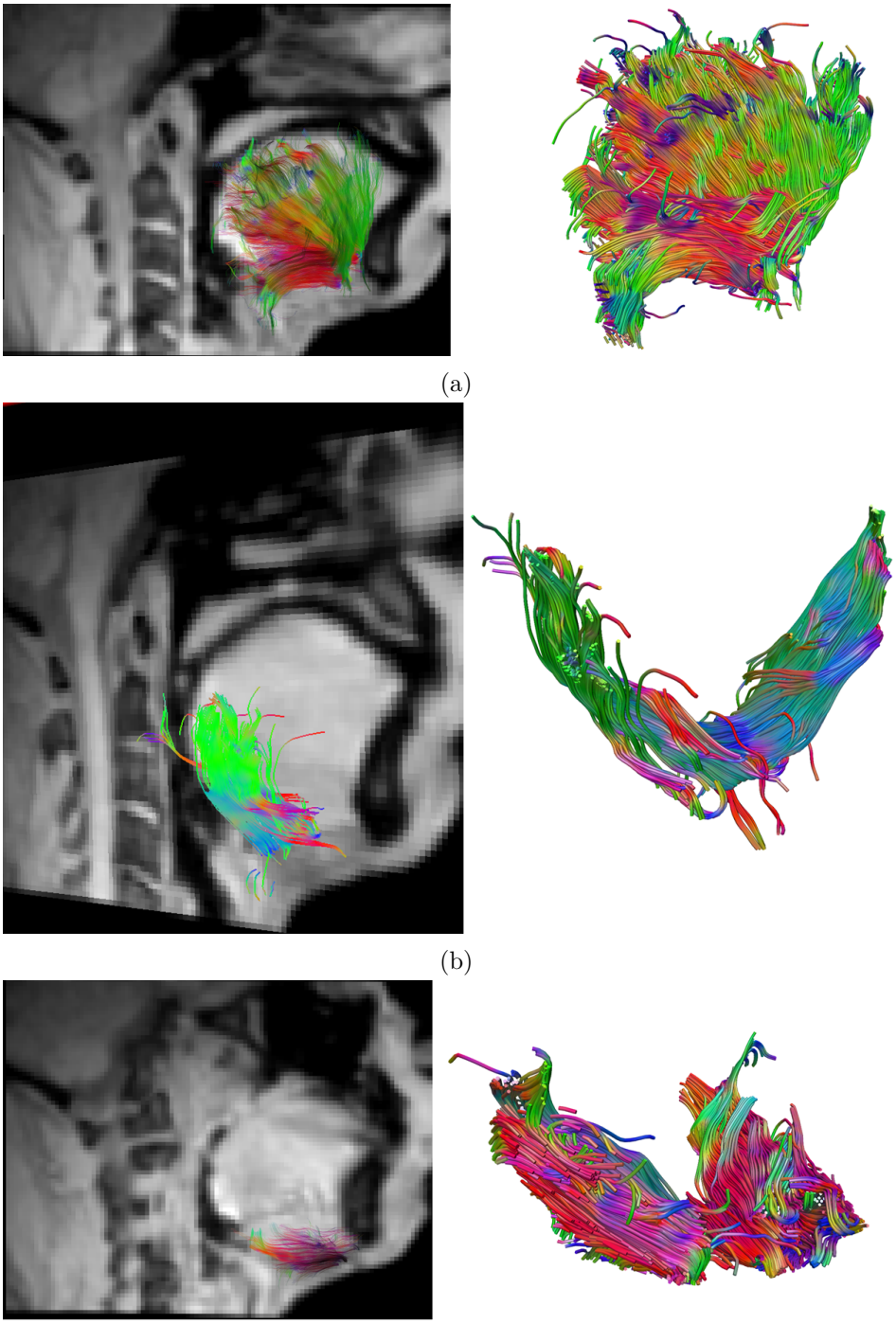

(a)

(b)

(c)

Figure 4.41: Atlas tongue fiber-bundles (3-5).

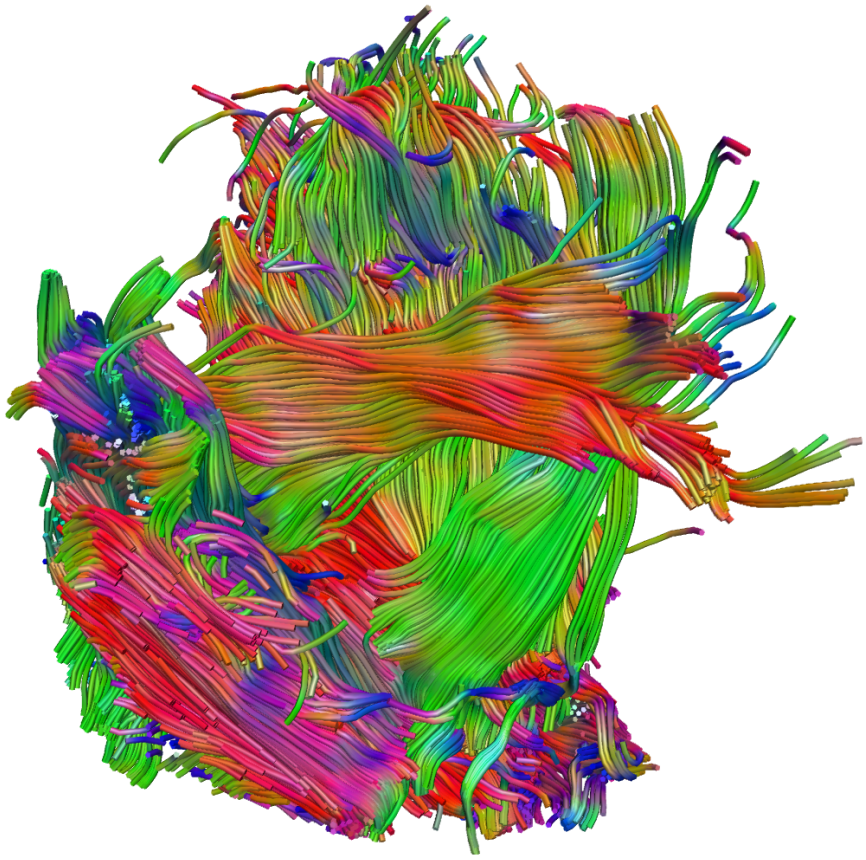

Figure 4.42: All five selected fiber-bundles in atlas data.

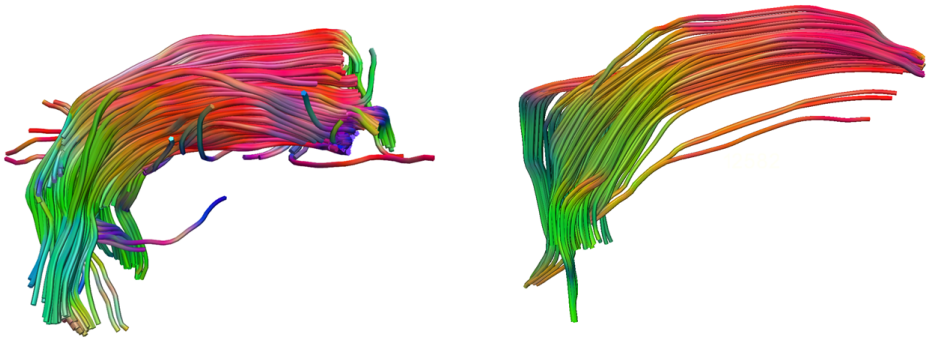

(a)

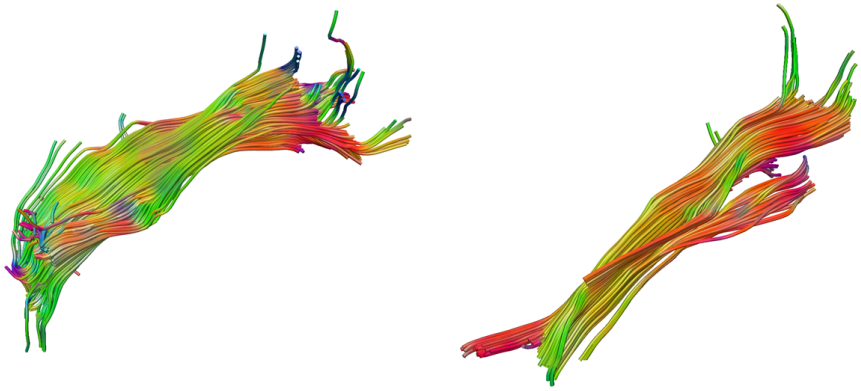

(b)

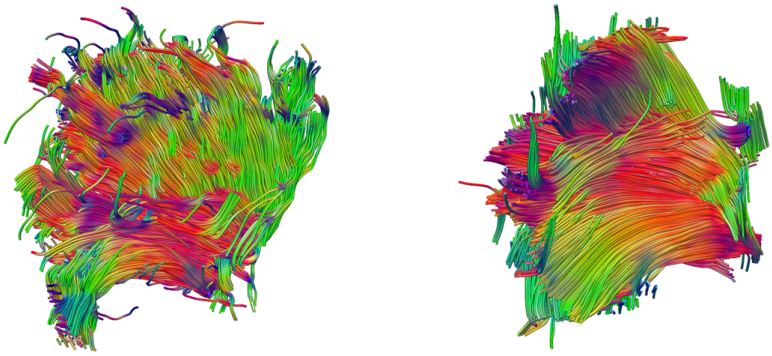

(c)

Figure 4.43: Atlas and subject's identified tongue fiber-bundles (1-3).

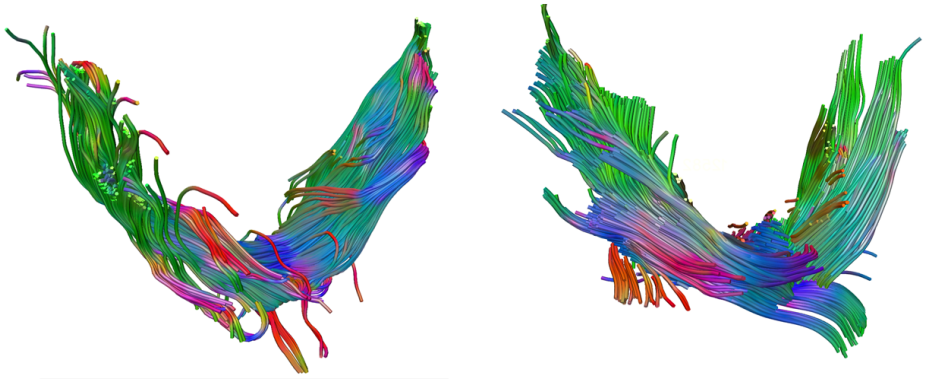

(a)

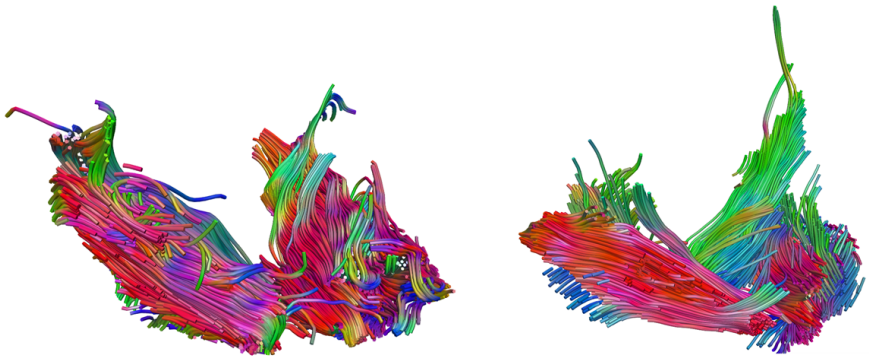

(b)

Figure 4.44: Atlas and subject's identified tongue fiber-bundles (4-5).

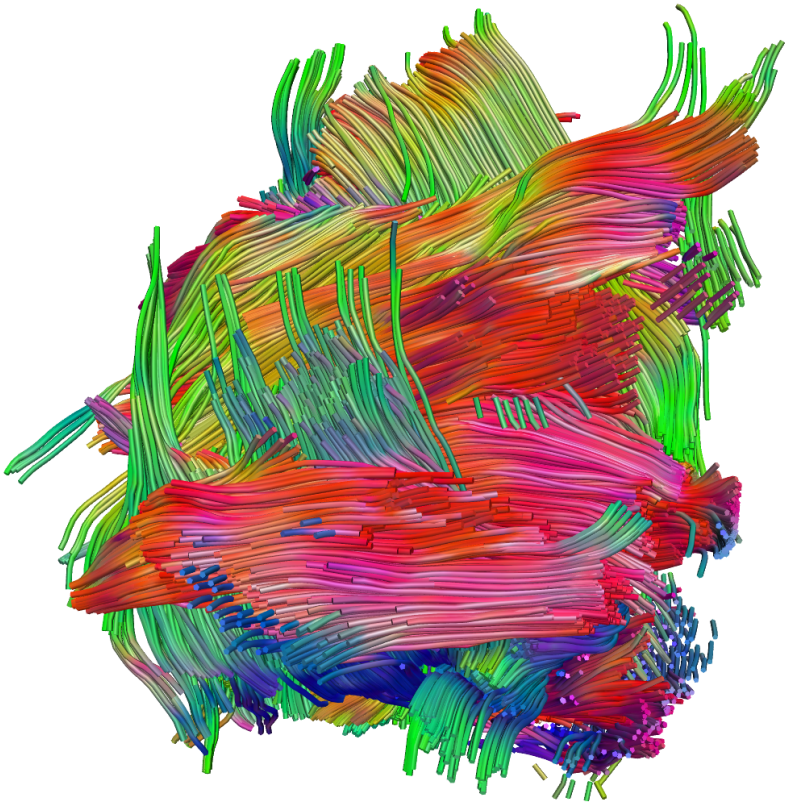

(a)

Figure 4.45: All five identified subject's fiber-bundles.

4.4.2.4 Phase III: Registration of atlas and subject's fiber-bundles

The atlas-deformed fiber-bundles, using $T_{Ref-Anat}$, and subject's detected fiber-bundles are registered non rigidly using the method explained in section 4.3.3. Atlas' fiber-bundles and their deformed ones, through phase III, are shown in Figs. 4.46 and 4.47. Looking at the resulting fiber-bundles, it is clear that the IFIR technique enables comparison of fiber-bundles ***on the basis of their inherent structures***. In another word, the inherent relationships between (1) the ***points*** that form a ***fiber***, and (2) the ***fibers*** that form a ***fiber-bundle*** is still preserved after applying deformations. This fact becomes very important and crucial as the anatomical transformation cannot manage to capture the distribution of subject's fiber-bundle and a further alignment of the fibers is necessary.

In short, as a principle statement, we can say that

> "***Anatomical transformations of muscular structures can approximately deform fibers distributed according to the geometrical shapes; however, for distributions not following the underlying geometries it is crucial to embed the orientation information within the registration process which is attainable by alignment on the level of fibers or diffusion tensors.***"

For a better understanding, let's come back to our selected fiber-bundles, where the forth and fifth fiber-bundles, which are respectively a section of tongue and neck muscles, support the tongue by providing a ***muscular housing***. This so called ***compartment***, containing these two fiber-bundles, is formed according to the shape of the tongue so that the tongue can be inserted into the housing. Therefore, any anatomical transformation extracted from geometrical shape of the tongue will accordingly affect the shape of the compartment, and subsequently its embedded fiber-bundles. On the other side, we have fiber-bundles like the first three ones having more complicated distributions of fibers' paths that may not have conformity with the shape. For an overall overview, the reader is refereed to atlas fiber-bundles, Fig. 4.42, subject's fiber-bundles, Fig. 4.45, and atlas-deformed fiber-bundles, Fig. 4.48. In addition, track density images of the fiber-bundles are created and the rendered volumes are shown in Fig. 4.49. We can see that the inner

muscle anatomy with the tongue is much better accounted for after the final transformation provided by Phase III.

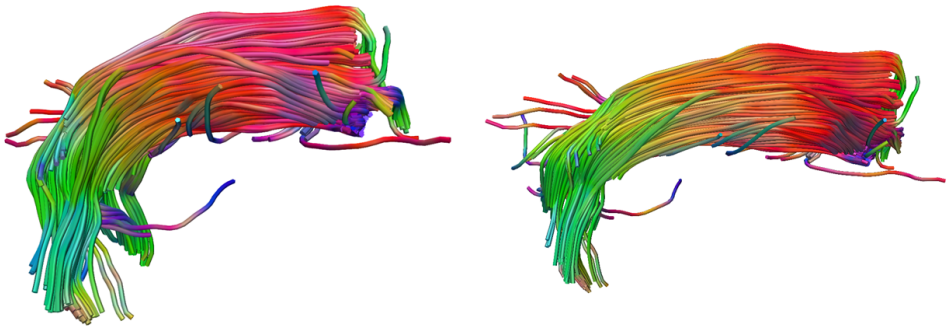

(a)

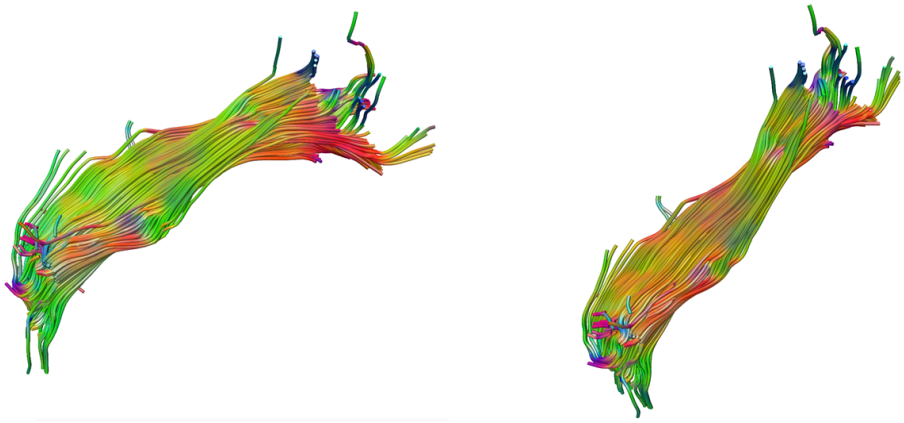

(b)

Figure 4.46: atlas fiber-bundles and their deformed ones (1-2).

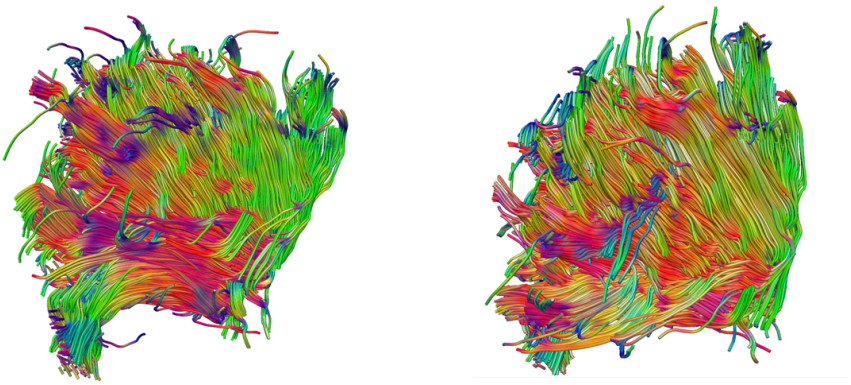

(a)

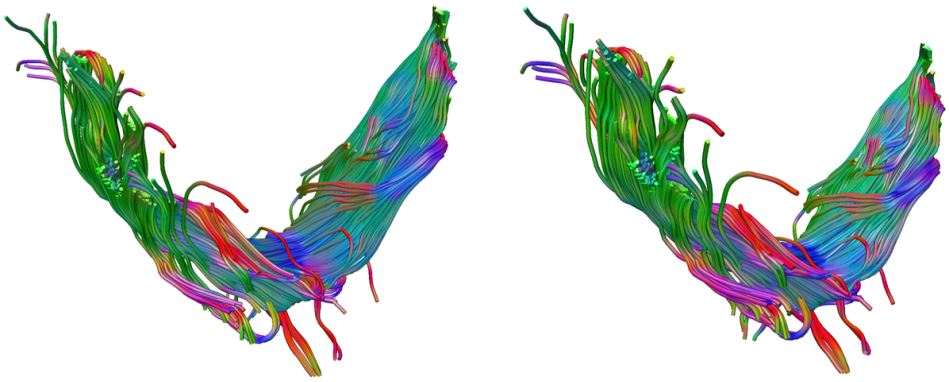

(b)

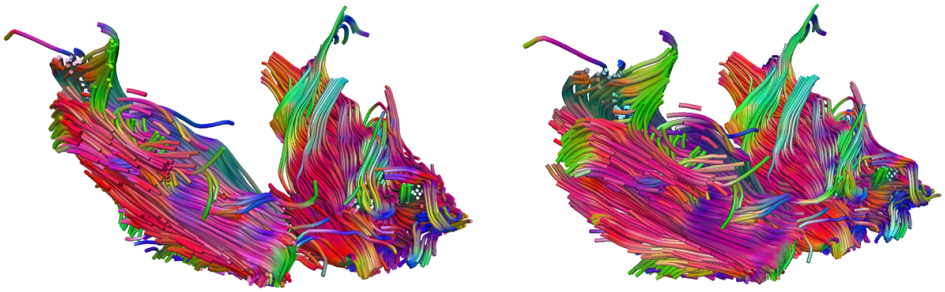

(c)

Figure 4.47: atlas fiber-bundles and their deformed ones (3-5).

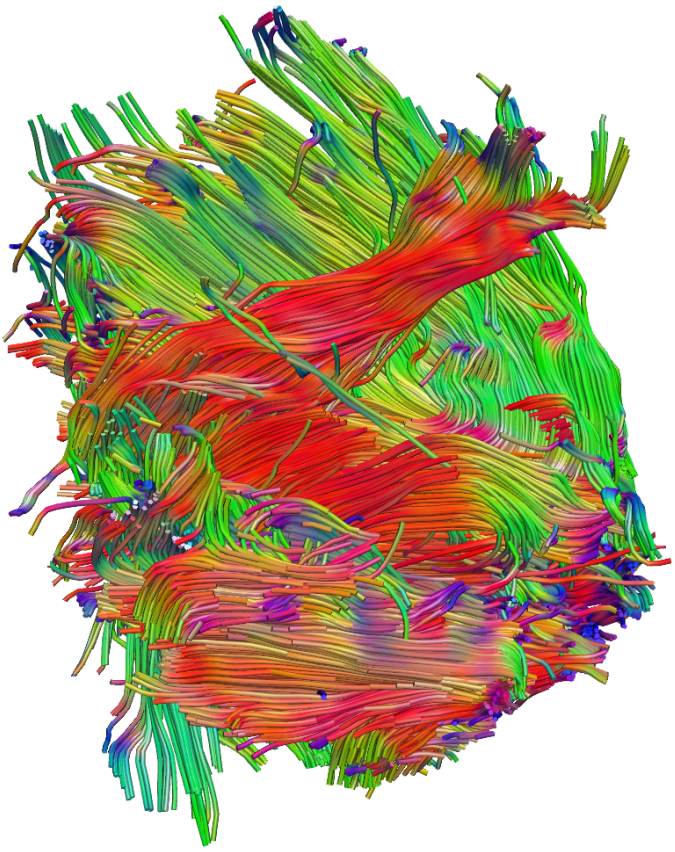

(a)

Figure 4.48: All atlas-deformed fiber-bundles.

Figure 4.49: Track density images of the fiber-bundles. From left to right: anatomically atlas deformed fiber-bundles ($T_{Ref-Anat}$), subject's fiber-bundles, atlas deformed fiber-bundles, based on phase III.

4.5 Discussion

In this chapter, a novel atlas-assisted approach for recognition and registration of fiber-bundles is presented and evaluated. The method exploits information from both the anatomical images and fibers. Contrary to the DT-MR images registration methods that need ***tensors reorientation*** within or after the transformation estimation, our IFIR technique avoids this issue and directly aligns fiber-bundles. The IFIR method is evaluated using a phantom and a human tongue data. In the following, we are going to discuss the proposed scheme methodology and its algorithm, more specifically based on the obtained results.

IFIR is basically a bundle-to-bundle registration technique, in which corresponding fiber-bundles are selected based on a similarity measure. In the FiberCup and Tongue experiments, it is assumed that for each atlas fiber-bundle, there exists a corresponding one in the subject data with the highest similarity (Algorithm 1). However, in the case of ***distorted***-DTI imaging, it is expected that some subject's fiber-bundles are not reconstructed through the fiber tracking process. This in turn means that there are some fiber-bundles in the atlas data that do not exist in the subject data. Therefore, utilizing IFIR based on the Algorithm 1 (IFIR-1) leads to a miss-recognition of corresponding fiber-bundles. Therefore, in such cases, IFIR based on the Algorithm 2 (IFIR-2) must be used (see section 4.3.2.2), and accordingly for the atlas fiber-bundles that do not have any corresponding in order to fit it, the transformation could be computed using interpolation techniques like thin-plate spline (TPS) (Bookstein [1988]). In this way, a complete set of fiber-bundles can be generated for the subject by deformation of atlas data, notwithstanding the ***distorted***-DTI imaging.

The IFIR-2 becomes very interesting when the ultimate goal of the DTI-registration is ***Spatial Normalization***. To clarify, let us imagine a study in which a set of DTI data are acquired and a DTI image registration technique (e.g., Park et al. [2003]) is being used for generation of an atlas that represents the statistical distribution of the whole data set. In the presence of distortions that may exist in some of DTIs, the generated atlas would be incomparably poorer or generally be biased towards the low quality of the

DTIs. In this respect, IFIR-2 could be used to put aside the distorted fiber-bundles based on their similarity degree and then implement normalization on the basis of ***non-distorted*** fiber-bundles.

By reviewing the obtained results for the tongue experiment (section 4.4.2) and considering the fact that segmentation of the tongue has always been a tremendous and challenging task since it is an extremely flexible organ that is in contact with many other structures in the oral cavity, namely cheeks, pharyngeal walls, palate, and lips, it brings to the mind that IFIR technique can be taken into account as an atlas-assisted DTI-based segmentation approach; and more over, it can be used for inter/intra-subject variability analysis of fiber-bundles. For more clarification, let's go over the anatomy of lingual musculature, as shown in Fig. 4.50.

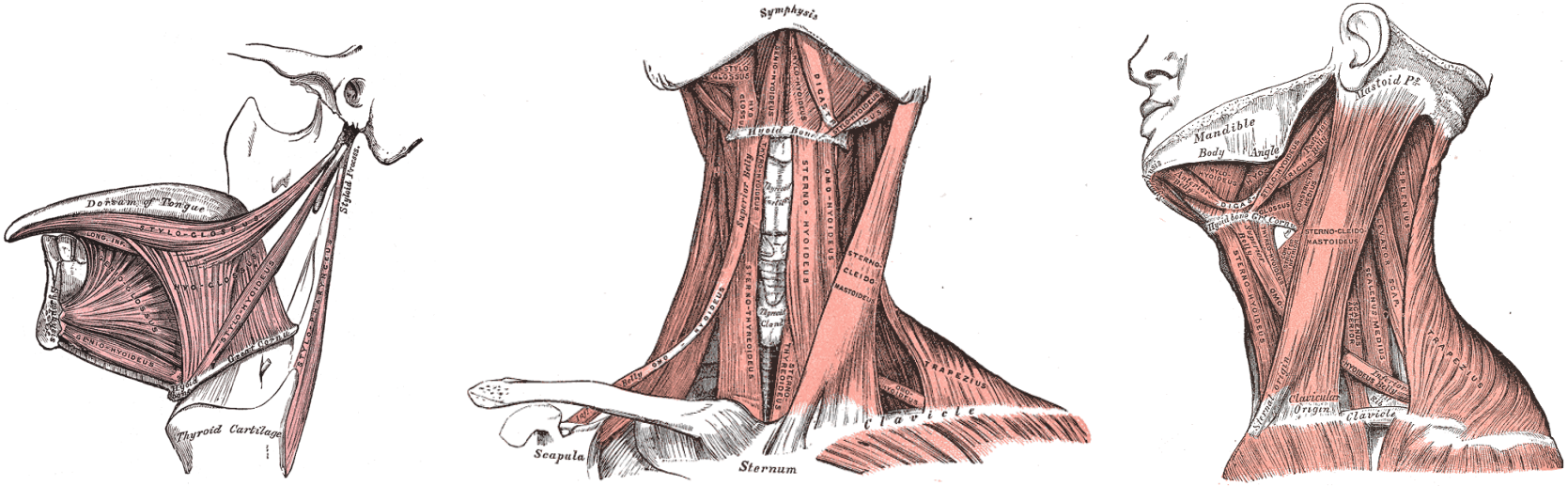

(a) (b) (c)

Figure 4.50: Anatomical drawings of lingual musculature derived from Gray's Anatomy (Williams et al. [1980]): (a) mid-sagittal plane of tongue muscle fibers (extrinsic), (b) muscles of the neck and the floor of the oral cavity of the mouth seen from the front, (c) lateral view of (b).

Although the atlas fiber-bundles in section 4.4.2 are not selected by interpretation of the lingual and jaw musculature, there is a good correspondence between them and the anatomical structures illustrated in Fig. 4.4.2. To investigate this correspondence, some fiber muscles are highlighted in Fig. 4.51 and explained below

- **Geniohyoid** (Red-colored): a narrow tongue muscle that originates from inferior mental spine of the mandible and runs backward and slightly downward to be inserted on to the anterior and upper border of the body of the hyoid bone in the throat. It is positioned superior to the medial border of the mylohyoid muscle.

- **Hyoglossus** (Blue-colored): a tongue muscle that arises from the hyoid bone on the superior border of the greater cornu and approximately passes upward to insert on the side of the tongue, between the the inferior longitudinal muscle of the tongue and styloglossus.

- **Genioglossus** (Orange-colored): the main tongue muscle having the shape of a fan located in the central part of the tongue along the left-right direction that forms the majority of tongue's body. It originates from the upper part of the mental spine of the mandible and inserts within the tongue at around $1cm$ below its surface and on the upper part of the body of the hyoid bone.

- **Mylohyoid** (Green-colored): a paired muscle of the neck that forms the floor of the oral cavity of the mouth and connects the mandible to the hyoid bone.

- **Digastric** (Yellow-colored): a curved formed muscle of the neck that lies below the jaw. This muscle is composed of two muscular sections called *bellies*, anterior and posterior, joined by an intermediate round tendon. The anterior belly extends from the lower section of the mandible while the posterior belly originates from the mastoid notch of the temporal bone. These two bellies are attaches to the hyoid bone by a fibrous membrane.

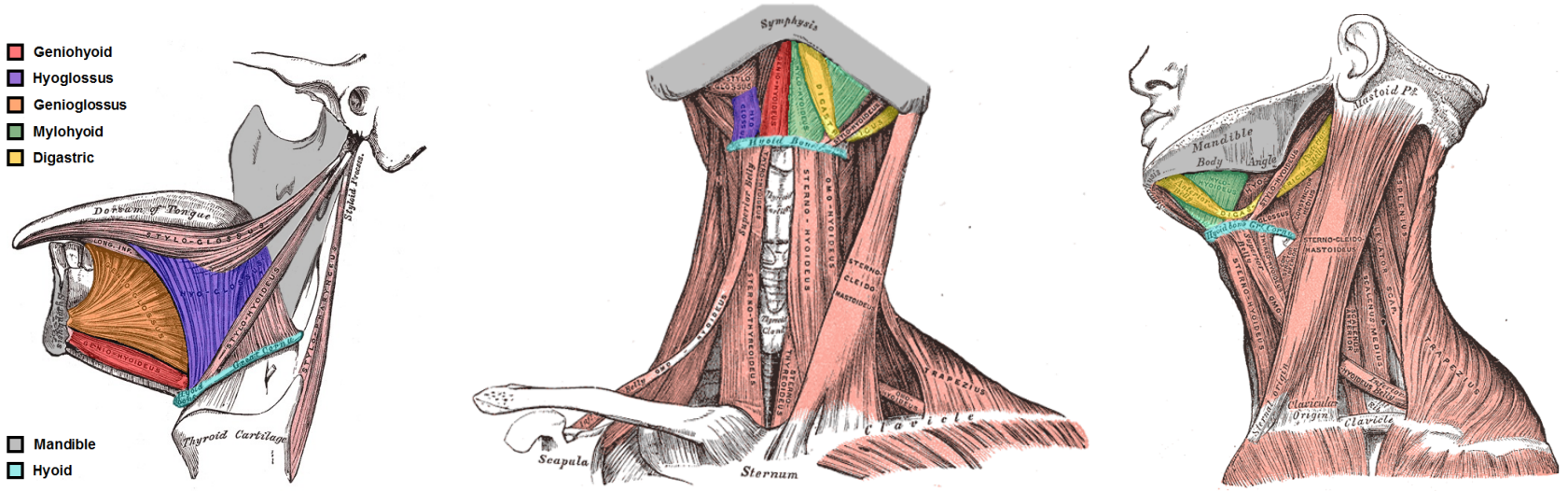

(a) (b) (c)

Figure 4.51: Anatomy of selected fiber-blondes for the human tongue experiment: (a) Geniohyoid, Genioglossus, and Hyoglossus, (b) Geniohyoid, Mylohyoid, and Digastric (c) Mylohyoid, and Digastric.

As can be seen, there is a good analogy between the hightailed-drawing muscles (Fig. 4.51) and the selected fiber-bundles (Figs. 4.40 and 4.41). It is likely that the first three fiber-bundles belong to the geniohyoid, hyoglossus, and genioglossus muscles, while the forth and fifth ones are associated to the mylohyoid and anterior belly of digastric. This correspondence reveals that if an accurate selection of tongue's and neck's fiber-bundles is performed, our method leads to the identification of all subject's fiber-bundles and finally to the segmentation of muscular structures.

In short, IFIR can be considered as an automatic atlas-assisted ***multi-purpose*** approach for

- generation of subject-specific meshes (anatomical or muscular),
- segmentation of soft tissues on the basis of their embedded fibers,
- analyzing the inter/intra-subject variability of fiber-bundles,
- implementation of the bundle-based normalization techniques.

"Everything in the universe is within you. Ask all from yourself."
- Jalaluddin Rumi

5

Conclusions and Future Works

Contents

Our aim in this chapter is to briefly conclude the thesis and introduce the critical contributions of this research project. This thesis is concerned with the automatic generation of subject-specific FE meshes. On this matter, an image-based registration method is proposed to deform an atlas FE mesh and to automatically generate subject-specific meshes. It is shown that DTI-based muscle fibers can also be embedded within the meshes using an atlas-assisted registration scheme. The pro-

posed approaches are successfully evaluated using different data sets. To demonstrate the importance of our methods in the clinical context, human tongue meshes are generated and it is investigated that associating and linking of subject-specific organization of muscular structures with the elements of meshes can be achieved in an automatic way.

5.1 Thesis contributions

In this section, the previous chapters are briefly reviewed and the main contributions made in each are described. In addition, the concluding results of the associated research works are presented.

5.1.1 Chapter 2: Introduction to the Subject-Specific FE Mesh Generation Techniques

In this chapter, a wide range of subject-specific mesh generation approaches are reviewed. Generally, all the methods produce meshes on the basis of a previously provided information on the geometry of the region of interest (ROI) or target organ. This information might be a set of landmarks, contours or a created surface, and depending on the strategy chosen, they are employed in different ways. The majority of methods utilize the provided information for deformation of an atlas/template mesh, while some methods are proposed to adapt the meshing process according to the subject-specific information. Notwithstanding all these efforts, there are some facts to consider: (1) it can not be expected that subject-specific information can easily or automatically be extracted for all the applications, and (2) deformation of an atlas/template mesh may lead to an irregular mesh or a low quality mesh that decreases the accuracy of subsequent numerical simulations. Therefore, finding a method which would allow to generate subject-specific meshes while avoiding difficulties due to the segmentation and meshing is of great importance and interest.

5.1.2 Chapter 3: Atlas-Based Automatic Generation of Subject-Specific Finite Element Tongue Meshes

In this chapter, an automatic approach is proposed for the automatic generation of subject-specific meshes. Our main objective has been to develop

a method that does not require any prior-knowledge about the organ's geometry from subjects' medical images and does not include any meshing process. On this matter, it is proposed to deform an atlas FE mesh using a 3D displacement field derived from the registration of atlas' and subject's medical images. This mapping is performed in such a way so that the resulted deformed meshes are not distorted while target's anatomical features are captured. To establish such a mapping that guaranties a non-folding and one-to-one correspondence, the transformation model is considered to be diffeomorphic (B-spline Free-Form Deformations). However, in practice, this is not sufficient to preserve the quality of atlas meshes; and therefore, two additional constraints are considered: (1) a maximum value of displacement for control points is defined, and (2) a regularization term which enforces a smooth transformation is added (leading neighboring control points to move in the same direction). To estimate registration parameters, a derivative-free optimization technique in utilized which enables to employ any user-defined or complicated similarity measure/cost function. The optimization problem is reformulated into a multi-labeling problem that is expressed by first-order Markov Random Fields (MRFs). Therefore, the parameters estimation problem is equivalent to a labeling problem in a discrete space. The proposed mesh generation approach is evaluated on the level of image registration and atlas mesh deformation. The obtained results reveal that even though mesh quality constraints are applied to the registration problem, the anatomical structures of target organ are successfully captured and high quality meshes are produced.

5.1.3 Chapter 4: Atlas-Based Automatic Integration of DTI-based Fibers in Subject-Specific FE Meshes

In this chapter, with the aim to extend our mesh generation technique to the diffusion tensor images, we present a novel approach for adding fibers' information to the meshes. To do this, the first solution that comes to mind is registration of diffusion weighted images and reorientation of estimated diffusion tensors, but our proposed method is basically developed on the idea of registration of the reconstructed fiber-bundles and anatomical images. This enables one to interact with **limited** or **distorted** DTIs and deforms an atlas fibers' structure toward the most reliable and non-distorted equivalent muscle structures detected in the subject's images. In this methodology, the

anatomical meshes are first generated using our method explained in chapter 3. Then, a similarity measure is evaluated between the thus deformed-atlas fiber-bundles (their centroids) and the reliable subject's fibers so that subject's corresponding fiber-bundles are detected. This classification of subject's fibers or identification of subject's fiber-bundles can directly be employed for assignment of each element of subject's anatomical mesh to a specific fiber-bundle. In the case of muscular meshes, we investigated that atlas fiber-bundles can smoothly be deformed according to the subject's ones and finally produce a transformation that can be used for deformation of muscular atlas meshes. To evaluate the performance of our method in identification of subject's fiber-bundles and accordingly deformation of atlas ones, a simulated data set is utilized. The feasibility of the proposed method is also demonstrated on a clinically acquired human tongue data set. The obtained results show the efficiency our method in identification and registration of fiber-bundles.

5.2 Future works perspectives

Although we intend to improve the obtained results of image/fiber registration and mesh generation techniques, some suggestions on future researches motivated by this thesis are put forward

- Anatomical subject-specific meshes are generated by deformation of an atlas mesh using a 3D displacement field. These displacement fields are estimated using an image registration process and without any consideration of the atlas mesh structure (e.g., being a large scale or low scale mesh). Therefore, our ongoing efforts are focused on inserting atlas mesh's information into the image registration process by defining new regularization constraints that accounts the distribution and relations of mesh nodes that the quality of all type of atlas meshes are preserved after deformations.

- Incorporating IFIR technique for group wise registration of DTIs and accordingly generation of muscular atlas meshes.

- It would be of great interest to evaluate the performance of IFIR technique for registration of data sets coming from different imaging protocols (e.g., DTI and DSI).

- Selection of all atlas tongue fiber-bundles on the basis of classical anatomical knowledge and subsequently creation of a muscular atlas tongue mesh.
- Incorporating IFIR technique for inter/intra-subject variability analysis of tongue fiber-bundles.

References

O. Acosta, A. Simon, F. Monge, F. Commandeur, C. Bassirou, G. Cazoulat, R. De Crevoisier, and P. Haigron. Evaluation of multi-atlas-based segmentation of CT scans in prostate cancer radiotherapy. In *2011 IEEE International Symposium on Biomedical Imaging: From Nano to Macro*, pages 1966–1969. IEEE, 2011.

I. A.D.A.M. *A.D.A.M., Inc.*, 2017. URL http://eclinicalworks.adam.com/content.aspx?productId=39&pid=1&gid=002344&print=1.

N. Adluru, H. Zhang, D. P. Tromp, and A. L. Alexander. Effects of dti spatial normalization on white matter tract reconstructions. In *SPIE Medical Imaging*, pages 86690A–86690A. International Society for Optics and Photonics, 2013.

R. Aggarwal, T. P. Grantcharov, J. R. Eriksen, D. Blirup, V. B. Kristiansen, P. Funch-Jensen, and A. Darzi. An evidence-based virtual reality training program for novice laparoscopic surgeons. *Annals of surgery*, 244(2):310–314, 2006.

R. Aggarwal, J. Ward, I. Balasundaram, P. Sains, T. Athanasiou, and A. Darzi. Proving the effectiveness of virtual reality simulation for training in laparoscopic surgery. *Annals of surgery*, 246(5):771–779, 2007.

J. Aguado-Sierra, A. Krishnamurthy, C. Villongco, J. Chuang, E. Howard, M. J. Gonzales, J. Omens, D. E. Krummen, S. Narayan, R. C. Kerckhoffs, et al. Patient-specific modeling of dyssynchronous heart failure: a case study. *Progress in biophysics and molecular biology*, 107(1):147–155, 2011.

D. Alexander, J. Gee, and R. Bajcsy. Elastic matching of diffusion tensor mris. In *Computer Vision and Pattern Recognition, 1999. IEEE Computer Society Conference on.*, volume 1. IEEE, 1999.

D. C. Alexander and J. C. Gee. Elastic matching of diffusion tensor images. *Computer Vision and Image Understanding*, 77(2):233–250, 2000.

D. C. Alexander, C. Pierpaoli, P. J. Basser, and J. C. Gee. Spatial transformations of diffusion tensor magnetic resonance images. *IEEE transactions on medical imaging*, 20(11):1131–1139, 2001.

J. Andersson. Maximum likelihood estimation of diffusion parameters with a rician noise model. In *Proc. ISMRM*, page 1881, 2007.

J. L. Andersson. Maximum a posteriori estimation of diffusion tensor parameters using a rician noise model: why, how and but. *Neuroimage*, 42 (4):1340–1356, 2008.

I. ANSYS. Fe modeler user's guide. *Ansys Inc*, 2013.

S. Ardekani and U. Sinha. Geometric distortion correction of high-resolution 3 t diffusion tensor brain images. *Magnetic resonance in medicine*, 54(5): 1163–1171, 2005.

V. Arsigny, O. Commowick, N. Ayache, and X. Pennec. A fast and log-euclidean polyaffine framework for locally linear registration. *Journal of Mathematical Imaging and Vision*, 33(2):222–238, 2009.

P. Badin, P. Borel, G. Bailly, L. Revéret, M. Baciu, and C. Segebarth. Towards an audiovisual virtual talking head: 3D articulatory modeling of tongue, lips and face based on MRI and video images. In *5th Speech Production Seminar*, pages 261–264, 2000.

A. Baldock, R. Rockne, A. Boone, M. Neal, C. Bridge, L. Guyman, M. Mrugala, J. Rockhill, K. R. Swanson, A. D. Trister, et al. From patient-specific mathematical neuro-oncology to precision medicine. *Frontiers in oncology*, 3:62, 2013.

D. C. Barratt, C. S. Chan, P. J. Edwards, G. P. Penney, M. Slomczykowski, T. J. Carter, and D. J. Hawkes. Instantiation and registration of statistical shape models of the femur and pelvis using 3d ultrasound imaging. *Medical image analysis*, 12(3):358–374, 2008.

P. J. Basser. Inferring microstructural features and the physiological state of tissues from diffusion-weighted images. *NMR in Biomedicine*, 8(7): 333–344, 1995a.

P. J. Basser. Inferring microstructural features and the physiological state of tissues from diffusion-weighted images. *NMR in Biomedicine*, 8(7): 333–344, 1995b.

P. J. Basser and C. Pierpaoli. Microstructural and physiological features of tissues elucidated by quantitative-diffusion-tensor mri. *Journal of magnetic resonance Series B*, 111(2):209–219, 1996.

P. J. Basser, J. Mattiello, and D. LeBihan. Mr diffusion tensor spectroscopy and imaging. *Biophysical journal*, 66(1):259, 1994a.

P. J. Basser, J. Mattiello, and D. LeBihan. Estimation of the effective self-diffusion tensor from the nmr spin echo. *Journal of Magnetic Resonance, Series B*, 103(3):247–254, 1994b.

P. J. Basser, S. Pajevic, C. Pierpaoli, J. Duda, and A. Aldroubi. In vivo fiber tractography using dt-mri data. *Magnetic resonance in medicine*, 44 (4):625–632, 2000.

P. G. Batchelor, D. L. Hill, D. Atkinson, and F. Calamante. Study of connectivity in the brain using the full diffusion tensor from mri. In *Biennial International Conference on Information Processing in Medical Imaging*, pages 121–133. Springer, 2001.

C. Beaulieu. The basis of anisotropic water diffusion in the nervous system–a technical review. *NMR in Biomedicine*, 15(7-8):435–455, 2002.

T. Behrens, M. Jenkinson, J. Brady, and S. Smith. A probabilistic framework for estimating neural connectivity from diffusion weighted mri. In *Proc. Int. Soc. Magn. Reson. Med*, volume 1142, 2002.

T. Behrens, H. J. Berg, S. Jbabdi, M. Rushworth, and M. Woolrich. Probabilistic diffusion tractography with multiple fibre orientations: What can we gain? *Neuroimage*, 34(1):144–155, 2007.

H. Bennink, J. Korbeeck, B. Janssen, and B. M. ter Haar Romeny. Warping a neuro-anatomy atlas on 3d mri data with radial basis functions. In *3rd Kuala Lumpur International Conference on Biomedical Engineering 2006*, pages 28–32. Springer, 2007.

B. Bilgic, K. Setsompop, J. Cohen-Adad, A. Yendiki, L. L. Wald, and E. Adalsteinsson. Accelerated diffusion spectrum imaging with compressed sensing using adaptive dictionaries. *Magnetic Resonance in Medicine*, 68(6):1747–1754, 2012.

S. S. Blemker, P. M. Pinsky, and S. L. Delp. A 3D model of muscle reveals the causes of nonuniform strains in the biceps brachii. *Journal of biomechanics*, 38(4):657–665, 2005.

F. Bookstein. Thin-plate splines and the decomposition of deformation. *IEEE Trans. Patt. Anal. Mach. Intell*, 10, 1988.

L. Breiman, J. Friedman, C. J. Stone, and R. A. Olshen. *Classification and regression trees*. CRC press, 1984.

K. K. Brock. *Image Processing in Radiation Therapy*. CRC Press, 2013.

A. Brun, H. Knutsson, H.-J. Park, M. E. Shenton, and C.-F. Westin. Clustering fiber traces using normalized cuts. In *International Conference*

on Medical Image Computing and Computer-Assisted Intervention, pages 368–375. Springer, 2004.

R. Bryan, P. S. Mohan, A. Hopkins, F. Galloway, M. Taylor, and P. B. Nair. Statistical modelling of the whole human femur incorporating geometric and material properties. *Medical engineering & physics*, 32(1):57–65, 2010.

S. Buchaillard, M. Brix, P. Perrier, and Y. Payan. Simulations of the consequences of tongue surgery on tongue mobility: implications for speech production in post-surgery conditions. *The international journal of medical robotics+ computer assisted surgery: MRCAS*, 3(3):252–261, 2007a.

S. Buchaillard, M. Brix, P. Perrier, and Y. Payan. Simulations of the consequences of tongue surgery on tongue mobility: Implications for speech production in post-surgery conditions. *arXiv preprint arXiv:0710.2747*, 2007b.

S. Buchaillard, P. Perrier, and Y. Payan. A biomechanical model of cardinal vowel production: Muscle activations and the impact of gravity on tongue positioning. *The Journal of the Acoustical Society of America*, 126(4): 2033–2051, 2009.

M. Bucki, C. Lobos, and Y. Payan. A fast and robust patient specific finite element mesh registration technique: application to 60 clinical cases. *Medical image analysis*, 14(3):303–317, 2010a.

M. Bucki, C. Lobos, and Y. Payan. A fast and robust patient specific finite element mesh registration technique: application to 60 clinical cases. *Medical image analysis*, 14(3):303–317, 2010b.

M. Bucki, C. Lobos, Y. Payan, and N. Hitschfeld. Jacobian-based repair method for finite element meshes after registration. *Engineering with Computers*, 27(3):285–297, 2011.

J. H. Burdette, D. D. Durden, A. D. Elster, and Y.-F. Yen. High b-value diffusion-weighted mri of normal brain. *Journal of computer assisted tomography*, 25(4):515–519, 2001.

J. C. Caendish, D. A. Field, and W. H. Frey. An apporach to automatic three-dimensional finite element mesh generation. *International journal for numerical methods in engineering*, 21(2):329–347, 1985.

E. G. Caiani, A. Colombo, M. Pepi, C. Piazzese, F. Maffessanti, R. M. Lang, and M. C. Carminati. Three-dimensional left ventricular segmentation from magnetic resonance imaging for patient-specific modelling purposes. *Europace*, 16(suppl 4):iv96–iv101, 2014.

F. Calamante, J.-D. Tournier, G. D. Jackson, and A. Connelly. Track-density imaging (tdi): super-resolution white matter imaging using whole-brain track-density mapping. *Neuroimage*, 53(4):1233–1243, 2010.

J. Campbell, L. Liang, A. Szymczak, and A. Petrella. Optimization of an automated mesh morphing algorithm for lumbar vertebrae. In *Annual Meeting of the Orthopaedic Research Society*, 2012.

J. Q. Campbell and A. J. Petrella. An automated method for landmark identification and finite-element modeling of the lumbar spine. *IEEE Transactions on Biomedical Engineering*, 62(11):2709–2716, 2015.

Y. Cao, M. I. Miller, S. Mori, R. L. Winslow, and L. Younes. Diffeomorphic matching of diffusion tensor images. In *2006 Conference on Computer Vision and Pattern Recognition Workshop (CVPRW'06)*, pages 67–67. IEEE, 2006.

J. C. Carr, R. K. Beatson, J. B. Cherrie, T. J. Mitchell, W. R. Fright, B. C. McCallum, and T. R. Evans. Reconstruction and representation of 3d objects with radial basis functions. In *Proceedings of the 28th annual conference on Computer graphics and interactive techniques*, pages 67–76. ACM, 2001.

M. Chabanas, V. Luboz, and Y. Payan. Patient specific finite element model of the face soft tissues for computer-assisted maxillofacial surgery. *Medical Image Analysis*, 7(2):131–151, 2003.

S. C. Chapra and R. P. Canale. Numerical methods for engineers. *Tata*, 2011.

D. Chen, M. Müller-Eschner, H. von Tengg-Kobligk, D. Barber, D. Böckler, R. Hose, and Y. Ventikos. A patient-specific study of type-b aortic dissection: evaluation of true-false lumen blood exchange. *Biomedical engineering online*, 12(1):1, 2013.

S. Chen, H. Lou, L. Guo, Q. Rong, Y. Liu, and T.-M. Xu. 3-d finite element modelling of facial soft tissue and preliminary application in orthodontics. *Computer methods in biomechanics and biomedical engineering*, 15(3): 255–261, 2012.

T. Chenchen. *Generation of Patient-Specific Finite-Element Mesh from 3D Medical Images*. PhD thesis, National University of Singapore, 2013.

Q. Collier, J. Veraart, B. Jeurissen, A. J. den Dekker, and J. Sijbers. Iterative reweighted linear least squares for accurate, fast, and robust estimation of diffusion magnetic resonance parameters. *Magnetic resonance in medicine*, 73(6):2174–2184, 2015.

T. E. Conturo, N. F. Lori, T. S. Cull, E. Akbudak, A. Z. Snyder, J. S. Shimony, R. C. McKinstry, H. Burton, and M. E. Raichle. Tracking neuronal fiber pathways in the living human brain. *Proceedings of the National Academy of Sciences*, 96(18):10422–10427, 1999.

I. Corouge, S. Gouttard, and G. Gerig. Towards a shape model of white matter fiber bundles using diffusion tensor mri. In *Biomedical Imaging: Nano to Macro, 2004. IEEE International Symposium on*, pages 344–347. IEEE, 2004.

S. Cotin, C. Duriez, J. Lenoir, P. Neumann, and S. Dawson. New approaches to catheter navigation for interventional radiology simulation. In *International Conference on Medical Image Computing and Computer-Assisted Intervention*, pages 534–542. Springer, 2005.

H. Courtecuisse, H. Jung, J. Allard, C. Duriez, D. Y. Lee, and S. Cotin. Gpu-based real-time soft tissue deformation with cutting and haptic feedback. *Progress in biophysics and molecular biology*, 103(2):159–168, 2010.

B. Couteau, Y. Payan, and S. Lavallée. The mesh-matching algorithm: an automatic 3d mesh generator for finite element structures. *Journal of biomechanics*, 33(8):1005–1009, 2000.

J. R. C. Crouch. *Medial techniques for automating finite element analysis.* PhD thesis, Citeseer, 2003.

S. L. Dawson, S. Cotin, D. Meglan, D. W. Shaffer, and M. A. Ferrell. Equipment and technology-designing a computer-based simulator for interventional cardiology training. *Catheterization and Cardiovascular Interventions*, 51(4):522–527, 2000.

S. De Putter, F. N. van de Vosse, F. A. Gerritsen, F. Laffargue, and M. Breeuwer. Computational mesh generation for vascular structures with deformable surfaces. *International Journal of Computer Assisted Radiology and Surgery*, 1(1):39–49, 2006.

A. de Vecchi, D. A. Nordsletten, R. Razavi, G. Greil, and N. Smith. Patient specific fluid–structure ventricular modelling for integrated cardiac care. *Medical & biological engineering & computing*, 51(11):1261–1270, 2013.

A. P. Dempster, N. M. Laird, and D. B. Rubin. Maximum likelihood from incomplete data via the em algorithm. *Journal of the royal statistical society. Series B (methodological)*, pages 1–38, 1977.

T. K. Dey. *Curve and surface reconstruction: algorithms with mathematical analysis*, volume 23. Cambridge University Press, 2006.

L. R. Dice. Measures of the amount of ecologic association between species. *Ecology*, 26(3):297–302, 1945.

T. Ditterrich. Machine learning research: four current direction. *Artificial Intelligence Magzine*, 4:97–136, 1997.

B. J. Doyle and T. M. McGloughlin. Computer-aided diagnosis of abdominal aortic aneurysms. In *Biomechanics and Mechanobiology of Aneurysms*, pages 119–138. Springer, 2011.

Q. Du and D. Wang. The optimal centroidal Voronoi tessellations and the gersho's conjecture in the three-dimensional space. *Computers & Mathematics with Applications*, 49(9):1355–1373, 2005.

H. Edelsbrunner. Surface reconstruction by wrapping finite sets in space. In *Discrete and Computational Geometry*, pages 379–404. Springer, 2003.

J. Fernandez, P. Mithraratne, S. Thrupp, M. Tawhai, and P. Hunter. Anatomically based geometric modelling of the musculo-skeletal system and other organs. *Biomechanics and modeling in mechanobiology*, 2(3): 139–155, 2004.

D. A. Field. Qualitative measures for initial meshes. *International Journal for Numerical Methods in Engineering*, 47(4):887–906, 2000.

P. Fillard, X. Pennec, V. Arsigny, and N. Ayache. Clinical dt-mri estimation, smoothing, and fiber tracking with log-euclidean metrics. *IEEE transactions on medical imaging*, 26(11):1472–1482, 2007.

P. Fillard, M. Descoteaux, A. Goh, S. Gouttard, B. Jeurissen, J. Malcolm, A. Ramirez-Manzanares, M. Reisert, K. Sakaie, F. Tensaouti, et al. Quantitative evaluation of 10 tractography algorithms on a realistic diffusion mr phantom. *Neuroimage*, 56(1):220–234, 2011.

M. Firl, R. Wüchner, and K.-U. Bletzinger. Regularization of shape optimization problems using fe-based parametrization. *Structural and Multidisciplinary Optimization*, 47(4):507–521, 2013.

H. Fuchs, Z. M. Kedem, and S. P. Uselton. Optimal surface reconstruction from planar contours. *Communications of the ACM*, 20(10):693–702, 1977.

A. G. Gallagher, E. M. Ritter, H. Champion, G. Higgins, M. P. Fried, G. Moses, C. D. Smith, and R. M. Satava. Virtual reality simulation for the operating room: proficiency-based training as a paradigm shift in surgical skills training. *Annals of surgery*, 241(2):364–372, 2005.

V. Garcia, O. Commowick, and G. Malandain. A robust and efficient block matching framework for non linear registration of thoracic CT images. In

Grand Challenges in Medical Image Analysis (MICCAI workshop), pages 1–10, 2010.

E. Garyfallidis, M. Brett, and I. Nimmo-Smith. Fast dimensionality reduction for brain tractography clustering. In *16th Annual Meeting of the Organization for Human Brain Mapping*, 2010.

J. C. Gee and D. C. Alexander. Diffusion-tensor image registration. In *Visualization and processing of tensor fields*, pages 327–342. Springer, 2006.

S. Geman and D. Geman. Stochastic relaxation, Gibbs distributions, and the Bayesian restoration of images. *IEEE Transactions on pattern analysis and machine intelligence*, (6):721–741, 1984.

J. Gérard, R. Wilhelms-Tricarico, P. Perrier, and Y. Payan. A 3D dynamical biomechanical tongue model to study speech motor control. Recent Research Developmentsin Biomechanics. *Transworld Research Network*, 1:49–64, 2003.

G. Gerig, M. Jomier, and M. Chakos. Valmet: A new validation tool for assessing and improving 3D object segmentation. In *International Conference on Medical Image Computing and Computer-Assisted Intervention*, pages 516–523. Springer, 2001.

G. Gerig, S. Gouttard, and I. Corouge. Analysis of brain white matter via fiber tract modeling. In *Engineering in Medicine and Biology Society, 2004. IEMBS'04. 26th Annual International Conference of the IEEE*, volume 2, pages 4421–4424. IEEE, 2004.

F. Girosi, M. Jones, and T. Poggio. Regularization theory and neural networks architectures. *Neural computation*, 7(2):219–269, 1995.

B. Glocker, N. Komodakis, G. Tziritas, N. Navab, and N. Paragios. Dense image registration through MRFs and efficient linear programming. *Medical image analysis*, 12(6):731–741, 2008.

A. Goh and R. Vidal. Algebraic methods for direct and feature based registration of diffusion tensor images. In *European Conference on Computer Vision*, pages 514–525. Springer, 2006.

G. Gomes, S. Van Cauter, M. De Beule, L. Vigneron, C. Pattyn, and E. Audenaert. Patient-specific modelling in orthopedics: from image to surgery. In *Biomedical Imaging and Computational Modeling in Biomechanics*, pages 109–129. Springer, 2013.

S. Goshima, M. Kanematsu, H. Kondo, R. Yokoyama, K. Kajita, Y. Tsuge, H. Watanabe, Y. Shiratori, M. Onozuka, and N. Moriyama. Diffusion-weighted imaging of the liver: optimizing b value for the detection and

characterization of benign and malignant hepatic lesions. *Journal of Magnetic Resonance Imaging*, 28(3):691–697, 2008.

A. Gramfort, C. Poupon, and M. Descoteaux. Sparse dsi: Learning dsi structure for denoising and fast imaging. In *International Conference on Medical Image Computing and Computer-Assisted Intervention*, pages 288–296. Springer, 2012.

L. Grassi, N. Hraiech, E. Schileo, M. Ansaloni, M. Rochette, and M. Viceconti. Evaluation of the generality and accuracy of a new mesh morphing procedure for the human femur. *Medical engineering & physics*, 33(1): 112–120, 2011.

K.-R. GrnhH. Automatic mesh generation with tetrahedron elements. *International Journal for Numerical Methods in Engineering*, 18(2):273–289, 1982.

N. M. Grosland, R. Bafna, and V. A. Magnotta. Automated hexahedral meshing of anatomic structures using deformable registration. *Computer methods in biomechanics and biomedical engineering*, 12(1):35–43, 2009.

P. Guevara, C. Poupon, D. Rivière, Y. Cointepas, M. Descoteaux, B. Thirion, and J.-F. Mangin. Robust clustering of massive tractography datasets. *Neuroimage*, 54(3):1975–1993, 2011.

A. Guimond, C. R. Guttmann, S. K. Warfield, and C.-F. Westin. Deformable registration of dt-mri data based on transformation invariant tensor characteristics. In *Biomedical Imaging, 2002. Proceedings. 2002 IEEE International Symposium on*, pages 761–764. IEEE, 2002.

M. He et al. *Study on cardiac biomechanics using idealized and patient-specific models*. PhD thesis, 2014.

W. Hecke, A. Leemans, E. D'Agostino, S. De Backer, E. Vandervliet, P. Parizel, and J. Sijbers. Affine coregistration of diffusion tensor magnetic resonance images using mutual information. *IEEE Trans. Medical Imaging*, 26(11):1598–1612, 2007.

T. Heimann and H.-P. Meinzer. Statistical shape models for 3d medical image segmentation: a review. *Medical image analysis*, 13(4):543–563, 2009.

C. R. Henak, A. E. Anderson, and J. A. Weiss. Subject-specific analysis of joint contact mechanics: application to the study of osteoarthritis and surgical planning. *Journal of biomechanical engineering*, 135(2):021003, 2013.

K. Ho-Le. Finite element mesh generation methods: a review and classification. *Computer-aided design*, 20(1):27–38, 1988.

M. O. Irfanoglu, R. Machiraju, S. Sammet, C. Pierpaoli, and M. Knopp. Automatic deformable diffusion tensor registration for fiber population analysis. In *International Conference on Medical Image Computing and Computer-Assisted Intervention*, pages 1014–1022. Springer, 2008.

M. O. Irfanoglu, C. G. Koay, S. Pajevic, R. Machiraju, and P. J. Basser. Diffusion tensor field registration in the presence of uncertainty. In *International Conference on Medical Image Computing and Computer-Assisted Intervention*, pages 181–189. Springer, 2009.

M. O. Irfanoglu, A. Nayak, J. Jenkins, E. B. Hutchinson, N. Sadeghi, C. P. Thomas, and C. Pierpaoli. Dr-tamas: Diffeomorphic registration for tensor accurate alignment of anatomical structures. *NeuroImage*, 132:439–454, 2016.

K. Iskarous. Patterns of tongue movement. *Journal of Phonetics*, 33(4): 363–381, 2005.

ISMRM−challenge. *ISMRM 2015 Tractography challenge*, 2015 (accessed November 28, 2016). URL http://www.tractometer.org/ismrm_2015_challenge/.

S. Ji, J. C. Ford, R. M. Greenwald, J. G. Beckwith, K. D. Paulsen, L. A. Flashman, and T. W. McAllister. Automated subject-specific, hexahedral mesh generation via image registration. *Finite Elements in Analysis and Design*, 47(10):1178–1185, 2011.

H. Jin and R. Tanner. Generation of unstructured tetrahedral meshes by advancing front technique. *International Journal for Numerical Methods in Engineering*, 36(11):1805–1823, 1993.

D. K. Jones. *Diffusion mri*. Oxford University Press, 2010.

D. K. Jones and P. J. Basser. "squashing peanuts and smashing pumpkins": How noise distorts diffusion-weighted mr data. *Magnetic Resonance in Medicine*, 52(5):979–993, 2004.

D. K. Jones, A. Simmons, S. C. Williams, and M. A. Horsfield. Non-invasive assessment of axonal fiber connectivity in the human brain via diffusion tensor mri. *Magnetic Resonance in Medicine*, 42(1):37–41, 1999.

D. K. Jones, L. D. Griffin, D. C. Alexander, M. Catani, M. A. Horsfield, R. Howard, and S. C. Williams. Spatial normalization and averaging of diffusion tensor mri data sets. *Neuroimage*, 17(2):592–617, 2002.

N. A. Kallemeyn, A. Natarajan, V. A. Magnotta, and N. M. Grosland. Hexahedral meshing of subject-specific anatomic structures using mapped building blocks. *Computer methods in biomechanics and biomedical engineering*, 16(6):602–611, 2013.

S. Kelly. *ANSYS Theory Reference: Release 5.5*, chapter Element shape testing. ANSYS, Incorporated, Oxford, 1998.

R. C. Kerckhoffs. *Patient-Specific Modeling of the Cardiovascular System: Technology-Driven Personalized Medicine*. Springer Science & Business Media, 2010.

J. Keyak, J. Meagher, H. Skinner, and C. Mote. Automated three-dimensional finite element modelling of bone: a new method. *Journal of biomedical engineering*, 12(5):389–397, 1990.

K. F. Klein, J. Hu, M. P. Reed, C. N. Hoff, and J. D. Rupp. Development and validation of statistical models of femur geometry for use with parametric finite element models. *Annals of biomedical engineering*, 43(10):2503–2514, 2015.

P. M. Knupp. Achieving finite element mesh quality via optimization of the Jacobian matrix norm and associated quantities. Part ii—a framework for volume mesh optimization and the condition number of the Jacobian matrix. *International Journal for numerical methods in engineering*, 48 (8):1165–1185, 2000.

P. M. Knupp. Remarks on mesh quality. In *45th AIAA Aerospace Sciences Meeting and Exhibit*, pages 7–10, 2007.

C. G. Koay. Least squares approaches to diffusion tensor estimation. *Diffusion MRI*, page 272, 2010.

C. G. Koay, J. D. Carew, A. L. Alexander, P. J. Basser, and M. E. Meyerand. Investigation of anomalous estimates of tensor-derived quantities in diffusion tensor imaging. *Magnetic Resonance in Medicine*, 55(4):930–936, 2006a.

C. G. Koay, L.-C. Chang, J. D. Carew, C. Pierpaoli, and P. J. Basser. A unifying theoretical and algorithmic framework for least squares methods of estimation in diffusion tensor imaging. *Journal of Magnetic Resonance*, 182(1):115–125, 2006b.

M. Koch, V. Glauche, J. Finsterbusch, U. Nolte, J. Frahm, and C. Büchel. Estimation of anatomical connectivity from diffusion tensor data. *NeuroImage*, 13(6):176, 2001.

N. Komodakis, G. Tziritas, and N. Paragios. Fast, approximately optimal solutions for single and dynamic MRFs. In *2007 IEEE Conference on Computer Vision and Pattern Recognition*, pages 1–8. IEEE, 2007.

N. Komodakis, G. Tziritas, and N. Paragios. Performance vs computational efficiency for optimizing single and dynamic MRFs: Setting the state of the art with primal-dual strategies. *Computer Vision and Image Understanding*, 112(1):14–29, 2008.

P. Lamata, S. Niederer, D. Barber, D. Norsletten, J. Lee, R. Hose, and N. Smith. Personalization of cubic hermite meshes for efficient biomechanical simulations. In *International Conference on Medical Image Computing and Computer-Assisted Intervention*, pages 380–387. Springer, 2010a.

P. Lamata, S. Niederer, G. Plank, and N. Smith. Generic conduction parameters for predicting activation waves in customised cardiac electrophysiology models. In *International Workshop on Statistical Atlases and Computational Models of the Heart*, pages 252–260. Springer, 2010b.

P. Lamata, S. Niederer, D. Nordsletten, D. C. Barber, I. Roy, D. R. Hose, and N. Smith. An accurate, fast and robust method to generate patient-specific cubic hermite meshes. *Medical image analysis*, 15(6):801–813, 2011.

P. Lamata, M. Sinclair, E. Kerfoot, A. Lee, A. Crozier, B. Blazevic, S. Land, A. J. Lewandowski, D. Barber, S. Niederer, et al. An automatic service for the personalization of ventricular cardiac meshes. *Journal of The Royal Society Interface*, 11(91):20131023, 2014.

B. A. Landman, J. A. Bogovic, H. Wan, F. E. Z. ElShahaby, P.-L. Bazin, and J. L. Prince. Resolution of crossing fibers with constrained compressed sensing using diffusion tensor mri. *NeuroImage*, 59(3):2175–2186, 2012.

J. Lee, J. Woo, F. Xing, E. Z. Murano, M. Stone, and J. L. Prince. Semi-automatic segmentation for 3D motion analysis of the tongue with dynamic MRI. *Computerized Medical Imaging and Graphics*, 38(8):714–724, 2014.

L. K. Lee, S. C. Liew, and W. J. Thong. A review of image segmentation methodologies in medical image. In *Advanced computer and communication engineering technology*, pages 1069–1080. Springer, 2015.

A. Leemans, J. Sijbers, S. De Backer, E. Vandervliet, and P. Parizel. Multiscale white matter fiber tract coregistration: A new feature-based approach to align diffusion tensor data. *Magnetic resonance in medicine*, 55 (6):1414–1423, 2006.

B. Li, G. E. Christensen, J. Dill, E. A. Hoffman, and J. M. Reinhardt. 3D intersubject warping and registration of pulmonary CT images for a human lung model. In *Medical Imaging 2002*, pages 324–335. International Society for Optics and Photonics, 2002.

S. Z. Li. *Markov random field modeling in image analysis*. Springer Science & Business Media, 2009.

C. Lobos, Y. Payan, and N. Hitschfeld. Techniques for the generation of 3D Finite Element Meshes of human organs. *Informatics in Oral Medicine: Advanced Techniques in Clinical and Diagnostic Technologies. Hershey, PA: Medical Information Science Reference*, pages 126–158, 2010.

C. Lobos et al. A set of mixed-elements patterns for domain boundary approximation in hexahedral meshes. In *MMVR*, pages 268–272, 2013.

R. Lohner. Three-dimensional grid generation by the advancing front method. *Int. J. Numer. Meths. Fluids.*, 8:1135–1149, 1988.

R. Löhner, J. Camberos, and M. Merriam. Parallel unstructured grid generation. *Computer Methods in Applied Mechanics and Engineering*, 95(3): 343–357, 1992.

W. E. Lorensen and H. E. Cline. Marching cubes: A high resolution 3d surface construction algorithm. In *ACM siggraph computer graphics*, volume 21, pages 163–169. ACM, 1987.

H. Lou, S. Chen, G. Chen, T. Xu, and Q. Rong. Patient-specific modeling of facial soft tissue based on radial basis functions transformations of a standard three-dimensional finite element model. *Chin Med J*, 125(22): 4066–4071, 2012.

N. M. Harandi, R. Abugharbieh, and S. Fels. 3D segmentation of the tongue in MRI: a minimally interactive model-based approach. *Computer Methods in Biomechanics and Biomedical Engineering: Imaging & Visualization*, 3(4):178–188, 2015.

M. Maddah, W. E. L. Grimson, S. K. Warfield, and W. M. Wells. A unified framework for clustering and quantitative analysis of white matter fiber tracts. *Medical image analysis*, 12(2):191–202, 2008.

F. Maes, A. Collignon, D. Vandermeulen, G. Marchal, and P. Suetens. Multimodality image registration by maximization of mutual information. *IEEE transactions on Medical Imaging*, 16(2):187–198, 1997.

V. A. Magnotta, W. Li, and N. M. Grosland. Comparison of displacement-based and force-based mapped meshing. *MIDAS journal*, 2008:629, 2008.

A. Mansoor, U. Bagci, B. Foster, Z. Xu, G. Z. Papadakis, L. R. Folio, J. K. Udupa, and D. J. Mollura. Segmentation and Image Analysis of Abnormal Lungs at CT: Current Approaches, Challenges, and Future Trends. *RadioGraphics*, 35(4):1056–1076, 2015.

D. Mattes, D. R. Haynor, H. Vesselle, T. K. Lewellen, and W. Eubank. PET-CT image registration in the chest using free-form deformations. *IEEE transactions on medical imaging*, 22(1):120–128, 2003.

A. Mayer and H. Greenspan. Direct registration of white matter tractographies and application to atlas construction. In *Workshop on Statistical Registration: Pair-wise and Group-wise Alignment and Atlas Formation*, 2007.

R. H. McGregor, B. A. Lloyd, D. Szczerba, and G. Székely. Efficient generation of corresponding meshes for biomedical flow simulations. In *International Symposium on Biomedical Simulation*, pages 49–58. Springer, 2010.

S. Merlet, E. Caruyer, and R. Deriche. Parametric dictionary learning for modeling eap and odf in diffusion mri. In *International Conference on Medical Image Computing and Computer-Assisted Intervention*, pages 10–17. Springer, 2012.

T. Metens, D. Miranda, J. Absil, and C. Matos. What is the optimal b value in diffusion-weighted mr imaging to depict prostate cancer at 3t? *European radiology*, 22(3):703–709, 2012.

D. Meyers, S. Skinner, and K. Sloan. Surfaces from contours. *ACM Transactions On Graphics (TOG)*, 11(3):228–258, 1992.

K. Miller, A. Wittek, and G. Joldes. Biomechanical modeling of the brain for computer-assisted neurosurgery. In *Biomechanics of the Brain*, pages 111–136. Springer, 2011.

K. Miller, A. Horton, G. Joldes, and A. Wittek. Beyond finite elements: A comprehensive, patient-specific neurosurgical simulation utilizing a meshless method. *Journal of biomechanics*, 45(15):2698–2701, 2012.

S. Mori and J.-D. Tournier. *Introduction to diffusion tensor imaging: and higher order models*. Academic Press, 2013.

S. Mori and P. Van Zijl. Diffusion weighting by the trace of the diffusion tensor within a single scan. *Magnetic Resonance in Medicine*, 33(1):41–52, 1995.

S. Mori, B. J. Crain, V. Chacko, and P. Van Zijl. Three-dimensional tracking of axonal projections in the brain by magnetic resonance imaging. *Annals of neurology*, 45(2):265–269, 1999.

R. Müller and P. Rüegsegger. Three-dimensional finite element modelling of non-invasively assessed trabecular bone structures. *Medical engineering & physics*, 17(2):126–133, 1995.

E. Muñoz-Moreno, R. Cárdenes-Almeida, and M. Martin-Fernandez. Review of techniques for registration of diffusion tensor imaging. In *Tensors in Image Processing and Computer Vision*, pages 273–297. Springer, 2009.

K. Murphy, B. Van Ginneken, J. M. Reinhardt, S. Kabus, K. Ding, X. Deng, K. Cao, K. Du, G. E. Christensen, V. Garcia, et al. Evaluation of registration methods on thoracic CT: the EMPIRE10 challenge. *IEEE transactions on medical imaging*, 30(11):1901–1920, 2011.

A. Myronenko and X. Song. Point set registration: Coherent point drift. *IEEE transactions on pattern analysis and machine intelligence*, 32(12): 2262–2275, 2010.

A. Myronenko, X. Song, and M. A. Carreira-Perpinán. Non-rigid point set registration: Coherent point drift. In *Advances in Neural Information Processing Systems*, pages 1009–1016, 2006.

S. Naomis and P. C. Lau. Numerical implementation. In *Computational Tensor Analysis of Shell Structures*, pages 101–156. Springer, 1990.

M. A. Nazari, P. Perrier, and Y. Payan. The Distributed Lambda (λ) Model (DLM): A 3-D, Finite-Element Muscle Model Based on Feldman's λ Model; Assessment of Orofacial Gestures. *Journal of speech, language, and hearing research*, 56(6):S1909–S1923, 2013.

P. F. Neher, F. B. Laun, B. Stieltjes, and K. H. Maier-Hein. Fiberfox: an extensible system for generating realistic white matter software phantoms. In *Computational Diffusion MRI and Brain Connectivity*, pages 105–113. Springer, 2014a.

P. F. Neher, F. B. Laun, B. Stieltjes, and K. H. Maier-Hein. Fiberfox: facilitating the creation of realistic white matter software phantoms. *Magnetic resonance in medicine*, 72(5):1460–1470, 2014b.

T. S. Newman and H. Yi. A survey of the marching cubes algorithm. *Computers & Graphics*, 30(5):854–879, 2006.

J. Nocedal and S. Wright. *Numerical optimization*. Springer Science & Business Media, 2006.

L. O'Donnell, M. Kubicki, M. E. Shenton, M. H. Dreusicke, W. E. L. Grimson, and C.-F. Westin. A method for clustering white matter fiber tracts. *American Journal of Neuroradiology*, 27(5):1032–1036, 2006.

N. S. Ottosen and H. Petersson. *Introduction to the finite element method*. Prentice-Hall, 1992.

S. J. Owen. A survey of unstructured mesh generation technology. In *IMR*, pages 239–267, 1998.

H. Park. Lofted b-spline surface interpolation by linearly constrained energy minimization. *Computer-Aided Design*, 35(14):1261–1268, 2003.

H. Park and K. Kim. Smooth surface approximation to serial cross-sections. *Computer-Aided Design*, 28(12):995–1005, 1996.

H.-J. Park, M. Kubicki, M. E. Shenton, A. Guimond, R. W. McCarley, S. E. Maier, R. Kikinis, F. A. Jolesz, and C.-F. Westin. Spatial normalization of diffusion tensor mri using multiple channels. *Neuroimage*, 20(4):1995–2009, 2003.

G. J. Parker, C. A. Wheeler-Kingshott, and G. J. Barker. Estimating distributed anatomical connectivity using fast marching methods and diffusion tensor imaging. *IEEE transactions on medical imaging*, 21(5):505–512, 2002.

S. Peled, O. Friman, F. Jolesz, and C.-F. Westin. Geometrically constrained two-tensor model for crossing tracts in dwi. *Magnetic resonance imaging*, 24(9):1263–1270, 2006.

E. Peleg, R. Herblum, M. Beek, L. Joskowicz, M. Liebergall, R. Mosheiff, and C. Whyne. Can a partial volume edge effect reduction algorithm improve the repeatability of subject-specific finite element models of femurs obtained from ct data? *Computer methods in biomechanics and biomedical engineering*, 17(3):204–209, 2014.

J. Peraire, M. Vahdati, K. Morgan, and O. C. Zienkiewicz. Adaptive remeshing for compressible flow computations. *Journal of computational physics*, 72(2):449–466, 1987.

L. A. Piegl and W. Tiller. *The NURBS book*. Springer, 1995.

M. J. Powell. A fast algorithm for nonlinearly constrained optimization calculations. In *Numerical analysis*, pages 144–157. Springer, 1978.

R. Preetha and G. Suresh. Performance analysis on three dimensional surface reconstruction of head magnetic resonance images. In *2012 12th International Conference on Intelligent Systems Design and Applications (ISDA)*, pages 351–356. IEEE, 2012.

D. Rajon and W. Bolch. Marching cube algorithm: review and trilinear interpolation adaptation for image-based dosimetric models. *Computerized Medical Imaging and Graphics*, 27(5):411–435, 2003.

A. Ramirez-Manzanares, M. Rivera, B. C. Vemuri, P. Carney, and T. Mareci. Diffusion basis functions decomposition for estimating white matter intravoxel fiber geometry. *IEEE transactions on medical imaging*, 26(8): 1091–1102, 2007.

M. P. Reed, M. M. Sochor, J. D. Rupp, K. D. Klinich, and M. A. Manary. Anthropometric specification of child crash dummy pelves through statistical analysis of skeletal geometry. *Journal of biomechanics*, 42(8): 1143–1145, 2009.

A. Roche, G. Malandain, X. Pennec, and N. Ayache. The correlation ratio as a new similarity measure for multimodal image registration. In *International Conference on Medical Image Computing and Computer-Assisted Intervention*, pages 1115–1124. Springer, 1998.

B. Roduit, C. Borgeat, S. Cavin, C. Fragniere, and V. Dudler. Application of finite element analysis (fea) for the simulation of release of additives from multilayer polymeric packaging structures. *Food additives and contaminants*, 22(10):945–955, 2005.

P.-Y. Rohan, C. Lobos, M. A. Nazari, P. Perrier, and Y. Payan. Finite element modelling of nearly incompressible materials and volumetric locking: a case study. *Computer methods in biomechanics and biomedical engineering*, 17(sup1):192–193, 2014.

G. Rohde, S. Pajevic, and C. Pierpaoli. Nonlinear registration of diffusion tensor images using directional information. In *Proc. Int. Soc. Magn. Reson. Med.*, volume 11, page 1213. Citeseer, 2004a.

G. K. Rohde, S. Pajevic, C. Pierpaoli, and P. J. Basser. A comprehensive approach for multi-channel image registration. In *International Workshop on Biomedical Image Registration*, pages 214–223. Springer, 2003.

G. K. Rohde, S. Pajevic, and C. Pierpaoli. Multi-channel registration of diffusion tensor images using directional information. In *Biomedical Imaging: Nano to Macro, 2004. IEEE International Symposium on*, pages 712–715. IEEE, 2004b.

M. Rousson, N. Paragios, and R. Deriche. Implicit active shape models for 3d segmentation in mr imaging. In *International Conference on Medical Image Computing and Computer-Assisted Intervention*, pages 209–216. Springer, 2004.

D. Rueckert, L. I. Sonoda, C. Hayes, D. L. Hill, M. O. Leach, and D. J. Hawkes. Nonrigid registration using free-form deformations: application to breast MR images. *IEEE transactions on medical imaging*, 18(8):712–721, 1999.

D. Rueckert, P. Aljabar, R. A. Heckemann, J. V. Hajnal, and A. Hammers. Diffeomorphic registration using B-splines. In *International Conference on Medical Image Computing and Computer-Assisted Intervention*, pages 702–709. Springer, 2006.

J. Ruiz-Alzola, C.-F. Westin, S. K. Warfield, C. Alberola, S. Maier, and R. Kikinis. Nonrigid registration of 3d tensor medical data. *Medical image analysis*, 6(2):143–161, 2002.

Z. Salo, M. Beek, and C. M. Whyne. Evaluation of mesh morphing and mapping techniques in patient specific modeling of the human pelvis. *International journal for numerical methods in biomedical engineering*, 29 (1):104–113, 2013a.

Z. Salo, M. Beek, and C. M. Whyne. Evaluation of mesh morphing and mapping techniques in patient specific modeling of the human pelvis. *International journal for numerical methods in biomedical engineering*, 29 (1):104–113, 2013b.

Z. Salo, M. Beek, D. Wright, and C. M. Whyne. Computed tomography landmark-based semi-automated mesh morphing and mapping techniques: Generation of patient specific models of the human pelvis without segmentation. *Journal of biomechanics*, 48(6):1125–1132, 2015.

R. Salvador, A. Peña, D. K. Menon, T. A. Carpenter, J. D. Pickard, and E. T. Bullmore. Formal characterization and extension of the linearized diffusion tensor model. *Human brain mapping*, 24(2):144–155, 2005.

N. Sarkalkan, H. Weinans, and A. A. Zadpoor. Statistical shape and appearance models of bones. *Bone*, 60:129–140, 2014.

S. P. Sastry, J. Kim, S. M. Shontz, B. A. Craven, F. C. Lynch, K. B. Manning, and T. Panitanarak. Patient-specific model generation and simulation for pre-operative surgical guidance for pulmonary embolism treatment. In *Image-Based Geometric Modeling and Mesh Generation*, pages 223–249. Springer, 2013.

R. J. Scalese, V. T. Obeso, and S. B. Issenberg. Simulation technology for skills training and competency assessment in medical education. *Journal of general internal medicine*, 23(1):46–49, 2008.

R. Shadmi, A. Mayer, N. Sochen, and H. Greenspan. Piecewise smooth affine registration of point-sets with application to dt-mri brain fiber-data. In *2010 IEEE International Symposium on Biomedical Imaging: From Nano to Macro*, pages 528–531. IEEE, 2010.

D. Shenton and Z. Cendes. Three-dimensional finite element mesh generation using delaunay tesselation. *IEEE transactions on Magnetics*, 21(6): 2535–2538, 1985.

M. N. Sheth. Patient-specific modeling of cardiac geometry in dyssynchronous heart failure. 2010.

V. B. Shim, R. P. Pitto, R. M. Streicher, P. J. Hunter, and I. A. Anderson. The use of sparse ct datasets for auto-generating accurate fe models of the femur and pelvis. *Journal of biomechanics*, 40(1):26–35, 2007.

V. B. Shim, R. P. Pitto, and I. A. Anderson. Quantitative ct with finite element analysis: towards a predictive tool for bone remodelling around an uncemented tapered stem. *International orthopaedics*, 36(7):1363–1369, 2012a.

V. B. Shim, R. P. Pitto, and I. A. Anderson. Quantitative ct with finite element analysis: towards a predictive tool for bone remodelling around an uncemented tapered stem. *International orthopaedics*, 36(7):1363–1369, 2012b.

V. B. Shim, T. F. Besier, D. G. Lloyd, K. Mithraratne, and J. F. Fernandez. The influence and biomechanical role of cartilage split line pattern on tibiofemoral cartilage stress distribution during the stance phase of gait. *Biomechanics and modeling in mechanobiology*, 15(1):195–204, 2016.

I. A. Sigal, M. R. Hardisty, and C. M. Whyne. Mesh-morphing algorithms for specimen-specific finite element modeling. *Journal of biomechanics*, 41(7):1381–1389, 2008.

M. B. Stegmann. Active appearance models: Theory, extensions and cases. *Informatics and Mathematical Modelling*, page 262, 2000.

E. V. Sullivan, T. Rohlfing, and A. Pfefferbaum. Longitudinal study of callosal microstructure in the normal adult aging brain using quantitative dti fiber tracking. *Developmental neuropsychology*, 35(3):233–256, 2010.

H. Talbot, C. Duriez, H. Courtecuisse, J. Relan, M. Sermesant, S. Cotin, and H. Delingette. Towards real-time computation of cardiac electrophysiology for training simulator. In *International Workshop on Statistical Atlases and Computational Models of the Heart*, pages 298–306. Springer, 2012.

G. Tang, Y. Liu, W. Li, J. Yao, B. Li, and P. Li. Optimization of b value in diffusion-weighted mri for the differential diagnosis of benign and malignant vertebral fractures. *Skeletal radiology*, 36(11):1035–1041, 2007.

M. Taylor, R. Bryan, and F. Galloway. Accounting for patient variability in finite element analysis of the intact and implanted hip and knee: a review.

International journal for numerical methods in biomedical engineering, 29 (2):273–292, 2013.

S. Timoshenko and J. Goodier. Theory of elasticity, mcgraw-hill, new york, 1970. *Fok-Ching Chong received the BS degree from the Department of Electrical Engineering, National Taiwan University, Taipei, Taiwan, in*, 1971.

D. S. Tuch, J. W. Belliveau, and V. J. Wedeen. A path integral approach to white matter tractography. In *Proceedings of the 8th Annual Meeting of ISMRM, Denver*, page 791, 2000.

D. S. Tuch, T. G. Reese, M. R. Wiegell, N. Makris, J. W. Belliveau, and V. J. Wedeen. High angular resolution diffusion imaging reveals intravoxel white matter fiber heterogeneity. *Magnetic Resonance in Medicine*, 48(4): 577–582, 2002.

S. P. Väänänen, L. Grassi, G. Flivik, J. S. Jurvelin, and H. Isaksson. Generation of 3d shape, density, cortical thickness and finite element mesh of proximal femur from a dxa image. *Medical image analysis*, 24(1):125–134, 2015.

E. M. Van Rikxoort, B. de Hoop, M. A. Viergever, M. Prokop, and B. van Ginneken. Automatic lung segmentation from thoracic computed tomography scans using a hybrid approach with error detection. *Medical physics*, 36(7):2934–2947, 2009.

T. Vercauteren, X. Pennec, A. Perchant, and N. Ayache. Diffeomorphic demons: Efficient non-parametric image registration. *NeuroImage*, 45(1): S61–S72, 2009.

E. Visser, E. H. Nijhuis, J. K. Buitelaar, and M. P. Zwiers. Partition-based mass clustering of tractography streamlines. *Neuroimage*, 54(1):303–312, 2011.

A. N. Voineskos, T. K. Rajji, N. J. Lobaugh, D. Miranda, M. E. Shenton, J. L. Kennedy, B. G. Pollock, and B. H. Mulsant. Age-related decline in white matter tract integrity and cognitive performance: a dti tractography and structural equation modeling study. *Neurobiology of aging*, 33(1):21–34, 2012.

Q. Wang, P.-T. Yap, G. Wu, and D. Shen. Application of neuroanatomical features to tractography clustering. *Human brain mapping*, 34(9):2089–2102, 2013a.

Q. Wang, P.-T. Yap, G. Wu, and D. Shen. Diffusion tensor image registration using hybrid connectivity and tensor features. *Human brain mapping*, 35 (7):3529–3546, 2014.

X. Wang and X. Qian. A statistical atlas based approach to automated subject-specific fe modeling. *Computer-Aided Design*, 70:67–77, 2016.

Y. Wang, A. Gupta, Z. Liu, H. Zhang, M. L. Escolar, J. H. Gilmore, S. Gouttard, P. Fillard, E. Maltbie, G. Gerig, et al. Dti registration in atlas based fiber analysis of infantile krabbe disease. *Neuroimage*, 55(4):1577–1586, 2011.

Y. Wang, Z. Chen, S. Nie, and C.-F. Westin. Diffusion tensor image registration using polynomial expansion. *Physics in medicine and biology*, 58 (17):6029, 2013b.

Z. Wang, B. C. Vemuri, Y. Chen, and T. H. Mareci. A constrained variational principle for direct estimation and smoothing of the diffusion tensor field from complex dwi. *IEEE transactions on Medical Imaging*, 23(8): 930–939, 2004.

D. Wassermann, Y. Rathi, S. Bouix, M. Kubicki, R. Kikinis, M. Shenton, and C.-F. Westin. White matter bundle registration and population analysis based on gaussian processes. In *Biennial International Conference on Information Processing in Medical Imaging*, pages 320–332. Springer, 2011.

V. J. Wedeen, P. Hagmann, W.-Y. I. Tseng, T. G. Reese, and R. M. Weisskoff. Mapping complex tissue architecture with diffusion spectrum magnetic resonance imaging. *Magnetic resonance in medicine*, 54(6):1377–1386, 2005.

P. L. Williams et al. Gray's anatomy. 1980.

A. Wittek and K. Miller. Letter to the editor: Current progress in patient-specific modeling by neal and kerckhoffs (2010). *Briefings in bioinformatics*, page bbr046, 2011.

C. D. Woodward. Skinning techniques for interactive b-spline surface interpolation. *Computer-Aided Design*, 20(8):441–451, 1988.

X. Wu, V. Pegoraro, V. Luboz, P. F. Neumann, R. Bardsley, S. Dawson, and S. Cotin. New approaches to computer-based interventional neuroradiology training. *Studies in health technology and informatics*, 111:602–607, 2005.

Y. Xia, U. Turken, S. L. Whitfield-Gabrieli, and J. D. Gabrieli. Knowledge-based classification of neuronal fibers in entire brain. In *International Conference on Medical Image Computing and Computer-Assisted Intervention*, pages 205–212. Springer, 2005.

D. Xu, S. Mori, D. Shen, P. Van Zijl, and C. Davatzikos. Spatial normalization of diffusion tensor fields. *Magnetic resonance in medicine*, 50(1): 175–182, 2003.

C. L. Yanez. *Amélioration des Techniques de Génération de maillages 3D des structures anatomiques humaines pour la Méthode des Éléments Finis*. PhD thesis, UNIVERSITE JOSEPH FOURIER, 2009.

J. Yang, D. Shen, C. Davatzikos, and R. Verma. Diffusion tensor image registration using tensor geometry and orientation features. In *International Conference on Medical Image Computing and Computer-Assisted Intervention*, pages 905–913. Springer, 2008.

P. Yap, H. Zhu, W. Lin, and D. Shen. Hierarchical diffusion tensor image registration based on tensor regional distributions. In *Proc. Intl. Soc. Mag. Reson. Med*, volume 17, page 1426, 2009a.

P.-T. Yap, G. Wu, H. Zhu, W. Lin, and D. Shen. Timer: Tensor image morphing for elastic registration. *NeuroImage*, 47(2):549–563, 2009b.

P.-T. Yap, G. Wu, H. Zhu, W. Lin, and D. Shen. F-timer: fast tensor image morphing for elastic registration. *IEEE transactions on medical imaging*, 29(5):1192–1203, 2010.

C. Ye, A. Carass, E. Murano, M. Stone, and J. L. Prince. A bayesian approach to distinguishing interdigitated muscles in the tongue from limited diffusion weighted imaging. In *Bayesian and grAphical Models for Biomedical Imaging*, pages 13–24. Springer, 2014.

C. Ye, E. Murano, M. Stone, and J. L. Prince. A bayesian approach to distinguishing interdigitated tongue muscles from limited diffusion magnetic resonance imaging. *Computerized Medical Imaging and Graphics*, 45:63–74, 2015.

P. Young, T. Beresford-West, S. Coward, B. Notarberardino, B. Walker, and A. Abdul-Aziz. An efficient approach to converting three-dimensional image data into highly accurate computational models. *Philosophical Transactions of the Royal Society of London A: Mathematical, Physical and Engineering Sciences*, 366(1878):3155–3173, 2008.

A. L. Yuille and N. M. Grzywacz. The motion coherence theory. In *Computer Vision., Second International Conference on*, pages 344–353. IEEE, 1988.

A. L. Yuille and N. M. Grzywacz. A mathematical analysis of the motion coherence theory. *International Journal of Computer Vision*, 3(2):155–175, 1989.

G. Zhang. *Computational Bioengineering*. CRC Press, 2015.

H. Zhang, P. A. Yushkevich, D. C. Alexander, and J. C. Gee. Deformable registration of diffusion tensor mr images with explicit orientation optimization. *Medical image analysis*, 10(5):764–785, 2006.

L. Zhang and J. M. Reinhardt. 3d pulmonary ct image registration with a standard lung atlas. In *Medical Imaging 2000*, pages 67–77. International Society for Optics and Photonics, 2000.

X. Zhang, Z. Tang, M. A. Liebschner, D. Kim, S. Shen, C.-M. Chang, P. Yuan, G. Zhang, J. Gateno, X. Zhou, et al. An eface-template method for efficiently generating patient-specific anatomically-detailed facial soft tissue fe models for craniomaxillofacial surgery simulation. *Annals of biomedical engineering*, 44(5):1656–1671, 2016.

Q. Zhou, O. Michailovich, and Y. Rathi. Resolving complex fibre architecture by means of sparse spherical deconvolution in the presence of isotropic diffusion. In *SPIE medical imaging*, pages 903425–903425. International Society for Optics and Photonics, 2014.

U. Ziyan, M. R. Sabuncu, L. J. O'donnell, and C.-F. Westin. Nonlinear registration of diffusion mr images based on fiber bundles. In *International Conference on Medical Image Computing and Computer-Assisted Intervention*, pages 351–358. Springer, 2007.

O. Zvitia, A. Mayer, R. Shadmi, S. Miron, and H. K. Greenspan. Co-registration of white matter tractographies by adaptive-mean-shift and gaussian mixture modeling. *IEEE transactions on medical imaging*, 29 (1):132–145, 2010.